

Quantifying the dispersion of turbidity currents generated by seafloor mining operations

A.A. BEDON VASQUEZ

DELFT UNIVERSITY OF TECHNOLOGY

Section of Dredging Engineering

7 August, 2020

Quantifying the dispersion of turbidity currents generated by seafloor mining operations

Author:

A.A. Bedón Vásquez, 4145399

Thesis Committee:

Prof. Dr. ir. C. van Rhee (**Chairman**)

Dr. ir. R.L.J. Helmons

Ir. M. Elerian

Dr. ir. C. Chassagne

Abstract

Turbidity currents are common in the waters around the world. They can be caused by earthquakes, collapsing slopes or other geological disturbances. However, turbidity currents can also be caused by deep sea mining activities. Deep sea mining is done with special mining vehicles. There are three main operations within this mining vehicle: collecting nodules, separating the nodules from the mixture and discharging the mixture of sediment and water towards the environment. After impingement of the discharged flow with the seabed, it is expected that the flow will take the form of a turbidity current. Turbidity currents belong to a larger class of flows called gravity currents. Furthermore, turbidity currents are typically defined as dilute flows in which particles are dominantly supported by fluid turbulence. These currents have an interstitial fluid that is a liquid, generally water.

The objective of this research is to increase knowledge of the behavior of these currents and to obtain experimental results that can be used for validation of CFD models. In this research the influence of the initial concentration on the dispersion, deposition and entrainment of the current is investigated. In addition, the spread of particles within the current is researched. Furthermore, different types of sediment are used with various particle size ranges and particle properties.

The experimental methodology can be divided in two parts. The first part are experiments that involve a full-depth lock release of a fixed volume suspension of a sediment with different particle size ranges and particle properties into water. The initial concentration is varied and the obtained current is recorded with a high-speed camera. The second part consists of multiple calibration procedures. During these procedures, different concentrations of sediment are mixed with water and the resulting solution is recorded. This data is used to create a calibration function that in turn can be used to quantify the concentrations of sediment in the previous recorded currents. The experimental methodology differs from previous work due to this calibration procedure. Afterwards, video processing is used to perform an analysis of the current.

The resulting turbidity currents go through three phases as observed in the experiments and previous work. At the start, there is an initial phase where the front is formed and the current accelerates. During this phase a limited amount of particles settle out of the current. Afterwards, the current transitions into a second phase when the velocity of the front starts to decrease due to inertial forces and due to the start of particle settling at the rear of the current. The last phase is when the backflowing bore created by the ambient fluid at the release of the gate reaches the front and decelerates the current until viscous forces start to dominate until the current vanishes. The experiments shows that currents transporting fine particles reach higher velocities and may travel for longer distances in comparison to currents composed of larger particles. Furthermore, the combination of fine and large particles has a substantial effect on the currents dynamics. The currents composed of a mixture of these two sediment types travel longer distances than currents with only large particles. The performed experiments also focus on varying the initial concentration and sediment type. These show that larger particles tend to entrain more with the ambient fluid in comparison to smaller particles and thus they have a larger vertical dispersion. Furthermore, currents composed of sediment with only fine particles will have a more rapid transition into a dense front and a less dense middle and rear part of the current. Currents composed of fine sediment and a combined sediment with small and large particles have a clear division between a dense basal layer and a less dense top layer within the current. At last, deposition patterns are different per sediment type. Sediment composed of larger particles will have a larger deposition rate than sediment composed of smaller particles. Furthermore combining both sediment types will increase the deposition rate at the beginning of the current.

Acknowledgments

This report is written to support the research that is undertaken to obtain the MSc degree in Dredging Engineering at the Delft University of Technology.

First, I would like to express my gratitude towards my supervisors. Dr. ir. Rudy Helmons, not only for introducing me to this topic and presenting the challenges that came along with it but also for his support and advice throughout the length of my research. I would also like to sincerely thank my daily supervisor Ir. Mohamed Elerian, who is currently pursuing his PhD degree at the TU Delft. His support, advice and enormous commitment helped me realize my thesis in time and got me through the difficult stages of the investigation. Both of my supervisors helped me to steer this research into the right direction that finally led to this result.

I would also like to thank Joris Lamers. He introduced me to a new method to realize my experiments when resources became limited. His support and helpful advice throughout this research contributed on improving this thesis.

Furthermore, I would like to thank the TU Delft dredging laboratory staff Ed Stok and Andre van den Bosch for helping me realize the experimental set-up.

Finally I would like to extend my gratitude to the third member of my graduation committee, Prof. Dr. ir. C. van Rhee. I am grateful for the discussions during the progress meetings and the advice that gave direction to this research.

Table of Content

List of figures	7
List of tables	12
Nomenclature	13
1 Introduction	15
1.1 General background	15
1.2 Deep sea mining	17
1.2.1 Mineral deposits and deep sea mining challenges	17
1.2.2 Deep-sea mining processes	19
1.3 Problem definition.....	22
1.4 Objective.....	22
1.5 Research approach	22
1.6 Report structure	23
2 Theoretical Framework	24
2.1 Turbidity Currents	24
2.1.1 Hydraulic theory	24
2.2 Anatomy of turbidity currents.....	26
2.2.1 The head	26
2.2.2 The Body	28
2.3 Flow properties	29
2.3.1 Velocity profiles	29
2.3.2 Concentration profiles	29
2.4 The Richardson number	30
2.5 Lock-exchange experiments with saline gravity currents	31
2.6 Particle-driven gravity currents.....	33
2.7 Influence of particle size distribution and deposition behavior.....	34
2.8 Settling velocity of particles	36
2.8.1 Forces on immersed objects	36
2.8.2 Hindered settling effect.....	38
2.8.3 Multi-sized mixture of particles.....	38
2.8.4 Settling velocity of a non-spherical particle	39
3. Experimental Methodology	41
3.1 Introduction.....	41
3.2 Experimental set-up for the lock exchange experiments	41
3.2.1 The tank.....	41
3.2.2 Recording camera and additional accessories	42

3.2.3	Other tools.....	44
3.2.4	Sediment.....	44
3.2.5	Experimental procedure for lock exchange experiments	45
3.3	Experimental set-up for the calibration	47
3.3.1	The tank and other tools	47
3.3.2	Experimental procedure for calibration	47
3.3.3	Concentration measurement	49
3.4	Experimental measurements	53
3.4.1	Flow Velocity	53
3.5	Experimental difficulties.....	55
4.	Experimental results and analysis.....	57
4.1	Head velocities	57
4.1.1	Froude number.....	67
4.2	Concentrations	69
4.2.1	Maximum measurable concentration	69
4.2.2	Concentration measurement	70
4.3	Mass calculation	79
4.3.1	Transition phase	79
4.3.2	Mass calculation over time.....	83
4.3.3	Total mass.....	89
5.	Conclusion and Recommendations	92
5.1	Conclusions.....	92
5.2	Further recommendations	93
	References.....	95
A.	First Appendix: Sediment properties	99
A. 1	Sediment type I ($75 - 125\mu m$).....	99
A.1.1	Civil engineering test results for sediment type I:	100
A. 2	Sediment type II ($4 - 60\mu m$):	101
B.	Particle settling velocity	102
C.	Third Appendix: Color Maps.....	104
D.	Fourth Appendix: Concentration profiles:	132
E.	Fifth Appendix: Mass over time graphs	138
F.	Sixth Appendix: Logbook of experiments	146
G.	Seventh Appendix: Python code	147
G.1.	Measuring of the head velocity in time:	147
G.2.	Digital filter used for results:	151

G.3.	Calibration table per sediment type.....	151
G.4.	Library used for the results	154

List of figures

Figure 1.1 Rare earth metal mines around the world (Li, 2019)	15
Figure 1.2 A world map showing the locations of the three main marine mineral deposits (Miller, Thompson, Johnston, & Santillo, 2018)	16
Figure 1.3 Types of Deep-sea mining (Nugent, 2018)	17
Figure 1.4 Polymetallic nodules on the seafloor (Nugent, 2018)	18
Figure 1.5 Polymetallic sulfides (Nugent, 2018)	18
Figure 1.6 Cobalt crusts (Nugent, 2018)	19
Figure 1.7 Deep-sea mining processes with different collectors, (Agravante, 2020)	20
Figure 1.8 Proposed hydraulic Mining System by GEMONOD, (ISA, 2020)	20
Figure 1.9 Different types of mining vehicles, from left to right (clockwise): Auxiliary cutter, Bulk cutter, Collecting machine (Nautilus Minerals, 2020) and Hydraulic polymetallic nodule collector, (IHC, 2020)	21
Figure 1.10 Hydraulic mining vehicle with discharge transitioning into a turbidity current. Modified from: (Decrop & De Wachter)	21
Figure 2.1. Gravity current with physical quantities defined (Moodie, 2002)	25
Figure 2.2. Turbidity current anatomy	26
Figure 2.3. Two dimensional image of the head and body illustrating well-developed Kelvin-Helmholtz billows. The inset shows the clefts and lobes structure under the head (Simpson 1969)	28
Figure 2.4. Schematic figure defining the regions in the body according to (Britter & Simpson, 1978) and (Simpson & Britter, 1979))	29
Figure 2.5. Schematic diagram of the head and body of a gravity current showing a vertical profile of the downstream velocity (Kneller & Buckee, 2000)	29
Figure 2.6. Schematic diagram showing various characteristic density/concentration profiles in particle-driven currents. (a) A two-layer model type concentration profile. (b) A smooth profile, characteristic low-concentration flow. (c) A stepped concentration profile observed in erosional flows. (d) A Rouse-type distribution of sediment grain-sizes observed in turbidity currents, coarse material is concentrated towards the lower part of the flow and fine-grained material is more evenly distributed throughout the depth of the flow (Kneller & Buckee, 2000)	30
Figure 2.7. Shadow of a volume of salt water collapsing into fresh water, the dotted line shows the position of the lock gates. The graphs represent the release of the volume at 5,7,9 and 17 seconds (Simpson, 1997)	31
Figure 2.8. Front position and bore position as functions of time after release with $h_0/H=1$, data taken from multiple experiments performed by (Rottman & Simpson, 1983); (Keulegan, 1957) modified by (Simpson, 1997)	32
Figure 2.9 Collapse of volume of dense fluid with $h_0/H=1$, (i),(ii) and(iii) represent the first stage with (iv) as the second stage (Simpson, 1997)	33
Figure 2.10. Photographs of a particle-driven gravity current at 3, 7 and 21 seconds after release, particles of $53\mu\text{m}$ are used. Modified from: (Bonnecaze, Huppert, & Lister, 1993)	34
Figure 2.11 Schematic representation of the forces acting on a spherical particle	37
Figure 2.12 Drag coefficient as a function of the particle Reynolds number (Matousek, 2004)	37
Figure 2.13 The shape factor ξ as a function of the dimensionless particle diameter d^* and the volumetric form factor K. (Matousek, 2004)	40
Figure 3.1 Schematic representation of the tank	42
Figure 3.2 Schematic representation of the total tank set-up	42
Figure 3.3 Level used on the tank	42

Figure 3.4 Aperture kept constant	43
Figure 3.5 High-speed camera used for experiments	43
Figure 3.6 High-speed camera on tripod facing the tank	43
Figure 3.7 Final set-up of the tank with backlight	44
Figure 3.8 Side view of the Tank set-up showing mixer, wooden panel with LED stripes and diffuse paper	44
Figure 3.9 Millisil M10 sediment put in the oven to dry out	45
Figure 3.10 Snapshots of a recorded video with Sediment Type II (4-60 μ m) and $\phi=0.01$	46
Figure 3.11 Tank set-up for the calibration experiments	47
Figure 3.12 Scale with sediment divided into specific masses	48
Figure 3.13 Shades of grey for Sediment Type II, with an increase of concentration	48
Figure 3.14 Snapshot of the calibration procedure	49
Figure 3.15 Standard Gaussian kernel for OpenCV (OpenCV Tutorial C++, 2020)	50
Figure 3.16 Pixel calibration by making use of curve fit. The dots are the measured data and the line is the curve fit graph	50
Figure 3.17 Image with current showing two dark lines where the concentration are determined	51
Figure 3.18 Concentration profile for two sections of the current	51
Figure 3.19 Color map of a calibrated current for sediment type II and a concentration of 0.25%	53
Figure 3.20 Snapshots of the original first frame of the video (1), the original video with the current (2), the corrected image (3) and the binary image of the current (4)	54
Figure 3.21 Velocity-time graph of sediment type II with initial concentration of 0.1%	54
Figure 3.22 Magnitude spectrum taken at the beginning of the tank for Sediment Type II and a concentration of 0.1%	55
Figure 4.1 Velocity-time graph of sediment Type II with initial concentration of 0.1% measured every 50 frames	57
Figure 4.2 Velocity-distance graph of sediment Type II with initial concentration of 0.1% measured every 5 pixel	57
Figure 4.3 (a) Filtered signal with time delay using a Chebyshev Bandpass filter type 2 and (b) a filtered signal with a correction using the function <code>filtfilt</code> for Sediment Type II and concentration of 0.1%. Blue line represents the original velocity and the orange line represents the filtered velocity	58
Figure 4.4 Starting point of measurement at the tank, at approximately 0.15m from the lock-gate	60
Figure 4.5 Comparison of head velocities for sediment type II with initial concentration of 1%	60
Figure 4.6 Comparison of head velocities for sediment type II with initial concentration of 2.5%	61
Figure 4.7 Head velocity over time for all three types of sediment. (a) Sediment type I, (b) Sediment type II and (c) Combined Sediment type I and II	62
Figure 4.8 Settling velocity of particles for Sediment type I	64
Figure 4.9 Settling velocity of particles for Sediment type II	64
Figure 4.10 Distance over time for the three types of sediment: (a) Sediment type I, (b) Sediment type II and (c) Sediment type I and II	65
Figure 4.11 Froude number for all sediment types with (a) sediment type I, (b) sediment type II and (c) combined sediment type I and II	68
Figure 4.12 Pixel-concentration graph for sediment type I and II combination, (4-125micro) for pixel nr.200 measured for concentrations up to 1%	69
Figure 4.13 Signal to Noise ratio (De Producer School, 2020)	70

Figure 4.14 Example of a calibrated color map for sediment type I for initial concentration of 1.0%	71
Figure 4.15 Example of a calibrated color map for sediment type II for initial concentration of 1.0%	72
Figure 4.16 Example of a calibrated color map for the combined sediment type I and II for initial concentration of 1.0%	73
Figure 4.17 Example of the tank divided into 5 sections for the measurement of vertical concentration profiles	74
Figure 4.18 Selection of vertical concentration profiles for sediment type I	77
Figure 4.19 Selection of vertical concentration profiles for sediment type II	78
Figure 4.20 Selection of vertical concentration profiles for combined sediment type I and II	78
Figure 4.21 Example of the tank displaying some positions where the rectangular surface was measured	79
Figure 4.22 Results for mass measurement at a fixed position in the body over time for sediment type I, (a) displays the maximum concentration found and (b) displays the calculated mass	81
Figure 4.23 Results for mass measurement at a fixed position in the body over time for sediment type II, (a) displays the maximum concentration found and (b) displays the calculated mass	81
Figure 4.24 Results for mass measurement at a fixed position in the body over time for the combined sediment type I and II, (a) displays the maximum concentration found and (b) displays the calculated mass	82
Figure 4.25 Example of the tank divided into 5 sections where the mass is measured at the vertical lines	83
Figure 4.26 Mass over time measured at 5 different sections of the tank for sediment type I, (a) displays the mass found and (b) displays the maximum concentration found	84
Figure 4.27 Mass over time measured at 5 different sections of the tank for sediment type II, (a) displays the mass found and (b) displays the maximum concentration found	85
Figure 4.28 Mass over time measured at 5 different sections of the tank for the combined sediment type I and II, (a) displays the mass found and (b) displays the maximum concentration found	86
Figure 4.29 Comparison between (a) sediment type II and (b) the combined sediment type I and II for initial concentration of 0.25%	88
Figure 4.30 Total mass measured for the complete current over time: (a) displays results for sediment type I, (b) displays results for sediment type II and (c) displays results for the combined sediment type I and II	90
Figure B.1 Settling velocity of Sediment type I	102
Figure B.2 Settling velocity of Sediment type II	102
Figure B.3 Settling velocity with multiple sizes particles	103
Figure B.4 Settling velocity with hindered settling for sediment type I and sediment type II	103
Figure C.1 Calibrated color map for sediment type II with 0.1% initial concentration	105
Figure C.2 Calibrated color map for sediment type II with 0.25% initial concentration	107
Figure C.3 Calibrated color map for sediment type II with 0.5% initial concentration	108
Figure C.4 Calibrated color map for sediment type II with 1.0% initial concentration	109
Figure C.5 Calibrated color map for sediment type II with 1.5% initial concentration	110
Figure C.6 Calibrated color map for sediment type II with 2.0% initial concentration	111
Figure C.7 Color map for sediment type II with 2.5% initial concentration	112
Figure C.8 Color map for sediment type II with 3.0% initial concentration	113

Figure C.9 Calibrated color map for the combined sediment type I and II with 0.1% initial concentration	115
Figure C.10 Calibrated color map for the combined sediment type I and II with 0.25% initial concentration	117
Figure C.11 Calibrated color map for the combined sediment type I and II with 0.5% initial concentration	118
Figure C.12 Calibrated color map for the combined sediment type I and II with 1.0% initial concentration	119
Figure C.13 Calibrated color map for the combined sediment type I and II with 1.5% initial concentration	120
Figure C.14 Calibrated color map for the combined sediment type I and II with 2.0% initial concentration	121
Figure C.15 Color map for the combined sediment type I and II with 2.5% initial concentration	122
Figure C.16 Color map for the combined sediment type I and II with 3.0% initial concentration	123
Figure C.17 Calibrated color map for sediment type I with 0.5% initial concentration	125
Figure C.18 Calibrated color map for sediment type I with 1.0% initial concentration	127
Figure C.19 Calibrated color map for sediment type I with 1.5% initial concentration	128
Figure C.20 Calibrated color map for sediment type I with 1.5% initial concentration	129
Figure C.21 Color map for sediment type I with 2.5% initial concentration	130
Figure C.22 Color map for sediment type I with 3.0% initial concentration	131
Figure D.1 Vertical concentration profiles for sediment type I, initial concentrations of: 0.5%, 1.0% and 1.5%	132
Figure D.2 Vertical concentration profiles for sediment type I, initial concentration of: 2.0%	133
Figure D.3 Vertical concentration profiles for sediment type II, initial concentration of: 0.1%, 0.25%	133
Figure D.4 Vertical concentration profiles for sediment type II, initial concentration of: 0.5%, 1.0% and 1.5%	134
Figure D.5 Vertical concentration profiles for sediment type II, initial concentration of: 2.0%	135
Figure D.6 Vertical concentration profiles for combined sediment type I and II, initial concentration of: 0.1% and 0.25%	135
Figure D.7 Vertical concentration profiles for combined sediment type I and II, initial concentration of: 0.5%, 1.0% and 1.5%	136
Figure D.8 Vertical concentration profiles for combined sediment type I and II, initial concentration of: 2.0%	137
Figure E.1 Mass over time measured at 5 different sections of the tank for sediment type I, initial concentrations: 0.5% and 1.0%	138
Figure E.2 Mass over time measured at 5 different sections of the tank for sediment type I, initial concentrations: 1.5% and 2.0%	139
Figure E.3 Mass over time measured at 5 different sections of the tank for sediment type II, initial concentration: 0.1% and 0.25%	140
Figure E.4 Mass over time measured at 5 different sections of the tank for sediment type II, initial concentration: 0.5% and 1.0%	141
Figure E.5 Mass over time measured at 5 different sections of the tank for sediment type II, initial concentration: 1.5% and 2.0%	142
Figure E.6 Mass over time measured at 5 different sections of the tank for combined sediment type I and II, initial concentration: 0.1% and 0.25%	143
Figure E.7 Mass over time measured at 5 different sections of the tank for combined sediment type I and II, initial concentration: 0.5% and 1.0%	144

Figure E.8 Mass over time measured at 5 different sections of the tank for combined sediment type I and II, initial concentration: 1.5% and 2.0%

145

List of tables

Table 3 1 Camera settings for all the experiments	44
Table 3 2 Summary of experiments	46
Table 3 3 Sediment concentration ranges and steps within	49
Table 4 1 Sample frequency per current	59
Table 4 2 Results for the total mass measured for the complete current over time for different types of sediment	91

Nomenclature

C: Initial sediment concentration [-]	24
C_D : Drag coefficient [-]	25
C_m : Mass Concentration	13
d: Particle diameter [m]	25
d^* : Dimensionless particle diameter [-]	28
f_b : Basal friction factor [-]	16
F_B : Buoyancy force [N]	25
F_D : Drag force [N]	25
F_G : gravitational force [N]	25
F_{Gp} : Force due to gravitational acceleration [N]	25
F_{wp} : Submerged weight for a spherical particle [N]	25
Fr: Froude number [-]	15
Fr_d : Froude number for the front condition [-]	16
g: Gravitational acceleratio [m/s ²]	14
g' : Reduced gravity [-]	14
H: Mean total depth [m]	13
h: Thickness of the bottom current [m]	13
h_0 : Height of the head of the current [m]	15
H_d : Height [m]	24
K: Volumetric factor [-]	28
p_1 : Pressure in upper layer [Pa]	14
p_2 : Pressure in lower layer [Pa]	14
q_{mix} : Buoyancy flux [m ⁴ /s ³]	16
Re: Reynolds number [-]	13
Re_p : Particle Reynolds number [-]	26
Ri_f : Flux Richardson number [-]	19
Ri_g : Gradient Richardson number [-]	19
t_c : Dimensional time [-]	22
u: Fluid velocity [m/s]	13
U: Local flow velocity in x-direction [m/s]	15
U^* : Shear velocity [m/s]	15
U_0 : Velocity of the head [m/s]	15
U_f : Flow velocity [m/s]	16
U_{max} : Maximum downstream velocity [m/s]	18
U_s : Characteristic particle settling velocity [m/s]	24
U_y : Mean downstream velocity at height y [m/s]	19
V: Initial volume [m ³]	24
$v_{r,i}$: Relative velocity of particles of fraction i [m/s]	27
v_0 : Terminal settling velocity of particle [m/s]	27
v_{0ns} : Terminal velocity of a non-spherical solid particle [m/s]	28
v_f : Fluid velocity [m/s]	25
v_p : Particle velocity [m/s]	25
v_r : Relative velocity [m/s]	25
v_{ts} : Terminal settling velocity [m/s]	26
W: Width [m]	24
y: Hydraulic mean depth of the flow [m]	15

z: Thickness of the bottom current [m]	14
Δ : Specific density [-]	27
η : Displacement of the free surface [m]	13
μ : Dynamic viscosity [Pa*s]	26
ν : Kinematic viscosity [m ² /s]	22
ξ : Shape factor [-]	28
ρ_0 : Reference density [kg/m ³]	19
ρ_1 : Constant density of upper fluid [kg/m ³]	13
ρ_2 : Constant density of lower fluid [kg/m ³]	13
ρ_a : Density of the ambient fluid [kg/m ³]	14
ρ_c : Density of the current [kg/m ³]	14
ρ_p : Particle density [kg/m ³]	25
φ : Volume concentration [-]	27

1 Introduction

1.1 General background

The population in the world is currently growing at a fast rate and it is expected to keep increasing with a linear trend the upcoming years (Roser, Ritchie, & Ortiz-Ospina, 2020). This phenomenon combined with the rapid rise of the middle class and the continuous emerge of new technologies and their applications leads to a greater demand on natural resources. On the other hand the supply of these resources faces shortage due to factors such as climate change, political instability, different ethic perspectives, resource nationalism and the need for yet to be discovered new technologies. A couple of the natural resources currently facing shortage are precious metals and minerals as the world turns to electrification to decarbonize in an effort to battle climate change. Demand for copper is predicted to increase by 2.6% annually and lithium by 650% before 2027. Furthermore, rare earth metals are expected to increase in demand by 3.5% per annum rising to \$4.5bn worth (Lempriere & Casey, 2019).

As the so called 'green revolution' continues, the need for more critical minerals and metals will increases rapidly. For example, 50% of the cobalt produced each year is being used by the battery sector (Lempriere & Casey, 2019). These batteries allow products like electric cars to boom in the current market. Currently more than 60% of cobalt is being mined in the Democratic Republic of Congo with another source of import being China (Lempriere & Casey, 2019).

China does not only export cobalt but 35% of global reserves of rare earth minerals that are commonly used in high-tech devices, clean energy and automotive are found there. These are the largest reserves in the world with china producing 70% of the demand of rare minerals in 2018 (Li, 2019).

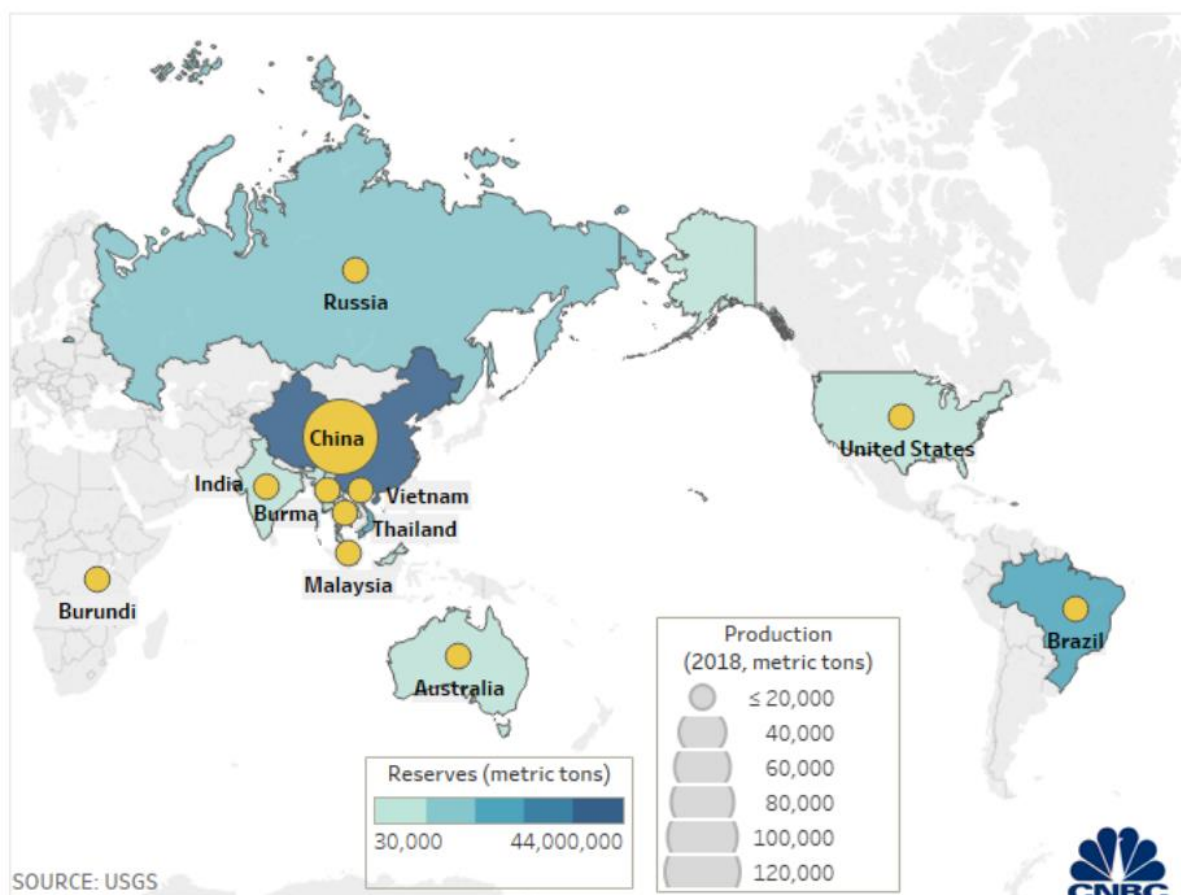


Figure 1.1 Rare earth metal mines around the world (Li, 2019)

Due to the restriction of China in its exports of rare materials to secure domestic supply and to address resource depletion a new source of rare earths is needed with new investment opportunities (Li, 2019).

The interest for commercial mining in the deep sea has increased in the last years. Deep-sea mining is the process of retrieving mineral deposits from the deep sea. The deep sea is the area of the ocean below 200m. This area covers around 65% of the Earth's surface (IUCN, 2019).

The interest in deep-sea mining also include other factors such as the unavoidable exhaustion of terrestrial deposits for metals over the last decades. This, combined with the increase in demand for rare metals to produce high-tech applications such as electric cars and also used in green technologies such as wind turbines and solar panels, gives a rise to overall global pressure to keep investing in the research of this new opportunity.

So far, the focus has been on exploring the deep sea. The seafloor contains large geological features such as abyssal plains, seamounts and deep trenches. These remote areas are the living environment of unique species most of who are still undiscovered. The deep sea remains a terrain that still has to be completely understood and studied.

Although no commercial scale in deep-sea mining has taken place, a range of mining operations are active in shallow seabed with shallow seabed mining for diamonds at the coast of Namibia since 2001 (Miller, Thompson, Johnston, & Santillo, 2018). Mineral extraction across the deep sea has been proposed at several regions. There are three main resources of commercial interest: manganese nodules (MN) on the abyssal plains, this is situated particularly in the Pacific Ocean; SMS (Seafloor massive sulfide) deposits at hydrothermal vents off the coast of Papua New Guinea; and cobalt-rich crusts (CRC), these are also found in the Pacific Ocean (Miller, Thompson, Johnston, & Santillo, 2018).

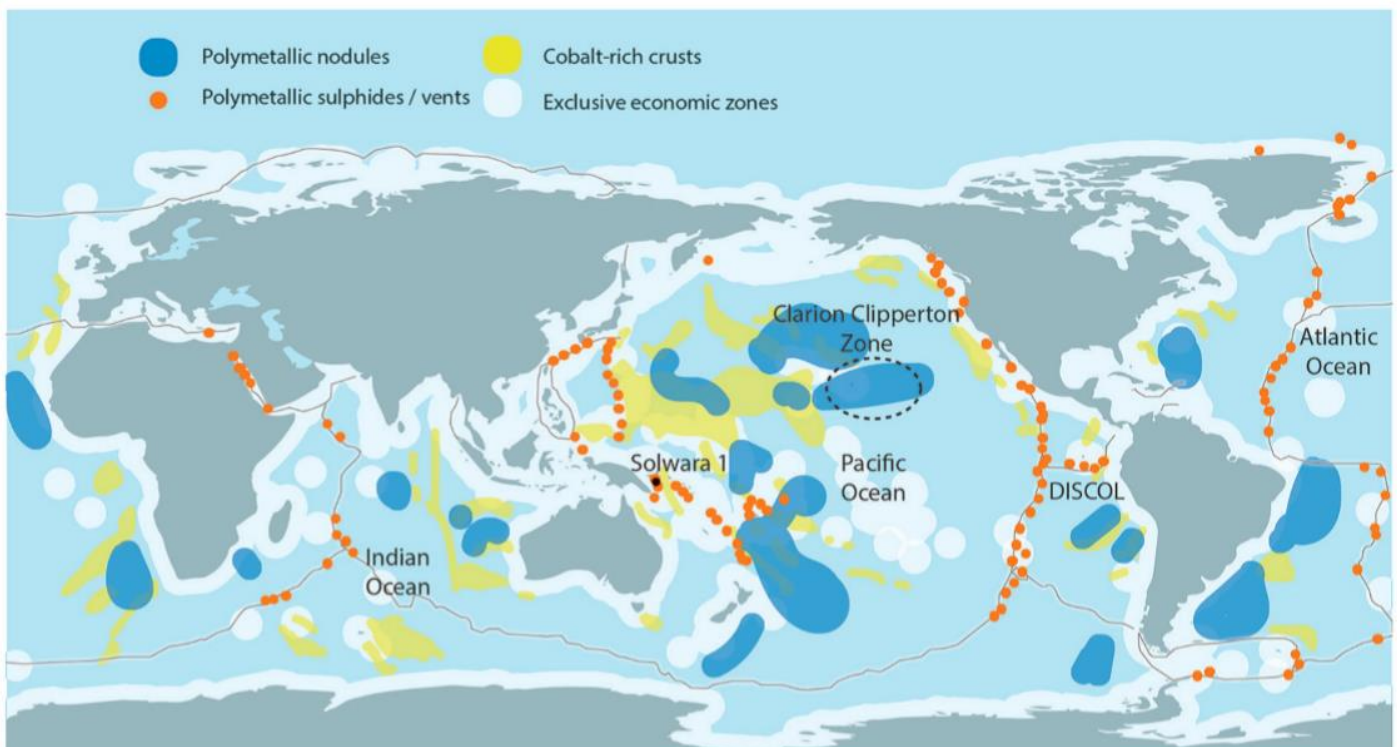


Figure 1.2 A world map showing the locations of the three main marine mineral deposits (Miller, Thompson, Johnston, & Santillo, 2018)

1.2 Deep sea mining

There are three different types of main resources that are of interest for extraction. This also means that there are three different types of deep-sea mining as can be seen in Figure 1.3. The mining activities are based on similar concepts but they also have their own unique challenges.

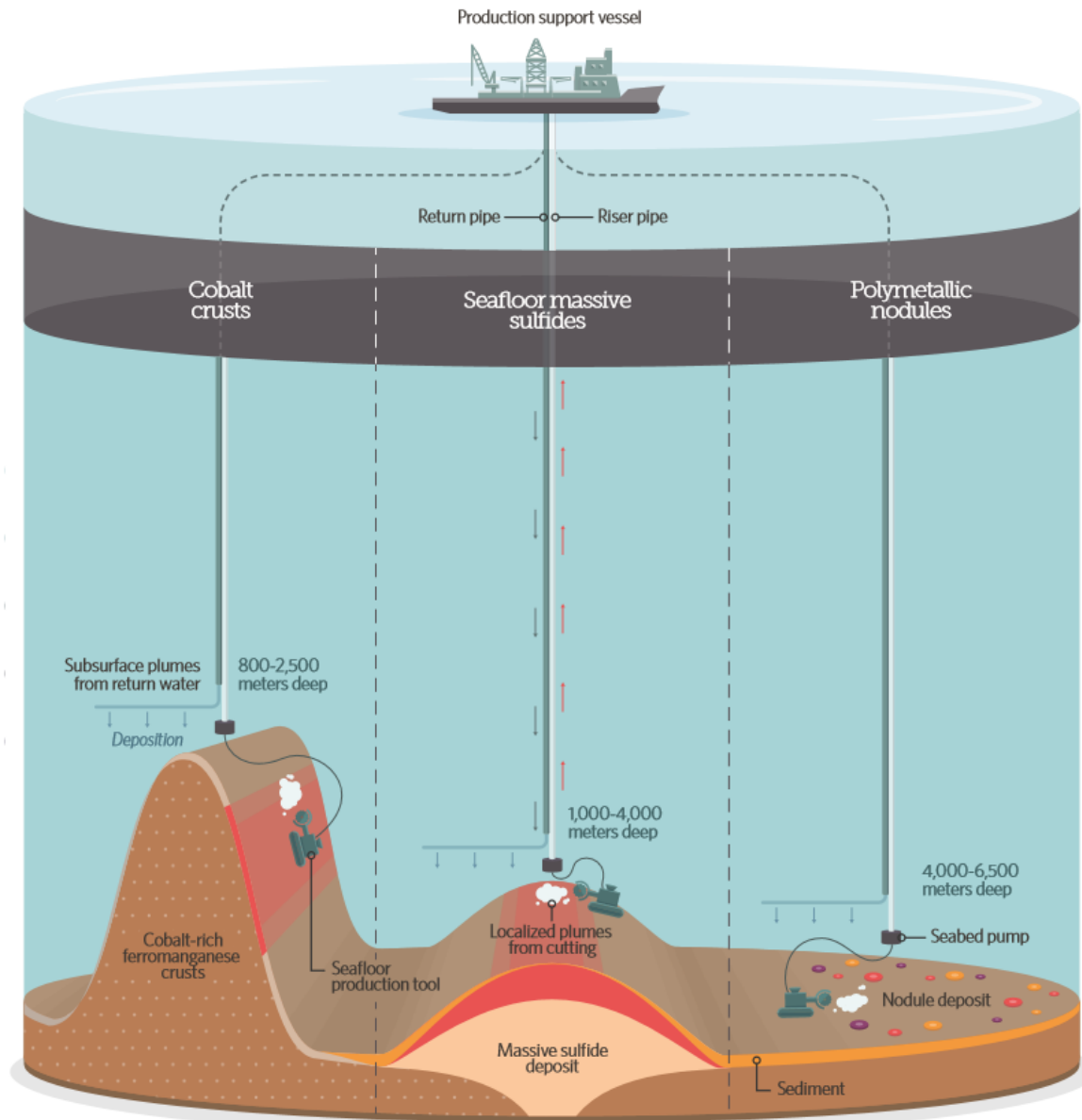


Figure 1.3 Types of Deep-sea mining (Nugent, 2018)

1.2.1 Mineral deposits and deep sea mining challenges

Manganese (Polymetallic) Nodules of the Abys

Currently there are 18 ISA (International Seabed Authority) exploration contracts (Nugent, 2018). Polymetallic nodules are rounded accretions that cover vast areas of the seafloor, see Figure 1.4, (MIDAS, 2020). These polymetallic nodules form on vast deep-water abyssal plains and contain primarily manganese and iron. They are found in abundance in a few ocean basins, most notably the Clarion-Clipperton Zone. This zone is a great abyssal plain as wide as the continental United States and

lies 4000 to 6000 meters below the surface of the eastern Pacific Ocean. Billions of potato-size nodules (4-10 cm in diameter) are scattered on top of or half-embedded within the muddy seabed. To exploit these nodules would probably involve scraping 5 to 10 centimeters off the top of the abyssal plain and separating the nodules from the mud. The nodules would then be pumped to the surface ship by means of a transport system. The entrained water and fine particles would be also returned through a transport system (Nugent, 2018).



Figure 1.4 Polymetallic nodules on the seafloor (Nugent, 2018)

Seafloor massive sulfides (Polymetallic sulfides)

Currently there are 7 ISA exploration contracts (Nugent, 2018). Polymetallic sulfide deposits are found in areas of underwater volcanic activity and seafloor spreading, usually at depths of 1000 to 4000 meters. They have a high sulfide content but are also rich in copper, gold, lead, zinc, silver and barium. This deposits are often located near tectonic plate boundaries where hydrothermal vents release superheated, mineral-rich solutions. When this solutions cool, the minerals precipitate out forming towers on the seafloor with high concentration of valuable minerals. More than 200 sites of hydrothermal mineralization occur on the seafloor and based on previous explorations around 10 of these deposits may have sufficient grade and tonnage to be considered for commercial mining. Operations would remove the sulfide-rich deposits and would return the remaining water and fine particles through a tube (Nugent, 2018) (Miller, Thompson, Johnston, & Santillo, 2018).



Figure 1.5 Polymetallic sulfides (Nugent, 2018)

Cobalt crusts

As of 2020 there are 5 ISA approved contracts for exploration in the area of western Pacific (International Seabed Authority, 2020). Cobalt-rich crusts form on the slopes and summits of seamounts and contain manganese, iron and a wide array of trace metals like copper, cobalt, nickel and platinum. The richest deposits are found at depths of 800 to 2500 meters as crusts of seamounts in the western Pacific. The crust thickness can reach 25 centimeters, but typical deposits run from 10 to 15 centimeters. The basic mode of exploitation would be to remove the cobalt-rich layer on the seamount surface and leave the less valuable rock beneath it (Nugent, 2018) (Miller, Thompson, Johnston, & Santillo, 2018).



Figure 1.6 Cobalt crusts (Nugent, 2018)

1.2.2 Deep-sea mining processes

All recent proposed seabed minerals mining operations are based on a similar concept. They use a seabed resource collector, a lifting system and a support vessel(s) involved in offshore processing and transporting ore, see Figure 1.7. Most proposed seabed collection systems are remotely operated vehicles. These vehicles would extract deposits from the seabed using pressurized or mechanical water drills (Miller, Thompson, Johnston, & Santillo, 2018).

Over the years different systems have been tested during test mining operations. Here, it was found that a vertical hydraulic transport system has the greatest potential (ISA, 2020). Such a system was first conceptualized in 1988 by the French GEMONOD (Groupement pour la mise au point des moyens nécessaires à l'exploitation des nodules) and it consisted of a semi-submersible surface platform, hydraulic pumps, a rigid pipe, a buffer, a flexible hose with buoyancy and a self-propelled collector with crusher. An ore carrier would then transport the nodule from the mining ship to the port where the processing would begin. This concept can be seen in Figure 1.8. Different types of resource collectors, also known as mining vehicles, have been developed depending on the mineral deposit one which to collect, see Figure 1.9, (ISA, 2020) (Nautilus Minerals, 2020).



Figure 1.7 Deep-sea mining processes with different collectors, (Agravante, 2020)

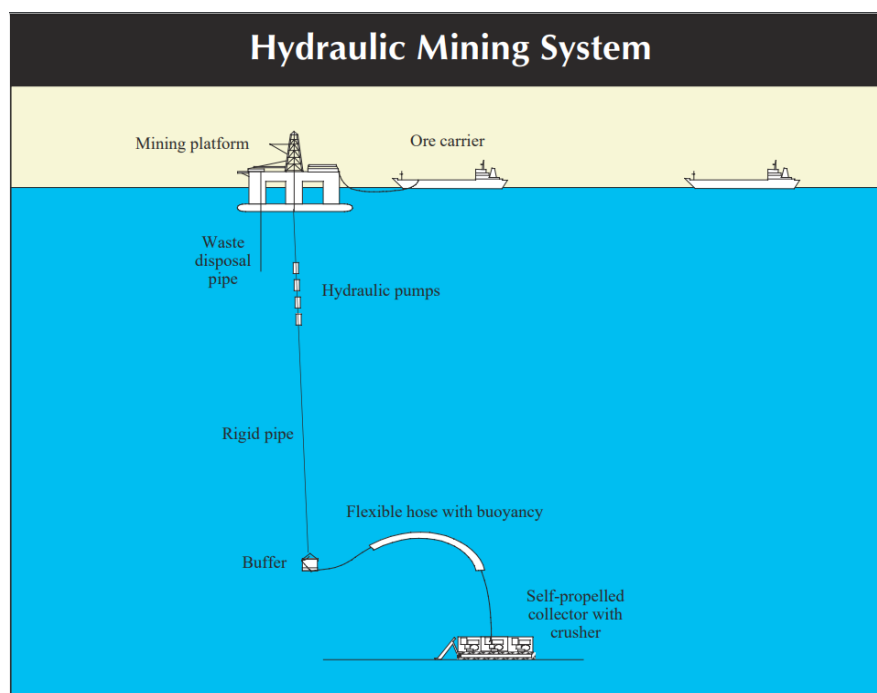


Figure 1.8 Proposed hydraulic Mining System by GEMONOD, (ISA, 2020)

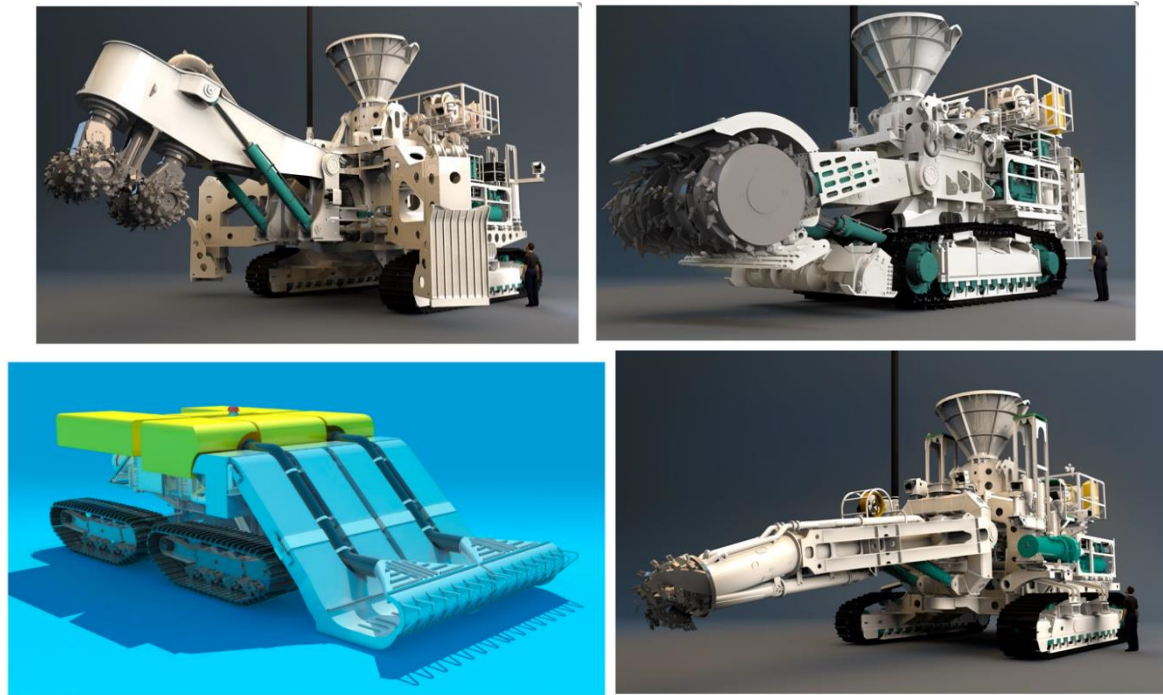


Figure 1.9 Different types of mining vehicles, from left to right (clockwise): Auxiliary cutter, Bulk cutter, Collecting machine (Nautilus Minerals, 2020) and Hydraulic polymetallic nodule collector, (IHC, 2020)

For polymetallic nodules two types of collectors were considered, a hydraulic or a mechanical one. The hydraulic collector, Figure 1.9, design proved to be a favorable functional concept as it is considered to only use moving water for collection of nodules, it is also considered to be reliable and to give minimal wear and abrasion (Brockett, 2014).

This hydraulic collector uses a suction head to gather the nodules on the sea bed together with sea water containing sediment. The mixture of nodules, water and sediment flows into the mining vehicle where the nodules are separated from the water-sediment mixture. The nodules are contained in the vehicle while the flow of water-sediment mixture is released from the mining vehicle towards the environment. When this flow is released, it is expected to first transition from a jet type into sediment plumes that will interact with the seabed and then transition towards a turbidity current.

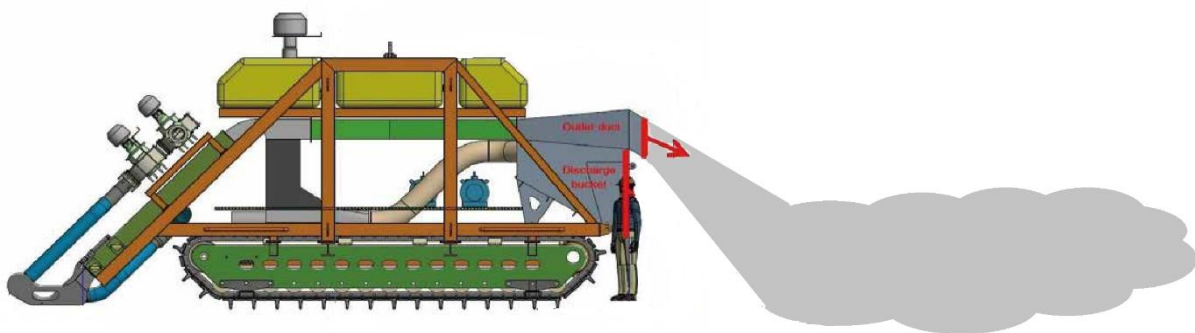


Figure 1.10 Hydraulic mining vehicle with discharge transitioning into a turbidity current. Modified from: (Decrop & De Wachter)

1.3 Problem definition

A turbidity current formation is expected and this current will propagate with a certain velocity over the seabed and through the water column. While propagating the current can bury the plants and animals that live on the seafloor because of sedimentation. The current can also possibly clog the feed path to the organisms which live in the seabed. The current also creates a cloud of particles that moves through the water column and this can affect the living conditions of marine life and other organisms. This could in the longer run lead to a loss of biodiversity of fauna and flora on the sea floor. Therefore, to predict the short- and long-term impact of turbidity currents resulting from polymetallic nodules mining on the near field area, information about the travel velocity and time scale of turbidity currents from when they start formation until they extinguish is needed.

Nowadays numerical modeling of different sediment plumes is being applied to determine how these plumes will develop and to help predict how they will impact the environment. The reliability of current numerical models depends on experimental validation data procured from different scaled experiments or field observations. Therefore, obtained experimental results are used as a basis for numerical modeling validation.

1.4 Objective

The main objective of this project is to come with a conclusion on what would be the optimum concentration of particles that give the least dispersion of the turbidity current for a sediment with different particle sizes and different particle properties.

It also involves to increase the knowledge of turbidity currents behavior and to obtain valuable experimental data that will be used as a basis for validation for CFD models.

Research questions

- How will distinct initial concentrations of particles with different particle sizes influence the dispersion of the turbidity current?
- How will the initial concentration affect the deposition of the turbidity current?
- How will the initial concentration affect the spread of particles within the current?
- How will the initial concentration affect the entrainment of the current?
- What would be the optimum concentration of sediment, with different ranges in particle size and different particle properties, that gives the least vertical and horizontal dispersion?

1.5 Research approach

The research approach is divided into several steps. The first step is a literature study which includes an overview of the relevant literature for this research. The second step is to create a suitable experimental set-up in the dredging laboratory at the TU Delft.

The experiments involve the release of a fixed volume suspension of a sediment tested for various particles size ranges and different particle properties. The release of the suspension is into water. The initial concentration will be varied and the obtained current will be recorded with a high-speed camera. Thereafter, video processing is used to perform an analysis of the current.

Finally, after the video analysis, several conclusions are drawn on the recorded current and the obtained data.

1.6 Report structure

Chapter 2: In this chapter the relevant literature study is explained. The literature focuses on the explanation of turbidity currents, influence of particle size distribution and particle settling velocity.

Chapter 3: The experimental set-up and procedure are explained in this chapter. The procedure includes the recording process, calibration, and how the data is processed.

Chapter 4: Experiment Results and Analysis of experiments. This chapter summarizes the most important results obtained after data processing. The results contain head velocities of the current as well as concentration profiles and calibrated color maps of the recorded current. Furthermore, this chapter provides data analysis of the results.

Chapter 5: Conclusions and further recommendations of this research are given.

2 Theoretical Framework

This first section focusses on the existing literature on turbidity currents. Hereby, the anatomy of turbidity currents is looked further into as well as the flow properties like, velocity profiles and concentration profiles. In addition, lock-exchange experiments with saline gravity currents and particle-driven currents are explained. Furthermore, the influence of particle size distribution on the current is explained as well as the deposition behavior and the settling velocity of particles.

The goal of this chapter is to obtain more insight on physical processes that can occur during particle-driven lock-exchange experiments.

2.1 Turbidity Currents

Turbidity currents belong to a larger class of flows called gravity currents, therefore they are often referred to as gravity currents or density currents. Also, turbidity currents are typically defined as relatively dilute flows in which particles are dominantly supported by fluid turbulence (Kneller & Buckee, 2000). Furthermore, turbidity currents are also the best studied mode of sediment gravity flows (Parsons, et al., 2007).

Turbidity currents have an interstitial fluid that is a liquid, generally water (Kneller & Buckee, 2000). They have dilute mass concentrations ($C_m < 10 \text{ kg/m}^3$) and are also fully turbulent $Re > 10^4$ (Parsons, et al., 2007). The speed is considerably faster than typical ocean currents ($> 10 \text{ m/s}$) and they form a new type of current that is driven by negative buoyancy resulting from the sediment itself. The current is driven by the horizontal pressure gradient resulting from the increase of hydrostatic pressure due to the addition of particles. (Parsons, et al., 2007)

Continuous turbidity currents are possible when the supply of sediment is naturally or unnaturally continuous, for example during mining processes (Parsons, et al., 2007). Lock exchange or fixed volume gravity currents are caused by fixed-volume release of dense material. This lock exchange flows approach continuous flows asymptotically. Furthermore, different models make use of the shallow-water equations with some adaptations to predict runout and flow characteristics, see (Parsons, et al., 2007).

2.1.1 Hydraulic theory

A physical configuration of a two-layer fluid system can be seen in Figure 2.1. In Figure 2.1, η represents the displacement of the free surface from an undisturbed configuration, u is the fluid velocity, H is the mean total depth, h is the thickness of the bottom current and ρ_1, ρ_2 with ($\rho_1 < \rho_2$) represent the constant densities of the upper and lower fluids respectively (Moodie, 2002).

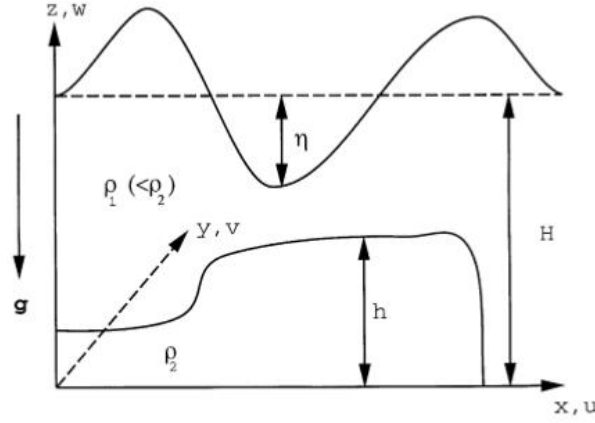


Figure 2.1. Gravity current with physical quantities defined (Moodie, 2002)

The argument leading to the shallow-water equations is based upon an important observation. This is that when the maximum height of the lower layer (the particle-driven flow) is small compared with its length, then the vertical accelerations in the motion will be very small compared with the horizontal acceleration. This observation leads to the assumption that the pressure at any point is effectively equal to the static pressure due to its depth below the free surface. For this assumption the flow is regarded as inviscid, immiscible, irrotational and the bed is considered horizontal, the dynamic boundary condition of a continuous pressure field across the interface at $z = h$ is also regarded (Pietrzak, 2016). This gives the total pressure field in each layer (Moodie, 2002):

$$p_1 = \rho_1 g [(H + \eta) - z] \quad (2.1)$$

Hereby is p_1 the pressure in the upper layer and g is the gravitational acceleration .

$$p_2 = -\rho_2 g z + \rho_2 g' h + \rho_1 g (H + \eta) \quad (2.2)$$

And, p_2 is the pressure in the lower layer and g' is the reduced gravity defined by $g' = g(\rho_c - \rho_a) / \rho_a$ where ρ_c and ρ_a are the densities of the current and the ambient fluid respectively.

From the equation above follows that the horizontal pressure gradient and thus also the horizontal velocity driving the flow are independent of depth. This is also called the hydrostatic assumption (Moodie, 2002).

2.2 Anatomy of turbidity currents

Turbidity currents have similar dynamics as gravity currents. A gravity current is a wedge of fluid intruding laterally into an ambient body of fluid with a different density. Gravity currents are described as having a well-defined head, body and in some cases a tail. See Figure 2.2.

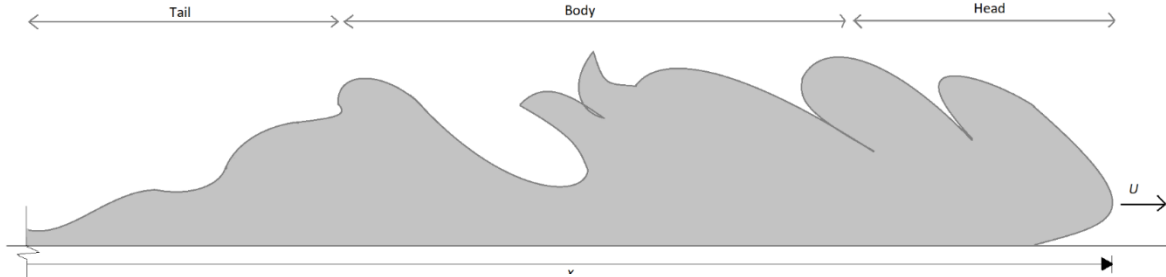


Figure 2.2. Turbidity current anatomy

2.2.1 The head

The dynamics of the head are important because the boundary condition set at this part influences the current as a whole (Simpson & Britter, 1979). The head has an overhanging nose, this is a result of the no-slip condition at the lower boundary (Britter & Simpson, 1978) where the velocity is set to 0 m/s and a frictional resistance in the upper boundary. At the rear of the head a series of vortices can be seen, these are identified as Kelvin-Helmholtz instabilities (Britter & Simpson, 1978).

(Middleton G. V., 1966) performed laboratory experiments in a lucite flume using a suspension of plastic beads. It was found that, for low slopes angles ($< 2^\circ - 3^\circ$), the head velocity can be described by (Keulegan, 1957) formula in which the head velocity is independent of the slope:

$$U_0 = Fr(g'h_0)^{\frac{1}{2}} \quad (2.3)$$

Hereby is U_0 the velocity of the head, h_0 the height of the head of the current, and Fr is a constant dimensionless number called the Froude number and this number defines the ratio of the flow inertia to the gravitational forces acting on the flow. The Froude number for an open channel flow is usually defined as (Brandt, Johnson, Elphinston, & Ratnayaka, 2017):

$$Fr = \frac{U}{\sqrt{gy}} \quad (2.4)$$

Hereby, is U the local flow velocity and y is the hydraulic mean depth of the flow.

The Froude number in a channel flow in its critical condition is equal to 1.0. This critical condition means that the flow velocity in a channel equals the wave velocity generated by a disturbance or obstruction. For a sub-critical flow the depth is greater and the velocity is lower, therefore the Froude number is always less than 1.0. For super-critical flow the opposite is true and the Froude number is always greater than 1.0 (Brandt, Johnson, Elphinston, & Ratnayaka, 2017).

The reduced gravity (g') depends on the flow density (ρ_c), which depends in turn on the density of the sediment and its concentration. This means that increasing the density or thickness of the flow will both have the effect of increasing U_0 . Increasing the current velocity also means increasing the shear velocity U^* (Al Ja'Aidi, 2004):

$$U^* = \sqrt{\frac{f_b}{8}} u \quad (2.5)$$

Hereby, u is the mean velocity of the flow below the height of the velocity maximum, f_b is the basal friction factor. As long as the shear velocity of the flow remains above the suspension threshold of the suspended grains, the flow will continue to suspend its load. Thus an increase in velocity has the effect of maintaining sediment in suspension for longer and this will extend the deposition, this analysis assumes fully turbulent suspension. At higher sediment concentrations, it can be the case that turbulence is suppressed (Middleton & Hampton, 1984) (Lowe, 1982).

The front condition based on (Keulegan, 1957) formula is an important assumption made. As a result. the front condition play a key role in regulating the overall runout and transport within the flow. Typically the condition of (Huppert & Simpson, 1980) is used. This condition use a Froude number of:

$$Fr_d = \frac{U_f}{\sqrt{g'h}} = 1.19 \quad (2.6)$$

For deeply submerged flows of $\frac{h}{H} < 0.075$, or:

$$Fr_d = \frac{U_f}{\sqrt{g'h}} = \frac{H^{\frac{1}{3}}}{2h^{\frac{1}{3}}} \quad (2.7)$$

For shallow flows of $\frac{h}{H} > 0.075$

Hereby, U_f is the flow velocity, h is the height of the current and H is the total water depth of the current.

Once the current is propagating, the front moves more slowly than the body due to enhanced mixing there. Moreover, at the front the entire thickness of the gravity current mixes with the ambient fluid (Parsons, et al., 2007). (Britter & Simpson, 1978) and later (Simpson & Britter, 1979) were the first to quantitatively describe a gravity-current front. Their experiments indicated that when the buoyancy flux mixed out of the front, q_{mix} was made dimensionless with the front velocity U_f and with the reduced gravitational acceleration g' , the dimensionless mix rate was:

$$\frac{g'q_{mix}}{U_f^3} = 0.1 \quad (2.8)$$

They determined that most of the mixing was associated with the Kelvin-Helmholtz instability. This instability is a result of a vortex intensification process associated with shear and is very common in natural flows. (Britter & Simpson, 1978) used slow motion pictures to trace the shapes of the billows created at the upper boundary and they showed that the ratio of billow amplitude to wavelength was the same as for Kelvin-Helmholtz billows.

(Middleton G. V., 1966) showed that flow lines (streamlines) are diverged within the head and that the head displaces the ambient fluid. Further experiments by (Simpson , 1969) and (Allen, 1971) on the displacement of ambient fluid by the head lead to the 'lobe and cleft' structure at the base of the head. This structure is formed due to a gravitational instability formed when less dense fluid is over-run and incorporated into the head. (Simpson , 1969) visualized the lobe and cleft structure as can be seen in Figure 2.3. He demonstrated that the clefts are located a substantial distance back from the head. Some studies shows that the lobe spacing scales with the flow thickness and that the lobe and cleft structure formation is probably attributed to an instability associated with Kelvin-Helmholtz vortex breakdown (Persons, 1998). (Simpson & Britter, 1979) calculated a flux of light ambient fluid moving under the head and found out that it only accounted for 1% of the total mixing, the rest of the mixing occurs at the upper boundary.

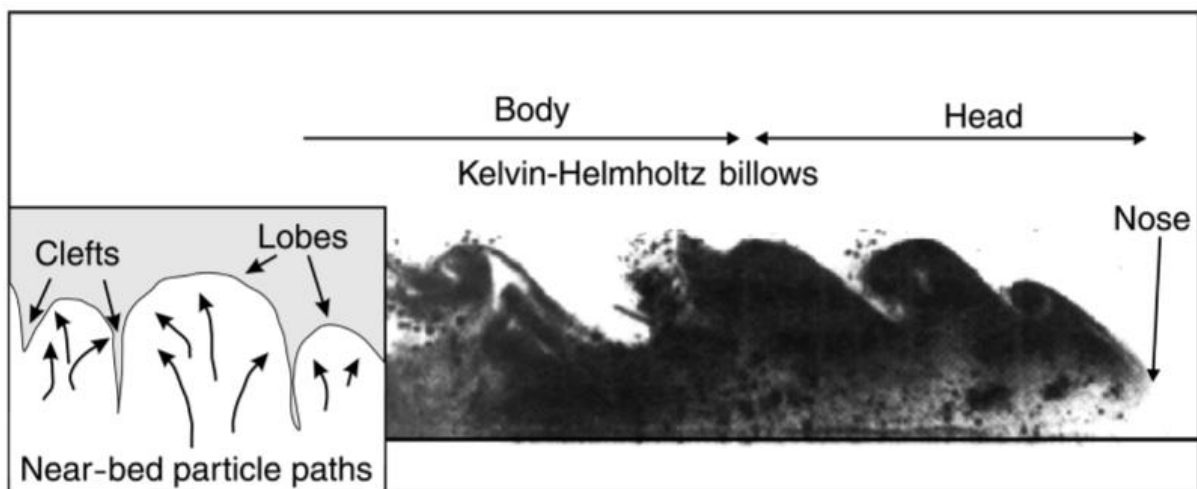


Figure 2.3. Two dimensional image of the head and body illustrating well-developed Kelvin-Helmholtz billows. The inset shows the clefts and lobes structure under the head. (Simpson 1969)

2.2.2 The Body

(Ellison & Turner, 1959) describe the body as a region of steady downstream velocity which has a thin, dense layer of fluid near the base of the current. When the downstream velocity increases then this layer mixes with the ambient fluid at the upper boundary in a succession of large eddies. (Britter & Simpson, 1978) and (Simpson & Britter, 1979) divided the current behind the head into two regions as can be seen in Figure 2.4. One region is the lower denser layer, also called 'the body of the turbidity current'. The other region is a region of less dense entrained fluid that has been mixed out of the head of the turbidity current. According to (Middleton G. V., 1966), the entrained region above the dense layer is not strictly part of the gravity current but should be described as a zone of 'clouded water' entrained by the underflow.

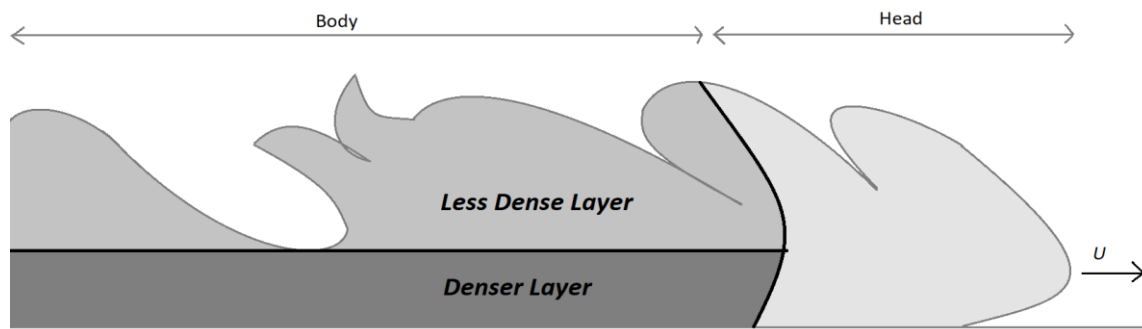


Figure 2.4. Schematic figure defining the regions in the body according to (Britter & Simpson, 1978) and (Simpson & Britter, 1979))

2.3 Flow properties

2.3.1 Velocity profiles

Gravity currents are also described as having an inner and outer region divided by the velocity maximum, see Figure 2.5. Figure 2.5 also shows the vertical profile of the downstream velocity (Altinakar, Graf, & Hopfinger, 1996) (Simpson, 1997). The inner region has a positive velocity gradient and this is generally less than half the thickness of the outer region. The outer region has a negative velocity gradient (Launder & Rodi, 1983). According to (Altinakar, Graf, & Hopfinger, 1996), the height of the velocity maximum is found in many experiments to occur at about 0.2 – 0.3 of the height of the current. It is possible to describe the velocity profile by using the characteristic scale of $y_{1/2}$, this is defined as the distance between the bed and the height in the outer region at which the downstream velocity is half the maximum downstream velocity ($0.5U_{max}$), this can also be seen in Figure 2.5.

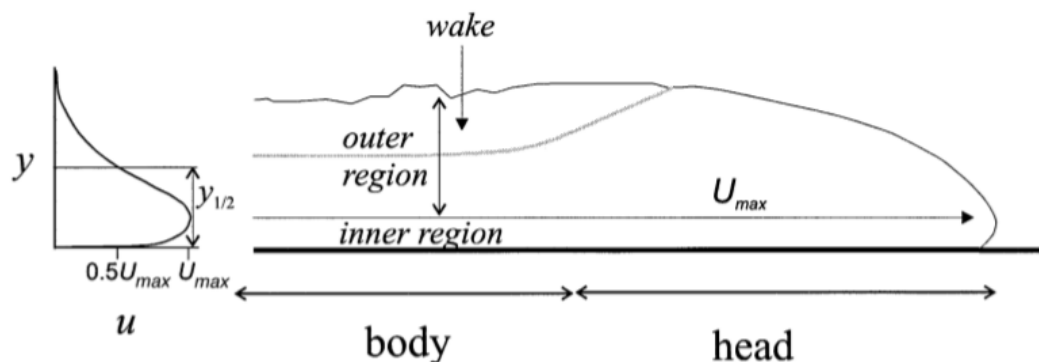


Figure 2.5. Schematic diagram of the head and body of a gravity current showing a vertical profile of the downstream velocity (Kneller & Buckee, 2000)

2.3.2 Concentration profiles

Gravity currents are density stratified and thus have a vertical gradient in concentration. They have a dense basal layer and a less dense more homogeneous mixed upper region. Two main types of sediment concentration profiles have been observed. A smooth profile is most commonly seen in low-concentrations, weakly depositional currents. These type of currents is still highly stratified with a density gradient that is greatest near the base of the current. Figure 2.6a shows a two-layer model type concentration profile, it divides the flow into a constant lower density region and an upper region of detrained fluid from the head. Figure 2.6b shows that the density gradient decreases rapidly around the level of the velocity maximum. The second class of density distribution is a 'stepped-concentration'

profile and is common for erosional currents or currents with a high entrainment rate at the upper boundary (Figure 2.6c). Experiments where the vertical grain size distributions are measured show that the fine-grained material is more uniformly distributed in the vertical than the coarse material, the coarse particles tend to be more concentrated in the lower part of the current, Figure 2.6d (Kneller & Buckee, 2000).

Laboratory experiments show that turbulence intensities around the body are highest at the top of a gravity current. This is related to the large scale shearing and mixing at the upper boundary. Around the level of the velocity maximum and at the base of the current, low turbulence intensities are observed (Kneller & Buckee, 2000).

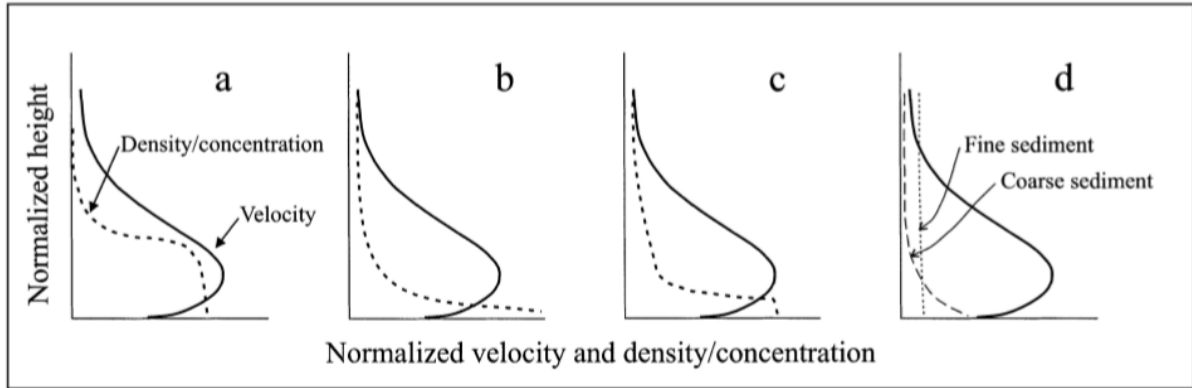


Figure 2.6. Schematic diagram showing various characteristic density/concentration profiles in particle-driven currents. (a) A two-layer model type concentration profile. (b) A smooth profile, characteristic low-concentration flow. (c) A stepped concentration profile observed in erosional flows. (d) A Rouse-type distribution of sediment grain-sizes observed in turbidity currents, coarse material is concentrated towards the lower part of the flow and fine-grained material is more evenly distributed throughout the depth of the flow (Kneller & Buckee, 2000).

2.4 The Richardson number

Turbulent mixing along the interface is a property that occurs at the head and at the body, therefore it must be estimated. This property can be estimated through the dimensionless flux Richardson number Ri_f , given in the form (Parsons, et al., 2007):

$$Ri_f = \frac{g'h}{U^2} \quad (2.9)$$

An alternative approach is to use the gradient Richardson number Ri_g (Kneller & Buckee, 2000):

$$Ri_g = -\frac{g \, d\rho_y/dy}{\rho_0 (U_y/dy)^2} \quad (2.10)$$

Hereby is ρ_0 some reference density (usually taken as the ambient fluid) and U_y is the mean downstream velocity at height y in the flow.

Turbulence in either the upper or lower layer influences stability. The entrainment of a stratified layer has a strong dependence on the Richardson number, therefore the Richardson number can be used to assess if a flow is stable or not (Pietrzak, 2016). Taking the gradient Richardson number into consideration, it can be seen that it varies over the depth, it can be possible to have a velocity gradient that is high near the bed and the associated low Ri_g , but as one moves towards the surface the velocity gradient can decrease and the stability will increase. So near the bed the flow is considered turbulent and near the surface it can be laminar (Pietrzak, 2016).

The associated Kelvin-Helmholtz instability usually occurs for a values of $Ri_f < 0.25$ (Simpson, 1997). A widely accepted criterion for the stability of stratification is that if $Ri_f > 0.25$ locally, then the stratification is strong enough to suppress vertical mixing at that level. However the presence of a stable stratification does not imply the absence of turbulence. During experiments, the Richardson number is a result rather than an initial estimation and therefore it is possible to calculate the degree of mixing along the turbidity current (Kneller & Buckee, 2000).

Supercritical currents ($Fr > 1$) were found to have a Ri_g in the range of 0.13 – 0.23 and subcritical currents ($Fr < 1$) had a range between 0.54 – 0.84 according to (Ellison & Turner, 1959). (Buckee, Kneller, & Peakall, 2001) showed through calculation that the strength of the stratification varies with the height of the current.

2.5 Lock-exchange experiments with saline gravity currents

It is shown during lock exchange experiments with saline driven gravity currents (homogeneous currents), the gravity current produced by release of the lock gate passes through two distinct phases with a possible third phase that can be achieved if viscous effects become dominant. After the initial collapse when the gate is removed there is an adjustment phase, at this first phase, the front advances at constant speed, see Figure 2.7. During the second phase, the front speed is observed to decrease with time (where t is the time measured from release). The transition from the first to the second phase is rather abrupt (Simpson, 1997).

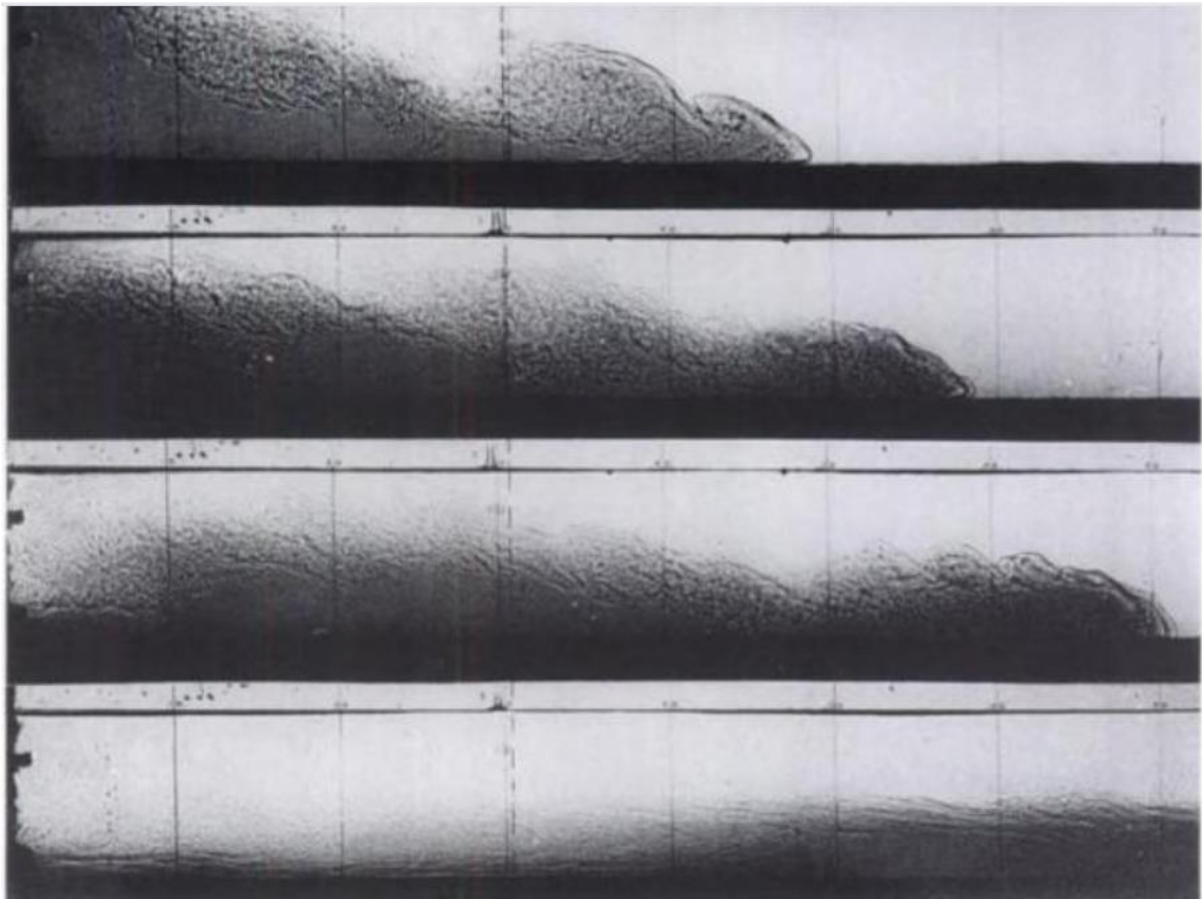


Figure 2.7. Shadow of a volume of salt water collapsing into fresh water, the dotted line shows the position of the lock gates. The graphs represent the release of the volume at 5,7,9 and 17 seconds (Simpson, 1997)

During the first phase of the lock exchange experiments (constant speed at the nose), where the segment of denser fluid has the same depth as the rest of the fluid ($h_0/H = 1$), as soon as the gate is

removed, the fluid from behind the gate will form a gravity current. The mixing area is just behind the head and above the gravity current. At the same time the displaced upper fluid forms a gravity current of its own, this propagates towards the end wall. When the backflowing current meets the wall a hydraulic drop is generated (Rottman & Simpson, 1983). This is pictured as an 'inverted bore', the lighter fluid is advancing through the upper part of the denser fluid under it. The disturbance will propagate away from the wall and it will eventually overtake the front. When this stage is reached the speed of the front will no longer be constant but will decrease with time: $t^{-1/3}$ (or the x varies with $t^{2/3}$) (Simpson, 1997). This stage of decreasing speed is also called the second phase. Figure 2.7 shows the first phase of the current just before reaching the second phase.

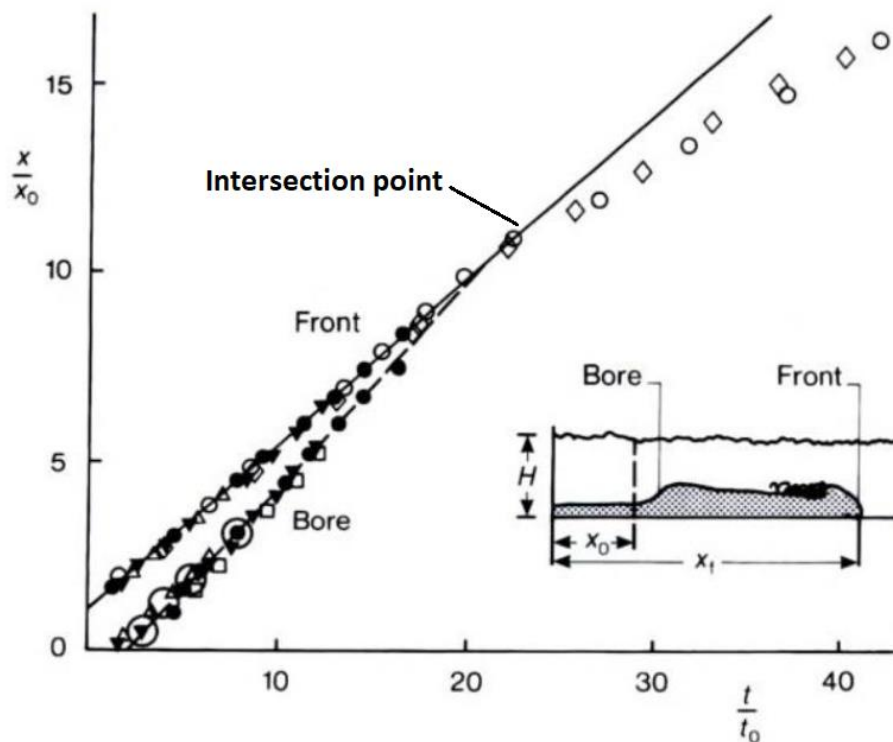


Figure 2.8. Front position and bore position as functions of time after release with $\frac{h_0}{H} = 1$, data taken from multiple experiments performed by (Rottman & Simpson, 1983); (Keulegan, 1957) modified by (Simpson, 1997)

In Figure 2.8, the solid lines represent the data at the first phase of the front and bore velocity. The front and the bore travel at a constant speed initially and the front speed begins to decrease at the intersection point. (Rottman & Simpson, 1983) describe that change of the gradient of the front line goes from 1 to $2/3$ and occurs when the distance is about 10 lock-lengths (10 times x_0 in Figure 2.8) for saline gravity currents. The experiments used for Figure 2.8 are making use of tap water and salt dissolved into the water behind the gate.

During the second phase (after the intersection point) the front speed has begun to decrease and the gravity current will be collapsing according to the so called box-model (Figure 2.9). This model describe the collapse of the current as a series of equal-area rectangles. The current depth is roughly uniform along the length of the current, but will decrease with time. The first and second phase can be seen in Figure 2.9 using the box model.

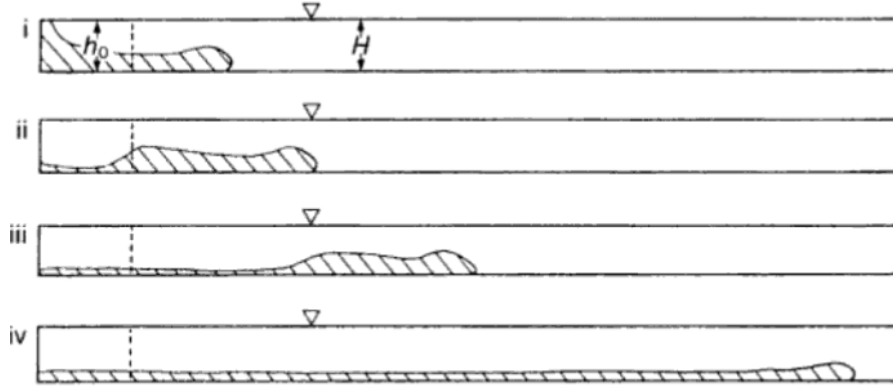


Figure 2.9 Collapse of volume of dense fluid with $h_0/H=1$, (i), (ii) and (iii) represent the first stage with (iv) as the second stage (Simpson, 1997)

A third phase can be achieved if the length of the current is developed sufficiently. Inertial forces do not dominate the dynamics of the gravity current indefinitely. When the current reaches a sufficient length the viscous forces acting on the bottom of the current along the horizontal surface become more important than the inertial forces. This will cause the front speed to decrease even more rapidly (Rottman & Simpson, 1983). The conditions for the transition from inertially to viscously dominated flow for a current of fixed volume has been determined experimentally and theoretically by (Huppert & Simpson, 1980) and (Huppert H. , 1982) respectively. The time for this transition from one regime to the other can be written in terms of the dimensional time t_c :

$$t_c = 0.5 \left(\frac{q^4}{\nu^3 g'^2} \right)^{\frac{1}{7}} \quad (2.11)$$

The left term is the dimensional time t_c , q as the volume per unit width of the current and ν as the kinematic viscosity of the current.

2.6 Particle-driven gravity currents

According to numerical results by (Bonnecaze, Huppert, & Lister, 1993), there are also different stages of the flow for particle-driven gravity currents.

For currents in deep surroundings the dynamics of the particle-driven gravity current can be divided into three phases. The first phase starts with the stationary fixed volume of fluid collapsing and it approaches a self-similar solution to the saline driven gravity currents with very few particles having settle out of the current. Following is a transition phase, hereby the particles from the rear of the current start settling and the tail decelerates less rapidly than the nose and a maximum velocity can be seen. The last phase is a travelling shock phase, during this phase a bore develops within the current and separates the current in a particle-free region in the rear and a relatively particle-rich current region at the front of the current. The formation of this traveling shock is due to the different settling of particles along the length of the current (Bonnecaze, Huppert, & Lister, 1993).

During the run of the current there is a variation of height between the front and the back of the current, this establish a pressure gradient that will decelerate the fluid behind the nose. The particles will settle out more rapidly at the rear of the current due to the smaller height there, and this will cause the density and pressure gradient in the tail to be reduced. Thus, the rearward fluid is not decelerating as rapidly as the front to maintain a self-similar profile to the saline gravity currents. This results in an accumulation of fluid behind the head due to the slower movement of the nose. The particle concentration in the tail will virtually vanish and the flow will be like a jet, since the motion of

the flow is due to the momentum of the particle-free fluid and the effects of buoyancy are to be neglected. Near the front, the current is still relatively rich in particles, but the concentration is small compared to the initial value, so it will continue to behave like a buoyancy-driven flow. The traveling shock comes as a consequence of matching the jet-like flow in the rear of the current to the buoyancy-driven flow in the front (Bonnecaze, Huppert, & Lister, 1993).

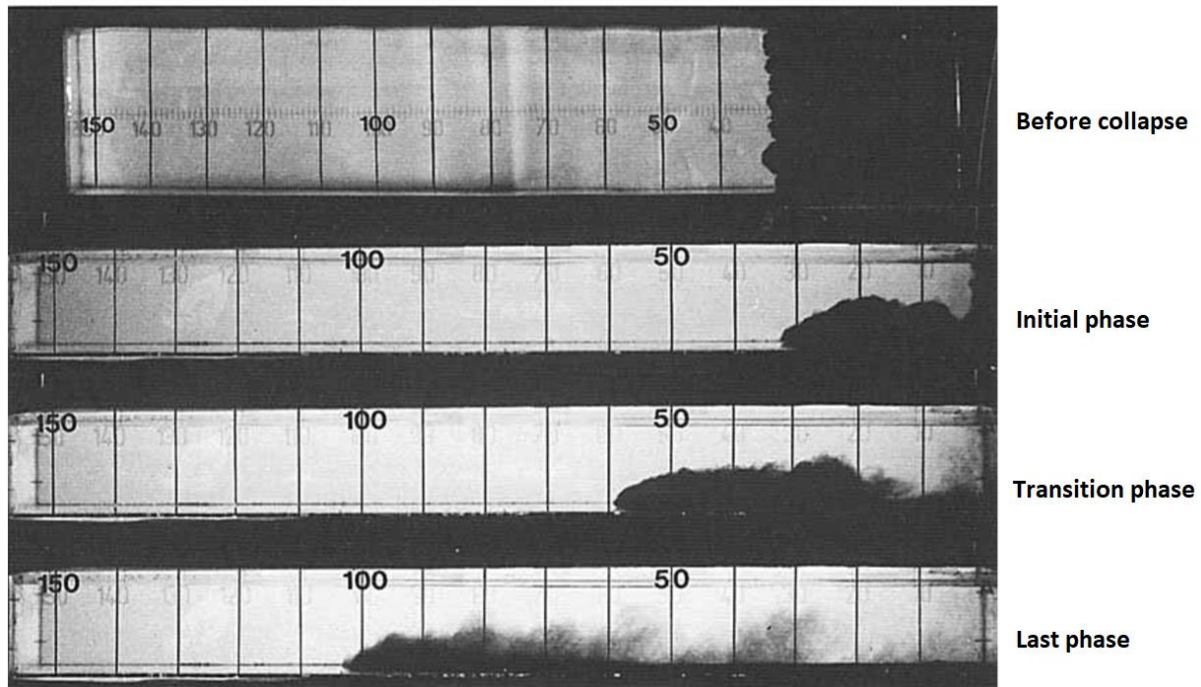


Figure 2.10. Photographs of a particle-driven gravity current at 3, 7 and 21 seconds after release, particles of $53\mu\text{m}$ are used. Modified from: (Bonnecaze, Huppert, & Lister, 1993)

For shallow surroundings the bore that occurs for the current in shallow surroundings strongly affects the deposition pattern of the sediment for particle-driven gravity currents. The sequence of events is initially similar to that for the homogeneous current. The dynamics can be divided into three phases: a slumping phase, at this stage the current collapses and the bore between the ambient and current fluid forms; a transition phase, in which the first bore vanishes and an internal bore begins to appear; the last stage is the where the internal traveling bore catches with the front as also noted with the saline driven gravity current (homogeneous current) (Bonnecaze, Huppert, & Lister, 1993).

The internal traveling bore is similar to the reflected wave from the end wall for the current into deep surroundings. The difference lies in the height of the current behind the bore, this is much shallower than the deep surrounding case. Also, the height of the front remains constant as the internal bore travels towards the nose, unlike the current collapsing for the deep surroundings case. Eventually when the bore reaches the front of the current the height near the front will increase. At this point an internal travelling shock will develop within the current and this will separate the current into a particle-free region near the rear and a particle-rich region near the front.

2.7 Influence of particle size distribution and deposition behavior

Particle driven gravity currents are more complex than homogeneous currents because the particle concentration, and thus the driving buoyancy force, changes with time and position along the current. When a particle settle, the local density difference is reduced. Both the settling and entrainment rates depend on the velocity and dimensions of the gravity current (Bonnecaze, Huppert, & Lister, 1993).

(Bonnecaze, Huppert, & Lister, 1993) performed several monodisperse experiments in which the grain-size distribution and density of turbulent suspensions were varied. For these experiments the dynamics of the current are assumed to be dominated by a balance between inertial and buoyancy forces with viscous forces neglected. The currents were considered two-dimensional and flow over a rigid horizontal surface. The results showed that flows of higher initial density or of finer particle size travelled further downstream. Particle diameters used for the experiments went up to $53\mu m$.

(Gladstone, Phillips, & Sparks, 1998), demonstrated that the propagation and sedimentation patterns of particle-laden gravity currents are strongly influenced by the size distribution of suspended particles. The laboratory experiments made by (Gladstone, Phillips, & Sparks, 1998) were made using bidisperse and polydisperse particle-driven gravity currents. For the bidisperse experiments silicon carbide particles were used with $25\mu m$ and $69\mu m$ mean diameter. The polydisperse experiments involved a mixture of five different particle sizes (17, 37, 63, 88 and $105\mu m$ average grain diameter) and a variation of the amounts of the finest and coarsest particles (Gladstone, Phillips, & Sparks, 1998). The results showed that the addition of small amounts of fine-grained sediment to a coarse-grained density current has a larger influence on the runout distance, flow velocity of the current and sedimentation pattern than adding a small amount of coarse sediment to a fine-grained density current. Both experiments of (Bonnecaze, Huppert, & Lister, 1993) and (Gladstone, Phillips, & Sparks, 1998) shows that the presence of fine-grained sediment reduces the rate of momentum loss because the fine particles tend to remain suspended. This maintains an excess on the current density for a longer period of time (Al Ja'Aidi, 2004).

The increase of the proportion of fines can lead to the distance travelled by the grains in a turbidity current to increase. One factor responsible for this is the settling velocity of the particles. The settling velocity of the particles is a function of the fluid viscosity and the size, shape and density of the particles. Another factor is the rate of decline of shear velocity exerted by the current, as mentioned before with an increase in shear velocity the grains tend to be suspended for a longer time. For particles with a small settling velocity, the shear velocity of the flow will need to approach zero for the particles to settle. This means that the particles can remain in suspension up until the flow has almost come to rest. The addition of fines to a coarser-grained load will allow for the particles to stay longer in suspension due to the rate of negative buoyancy not decaying as fast because of sedimentation. Another factor contributing to the efficiency of the flow is that the presence of a significant amount of fines in the current reduces the density difference between the interstitial fluid and the coarse-grains, which leads to the reduction of the settling velocity of the coarser grains (Al Ja'Aidi, 2004).

Theoretical analysis by (Dade & Huppert, 1995) performing a box-model-type analysis (Figure 2.9) determine the governing equation of a radially spreading, deposit-forming gravity current with monodisperse particles:

$$\frac{W}{H_d} \sim \left(\frac{V}{U_s^6 C^5} \right)^{\frac{1}{8}} \quad (2.12)$$

Where W/H_d is the cross-sectional aspect ratio (width/height) of the deposit, V is the initial volume, C is the initial sediment concentration, U_s is a characteristic particle settling velocity. Thus the deposit aspect ratio should increase with increasing flow volume, diminishing particle settling velocity or decreasing initial sediment concentration.

According to (Gladstone, Phillips, & Sparks, 1998) for experiments with polydisperse particle size distribution the flow containing more coarse particles tend to have the largest deposits closer to the lock-gate. The deposit density then gradually decrease for coarser flows as for finer flows.

2.8 Settling velocity of particles

2.8.1 Forces on immersed objects

An object immersed in a flowing fluid will experience forces. Also with particles, they will experience forces that are either due to gravitational force, fluid-particle interaction or particle-particle interaction. The fluid-particle interaction forces can be divided into buoyancy force, drag force and lift force (Jamshidi & Mazzei, 2018). Among these forces, the buoyancy force and drag force are dominant. The lift force accounts for the additional resistance experience by solids undergoing acceleration. Due to the flow considered uniform, the velocities will be constant and so the particles will not experience a lift force (Yeoh & Tu, 2010). Forces through particle-particle interaction are transmitted as interparticle stress via physical contact of particles. Analysis of gravity separation is first started with a force balance on a single particle. The total sum of forces acting on a particle is equal to (Matousek, 2004):

$$F_B + F_D - F_G = 0 \quad (2.13)$$

Hereby is F_B the buoyancy force, F_D is the drag force and F_G is the gravitational force.

The two primary forces are gravity and drag. Gravity pulls the particle down while drag is experienced by a particle as it moves through a fluid. Drag acts in the opposite direction to the particles direction of travel. The direction of movement of a particle will depend whether the density of the particle is higher or lower than that of the bulk fluid in which it is contained. If the particle density is lower, then the particle will rise. In contrast, if the particle density is higher, the particle will fall (Neutrium, 2020).

Gravitational force

The force due to gravitational acceleration is determined from the solid particle density and volume. For spherical solid particles the gravitational force will be (Matousek, 2004):

$$F_{Gp} = \rho_p g \frac{\pi d^3}{6} \quad (2.14)$$

Hereby is ρ_p the particle density and d is the particle diameter.

According to Archimedes law, when a solid particle is submerged it will experience a buoyancy force. This force will reduce its weight in the carrying medium. The submerged weight of the solid particle is the result of gravitational and buoyancy effects on the particle. For a spherical particle the submerged weight is determined by the following equation (Matousek, 2004), see Figure 2.11:

$$F_{wp} = (\rho_p - \rho_a) \frac{\pi d^3}{6} g \quad (2.15)$$

Drag force

When the surrounding fluid moves relative to a solid particle, an additional force is exerted onto the submerged particle. The drag force acts in the direction of the relative velocity between the liquid and the solid particle: $v_r = v_f - v_p$. Hereby is v_f the fluid and v_p is the particle velocity. The drag force is expressed in terms of the drag coefficient C_D (Matousek, 2004):

$$F_D = \frac{1}{8} C_D \pi d^2 v_r |v_r| \rho_a \quad (2.16)$$

A balance of the total forces on the submerged solid particle determines a settling velocity of the body, see Figure 2.11

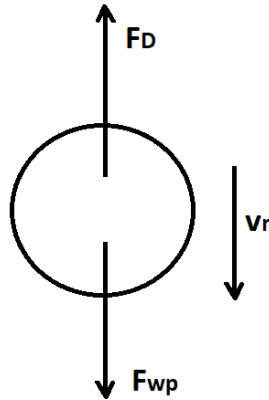


Figure 2.11 Schematic representation of the forces acting on a spherical particle

The drag coefficient C_D is sensitive to a regime of the liquid flow around the settling solid particle, this relation can be expressed as $C_D = f_n(Re_p)$. The particle Reynolds number is defined as:

$$Re_p = \frac{\rho_a |v_r| d}{\mu} \quad (2.17)$$

Hereby is μ the dynamic viscosity of the fluid.

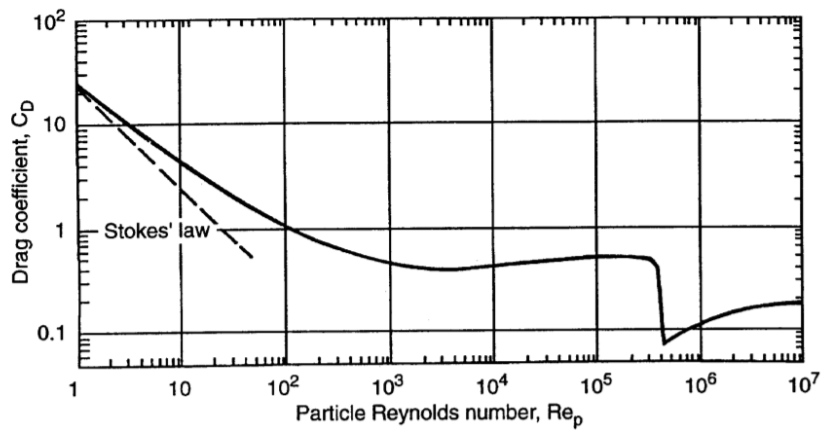


Figure 2.12 Drag coefficient as a function of the particle Reynolds number (Matousek, 2004)

Experimental determination of the drag coefficient is based on measurement of the terminal settling velocity of a spherical particle v_{ts} in a quiescent liquid, see Figure 2.12 . For these experiments the measured v_{ts} is the relative velocity v_r .

Settling velocity of a single particle

The particle Reynolds number knows three regimes; the regime for small $Re_p < 0.1$, the regime for medium $1 < Re_p < 2000$ and the regime for large $Re_p > 2000$. The equation by (Ferguson & Church, 2004) can be used to compute the settling velocity of a single particle over a wide range of particle Reynolds number:

$$v_0 = \frac{\Delta g d^2}{C_1 \nu + \sqrt{0.75 C_2 \Delta g d^3}} \quad (2.18)$$

Hereby is $C_1 = 18$ and $C_2 = 1$ for natural sands and $C_2 = 0.44$ for spheres, ν is the kinematic viscosity of the fluid and $\Delta = (\rho_p - \rho_a)/\rho_a$ is the specific density. For this case the terminal settling velocity of a single particle $v_0 = v_r$.

2.8.2 Hindered settling effect

Hindered settling refers to the reduced sedimentation rate of a concentrated suspension of particles in comparison with the settling velocity of particles that are falling in isolation (Tomkins, Baldock, & Nielsen, 2005). When a large number of particles is settling in a confined space, the settling velocity of the individual particles will be reduced (van Rhee, 2018). The influence of the volume concentration on the settling velocity of a mono-sized mixture, this is a mixture with particles of the same size, is written according to (Richardson & Zaki, 1954):

$$v_s = v_0 (1 - \varphi)^n \quad (2.19)$$

Hereby is φ the volume concentration and the exponent n is a function of the particle Reynolds number and varies between 2.4 for coarse particles and 4.65 for fine particles (van Rhee, 2018). The value of n can also be computed by the method of (Rowe, 1987):

$$n = \frac{4.7 + 0.41 Re_p^{0.75}}{1 + 0.175 Re_p^{0.75}} \quad (2.20)$$

The settling of particles in an aqueous suspension are strongly affected by suspension concentration. Lone particles or particles in very-low concentration suspensions will settle freely through a fluid without the hydrodynamic influences of other particles (Major, 1978).

2.8.3 Multi-sized mixture of particles

Natural sediments consist of multiple particle sizes and all these different sizes will have a mutual influence during settling. This effect can be quantified using the approach of (Smith, 1966). When the particle is settling, it will have a velocity relative to the surrounding water velocity. The water velocity is created by the displacement of water due to the settling particles. When a fraction of particles with the same size is considered, the settling velocity of this fraction is:

$$v_s = v_f + v_r \quad (2.21)$$

This represents the sum of the fluid velocity v_f and the relative velocity v_r .

As we are dealing with an incompressible fluid and the densities are constant, mass conservation will dictate that the total volume displacement is zero. Thus, when a volume fraction of particles leaves the domain with a certain settling velocity v_s (as mentioned above), there must be an equal volume fraction of water entering the domain, hence:

$$\varphi v_s + (1 - \varphi) v_f = 0 \quad (2.22)$$

Or, the water velocity would be:

$$v_f = -\frac{\varphi}{1-\varphi} v_s \quad (2.23)$$

Substitution of this expression into equation 2.21 and substituting the result of (Richardson & Zaki, 1954) equation 2.19. Yields the following expression for the relative velocity is:

$$v_r = v_0(1 - \varphi)^{n-1} \quad (2.24)$$

When dealing with a mixture of particles with different sizes, the relative velocity $v_{r,i}$ of particles of fraction i reads according to (Mirza & Richardson, 1979):

$$v_{r,i} = v_{0,i}(1 - \varphi)^{n_i-1} \quad (2.25)$$

With φ as the total volumetric concentration.

When combining the relative velocity of each fraction determined by equation 2.25 And the total volume displacement being zero as per equation 2.22. This leads to the formulation of the settling velocity for each fraction i :

$$v_{s,i} = -\sum_{k=1}^N \varphi_k v_{r,k} + v_{r,i} \quad (2.26)$$

Hereby is N the amount of different fractions of particles sizes, φ_k is the concentration of fraction k and v_r is the relative velocity that can be determined using equation 2.25.

2.8.4 Settling velocity of a non-spherical particle

The equations mentioned above are suitable for spherical particles. However the particles in the deep sea are not spherical. Consequently, the non-spherical shape of particles reduces its settling velocity (Matousek, 2004).

Shape factor of a solid particle

The reduction of the settling velocity of a solid particle due to its non-spherical shape can be quantified by the velocity ratio (Matousek, 2004):

$$\xi = \frac{v_{0ns}}{v_{0s}} \quad (2.27)$$

Hereby is ξ the shape factor of a solid factor, v_{0ns} is the terminal settling velocity of a non-spherical solid particle and v_{0s} is the terminal settling velocity of a spherical solid particle.

To determine the shape factor, the Grace method can be used (Grace, 1986). This method states that ξ is a function of the volumetric form factor K (with $K = 0.26$ for sand and gravel) and the dimensionless particle diameter d^* , see Figure 2.13, with d^* :

$$d^* = \sqrt[3]{\frac{\rho_a(\rho_p - \rho_a)g}{\mu_f^2}} d \quad (2.28)$$

The terminal velocity for sand particles is typically 50 – 60% of the value for the sphere of the equivalent diameter.

Another method suggest that the value of the shape factor for sand and gravel lies at $\xi = 0.7$ (Matousek, 2004).

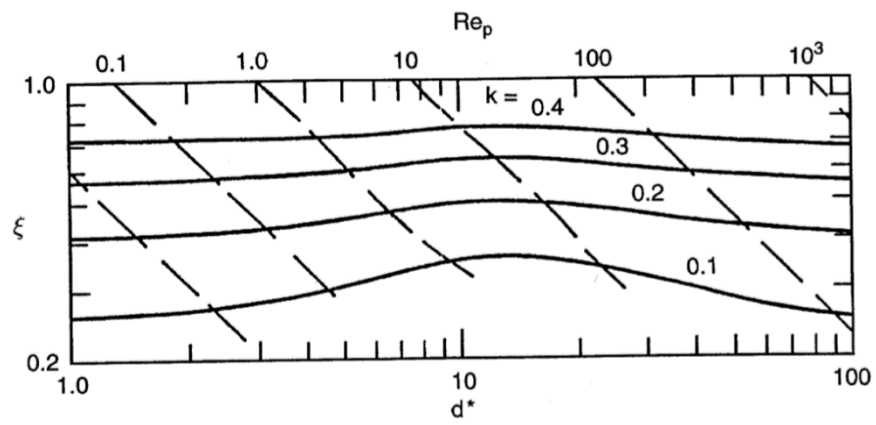


Figure 2.13 The shape factor ξ as a function of the dimensionless particle diameter d^* and the volumetric form factor K . (Matousek, 2004)

3. Experimental Methodology

3.1 Introduction

The objective of these experiments is to obtain video data in order to use video analysis to investigate how a turbidity current behave when various concentrations and sediment properties are used for the current. Similar experiments were performed by (Bonnecaze, Huppert, & Lister, 1993), (Gladstone, Phillips, & Sparks, 1998) and (Simpson, 1997).

The experimental methodology is based on the effect that particles have when they are added to clear water. The particles will block the incoming light and the more particles are added, the more light will be blocked. This effect can be captured by a camera. For this reason, it was decided to adjust the set-up of the experiments so that the current would have a background light. The current will create a shadow due to the particles blocking of the light. The changes of darkness in the created shadow can be recorded and the captured images can be analyzed by making use of machine vision tools like OpenCV and by algorithms created in Python.

The experimental methodology can be divided in two parts. The first part are experiments based on a so-called lock exchange experiment. With this kind of experiment one releases a fixed volume suspension by opening the lock gate vertically. The suspension is then released into a homogeneous fluid of lower density. The sediment used for this research has various particle size ranges and sediment properties.

The second part consists of multiple calibration procedures. During these procedure, different concentrations of sediment are mixed with water and the resulting solution is recorded. This data is used to create a calibration function that in turn can be used to quantify the concentrations of sediment in the previous recorded current. The experimental methodology differs with previous work due to this calibration procedure.

Both parts of the experiments are carried out in the TU Delft Dredging Laboratory under supervision of TU Delft.

Possible effects of flocculation and scattering of light are not part of the scope for this research.

3.2 Experimental set-up for the lock exchange experiments

3.2.1 The tank

The TU Delft Dredging Laboratory provided an existing tank of $L = 3m$, $W = 0.2m$ and $D = 0.4m$. The tank was adapted with an inbuild lock gate positioned at $x_0 = 0.2m$, see Figure 3.1. All the experiments were carried out in this tank.

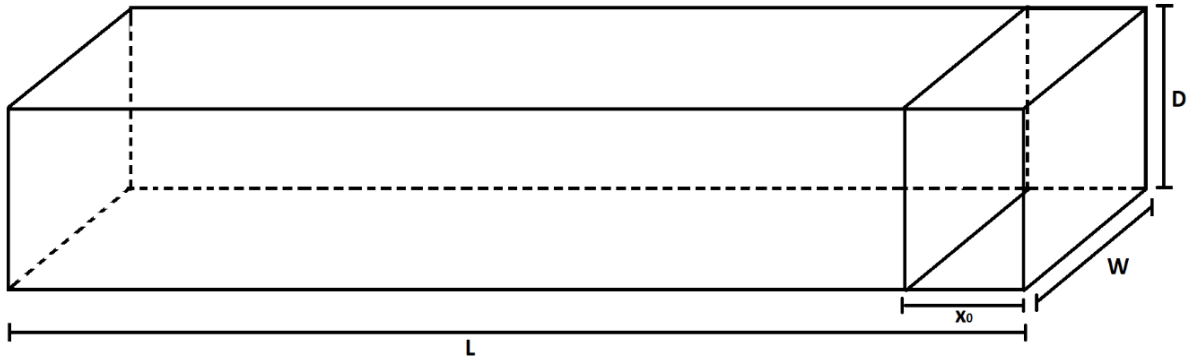


Figure 3.1 Schematic representation of the tank

A table was fixed in the lab with some additional supports on the table to carry the tank. This made the maintenance and cleaning of the tank easier. The tank was calibrated with a level to make sure that there were no height differences between both sides. Diffuse paper is cut to size and placed at the back of the tank. A white wood panel with LED stripes positioned at 0.15m from each other was placed on a support behind the tank, see Figure 3.2. The LED stripes have the function of creating a white light throughout the length of the tank to illuminate the current. The diffuse paper is used to create as much of a homogeneous light throughout the length and height of tank, see Figure 3.7.

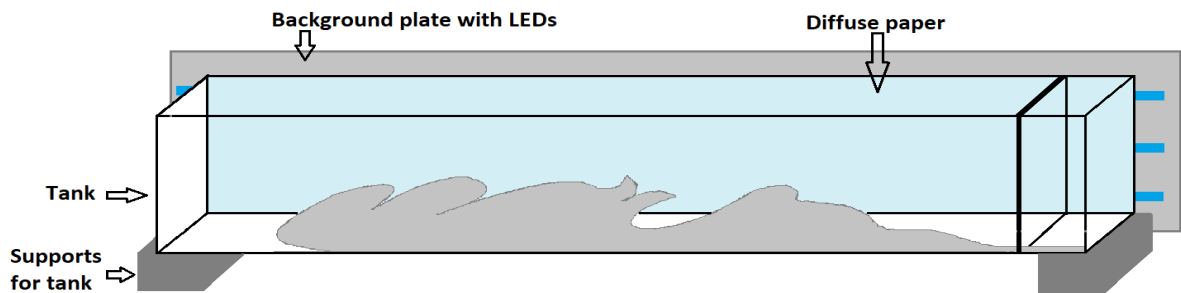


Figure 3.2 Schematic representation of the total tank set-up



Figure 3.3 Level used on the tank

3.2.2 Recording camera and additional accessories

The recording camera that is used during all the experiments is a IL5HM8512D: Fastec highspeed camera with a DO-2595 Highspeed lens Navitar 25mm (Figure 3.5). Video recordings are made to capture the formation and run-out of each turbidity current over time. In order to capture as much detail possible of the current, it is important to see what the dynamic range of the camera is. For these experiments a 8 bit sensor is used, this makes the range from 0 to 255 pixel values. Therefore, all

measurements should stay within the range of the sensor to prevent data loss. Additionally, to be able to compare the experiments it is important that the camera settings are kept constant throughout the experiments. The settings are listed in Table 3-1. Further, the aperture is also fixed at one position for all the experiments as this influences the light intensity (Figure 3.4), it is important to have the same intensity of light for all the experiments so that they can be compared. A tripod is also used to fix the camera at one position in the laboratory, see Figure 3.6.



Figure 3.4 Aperture kept constant



Figure 3.5 High-speed camera used for experiments



Figure 3.6 High-speed camera on tripod facing the tank

Table 3-1 Camera settings for all the experiments

Setting	
Frame Rate (FPS)	130
Shutter Speed	860
Bit Depth	8 Bits [12:5]
FPN	Pixel

3.2.3 Other tools

Additionally, a frame where a dark cloth could be positioned was made and used for this research. The LED lights benefit from the dark cloth and they create a higher contrast inside the tank. The dark cloth creates a darker background which is also beneficial for the quality of the recordings and to block external lights from the background. Further, a mixer is used to create a homogeneous mixture before releasing the lock gate. The final set-up of the tank with other additional tools can be seen in Figure 3.7 and Figure 3.8

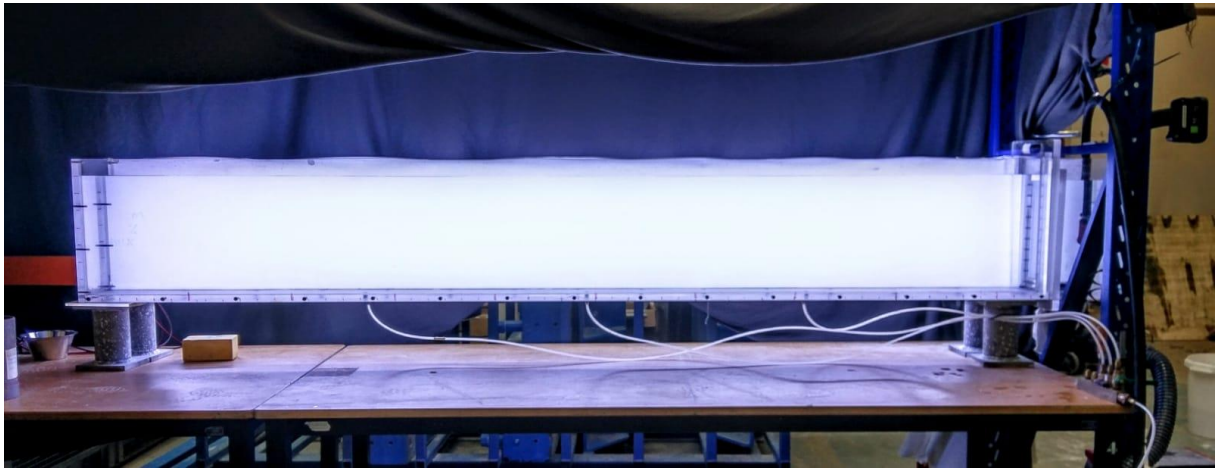


Figure 3.7 Final set-up of the tank with backlight



Figure 3.8 Side view of the Tank set-up showing mixer, wooden panel with LED stripes and diffuse paper

3.2.4 Sediment

Two types of sediment are used for the experiments. The purpose was to have a wide particle size range of sediment, varying between $4 - 125 \mu m$, with different particle shapes.

The first type (I) of sediment used are synthetic white, round shaped glass beads produced by Holland Mineraal. The glass beads have a particle size range between $75 - 125\mu m$. This type of sediment was chosen due to their rather large particle size and also due to its uniform shape.

The second type (II) of sediment used consist of fine grinded quarts particles (Millisil M10) produced by Sibelco Benelux. The sediment provides a small particle size range between $4 - 60\mu m$. Previous experiments by (Grunsven, Keetels, & Rhee, 2018) conducted in the TU Delft also make use of this sediment. This type of sediment was chosen due to its closest similarity to real deep sea sand. The sediment was left un-sieved and was put in the oven to dry out possible water content before it was weighted for each experiment. More details about both types of sediment are shown in Appendix A.



Figure 3.9 Millisil M10 sediment put in the oven to dry out

3.2.5 Experimental procedure for lock exchange experiments

The experiments consist of the release of a fixed volume suspension by opening the lock gate vertically. The suspension is then released into tap water as shown in Figure 3.2. The suspension is originally separated from the ambient fluid by the lock-gate positioned at $0.2m$ as can be seen in Figure 3.1, both fluids have the same initial height H set at $0.35m$. The suspension is a mixture of sediment and fresh water with density ρ_c . The ambient fluid is fresh water with density ρ_a .

The initial concentration of sediment in suspension will be varied from 0.1% to 3%. The needed mass per volume fraction of particles φ_0 behind the lock-gate at t_0 , can be determined by using equation:

$$\varphi_0 = \frac{M}{\rho_p x_0 W H}$$

With M the mass of the sediment behind the lock-gate and ρ_p is the density of particles used.

The sediment is divided into three groups, the first group consist of sediment type II with a particle range between $4 - 60\mu m$. The second group consist of a mixture of sediment type I and type II creating a particle range between $4 - 125\mu m$. The third group consist of only sediment type I with a particle range between $75 - 125\mu m$. Then the needed mass per initial concentration for all the three groups is calculated by using a scale.

Once the needed mass per experiment run is calculated. For the second group the desired initial concentration is divided by 2 and the required mass per divided concentration is calculated. The tank is filled until the initial height H is reached. After this, the weighted material is poured inside the mixing section that is still separated by the lock-gate. Afterwards, this mixing section will also be filled with water until height H is reached. A mixer is then used for 1 minute to create the suspension. Then the lock-gate is released vertically and the current will be formed. A snapshot of one recorded video can be seen in Figure 3.10.

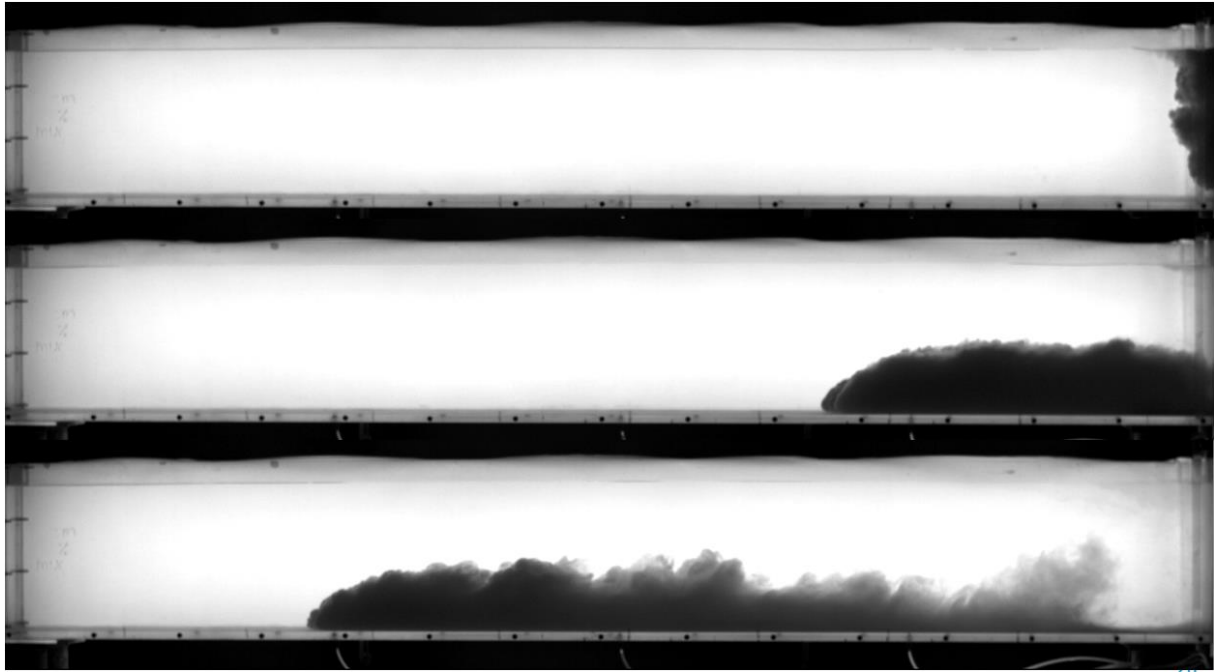


Figure 3.10 Snapshots of a recorded video with Sediment Type II ($4 - 60\mu m$) and $\phi = 0.01$

A total of 22 experiments are carried out with a variation in sediment type and initial concentration. A summary of all the experiments and additional experimental parameters can be seen in Table 3-2.

Table 3-2 Summary of experiments

#	Sediment	Particle Size range [μm]	Mass total [kg]	ϕ [—]	ρ_p [kg/m^3]	T [$^{\circ}C$]
1	Type I	75 – 125	0.172	0.0050	2460	13.4
2	Type I	75 – 125	0.344	0.0100	2460	13.4
3	Type I	75 – 125	0.517	0.0150	2460	14.6
4	Type I	75 – 125	0.689	0.0200	2460	14.6
5	Type I	75 – 125	0.861	0.0250	2460	14.1
6	Type I	75 – 125	1.033	0.0300	2460	14.1
7	Type II	4 – 60	0.037	0.0010	2650	14.0
8	Type II	4 – 60	0.093	0.0025	2650	14.9
9	Type II	4 – 60	0.186	0.0050	2650	14.7
10	Type II	4 – 60	0.371	0.0100	2650	14.7
11	Type II	4 – 60	0.557	0.0150	2650	13.3
12	Type II	4 – 60	0.742	0.0200	2650	13.1
13	Type II	4 – 60	0.928	0.0250	2650	14.3
14	Type II	4 – 60	1.113	0.0300	2650	14.3
15	Type I and Type II	4 – 125	0.036	0.0010	2650 and 2460	14.5
16	Type I and Type II	4 – 125	0.089	0.0025	2650 and 2460	14.0
17	Type I and Type II	4 – 125	0.179	0.0050	2650 and 2460	14.6
18	Type I and Type II	4 – 125	0.358	0.0100	2650 and 2460	14.3
19	Type I and Type II	4 – 125	0.537	0.0150	2650 and 2460	14.1

20	Type I and Type II	4 – 125	0.715	0.0200	2650 and 2460	14.1
21	Type I and Type II	4 – 125	0.894	0.0250	2650 and 2460	14.1
22	Type I and Type II	4 – 125	1.073	0.0300	2650 and 2460	14.3

3.3 Experimental set-up for the calibration

3.3.1 The tank and other tools

The same existing tank as the previous set-up is used for the calibration. The tank remains in the same position and configuration as the previous experiment set-up (same back light, diffuse paper and dark cloth). The tank is only modified by moving the lock-gate to $x_0 = 0.4m$, see Figure 3.11. The lock-gate is moved to create a bigger mixing space for the suspension. The same high speed camera as the previous set-up will be used with the same settings. Additional tools like the mixer and scale are also used for these process.

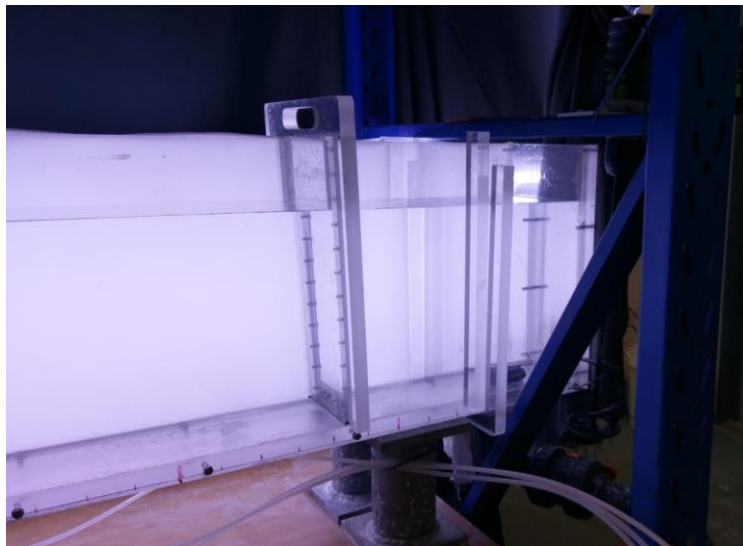


Figure 3.11 Tank set-up for the calibration experiments

3.3.2 Experimental procedure for calibration

The procedure involves the measuring of specific masses of sediment that can be added one after another in a period of time, see Figure 3.12. Furthermore, every time that a new mass is added, one will have to mix the added sediment and previous suspension well with the mixer to create a new suspension with a specific concentration. The section of the tank where this suspension is mixed is separated by the lock-gate.



Figure 3.12 Scale with sediment divided into specific masses

The procedure of when mass is added and mixed with a new suspension as a result, will be recorded so that images can be retrieved. Consequently, every image is specific to a concentration per type of sediment, see Figure 3.13. For this reason, the calibration procedure has to be repeated per all three sediment types. A snapshot of the used section of the tank during the calibration procedure can be seen in Figure 3.14.

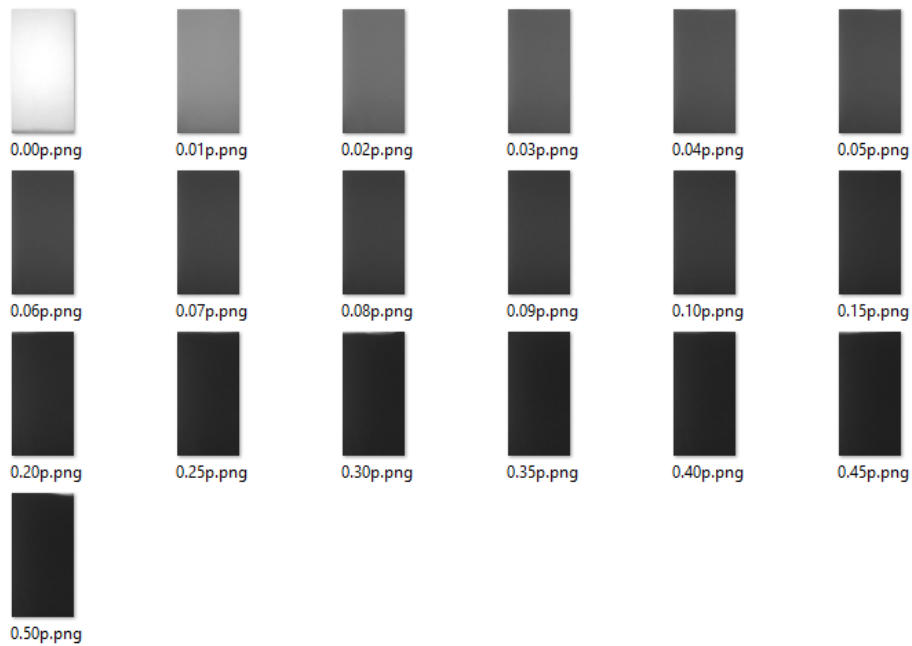


Figure 3.13 Shades of grey for Sediment Type II, with an increase of concentration

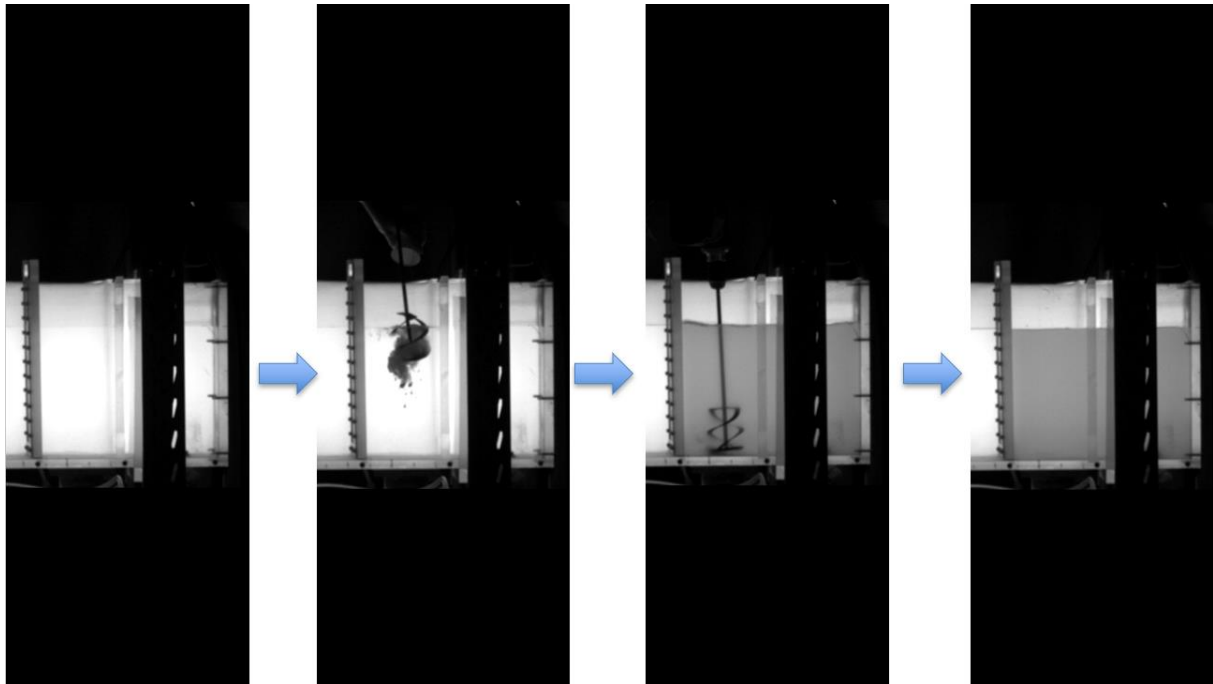


Figure 3.14 Snapshot of the calibration procedure

Per sediment type, the calibration is made for concentrations between certain ranges with different steps, a summary can be seen Table 3-3.

Table 3-3 Sediment concentration ranges and steps within

Sediment	Concentrations ranges	Steps
Type I	0.0% - 0.1%	0.01%
	0.1% - 0.5%	0.05%
	0.5% - 1.0%	0.10%
	1.0% - 2.0%	0.25%
Type II	0.0% - 0.1%	0.01%
	0.1% - 0.5%	0.05%
Type I and Type II	0.0% - 0.1%	0.01%
	0.1% - 0.5%	0.05%

3.3.3 Concentration measurement

Calibration

A different calibration procedure is done for each sediment type in order to measure the concentration of the current. The more particles are added to clear water to increase the concentration, the more light will be blocked by the particles. This will give different shades of grey specific per sediment and concentration. As an example, Figure 3.13 shows the shades of grey obtained for sediment Type II, the concentration is increased from 0.0% (clear water) to 0.5%.

To calculate the concentration of the current, the pixel changes of obtained images from the recordings are used. As a consequence to the light not being completely homogeneous over the length and height of the tank, different pixel values are read at the start of the experiments when the tank is filled with only clear water. Most values lie close to or are equal to the maximum dynamic range of 8 bit (255 pixel). It is important to not try to make the whole tank 255 pixel value as this could mean that

a large portion of the tank is overexposed and thus detail will get lost. Consequently, a pixel value of 255 represents complete white and a value of 0 complete black.

Each starting pixel value found in the tank will have its own calibration curve. To determine this curve it is important to first use a Gaussian blur to remove noise from the images. This blur takes the noise out of an image by using a weighted convolution filter. It is achieved by doing a convolution between a kernel and an image. For this calibration a standard Gaussian kernel of 3x3 was used (OpenCV Tutorial C++, 2020). The kernel uses the standard deviation of the Gaussian distribution in the X and Y direction, see Figure 3.15. At last, the average of measurements per pixel are taken and by using non-linear regression the concentration graph for each pixel is calculated. Figure 3.16 shows the measured values for a starting pixel value of 255 with the calculated graph using non-linear regression.

	1	2	1
$\frac{1}{16}$	2	4	2
	1	2	1

3 x 3 Gaussian Kernel

Figure 3.15 Standard Gaussian kernel for OpenCV (OpenCV Tutorial C++, 2020)

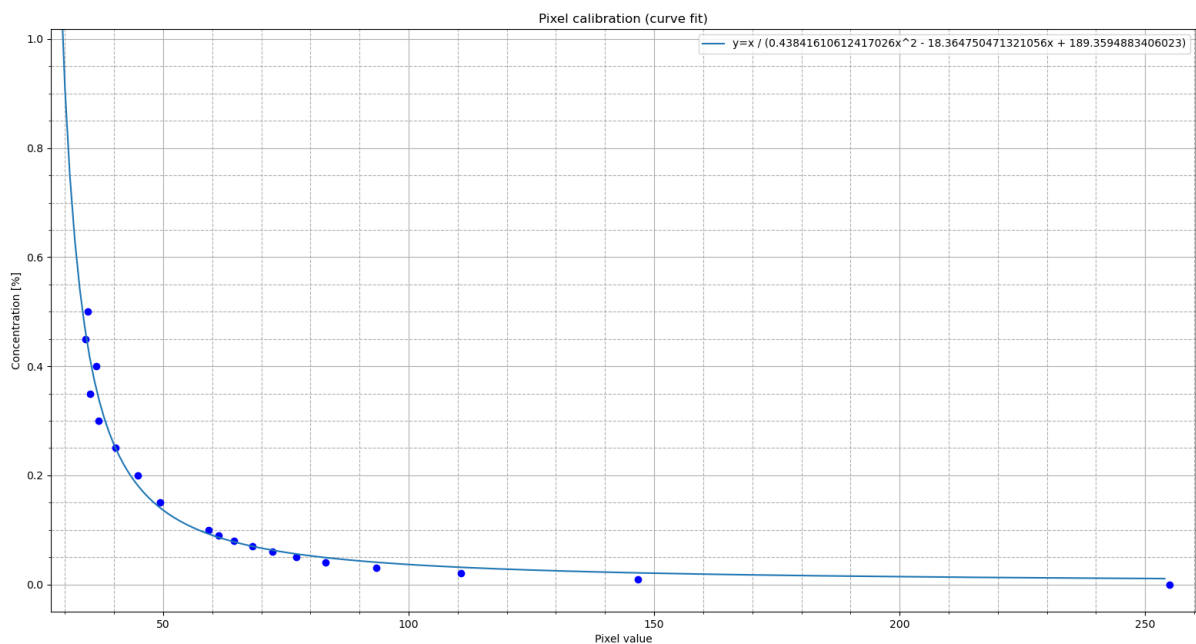


Figure 3.16 Pixel calibration by making use of curve fit. The dots are the measured data and the line is the curve fit graph

Measurement

Before the measurement of the concentration, a Gaussian blur is applied to the used images. The concentration is then measured by using an algorithm that compares the starting image and the image with the current. It reads the pixel value changes over a vertical line, see Figure 3.17. First, if a pixel value change is detected, the starting pixel value is read and a curve fit graph is made for that pixel value. Consequently the darker pixel value is read and finally, the concentration value of that pixel can be determined. Therefore, a concentration profile can be obtained at different sections of the current, see Figure 3.18 as an example of concentration profiles.

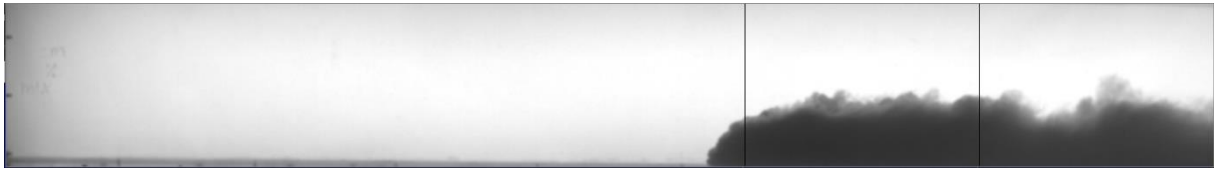


Figure 3.17 Image with current showing two dark lines where the concentration are determined

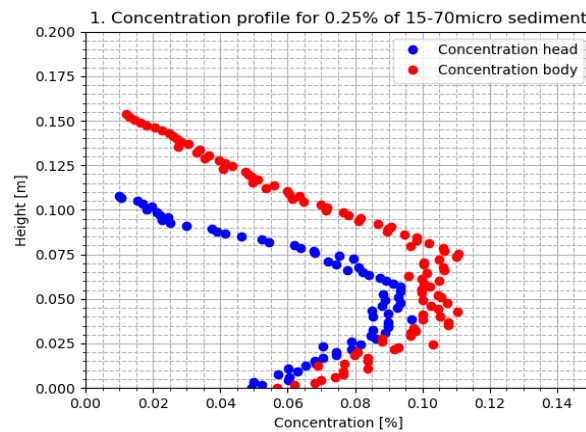


Figure 3.18 Concentration profile for two sections of the current

Color maps

Color maps can be used and calibrated to visualize the concentration densities within the current. The color maps are calibrated with dark blue being a concentration of 0% and dark red a given maximum concentration per type of sediment. The calibration is explained as follow by using a starting picture of 2x2 pixels:

1. The starting picture divided in pixels.



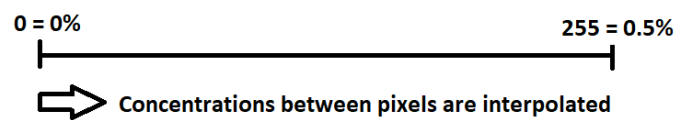
2. The picture is then converted to a pixel array with different pixel values. A pixel value of 255 is white and a pixel value of 0 is black.

255	0
0	0

3. Each pixel value has its own concentration value obtained from a different program which is then given as a matrix of different concentrations. For this example, the maximum measurable concentration was 0.5%.

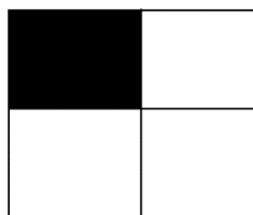
0%	0.5%
0.5%	0.5%

4. The obtained matrix is then converted in pixel values.

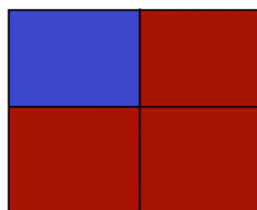


0	255
255	255

5. The matrix is then converted in a black, white and grey picture.



6. The grey picture is then converted into 3 channel colors (red, green and blue)



Pixel value	R	G	B
0	0	0	255
128	0	255	0
255	255	0	0

The calibrated current by making use of a color map will look like Figure 3.19.

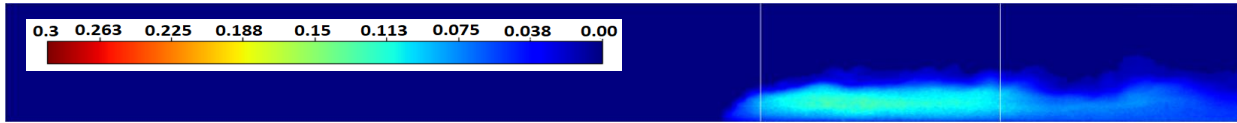


Figure 3.19 Color map of a calibrated current for sediment type II and a concentration of 0.25%

3.4 Experimental measurements

3.4.1 Flow Velocity

The velocity of the current is measured by making use of machine vision tools like OpenCV and algorithms made in Python.

First, the video is cropped so that only the length of the tank ($L = 2.83m$) where the current propagates fits the video window. The obtained video window for this research has a total pixel length of 1840. Then, measurements can then be done by using the pixel length (1 pixel = 0.00154m) or by using the frames of the video (FPS = 130).

Furthermore, a subtraction procedure is needed to calculate the velocity of the head. This procedure goes as follow:

1. Obtain a first frame, from the beginning of the video, with the tank only filled with clear water, Figure 3.20 (1).
2. After step 1, the following frames are subtracted from the first frame by the Python algorithm, Figure 3.20 (2) .
3. The result is a corrected video without the imperfections of the tank or initial background and only with the isolated current, Figure 3.20 (3).
4. Using this corrected image a binary image can be made using a threshold value. This binary image will only produce a video with the contour of the wave, Figure 3.20 (4).
5. From the binary image a head velocity can be calculated by using the Python algorithm.

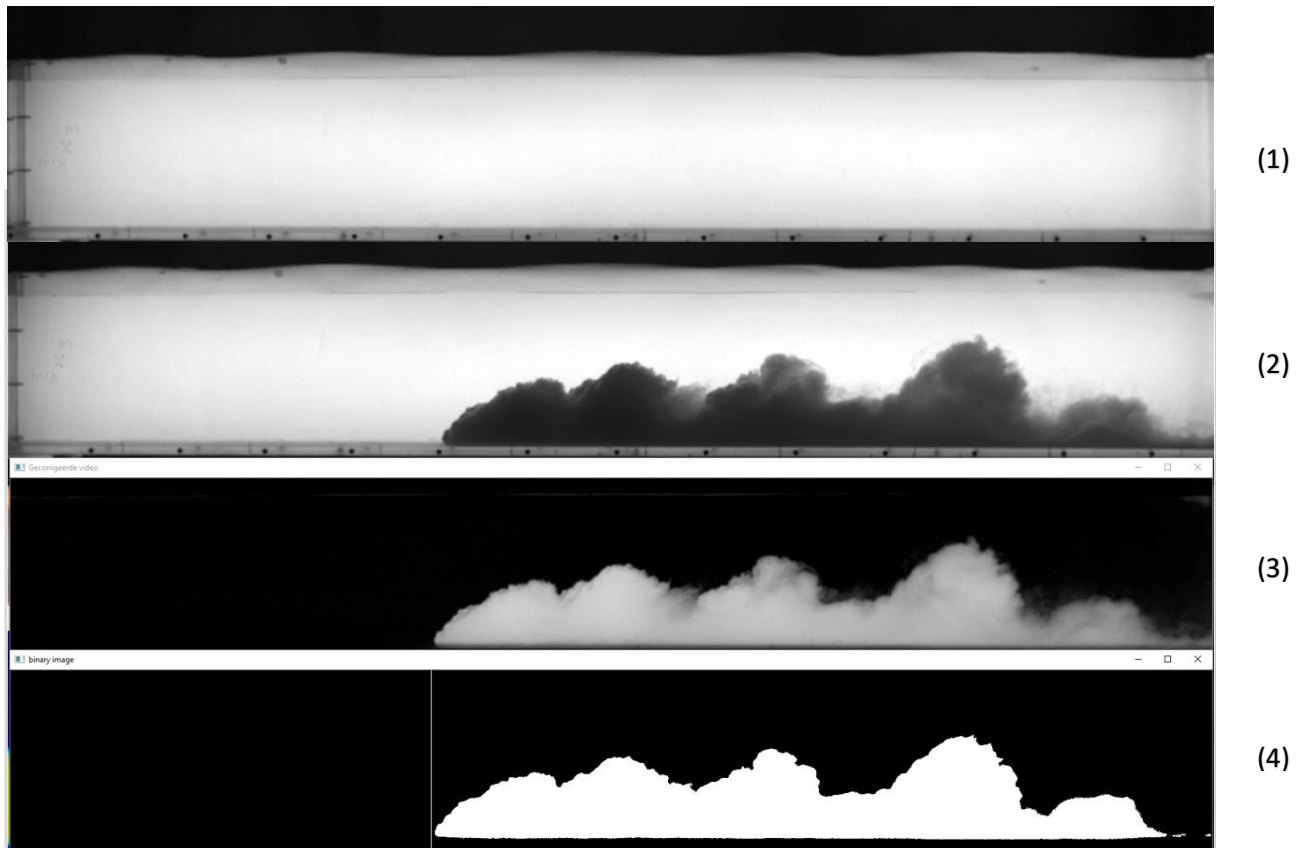


Figure 3.20 Snapshots of the original first frame of the video (1), the original video with the current (2), the corrected image (3) and the binary image of the current (4)

By making use of the binary image, the velocity of the head can be calculated by measuring the position of the head of the current in distance and time, see Figure 3.21 for an example.

During calculations of the head velocity it was observed that the velocity oscillates. This mainly happens due to a surface wave created at the time the lock gate opens to release the suspension into the tank at the start of every experiment. This means that the results of the head velocity are polluted with a certain frequency caused by the surface wave.

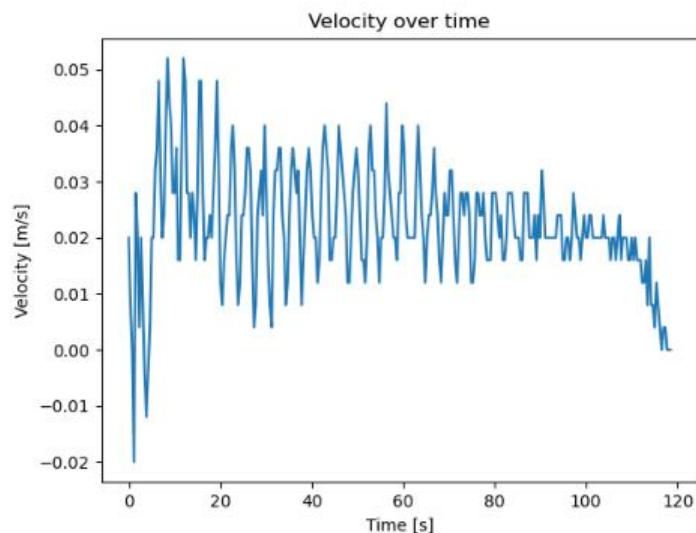


Figure 3.21 Velocity over time for sediment type II with initial concentration 0.1%

If we measure the velocity of the head over time it can be considered as a discrete time signal. Therefore, a digital filter may be used to filter out a specific frequency from this signal.

First, a sampled time can be determined per current so that no aliasing takes place. Then, the sampled velocity-time data is used to create a magnitude spectrum. This spectrum gives information about the frequencies that are present in the signal, see Figure 3.22. By comparing the magnitude spectrum at different lengths of the tank, it can be determined what the frequency of the surface wave is and thus, what frequency should be filtered out.

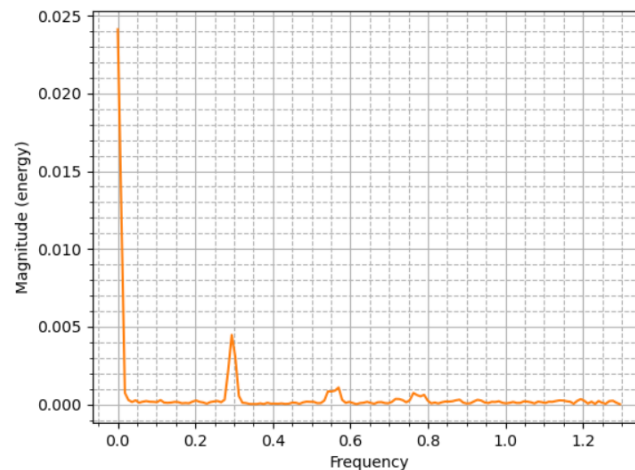


Figure 3.22 Magnitude spectrum taken at the beginning of the tank for Sediment Type II and a concentration of 0.1%

A Chebyshev bandstop filter Type 2 is used to filter out the frequency of the surface wave for all the experiments. This filter was chosen as it gives no ripples in the passband and also due to its steeper roll off.

Filtering a signal introduces a delay which means that the output signal is shifted in time with respect to the input signal. To compensate for the delay introduced by an IIR Filter, as the one that is used for all the experiments, the function *filtfilt* is used. The function *filtfilt* compensates for delays introduced by the filter and corrects for filter distortions (MathWorks, 2020) (SciPy.org, 2020).

A filter order of 6th was chosen as it produces a sharp roll off without becoming unstable or introducing distortion.

3.5 Experimental difficulties

Reaching the end-wall

When the current reaches the end-wall the current will be reflected back creating a bore to the opposite direction and adding material to other sections in the current or creating unwanted deposition. Data obtained after the current reaches the end-wall would be useless for further analysis of the velocity and concentration to determine the dispersion of the current. Therefore, the recording of the current ends when the end-wall is reached.

Mixing

Before the lock-gate is released, mixing of the sediment and water to a suspension is performed by using a mixing tool for at least 40 seconds to make sure that the suspension is homogeneous when the experiment begins. The tool is also used to introduce turbulence to the current. After well mixing the

suspension, the mixing tool is removed from the tank and put aside before releasing the gate, see Figure 3.8. The time it took to place the mixing tool in its designated place and releasing the gate is around 3 seconds. It could be noted that after the release of the lock-gate, some sediment is left in the mixing part of the tank.

Ambient light and Covid-19 restrictions

It has been found that the ambient light coming from the windows of the laboratory have affected some experiments. This was not clearly visible during testing, but could only be notice when analyzing the data in detail. Most of the days the light did not have an influence, however only in days when it was extremely sunny it was noticeably. Unfortunately, some of the last experiments made were polluted with this light and it was no longer possible to get concentration results using the calibration process. Furthermore, the imposed restrictions on the faculty during the outbreak of Covid-19 prevented further experiments. For details on the light conditions during the experiments, see Appendix F. To prevent ambient light influence in future experiments a controlled environment can be created around the camera and tank.

4. Experimental results and analysis

This chapter discusses the experimental results obtained after data processing. The results obtained consist of a filtered head velocity for each current, concentration profiles at different sections of the current and sediment deposition measurements. This chapter focuses on presenting and interpreting the final processed results for each type of sediment. Afterwards a comparison can be made between sediment types.

Turbidity currents are buoyancy-driven flows due to the suspension of dense particles in an ambient fluid. The dynamics of the currents considered are assumed to be dominated by a balance of buoyancy and inertial forces with viscous forces playing a smaller part at the start of the current and eventually dominating near the end. The currents are considered two-dimensional for the analysis of concentration profiles and head velocity but the width of the tank is taken into account for the mass analysis. The current flows over a horizontal surface.

4.1 Head velocities

The head velocity can be calculated by using the traveled distance at different times. Figure 4.2 shows a velocity-distance graph of sediment Type II with a starting concentration of 0.1% and the distance is measured every 5 pixel (0.0077m). Figure 4.1 shows a velocity-time graph of sediment Type II with similar initial concentration where the time is sampled every 50 frames (0.385s).

It can be seen in Figure 4.1 and Figure 4.2 that the head velocity is polluted with a certain frequency caused by the surface wave.

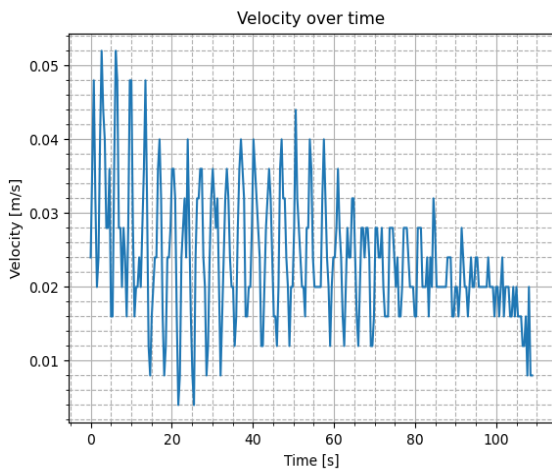


Figure 4.1 Velocity-time graph of sediment Type II with initial concentration of 0.1% measured every 50 frames

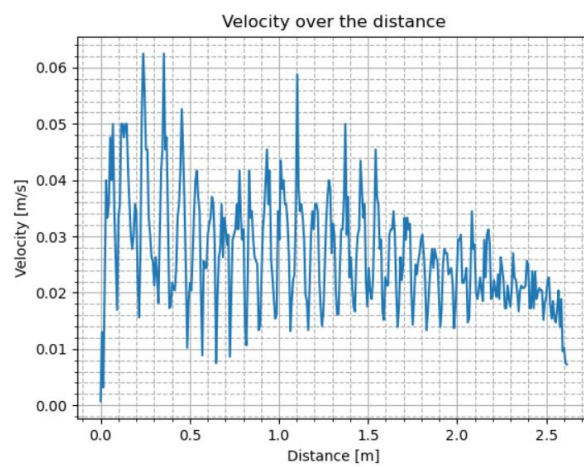


Figure 4.2 Velocity-distance graph of sediment Type II with initial concentration of 0.1% measured every 5 pixel

The obtained signal is a summation of different sine waves including the surface wave, therefore it is possible to filter out the frequency of the surface wave by making use of a digital filter. The signal is filtered with a Chebyshev Type 2 band-stop filter. This filter introduces a time delay. To compensate the time delay, the *filtfilt* function is used, see Chapter 3.4.1 for further details. A comparison between a filtered signal with time delay and with a corrected signal can be seen in Figure 4.3a and Figure 4.3b.

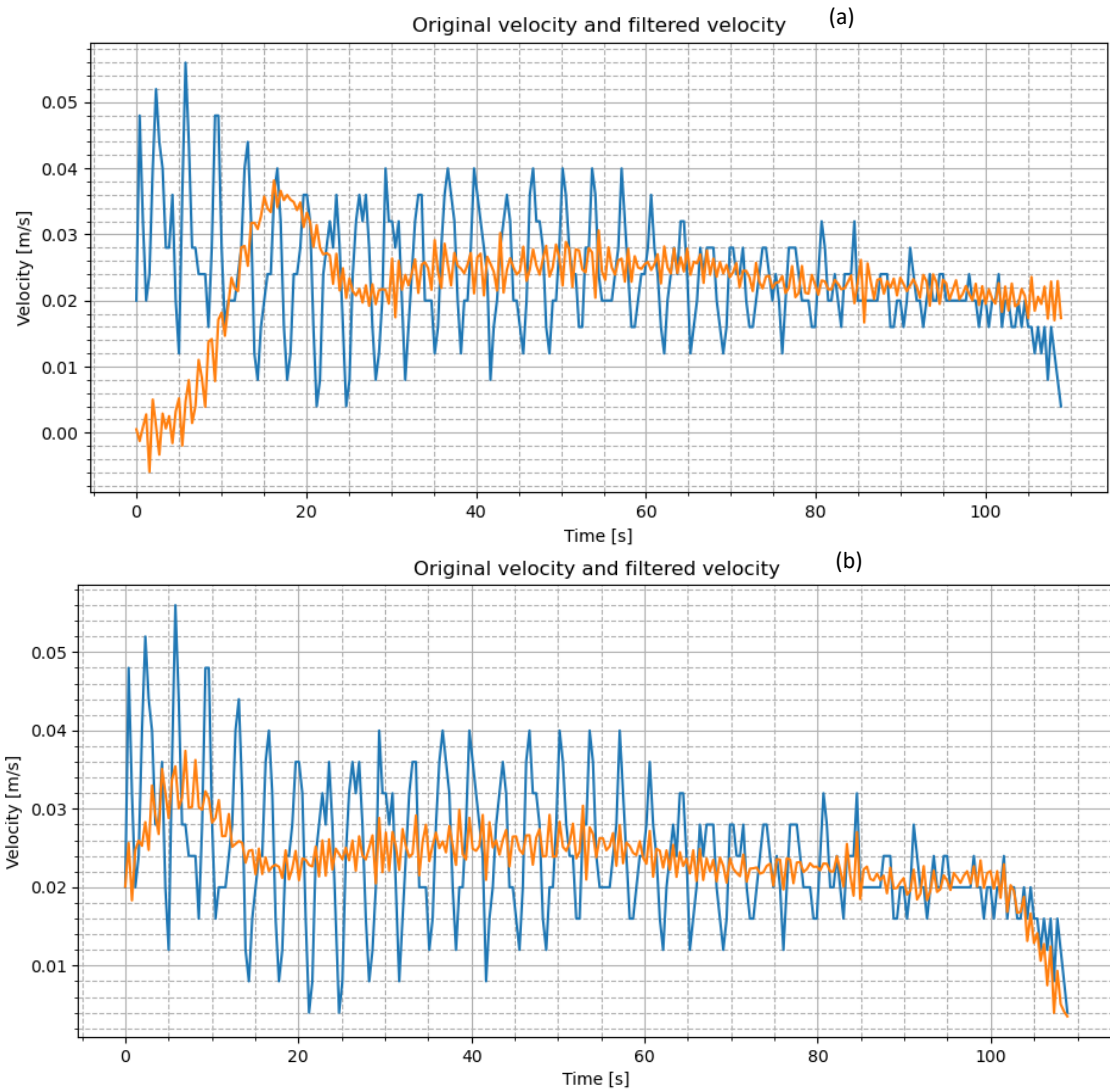


Figure 4.3 (a) Filtered signal with time delay using a Chebyshev Bandpass filter type 2 and (b) a filtered signal with a correction using the function `filtfilt` for Sediment Type II and concentration of 0.1%. Blue line represents the original velocity and the orange line represents the filtered velocity

Several experiments were performed for sediment type I, sediment type II and the combined sediment type I and II to determine the head velocity of the current as a function of time. An algorithm made in Python is used to track the front position of the current. Depending on the initial concentration and speed of the current the front position was tracked for every 30 to 50 frames (0.23s – 0.38s) along the length of the tank. For currents that are not as fast, 50 frames per second was enough to measure the front speed. However, for currents with higher speeds, 30 frames per second was needed to prevent aliasing of the measurements. The used sample frequency can be seen per experiment and sediment type at Table 4-1.

Table 4-1 Sample frequency per current

Sediment	Particle Size range [μm]	Initial Concentration (%)	Frames per measurement	Fs [Hz]
Type I	75 – 125 μm	0.5	50	2.6
	75 – 125 μm	1.0	50	2.6
	75 – 125 μm	1.5	50	2.6
	75 – 125 μm	2.0	50	2.6
	75 – 125 μm	2.5	50	2.6
	75 – 125 μm	3.0	50	2.6
Type II	4 – 60 μm	0.1	50	2.6
	4 – 60 μm	0.25	50	2.6
	4 – 60 μm	0.5	30	4.3
	4 – 60 μm	1.0	30	4.3
	4 – 60 μm	1.5	30	4.3
	4 – 60 μm	2.0	30	4.3
	4 – 60 μm	2.5	30	4.3
	4 – 60 μm	3.0	30	4.3
Type I and Type II	4 – 125 μm	0.1	50	2.6
	4 – 125 μm	0.25	50	2.6
	4 – 125 μm	0.5	30	4.3
	4 – 125 μm	1.0	30	4.3
	4 – 125 μm	1.5	30	4.3
	4 – 125 μm	2.0	30	4.3
	4 – 125 μm	2.5	30	4.3
	4 – 125 μm	3.0	30	4.3

The python algorithm starts the measurement when a distinctive head is detected. Since this starting point was at around the same section of the tank for all the experiments it was decided to fix the starting point in the tank, this point is considered $t_0 = 0$ (see Figure 4.4). The starting point is situated at approximately 0.15m from the lock-gate.

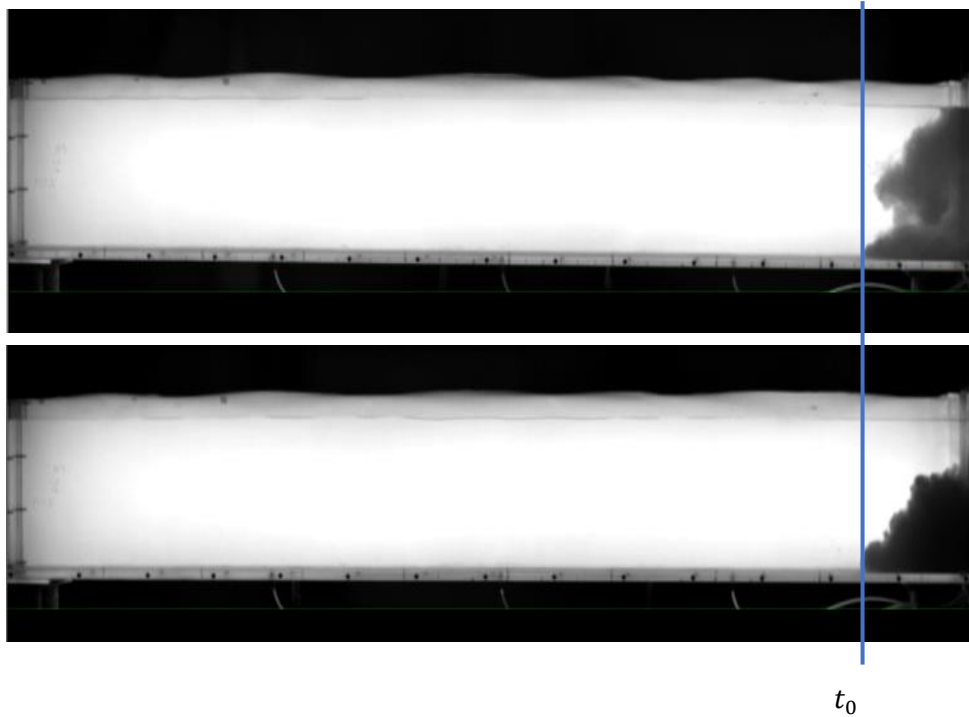


Figure 4.4 Starting point of measurement at the tank, at approximately 0.15m from the lock-gate

Comparing experiments recorded with an experimental set-up where the camera is not positioned at a fixed position and where the mixing is not consistent gives a clear difference in the measured head velocities, as can be seen in Figure 4.5.

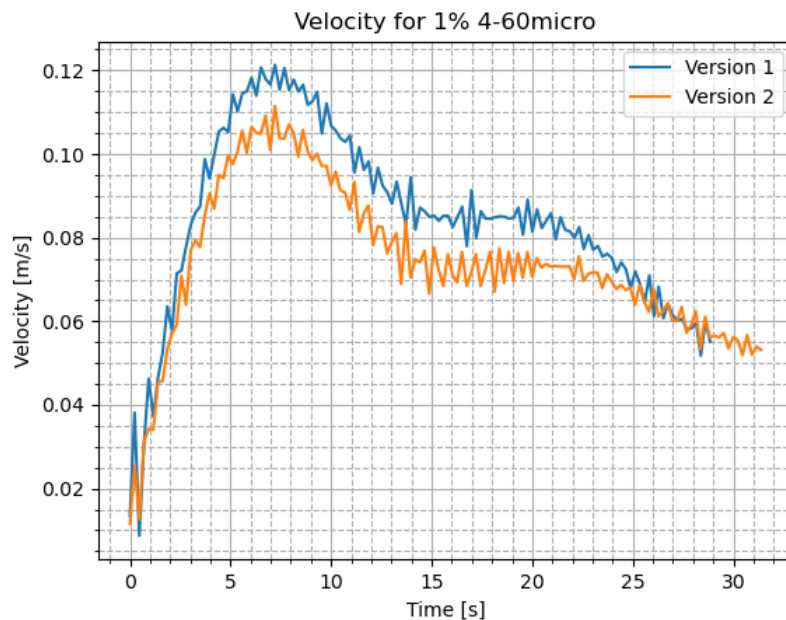


Figure 4.5 Comparison of head velocities for sediment type II with initial concentration of 1%

However, when the experimental set-up and mixing is kept constant for all experiments, the error margin is minimized and the runs become more consistent. This can be seen in Figure 4.6. All the experiments used in this research are recorded with a fixed experimental set-up and constant mixing time.

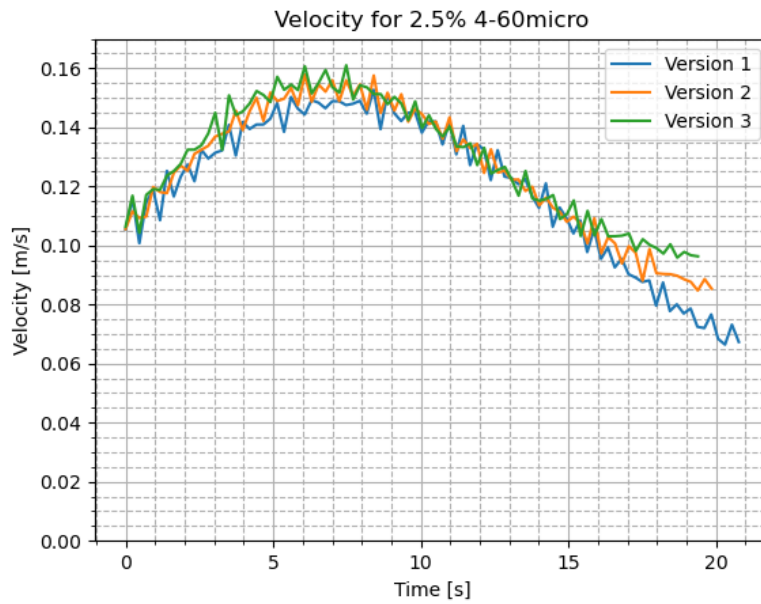


Figure 4.6 Comparison of head velocities for sediment type II with initial concentration of 2.5%

Results of the filtered head velocity over time can be seen in Figure 4.7 for the three types of sediment with different initial concentrations. The horizontal axis displays the time in [s] and the vertical axis represents the filtered head velocity of the current measured in [m/s].

According to (Rottman & Simpson, 1983) and (Simpson, Gravity Currents: In the Environment and the Laboratory, 1997) there are two distinct phases with a possible third phase that can be achieved when a homogeneous gravity current is released during a lock exchange experiment, for more details about the discussed phases see Chapter 2.5. (Bonnecaze, Huppert, & Lister, 1993) also describe similar stages of the flow for particle-driven gravity currents, see Chapter 2.6. Furthermore, Figure 2.10 can be consulted for a graphic representation of the three phases seen for particle-driven gravity currents.

The initial phase starts just after the lock is removed and the suspension collapses. During this phase, the collapsed suspension will form a flow that travels towards the end wall. At the same time, the displaced upper fluid will form a flow of its own that propagates in the opposite direction creating an inverted bore. Consequently, the inverted bore will have a retarding effect on the suspension flow.

The graphs of the three types of sediment (Figure 4.7) show that some of the currents with different initial concentrations are accelerating until they reach a maximum velocity. Then, they start to decelerate. The following currents display this behavior:

- Sediment type I: 0.5% up until 3.0%
- Sediment type II: 0.1% and 0.5% up until 3.0%
- Combined sediment type I and II: 0.5% up until 3.0%

This behavior is in line with the initial phase theory. However, Figure 4.7 also shows that lower initial concentration values such as 0.25% of sediment type II, 0.1% and 0.25% of the combined sediment type I and II do not reach this acceleration phase but start decreasing in speed as soon as the head is formed. A reason for this is the buoyancy force that initially drives the current. For lower initial concentrations this driving buoyancy force will not be as large as for higher initial concentrations due to less initial suspended particles. This will lead to a longer adjustment phase until a distinctive head is formed and by this time, the head will already be decelerating due to inertial forces applied by the lighter ambient fluid. For sediment type II and the combined sediment type I and II, it can be observed

that from an initial concentration of 0.5% a distinctive transition from acceleration to maximum velocity to decreasing velocity can be seen for both types of sediment. This can indicate that a distinctive propagating head is formed shortly after the release of the suspension.

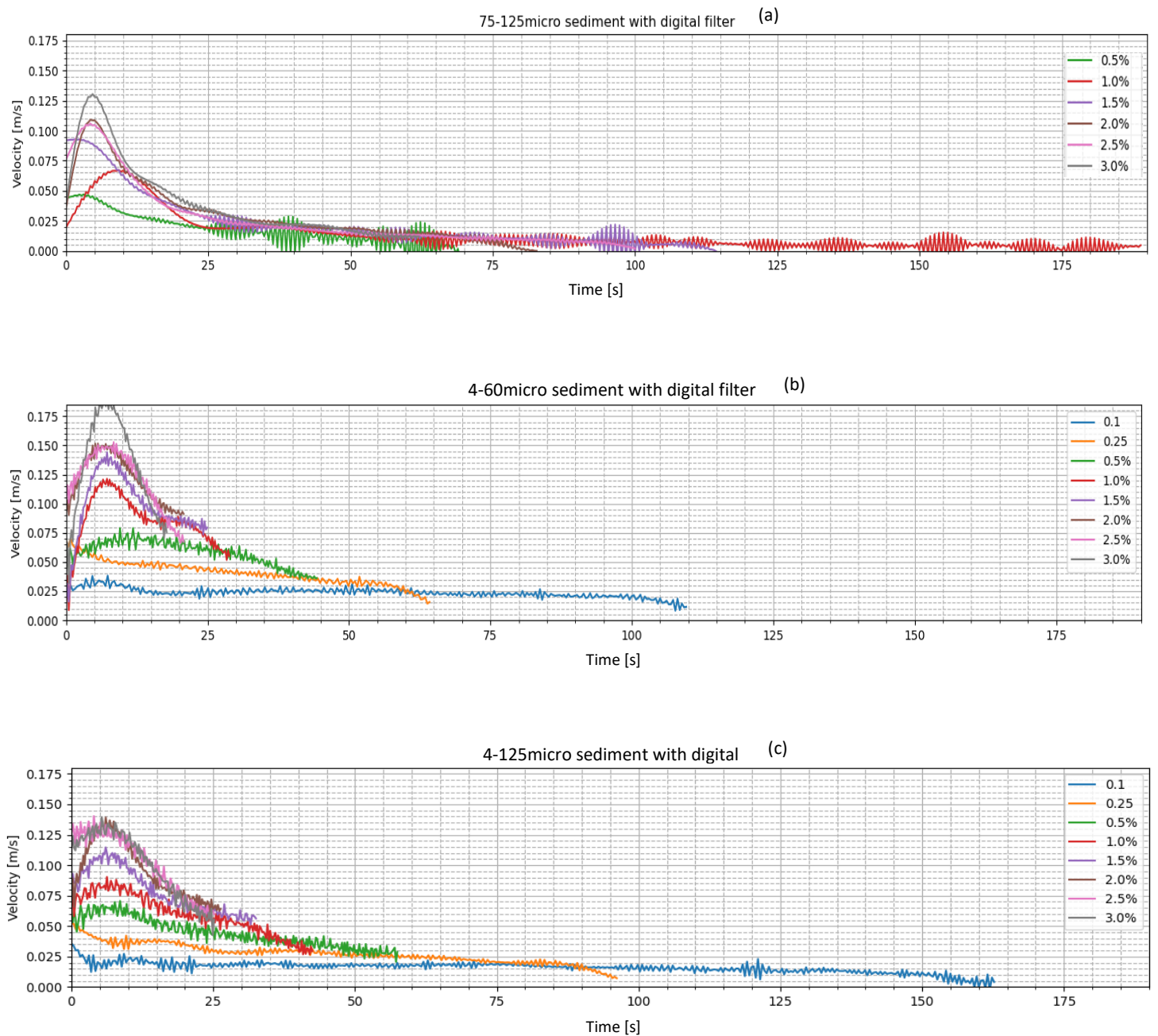


Figure 4.7 Head velocity over time for all three types of sediment. (a) Sediment type I, (b) Sediment type II and (c) Combined Sediment type I and II

The second phase is initiated when the velocity starts to decrease after the maximum velocity is reached. Afterwards, a constant speed is reached by the current. During this phase, the buoyancy forces of the current are balanced by the inertial force of the ambient fluid. This phase is reached by all initial concentrations of sediment type I (75 – 125µm). This phase can also be observed for all initial concentrations of Sediment type II (4 – 60µm). However, only concentrations up to 2.0% reach

the constant speed and concentrations above 2.0% only reach the start of the phase where the velocity decreases. At last, for the combined sediment type I and II ($4 - 125\mu m$) this phase is reached for all initial concentrations. For the latter type of sediment, the second phase is not completed (they do not reach the constant velocity) for higher concentration of 2.0%, 2.5% and 3.0%, but a start of the phase can be observed. Due to the buoyancy force, these initial concentrations do not reach a constant speed during this phase. For higher initial concentrations the driving buoyancy force will be larger as a result of more particles that remain suspended for a longer time. As a consequence it will take a longer time to reach a balance between inertial forces and buoyancy forces. Due to the limited length of the tank, the currents do not have enough time to evolve and fully reach the constant velocity during this phase.

A third phase is reached, according to literature, when the ambient fluid forms a current of its own during the initial phase after the release of the gate. After this, the resulting bore is reflected by the wall of the tank and the backflowing bore eventually reaches the propagating current and overtakes the front. When the bore reaches the current it causes the propagating current to decelerate until viscous forces eventually start to dominate the behavior of the current. Hereby, the viscous forces start to damp the inertial forces of the current and then the particles start to settle due to the settling effect until the current vanishes completely. This phase is reached by sediment type I for initial concentrations of 0.5% – 2.5%. For sediment type II and the combined sediment type I and II, only initial concentrations of 0.1% and 0.25% reach the start of this third phase. The lower concentrations of sediment type II and the combined sediment type I and II reach the start of this phase due to a combination of smaller particles (between $4 - 60\mu m$) contained by the currents and a low driving buoyancy force. Firstly, due to the low initial concentrations the particles will approach a settling velocity without much effect of hindered settling. The settling velocity of these particles is small and very few settle out during the current's run keeping the smaller particles suspended. Secondly, due to the small initial concentration the driving buoyancy force will be low and the currents will propagate at a low velocity. The lower speed will lead to the backflowing bore catching up with the currents head as it propagates, eventually decelerating the head velocity and introducing the third phase.

Sediment type I reach the third phase due to the settling velocity of these particles being high. Consequently settling out much faster and decreasing the driving buoyancy force, with this decrease the current then propagates at a low velocity and the backflowing bore can catch up with the head and the third phase is initiated.

By comparing the three types of sediment, it can be noted that the highest velocity is achieved by sediment type II for each initial concentration. Hereby, the particles stay in suspension for a longer time due to their relative low settling velocity, keeping the driving buoyancy force high and thus reaching a higher velocity.

Furthermore, it can be observed that sediment type I takes a longer time to reach the end-wall. This, in comparison with the other types of sediment for all initial concentrations with the exception of initial concentration of 0.5% as this current does not reach the end-wall. In addition, the constant head velocity during the second phase of the currents of sediment type I are similar to head velocities of low concentrations (0.1% and 0.25%) for sediment type II and the combined sediment type I and II at the same phase. The last two events can be derived by making use of Appendix B or Figure 4.8. Hereby, the settling velocity is high for particles of sediment type I. The larger particles of sediment type I have a significantly higher settling velocity than particles of smaller sizes of the same type of sediment. Therefore, the larger particles of sediment type I settle faster leaving the smaller particles of this sediment longer in suspension. As a result, the driving buoyancy force will be kept in balance with the inertial force of the ambient fluid for a longer time keeping the current propagating at a low

speed. As the initial concentration of currents for sediment type I increase from 0.5% – 3.0%, the suspended particles start to play a bigger part. The higher the initial concentration the more suspended particles there will be. Therefore, for higher initial concentrations currents, it can be noticed that it takes them a longer time to reach the balance between inertial and buoyant forces. However, once they reach this point, they have almost the same constant speeds as lower initial concentrations.

In addition, it can be observed that the addition of smaller particles (sediment type II) to larger particles (sediment type I) forming the combined sediment type I and II creates a substantial change in flow behavior. It decreases the time that the flow takes to reach the end-wall for all initial concentrations in comparison with currents containing only large particles (sediment type I). However, the currents are not as fast in reaching the end-wall in comparison with currents containing only small particles (sediment type II). This behavior can be explained due to the smaller particles that remain suspended for a longer time. Consequently reducing momentum loss as they maintain an excess on the current density for a longer period of time.

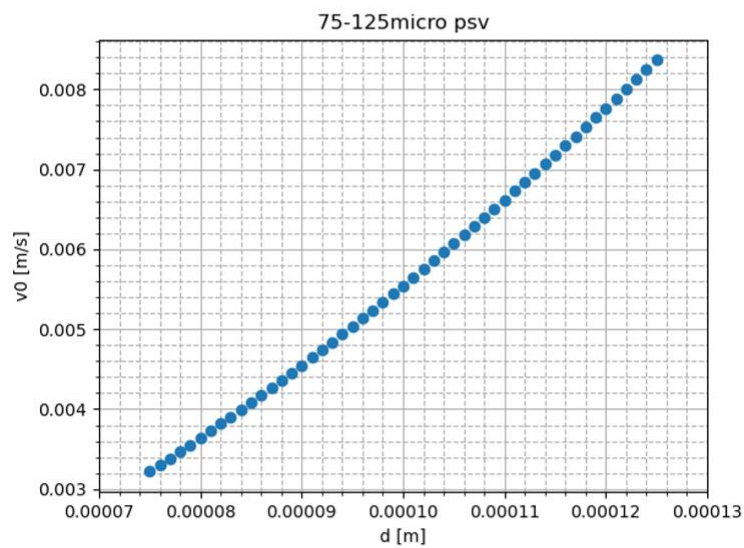


Figure 4.8 Settling velocity of particles for Sediment type I

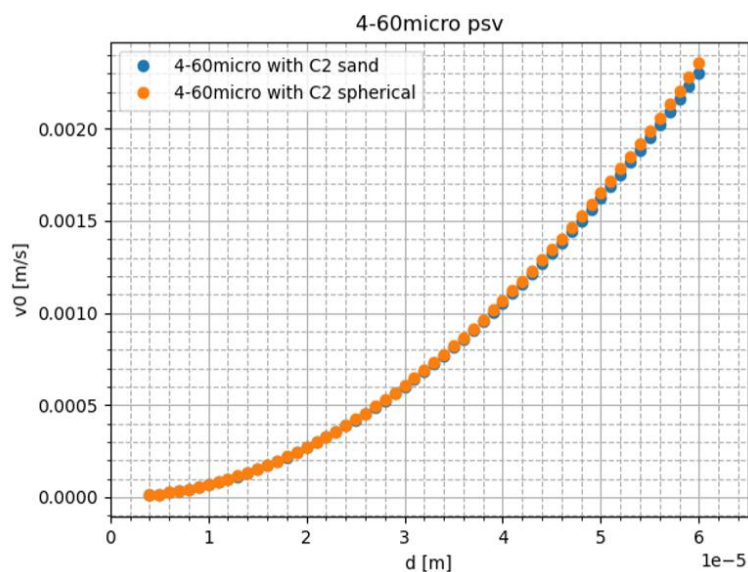


Figure 4.9 settling velocity of particles for Sediment type II

The flow-front progression can be further analyzed by plotting distance against time. Figure 4.10 shows the travel distance of the current as a function of time for each type of sediment with different initial concentrations per sediment type. The vertical axis represents the distance the current travels in [m] and the horizontal axis represents the time in [s].

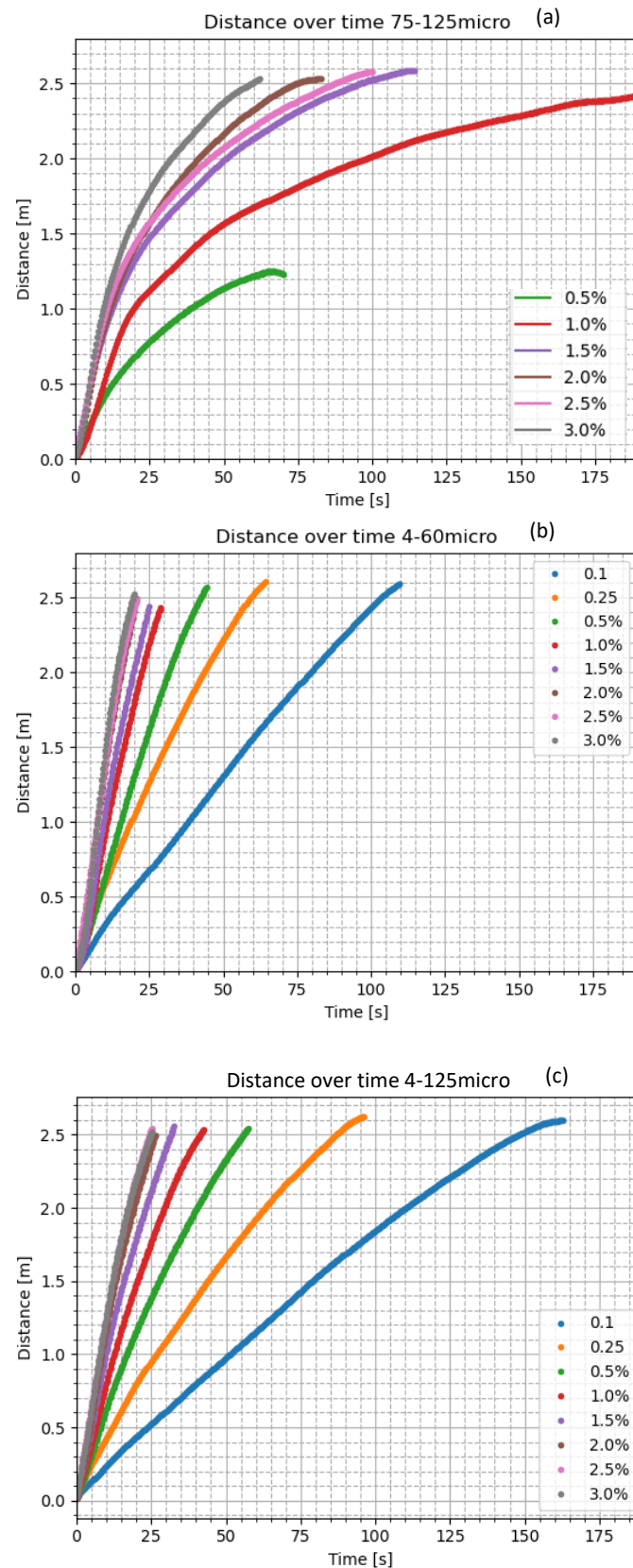


Figure 4.10 Distance over time for the three types of sediment: (a) Sediment type I, (b) Sediment type II and (c) combined Sediment type I and II

For sediment type I, Figure 4.10a, the lengths have a steep initial section while they are in the first phase for all initial concentrations. After the initial phase, the lengths of the currents continue to increase but at a slower rate. Moreover, it can be seen that initial concentration 0.5% does not reach the end wall. In addition, it can also be observed that as the initial concentrations get higher, it takes less time to reach the end wall.

For sediment type II, Figure 4.10b, the initial phase takes a longer time to complete, as a result the length will grow at a steep rate for a longer period of time. Initial concentrations of 2.0%, 2.5% and 3.0% never transition into the second phase. As a result the length keeps growing almost linear with time until it reaches the end wall. Lower concentration of 0.5% – 1.5% keep increasing in time at a slower rate during the second phase of the current.

It can also be observed that concentrations of 0.1% and 0.25% have a constant velocity for a longer period of time as they stay in the second phase longer. As a consequence, the length increases constant with time for this phase. Finally, it can be observed for the latter concentrations that they start to reach the third phase of the current. At this final point the length of the current has a slower rate of increasing. In addition initial concentrations of 2.5% and 3.0% have similar travel distances.

A similar pattern can be seen for the combined sediment type I and II, Figure 4.10c. Hereby, lower concentrations of 0.1% and 0.25% have approximately a constant velocity throughout the experiment as they stay longer in the second phase. As a result, the distance also increases at a constant rate. The start of a third phase can be observed for the latter concentrations and at this point the length keeps increasing but at a slower rate. Initial concentrations of 0.5% – 3.0% go through the first and second phase and accordingly their lengths increase first with a steep section and after this at a slower rate. The currents of higher initial concentrations of 2.0%, 2.5% and 3.0% show similar travel distances.

Comparing all three types of sediment shows that all the curves have a common shape with a steep initial section that becomes less steep over time as the current velocity decreases. Hereby, the steepest section of the curve corresponds to the initial phase of the current. During this phase, the velocity gradually increases until it reaches a maximum value and starts decreasing afterwards. This is the result of a large initial density difference between the current and ambient fluid. Limited settling of particles during this phase keeps the driving buoyancy force and momentum high. Therefore, the velocity increases until it reaches a maximum. Thus, the current can run for a longer distance until the velocity starts decreasing (as more particles start to settle) indicating the initiation of the second phase. During the second phase, the current's distance covered in time is seen decreasing and it reaches almost linear growth as the flow remains at constant speed. This is the result of the settling of particles after the first phase. As the particles start to settle, the density of the current decreases and thus the driving force will become less. For currents that start to reach the third phase, a buckling point can be observed at the end of the currents run distance. This indicates a gradual decrease in speed.

The curves differ between sediment type reflecting a dependence upon grain size. Larger particles (sediment type I) will have a higher settling velocity, thus the currents generated by these type of particles will lose excess density more rapidly than the currents with smaller particles (sediment type II). This would mean that they reach the second phase sooner and will also stay there for a longer time. Consequently, currents with smaller particles (sediment type II) reach the end-wall of the tank sooner than currents with the larger particles (sediment type I) and the mixed suspension (combined sediment type I and II). Lastly, it can be noted that adding small particles (sediment type I) to larger particles (sediment type II) forming the combined sediment type II and I, has a non-linear effect upon the current motion.

4.1.1 Froude number

The Froude number is calculated for each current by making use of equation 2.7. Results per sediment type and initial concentration are shown in Figure 4.11.

The Froude number for all types of sediment is decreasing with time and remains $Fr < 1$ for the entire currents run which is the case for subcritical currents. This type of currents will have a Ri_g (gradient Richardson number) in range between 0.54 – 0.84 (Ellison & Turner, 1959). The gradient Richardson number has a critical value of $Ri_{cr} = 0.25$ (Parsons, et al., 2007). If $Ri_g > Ri_{cr}$ the production of turbulence by shear instability is reduced and the stratification can be considered stable (Parsons, et al., 2007). Hereby, the damping of turbulence balances the generation of turbulence and the mixing layer will not grow any further (Pietrzak, 2016).

Sediment type I, Figure 4.11a, shows a rapid decrease of the Froude number until it starts to stabilize into a more constant value. This is in line with the currents second phase. During this phase the head velocity is decreasing until it reaches a constant speed when the inertial and buoyancy forces are balanced out. In addition, it can be observed that for currents with initial concentration of 2.0% until 3.0%, the Froude number reach a low value near the ends of the currents run. This indicates that the gravity force is damping the current at a higher rate. Furthermore, it can be seen that for initial concentrations of 0.5%, 1.0% and 1.5% the Froude number is increasing towards the end of the currents run. This is due to the currents being divided into sections for this lower concentrations. Therefore the algorithm that measures the height is not able to detect the height of the currents near the end as it measures the height of the current at an assigned distance from the head. This causes the Froude number to increase.

Sediment type II, Figure 4.11b, also displays a decreasing Froude number. However, the value of the Froude number does not reach a low value as observed for sediment type I. This indicates that the driving force of the current is still high during the currents run and it is not being damped as much due to gravity force. The gravity force will have a smaller influence on the current due to relative small particles present in this type of sediment. Furthermore, it can be observed that varying the initial concentration does not have much effect on the value of the Froude number for the different currents. The maximum value of the Froude number that is reached is almost the same for each current.

The combined sediment type I and II, Figure 4.11c, shows a decreasing Froude number for the currents run. However the values of the Froude number are not as high as for sediment type II and not as low as for sediment type I. Therefore, the driving force of the currents is not being damped as much due to the gravity force. However, the gravity force plays a larger role on the propagation of the currents in comparison to sediment type II due to presence of larger particles in this sediment type. Furthermore, varying the initial concentration does not have much effect on the value of the Froude number for initial concentrations larger than 0.25%.

Comparing the three sediment types, it can be observed that sediment type II reach higher values of the Froude number. This is due to the smaller particles present in this type of sediment. They keep the driving force high as there is not much settling of particles throughout the currents run. However, sediment type I reach lower values of the Froude number. As sediment type I has larger particles present, they will damp the current at a higher rate due to the larger gravity force and thus the value of the Froude number will be lower. Furthermore, the values of the Froude number for the combined sediment type I and II are in between the Froude number values of the other sediment types.

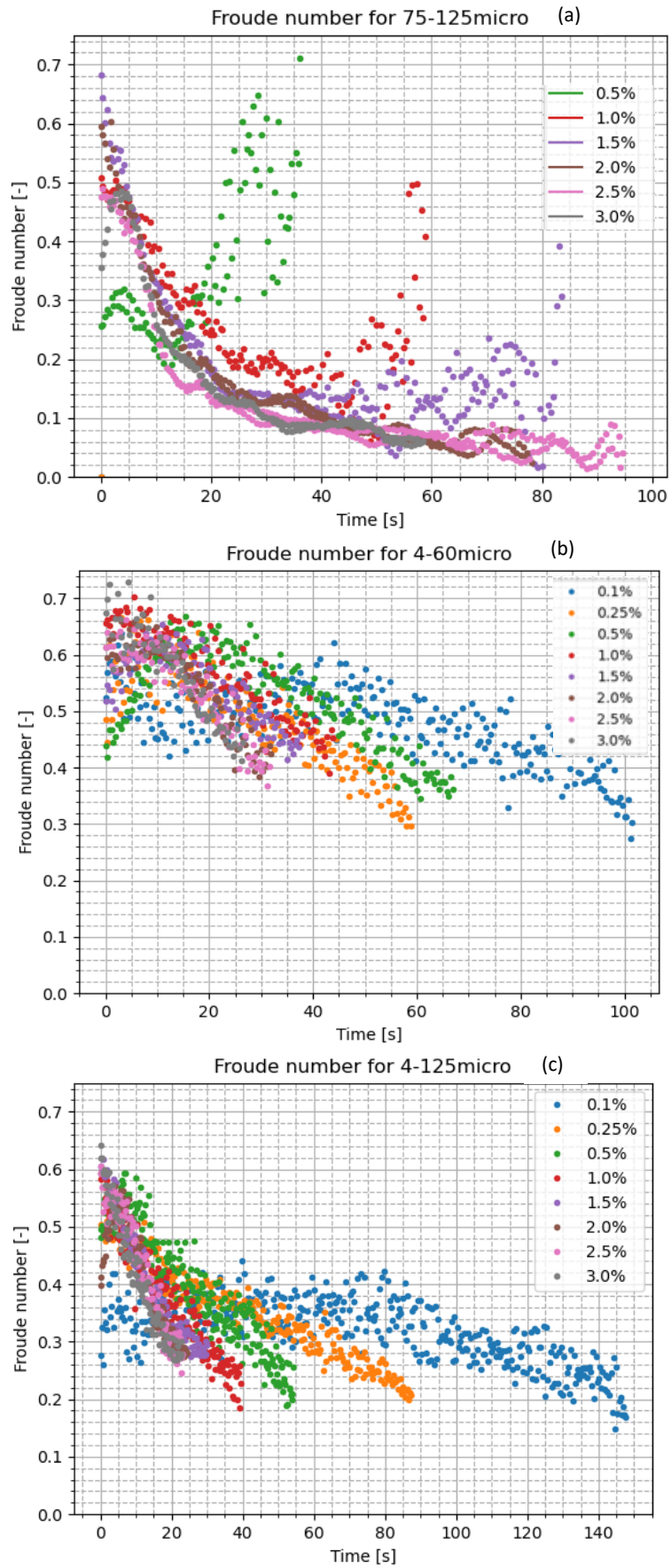


Figure 4.11 Froude number for all sediment types with (a) sediment type I, (b) sediment type II and (c) combined sediment type I and II

4.2 Concentrations

4.2.1 Maximum measurable concentration

In summary, at the start of each experiment, the tank will have for each pixel an starting pixel value (clear water). When the current starts to run, the pixel value will change as the current blocks the light and this will make the pixel value go lower and thus towards 0 (complete black).

The starting pixel values found in the tank varied from 142 - 255 and each pixel value will have its own calibration curve.

Concentrations during the calibration experiments were measurable up to a certain value. After this concentration value, the pixel value started to get higher instead of lower as would be expected. The maximum measurable concentration for sediment type II ($4-60\mu m$) and for combined sediment type I and II ($4-125\mu m$) was 0.5% . For sediment type I ($75-125\mu m$) it was 2%.

Pixel values beyond the maximum measurable concentration became higher, as can be seen in Figure 4.12. This was contrary to expectations as a higher concentration in the tank would mean more particles and these would block more light, thus the pixel value should decrease towards 0 (complete black).

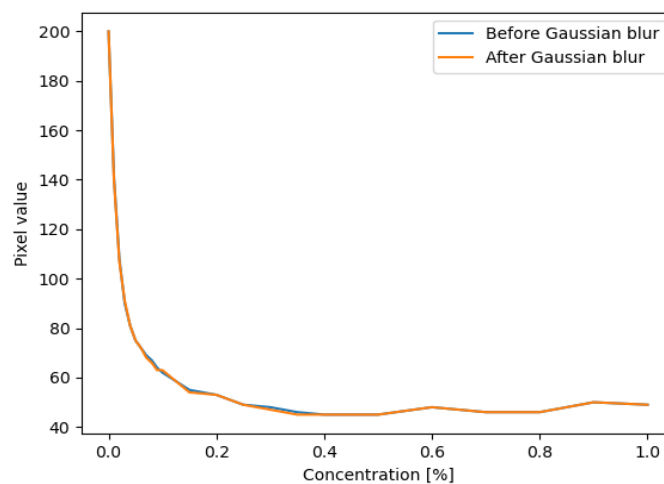


Figure 4.12 Pixel-concentration graph for sediment type I and II combination, (4-125 micro) for pixel nr. 200 measured for concentrations up to 1%

The deviations of pixel values for higher concentrations were caused by light pollution present in the set-up. Therefore, the pixel value was not being able to go any lower for the camera sensor to measure with this set-up and thus the measured values after a certain point would be background noise. This can also be explained using the SNR (signal to noise ratio), Figure 4.13 .Every measurement up until a certain point is significant with the noise, after this the SNR becomes very low which means that the only measured value is the noise.

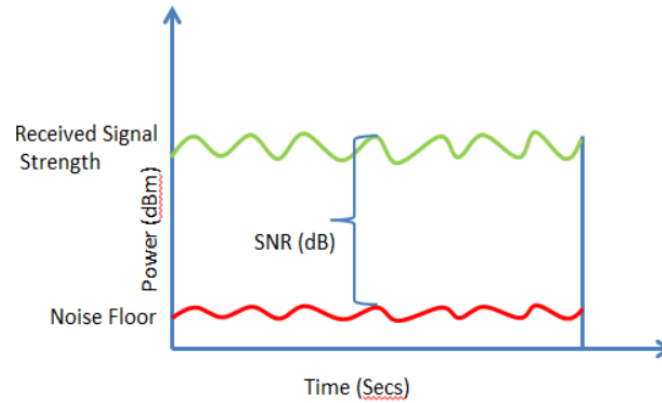


Figure 4.13 Signal to Noise ratio (De Producer School, 2020)

4.2.2 Concentration measurement

After the calibration it was possible to measure the concentration values of a running current at any given time and distance by making use of a python algorithms. The following results were obtained for currents with different initial concentrations and sediment types.

Calibrated color maps

The tank was divided into 5 sections as per Figure 4.14 and $t = 0$ was defined as the moment when the current enters the field of view. This moment is when a distinctive head is formed (Figure 4.4). A series of calibrated color maps were obtained for each section. Each color map shows the concentration values within the current. Each type of sediment was measured up until its maximum measurable concentration value, beyond this value the concentrations are not certain. Therefore, the dark red color on the maps are the maximum measurable concentration value or higher. Below is a selection of color maps per sediment type (Figure 4.14, Figure 4.15 and Figure 4.16), see Appendix C for the complete calibrated color maps.

Results show that sediment type I settled out rapidly. This reduces the density difference between the current and fresh water flow and hence the driving buoyancy force. Furthermore, density differences within the current can be observed from the start up until $1/5L$ of the tank. During later stages, from $2/5L$ of the tank, the density difference within the current seem to disappear and a more uniform density distribution can be seen throughout the current. Moreover, it can be observed that the height of the body of the current is significant in comparison to the height of the surrounding water. At latter stages, from $3/5L$ of the tank, the height of the body continues to be large but the current seems to be getting divided into sections. In addition, a large height difference between head and body is observed throughout the runout length of every current. A clear tail cannot be distinguished for all currents with this type of sediment.

According to Appendix B larger particles of sediment type I will start to settle faster than smaller particles of the same sediment. Therefore, there is a clear density difference within the current as the larger particles of this sediment start to settle as soon as the current is released. Once the larger particles settle, the smaller particles of this sediment continue to be suspended and they create the driving buoyancy force. Furthermore, the d_{50} of this type of sediment tends to be high ($122\mu m$) and close to the maximum grain size for this sediment type ($125\mu m$), see Appendix A. This would mean that 50% or more particles are significantly large and will have a high settling velocity.

The height of the current is relatively large in comparison to its head. Therefore, more entrainment can be observed between the ambient fluid and the current throughout the height of the body. In addition, the larger height of the body in comparison with its head could create a pressure gradient that continues driving the current maintaining it longer in the second phase. See Figure 4.14 for an example of the calibrated color maps for sediment type I.

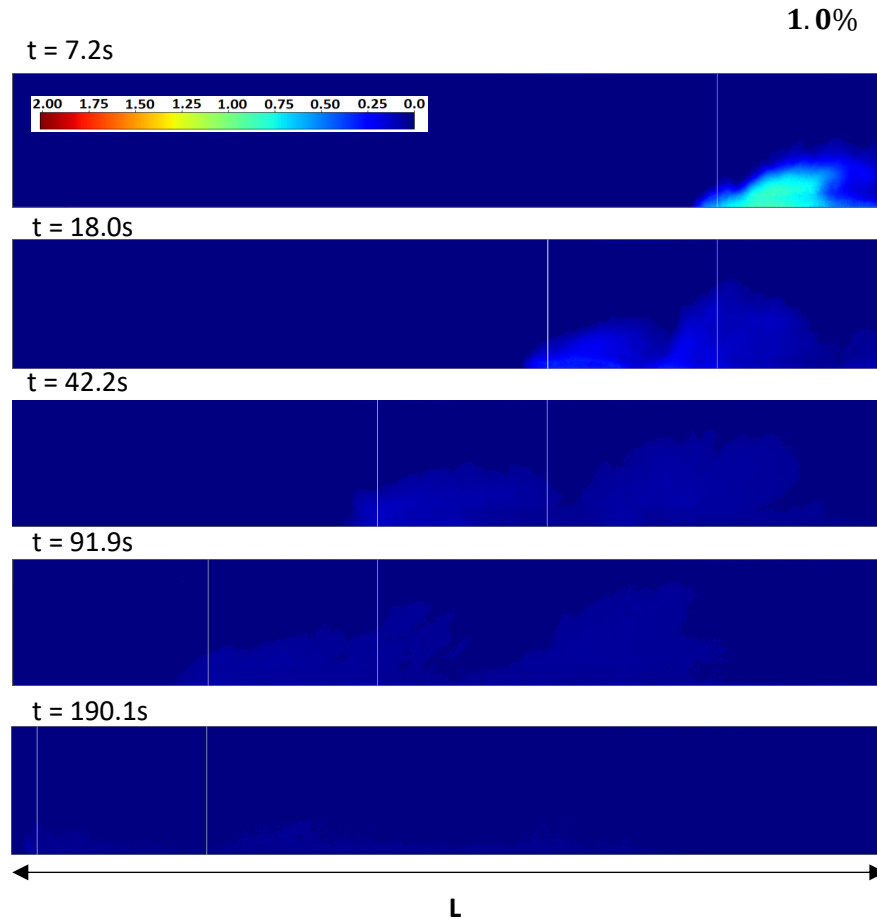


Figure 4.14 Example of a calibrated color map for sediment type I for initial concentration of 1.0%

Results for sediment type II reveal that the particles remain longer in suspension. However, clear density differences between head and body can be seen after some time. The higher density within the current shifts to the head, with the body showing considerably less density. This transition period starts for all of the currents with different initial concentrations at around $2/5L$ of the tank, with the exception of initial concentration of 0.1%. For the current with initial concentration of 0.1%, the transition period happens at $3/5L$ of the tank. Furthermore, the currents have different runout times and thus this transition period is at a different time for each current. In addition, the height of the body for all currents remain almost constant for initial concentrations up until 0.25%. For higher initial concentrations, clear entrainment with the surrounding ambient fluid can be seen. Therefore, defined billows are visible throughout the body of the currents. In addition, a defined tail cannot be distinguished for all the currents. Lastly, the middle and rear part of the currents for all initial concentrations can be divided into a basal dense layer region and a less dense top layer region, see Figure 2.9. This division is caused by the different settling velocities of the particles and due to hindered settling not playing such a big part as can be observed in Appendix B. Therefore, the sediment is easily split into a dense and less dense region. However, as the settling velocities remain small, even the

larger particles of this sediment will take a longer time to settle and thus this separation would be seen almost for the entire current's run.

The small density difference within the current for initial concentration of 0.1% up until $3/5L$ of the tank can be attributed to the relative low settling velocity of the particles and the small height differences throughout the current. Due to the minimal variation between the head, body and tail's height, the particles will remain densely suspended as there is not much entrainment with the ambient flow. See Figure 4.15 for an example of the calibrated color maps for sediment type II.

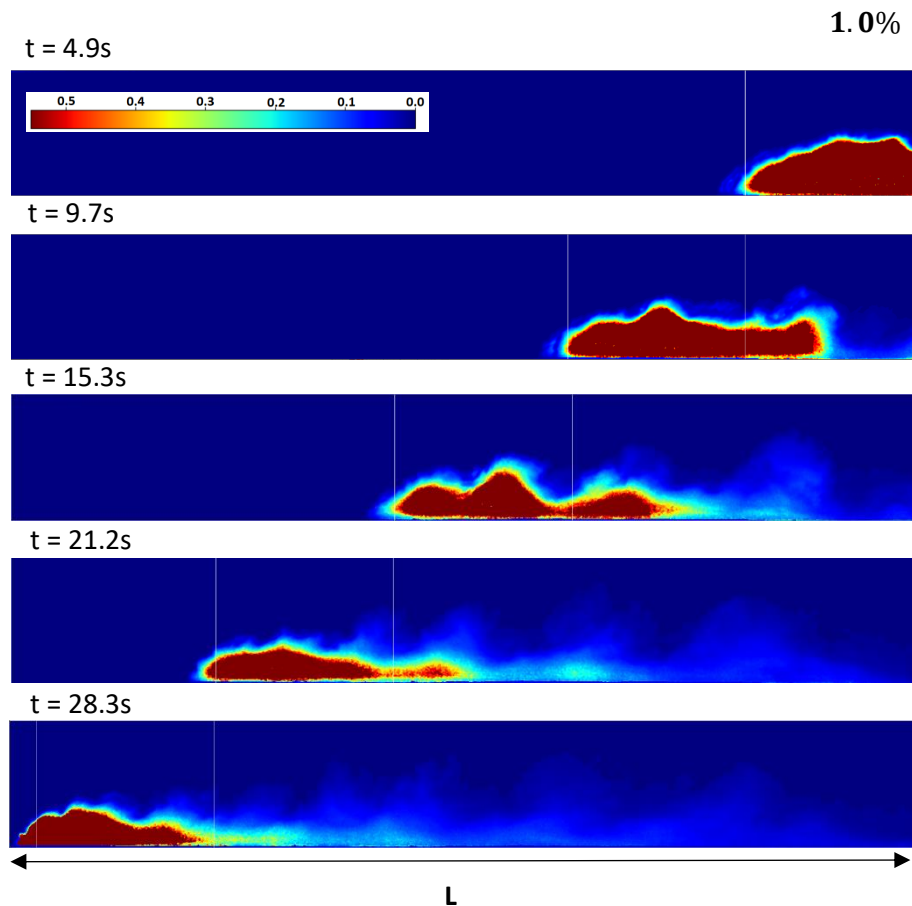


Figure 4.15 Example of a calibrated color map for sediment type II for initial concentration of 1.0%

Results for the combined sediment type I and II show a clear transition period at $2/5L$ of the tank for all initial concentrations, hereby a distinct density difference between head and body can be observed. However, the transition period is at a different time for each current. It can be noted that a pronounced height difference exist throughout the currents length. The middle part of the current is higher than the front and back, this difference creates a pressure gradient that can accelerate the fluid behind the nose. Consequently, the lower height at the rear part of the current can leads to more settling of particles and thus creating a more pronounced density gradient within the current. Furthermore, defined entrainment with the surrounding fluid can be seen for initial concentrations higher than 0.1%. For an initial concentration of 0.1% the height of the body remains almost constant up until $3/5L$ and a clear tail can be distinguished when the current reaches the end wall. See Figure 4.16 for an example of the calibrated color maps for the combines sediment type I and II.

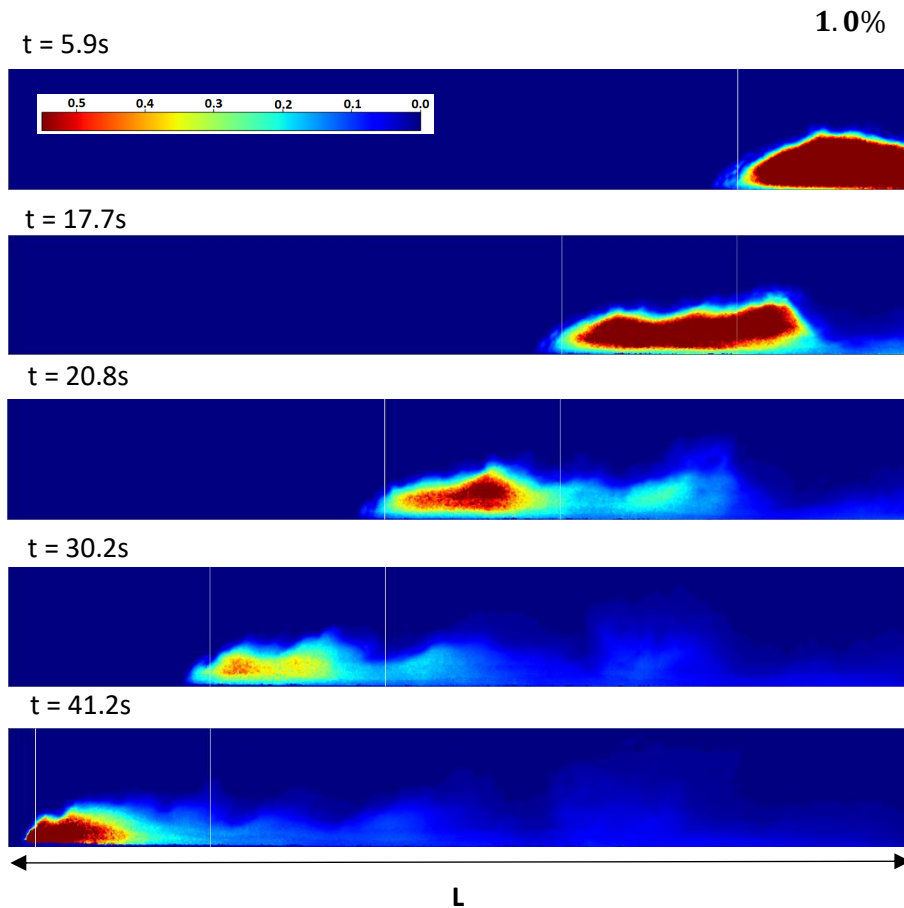


Figure 4.16 Example of a calibrated color map for the combined sediment type I and II for initial concentration of 1.0%

Comparing the three types of sediment, it can be noted that sediment type II and the combined sediment type I and II show a clear difference between higher density and lower density regions within the current after $2/5L$ of the tank. However, sediment type I already starts transitioning from $1/5L$ of the tank. This can be explained by the relative high difference between the settling velocity of sediment type I and sediment type II particles.

It can be observed that there is a difference in height between the front and rear part of the current for sediment type II. As the front is taller than the rear, it can establish a pressure gradient that can decelerate the fluid behind the nose. As more particles settle at the rear due to the lower height, there is a reduced density and pressure gradient at this part of the current. This can lead to the particle concentration in the tail virtually vanishing. Thus, the motion of the flow there would be more due to the momentum of the 'particle-free' fluid and consequently, the effects of buoyancy would be minimum.

Concentration profiles

Besides calibrated color maps it is also possible to obtain vertical concentration profiles. The tank is divided into 5 sections as per Figure 4.17 and $t = 0$ was defined as the moment when the current enters the field of view. This moment is when a distinctive head is formed (Figure 4.4). Vertical concentration profiles are taken in order as depicted in Figure 4.17.

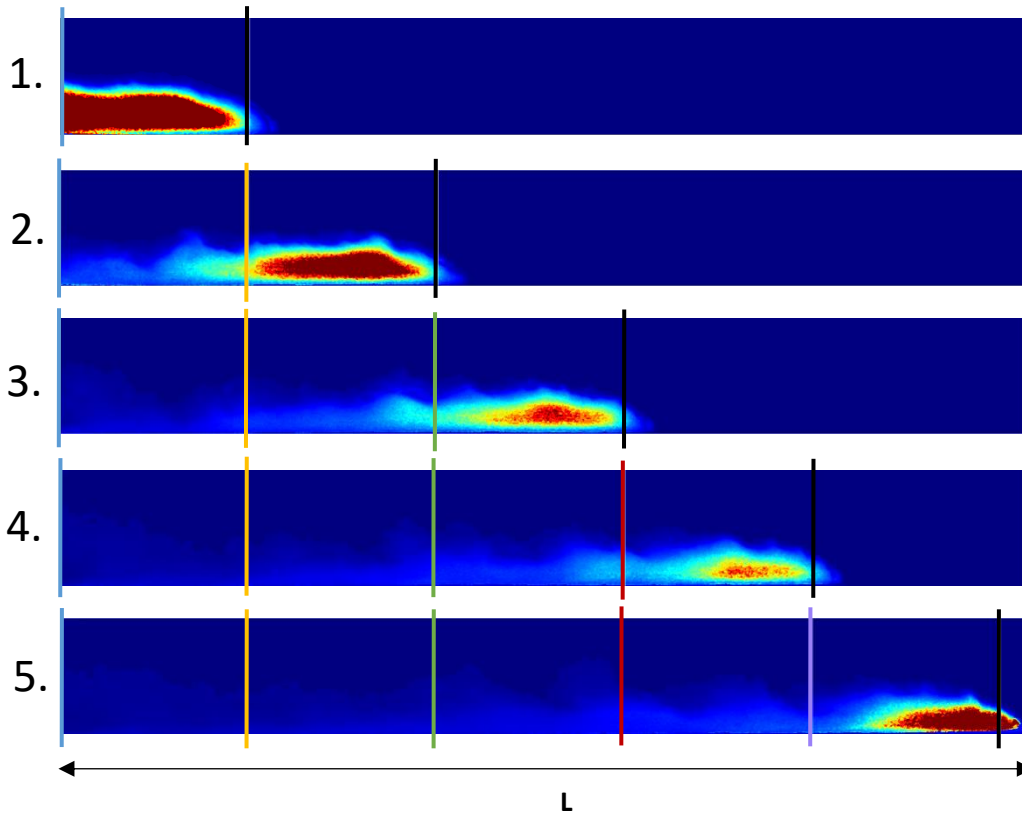


Figure 4.17 Example of the tank divided into 5 sections for the measurement of vertical concentration profiles

Examples of vertical concentration profiles obtained for different initial concentrations can be seen in Figure 4.18, Figure 4.19 and Figure 4.20. The complete obtained vertical concentration profiles per sediment type can be seen in Appendix D. The vertical axis represent the height in [m] and the horizontal axis represent the concentration in [%]. Furthermore, the head concentration profile is measured at 5 sections of the tank and is represented as the black line, see Figure 4.17. Lastly, the vertical dotted line represent the maximum measurable concentration that differs per sediment type.

The profiles show that the maximum concentrations are closer to the bed. Furthermore, most concentration profiles have a dense basal layer and a less dense more homogeneous mixed upper region. The basal layer can be attributed to the settling of larger particles while smaller particles remain suspended.

Results for sediment type I (Figure 4.18) show that the maximum concentration can be found at the head up until $1/5L$ of the tank for initial concentrations of 0.5% and 1.0%. For higher initial concentrations, the maximum concentration can be found at the head up until around $3/5L$ of the tank. After this a transition starts to occur where it can be seen that the concentration starts to distribute more evenly across the current. Besides, it can also be observed that there is a significant height difference between the head and the rest of the body for all currents throughout its runout

length. This measurement reinforces the idea that larger particles are settling faster at the start of every current leaving the smaller particles more evenly suspended. In addition, the homogeneous density distribution of the current could also represent more entrainment with the ambient fluid. More entrainment could explain why the current's middle and rear sections are relatively tall in comparison to its front. Furthermore, more entrainment can explain why the current tends to break in sections as it propagates further down the tank. Lastly, as there is no concentration gradient for the middle and rear part of the current as it propagates, this implies that the current propagates due to a pressure gradient in this part of the flow.

Sediment type II (Figure 4.19) displays a smooth concentration profile that has a dense basal density region which is most commonly seen in low-concentration, weakly depositional currents according to literature. The vertical profiles show the maximum concentration in the body in comparison to the head from $1/5L$ of the tank for all initial concentration values. A transition can be observed where the maximum concentration shifts from the body towards the head. This transition occurs for initial concentration values of 0.1% at $5/5L$ of the tank, when the current almost reaches the end wall. For this low initial concentration value, it is possible that the sediment remains longer in suspension due to its low particle settling velocity. Furthermore, as the height of the middle section of this current almost do not change, there are no pressure gradient differences and particles remain suspended. For higher initial concentration values, the head has the maximum concentration value from around $4/5L$ of the tank. It can also be observed that when these currents reach $4/5L$ of the tank, the body starts to become highly stratified with a dense basal layer and a less dense more homogeneous upper region. This observation leads to a reinforcement of the explanation that the body is split into a dense and less dense region and that as the fall velocities remain small, even the larger particles of this sediment would take a longer time to settle and thus this separation would be seen for almost the entire currents run. In contrast, the front of the current maintains the same density and shape for all lengths of the tank. In addition, the middle section is higher than the rear part of the current.

The combined sediment type I and II (Figure 4.20) displays a similar concentration profile than the previous sediment type. The middle and end section of all currents is stratified with a dense basal layer and a less dense more homogeneous upper layer for all initial concentrations. However, the stratification is more pronounced for all initial concentrations in comparison with the previous sediment type (sediment type II). This is due to the large differences in settling velocities between sediment types. In contrast with the body, the head maintains the same density and shape for all lengths of the tank. The maximum concentration can be observed at the body for all initial concentrations from $1/5L$ of the tank. After this, the transition point where the maximum concentration shifts from the body to the front of the current differs per initial value. For initial values of 0.1% and 0.25%, the transition lies at around $5/5L$ of the tank. For higher initial values, this transition point occurs at around $4/5L$ of the tank. Lastly, the middle section of the current remains significantly taller than both the front and rear of the current.

The density differences within the current that are observed for all three types of sediment can additionally be related to the backflowing bore that travels towards the head of the current once reflected. This bore pushes the rear and middle part of the current down, decreasing the height at this section as it moves forward. Therefore, the particles are forced to settle more rapidly once the height decreases and separates the current in a particle-rich and particle-free region

The less dense upper layer seen in sediment type II and combined sediment type I and II, could represent the entrainment with the upper ambient fluid. It was noticed that the combined sediment type I and II displays a more stratified current with a more pronounced homogeneous upper layer. This could mean more entrainment for this type of sediment.

Comparing the entrainment regions of all the tree types of sediment, it can be noted that sediment type I tends to entrain more than sediment type II. An explanation could be that as the currents of sediment type I propagate slower than sediment type II currents, the upper layer has more time to entrain with the ambient fluid. In addition, combining both types of sediment causes the current to entrain more with the ambient fluid.

Sediment type I ($75 - 125\mu m$) :

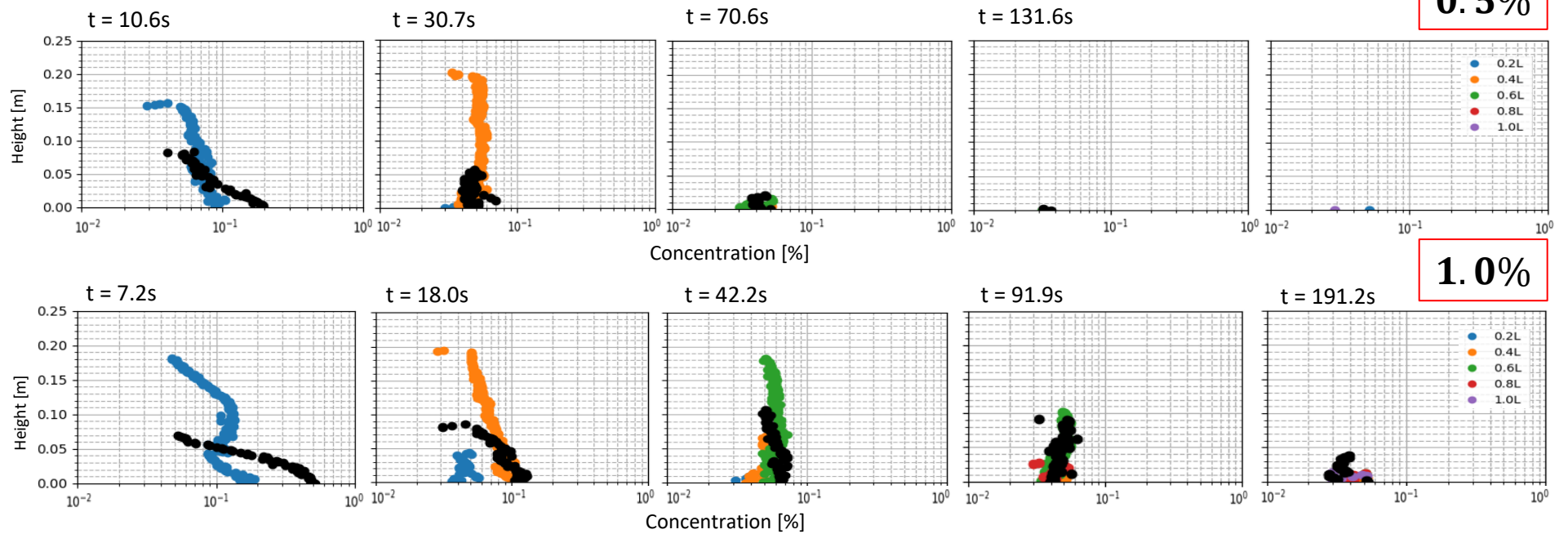
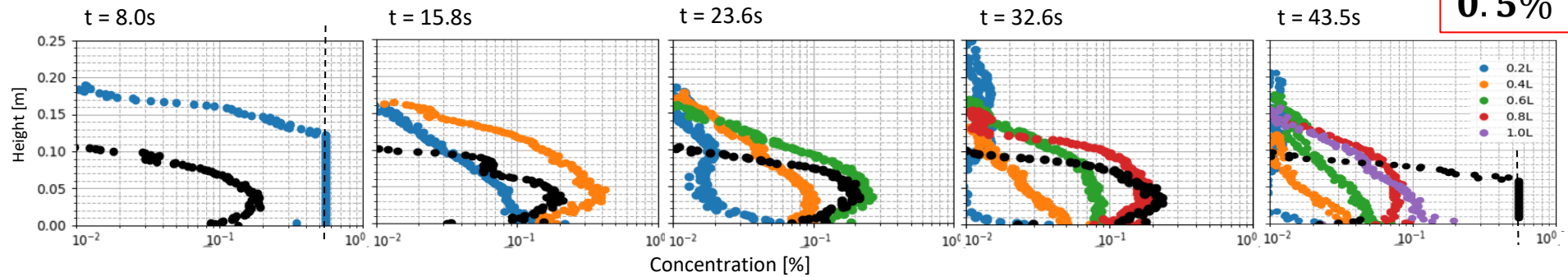


Figure 4.18 Selection of vertical concentration profiles for sediment type I

Sediment type II ($4 - 60\mu m$) :



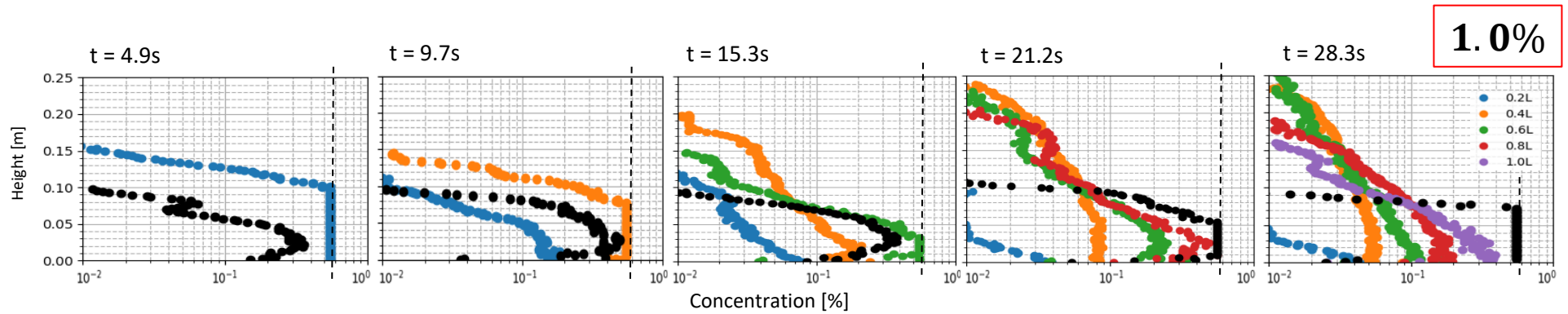


Figure 4.19 Selection of vertical concentration profiles for sediment type II

Combined sediment type I and II ($4 - 125\mu\text{m}$):

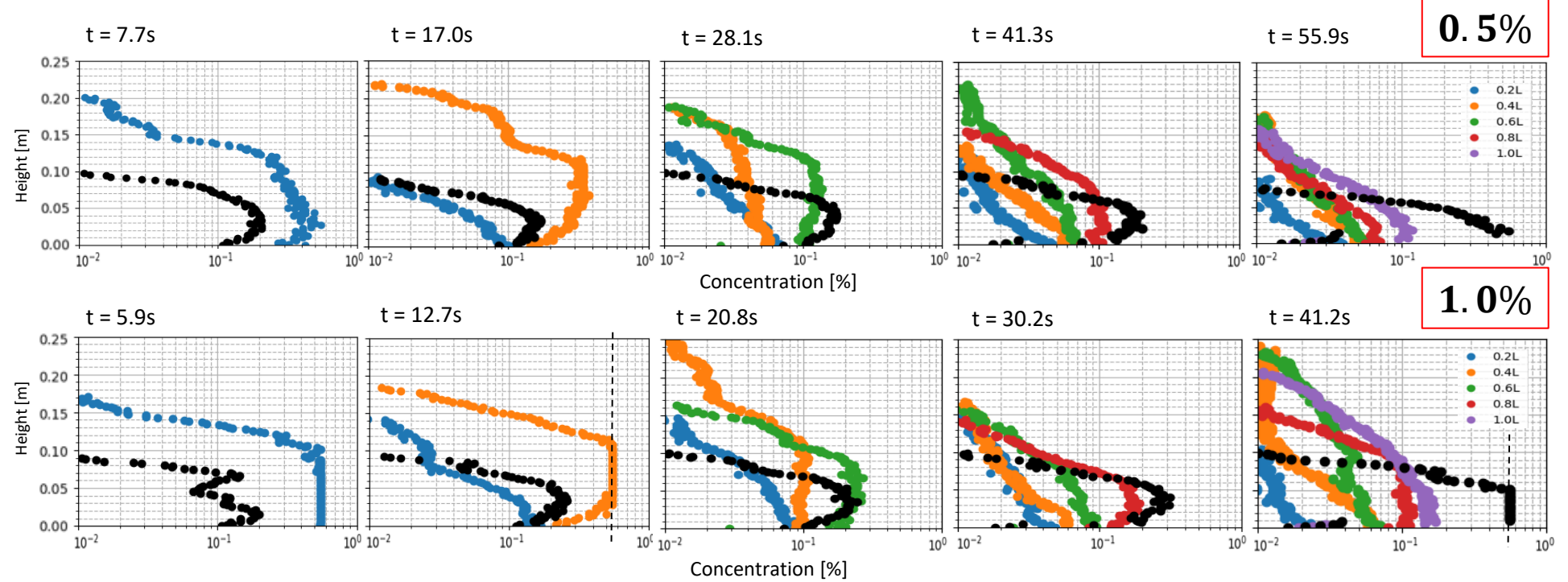


Figure 4.20 Selection of vertical concentration profiles for combined sediment type I and II

4.3 Mass calculation

By making use of the concentration measurements within the current, it is possible to calculate the mass of the currents at different stages. The mass is computed by making use of the density of the sediment and the concentration, length, height and depth of each pixel.

4.3.1 Transition phase

The dynamics of a particle-driven current can be divided into different phases. The first phase involves very few particles having settle out of the current. After this, a transition phase can be observed where the particles from the body of the current start settling. The last phase involves the separation of the current in a particle-free region at the rear and a relatively particle-rich region at the front of the current (Bonnecaze, Huppert, & Lister, 1993).

The transition phase can be found by calculating the changes of mass over time within the current by making use of a python algorithm. The mass is computed for a rectangular surface with 1 pixel width and the height of the tank situated at a fixed position from the head as shown in Figure 4.21. The mass is computed for every 150 frames until the current reaches the end-wall or until it was no longer computable. The rectangular surface is situated at 384 pixel (0.59m.) from the distinctive head when measurements start. Results can be seen in Figure 4.22b, Figure 4.23b and Figure 4.24b for different sediment types and initial concentrations. Hereby, is the vertical axis the mass in $[kg]$ and the horizontal axis is the time in $[s]$. Due to each type of sediment having a maximum measurable concentration value, masses calculated for pixels with this concentration value and beyond it are not certain.

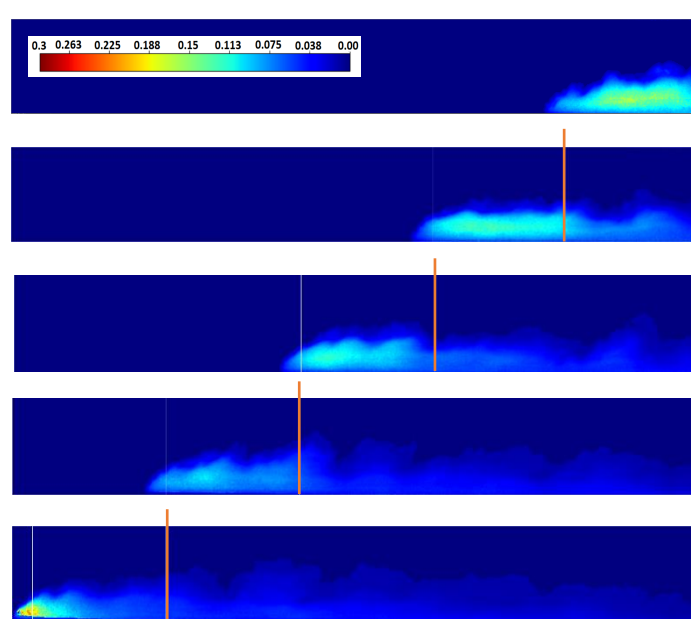


Figure 4.21 Example of the tank displaying some positions where the rectangular surface was measured

Results for sediment type I (Figure 4.22) reveal that for all initial concentrations the mass can be calculated as the maximum measurable concentration value for this type of sediment is not reached, see Figure 4.22a. Figure 4.22a shows the maximum concentration found at the rectangular surface for every 150 frames until the current reaches the end wall. For initial concentrations from 2.0% – 3.0%, it can be observed from Figure 4.22b that the mass is decreasing rapidly over time at first. After this, the mass continues to decrease but at a slower rate. At last, it can be seen that the mass reaches a constant value after decreasing with time. The rapid decrease in mass for the first section, enforces

the previous results that noted how the density of the current started decreasing as soon as the current started to run. This result can be attributed to the fast settling of particles of sediment type I. In addition, the d50 of the particles is relatively large ($122\mu m$) and close to the maximum grain size ($125\mu m$) for this sediment type. The latter could imply a fast settling of the large particles as soon as the current propagates leaving the remainder 50% of the grains suspended for a longer time. The second part of the observed results when the mass is decreasing at a slower rate, displays the further settling of particles until it reaches a constant value where the density is spread evenly. The constant mass implies the entrainment of the current with the ambient fluid and limited settling of particles. Furthermore, initial concentrations of 0.5% – 1.5% display from the beginning a decrease in mass at a slower rate until they finally reach a constant value of mass. In addition, initial concentrations of 0.5% – 1.5% reach a constant mass sooner which could imply that they are more effortlessly entrained. Higher initial concentrations (2.0% – 3.0%) reach the transition period sooner, as their mass decreases almost immediately.

Results for sediment type II (Figure 4.23) show that the mass can be calculated for initial concentrations until 0.5%. For currents with higher initial concentrations, the maximum measurable concentration value is found throughout the currents run and therefore the mass calculations would be uncertain. For an initial concentration of 0.1%, it can be observed that the mass decreases over time at a slow rate until it reaches a constant value for the remainder of the currents run. This observation is consistent with the previous results suggesting that the particles remain longer in suspension due to their low settling velocity and small height differences throughout the current. An initial concentration of 0.25% shows that the mass is decreasing with time at a faster rate until it reaches a constant mass value at the end. In addition, for initial concentration of 0.5%, it can be observed that the mass decreases with time at a fast rate but does not reach a constant value. Therefore, it can be noted that the transition phase starts and ends sooner for an initial concentration of 0.25%. However, the decrease in mass and thus the settling of particles is more rapid for initial concentration of 0.5% suggesting that this could be the case for higher initial concentrations as well.

Results for the combined sediment type I and II (Figure 4.24) show that the mass can be calculated until 1.5%. It can be observed that the mass for all initial concentrations of 0.1%, 0.25% and 0.5% decreases with time and reach a constant mass until the end of the currents run. For initial concentration of 1.0%, the mass decreases with time and it seems like it starts to reach a constant value. Therefore, higher initial concentrations (0.5% – 1.0%) go through this transition period at a high rate and end this phase sooner than lower initial concentrations.

Reaching a constant mass value suggest that settling of particles is low from that point on for all three types of sediment and that the transition phase has ended as the current is now divided into a dense front and a less dense region at the rear. A distinct evolution from a decreasing value to a constant mass value can be seen for sediment type I and the combined sediment type I and II. For sediment type II an indication of a constant mass value at the end of the currents run is given.

Higher initial concentration values for sediment type II and the combined sediment type I and II have a transition period at a higher rate. This could be related to the high degree of stratification within the current seen for these concentrations. Therefore, the stratification could create less height for the basal layer forcing the particles to settle faster here.

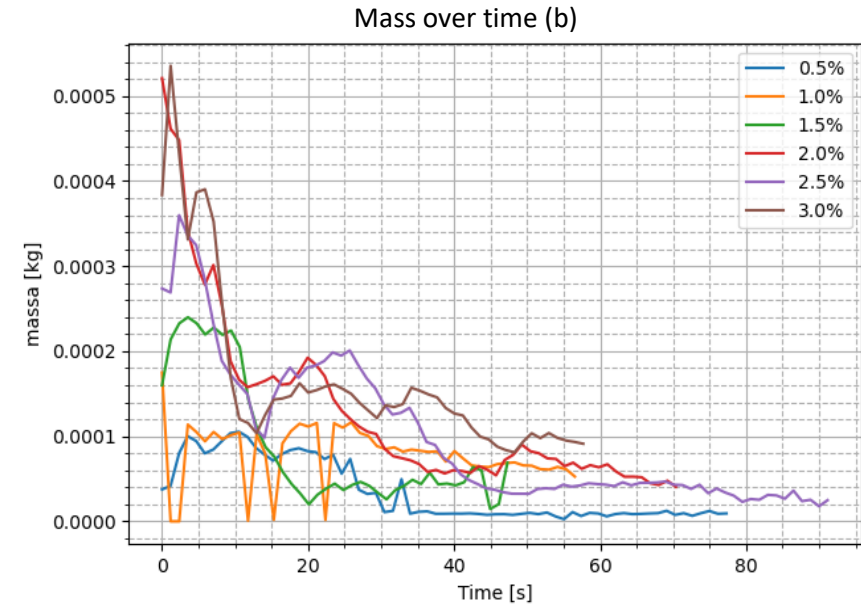
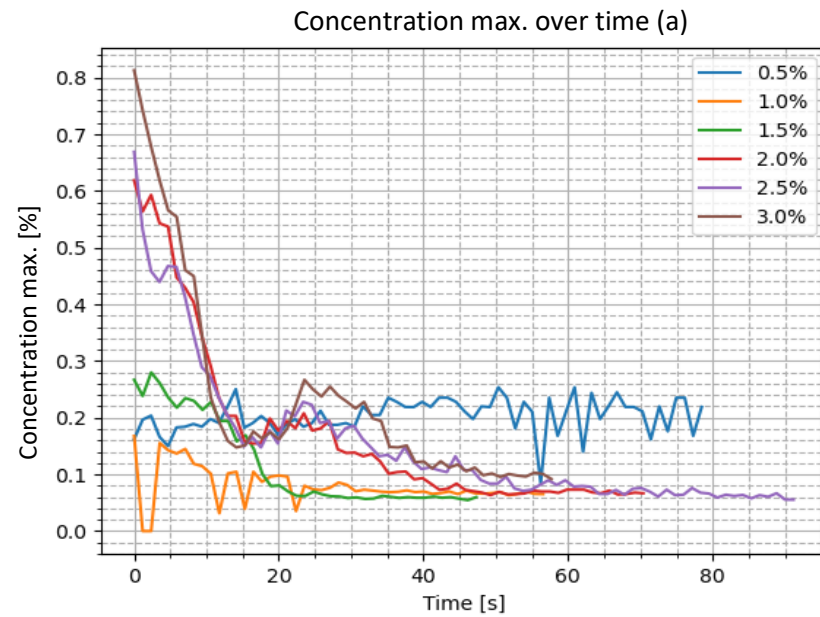


Figure 4.22 Results for mass measurement at a fixed position in the body over time for sediment type I, (a) displays the maximum concentration found and (b) displays the calculated mass

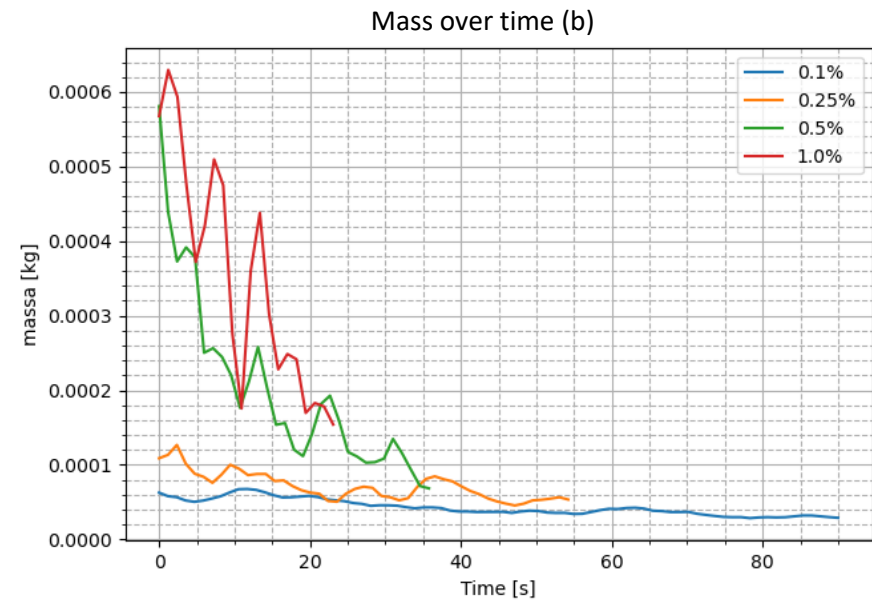
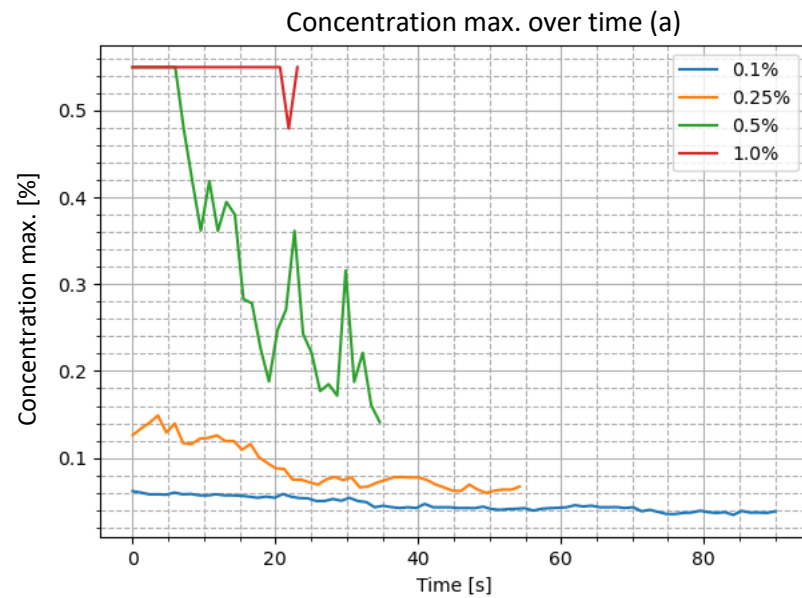


Figure 4.23 Results for mass measurement at a fixed position in the body over time for sediment type II, (a) displays the maximum concentration found and (b) displays the calculated mass

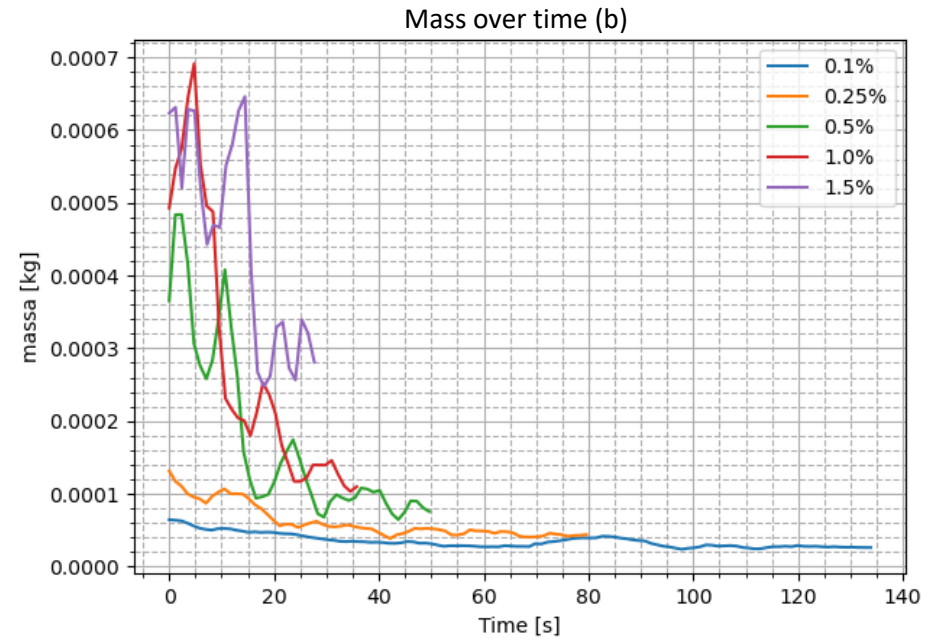
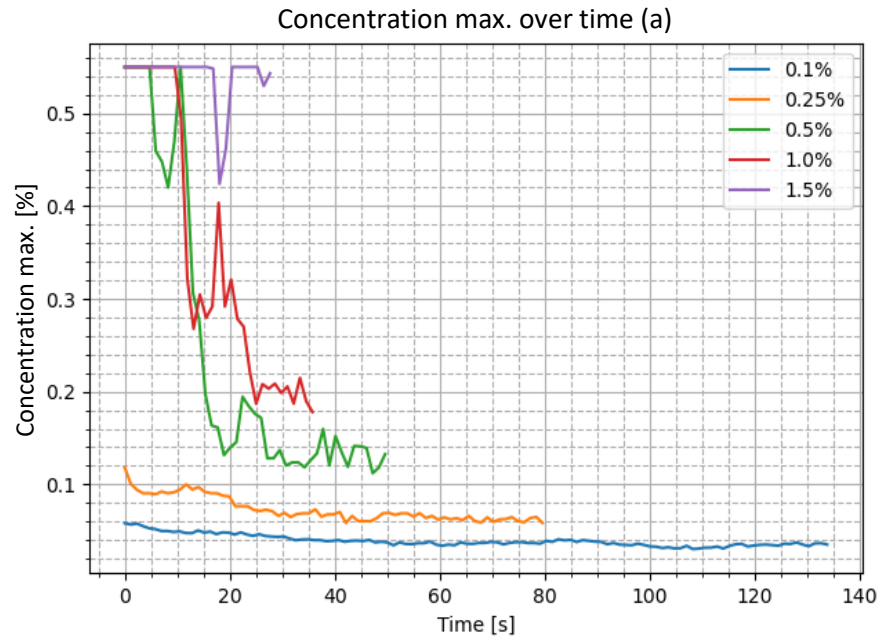


Figure 4.24 Results for mass measurement at a fixed position in the body over time for the combined sediment type I and II, (a) displays the maximum concentration found and (b) displays the calculated mass

4.3.2 Mass calculation over time

Mass calculations are performed at 5 vertical sections of the tank by using a python algorithm. The tank was divided as per Figure 4.25 and $t = 0$ was defined as the moment when the current enters the field of view as per Figure 4.4. Once the current enters the field of view the mass is computed for the 5 vertical lines every 100 frames until the current reaches the end-wall. Due to each type of sediment having a maximum measurable concentration value, masses calculated for pixels with this concentration value and beyond it are not certain. The maximum concentration [%] found in the vertical line per time [s] can be seen in Figure 4.26b, Figure 4.27b and Figure 4.28b.

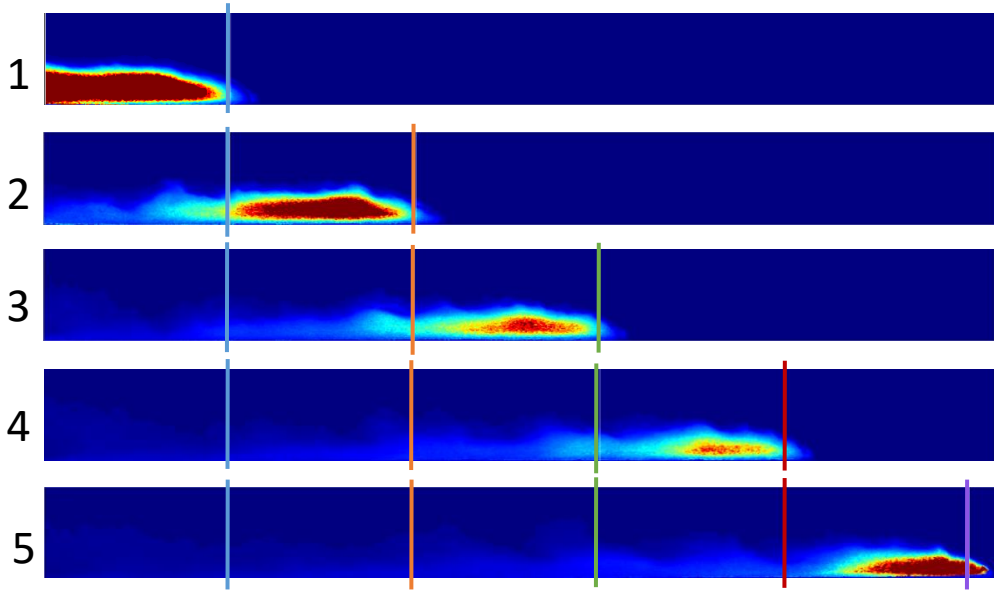


Figure 4.25 Example of the tank divided into 5 sections where the mass is measured at the vertical lines

An example of the obtained masses for different types of sediment can be seen in Figure 4.26a, Figure 4.27a and Figure 4.28a. The vertical axis is the total mass calculated in the vertical line in [kg] and the horizontal axis is the time in [s]. All the results of the obtained masses per sediment type can be found in Appendix E. Masses that are not certain due to the maximum measurable concentration being found at that time, are marked with a black line. These masses are at least the value represented in the graph.

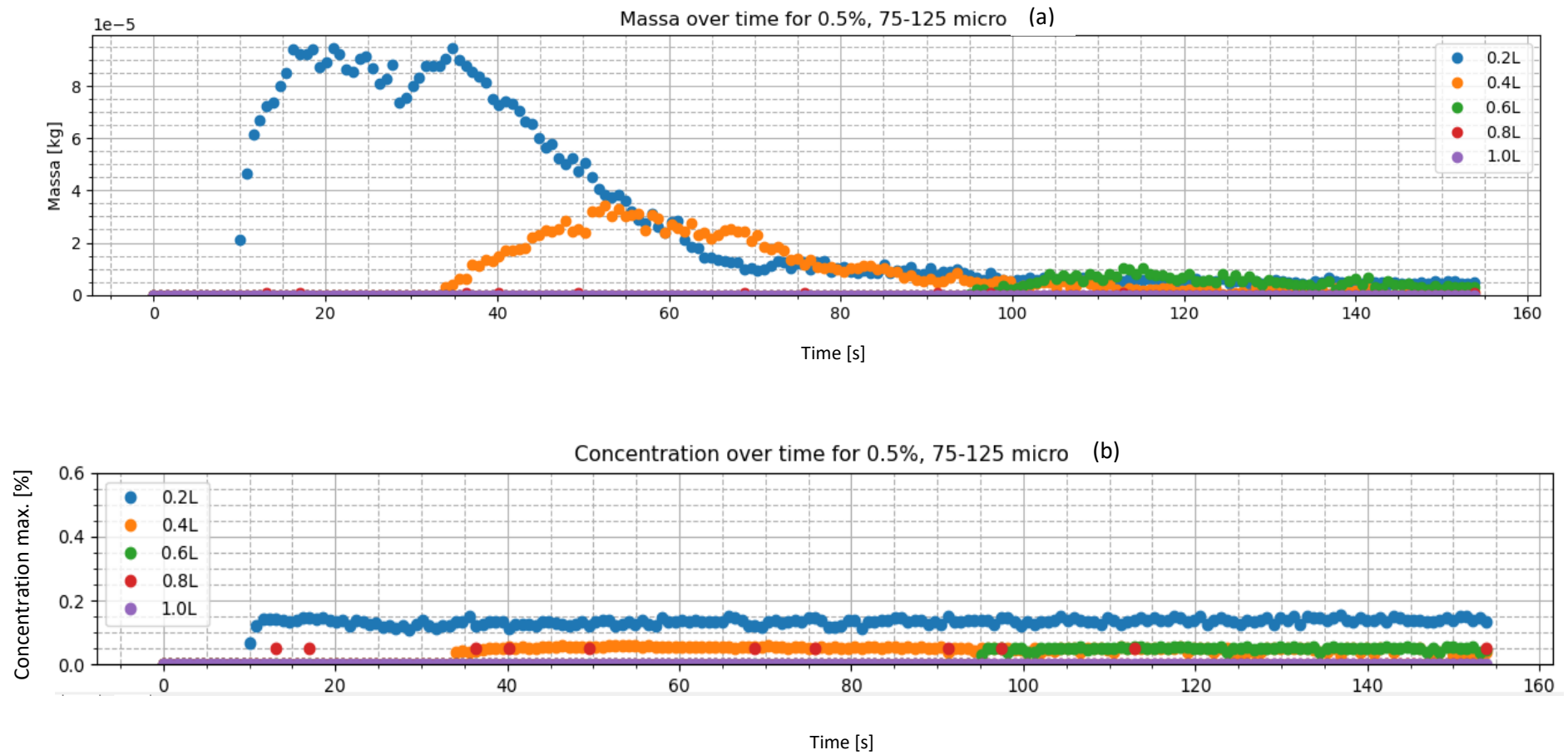


Figure 4.26 Mass over time measured at 5 different sections of the tank for sediment type I, (a) displays the mass found and (b) displays the maximum concentration found

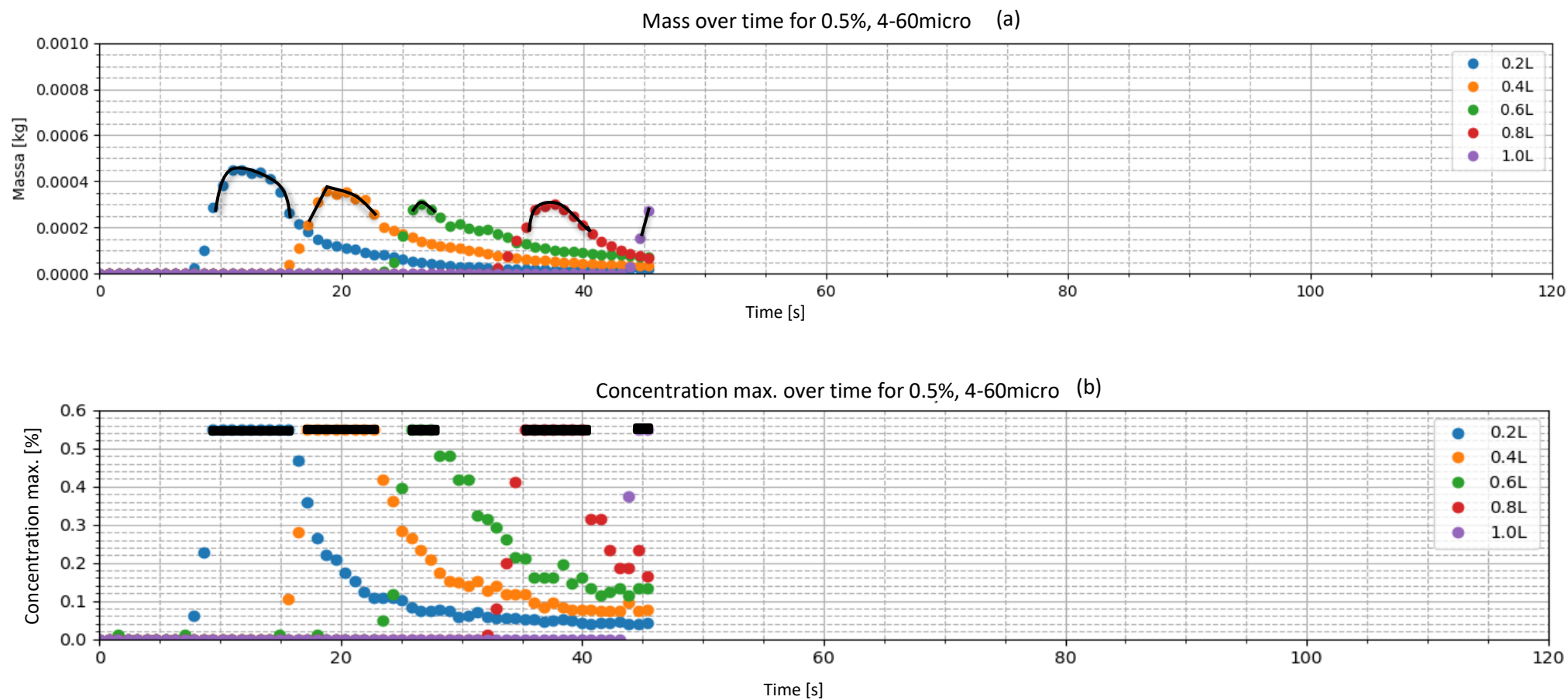
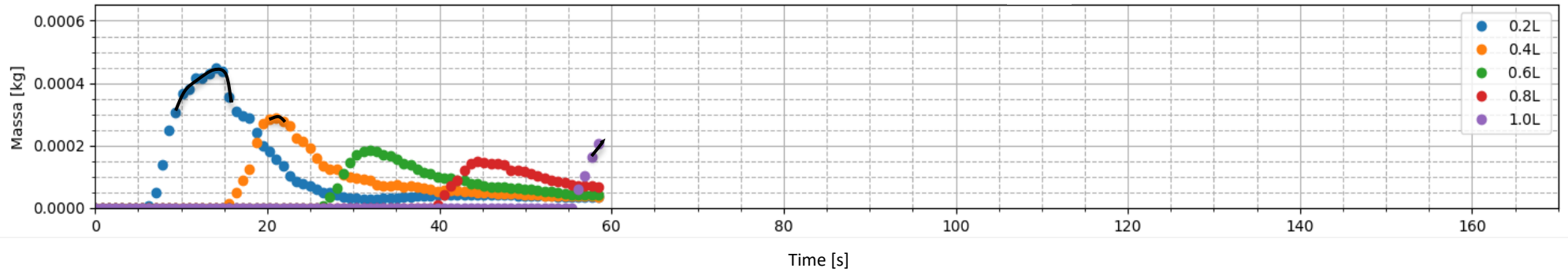


Figure 4.27 Mass over time measured at 5 different sections of the tank for sediment type II, (a) displays the mass found and (b) displays the maximum concentration found

Mass over time for 0.5%, 4-125micro (a)



Concentration max. over time for 0.5%, 4-125micro (b)

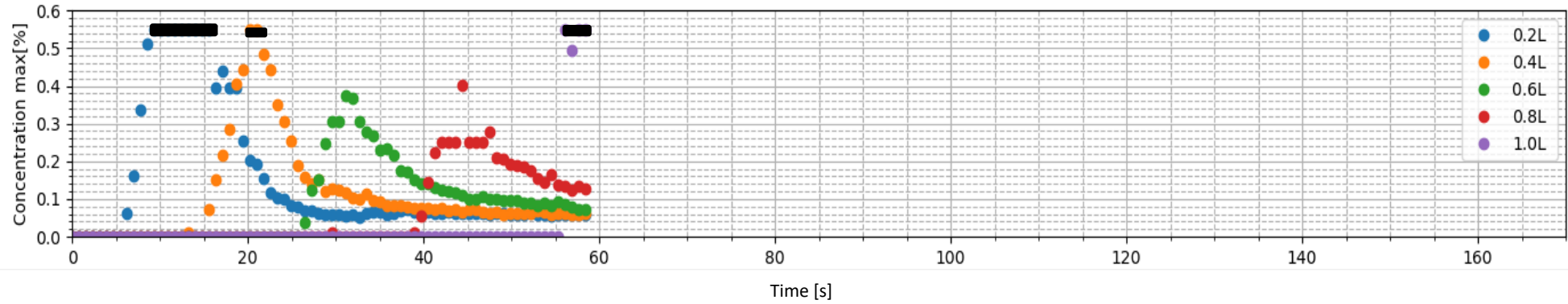


Figure 4.28 Mass over time measured at 5 different sections of the tank for the combined sediment type I and II, (a) displays the mass found and (b) displays the maximum concentration found

The mass graphs for sediment type I (Figure 4.26a) show that the masses for all initial concentrations have a sharp increase in value when the current enters the 1st vertical (light blue) line until it reaches a maximum value. After this the mass value shows a slightly decrease until it reaches a constant value. Furthermore, as long as the current keeps progressing each vertical line shows a similar pattern. The difference between the measurements in each vertical line lies in the maximum mass value that is found. Each consecutive vertical line shows a decrease in the maximum mass value.

From the previous results, it can be deduced that the deposition of sediment type I is largest close to the lock-gate (between first and second vertical line). The sediment is more likely to be deposited as a high particle settling velocity will only allow for short-term suspension. The current reaches a low constant mass near the end of the tank. This mean that most of the particles have settled and only a few remain in suspension.

Sediment type II (Figure 4.27a) displays a similar pattern. The mass increases rapidly until the maximum and decreases afterwards at a slower rate until it finds a constant mass value for each vertical line. The maximum measurable concentration value is found for initial concentrations of 0.5% – 2.0%, therefore the actual measured mass is not certain. However, for initial concentrations of 0.1% and 0.25%, it can be observed that the maximum mass found is almost the same for each consecutive vertical line.

Finer sediment (sediment type II) has settling velocities that are sufficiently small that many particles remain suspended during of the current propagation. Therefore, the deposition is not that high close to the first vertical line of the tank and the mass lines remain the same shape almost up to the end-wall.

The combined sediment type I and type II (Figure 4.28a) shows a rapid increase in mass until it reaches a maximum value and a decrease in mass afterwards at a slower rate until it reaches a constant mass value for each vertical line. The maximum measurable concentration value is found for initial concentrations of 0.5% – 2.0%. However, for an initial concentration of 0.5% the maximum measurable concentration value is not found after the second vertical line. Furthermore, for initial concentrations of 0.1%, 0.25% and 0.5% it can be observed that the maximum mass decreases for each consecutive vertical line.

The combined sediment type I and II show a maximum deposition near the lock-gate (between the first and second vertical line). Afterwards, the deposition is more evenly distributed. The fast deposition near the beginning of the tank probably consists mostly of the large particles (sediment type I) included in the suspension. Once the larger particles are settle, the deposition shifts to a pattern seen for sediment type II. The finer particles remain longer in suspension and the deposition is not that large.

Comparing the three types of sediment shows that the mass shape is similar for all the currents. However, the deposition patterns are different per sediment type. Larger particles will allow for a faster decrease in mass in contrast with smaller particles that allow the mass to retain the same maximum for a longer time. Furthermore, combining larger particles with smaller ones gives a significant change in mass maximum (between the first and second vertical line) indicating a larger deposition. Moreover, it keeps the particles more distributed throughout the front of the current as the smaller particles keep the remaining larger ones longer in suspension, see Figure 4.29. Finally, the presence of larger particles has a retarding effect on the flow.

The magnitude of the maximum mass depends on the particle size, smaller particles (sediment type II) have a slightly higher maximum mass than larger particles (sediment type I).

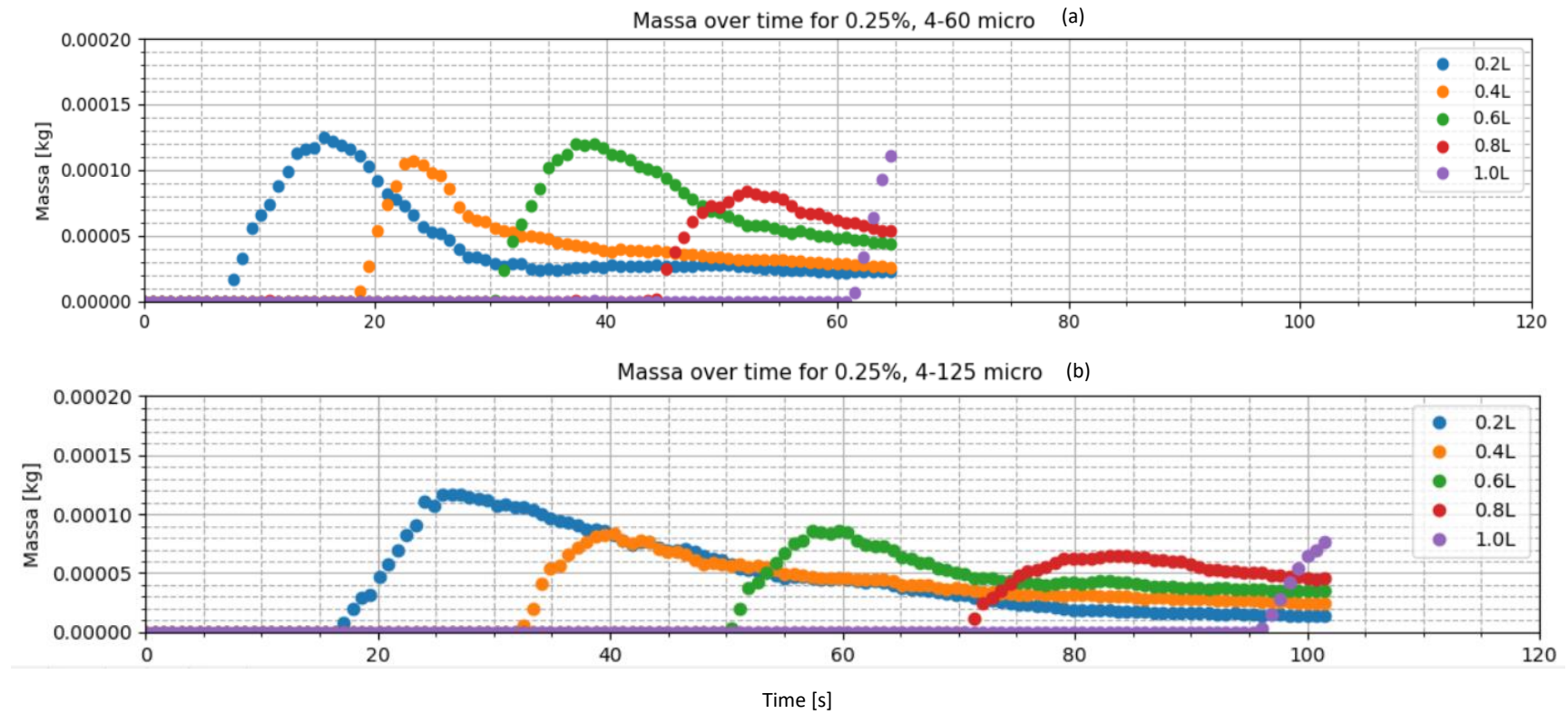


Figure 4.29 Comparison between (a) sediment type II and (b) the combined sediment type I and II for initial concentration of 0.25%

4.3.3 Total mass

The total mass of the current was measured using a python algorithm with $t = 0$ defined as the moment when the current enters the field of view as per Figure 4.4. Once the current enters the field of view the total mass of the current is computed once every 200 frames until the current reaches the end-wall. Results can be seen in Figure 4.30. The total mass for all the initial concentrations of sediment type I are calculated. However, the maximum measurable concentration value was found for sediment type II and the combined sediment type I and II for initial concentrations higher than 0.25% and 0.5% respectively. Therefore, the total mass could not be calculated for all the initial concentrations for both types of sediment. A summary of the obtained results can be found at Table 4-2

Results for all the three types of sediment displays a rapid increase in mass once the measurements start. After this, it can be observed that sediment type I is significantly decreasing in mass until it reaches a section where the mass keeps decreasing at a slower rate. However, results for sediment type II shows an ongoing increase in mass at a slower rate. Finally, results for the combined sediment type I and II contain a continuing increase in total mass at a slower rate with the exception of initial concentration 0.5%. It can be noticed from this concentration that it starts to decrease at a fast rate until it reaches a section where the total mass becomes almost constant.

The significant decrease in mass value for sediment type I is related to the strong deposition due to the high settling velocity of this sediment. In addition, it can be noted from Table 4-2. That almost all of the particles settle at the end of the currents run. This could mean that the current would probably not be propagating much longer after the last measurement. Furthermore, results from sediment type II and the combined sediment type I and II display not as much deposition as the previous sediment type. Thus, a current transporting fine particles can travel for a longer distance in comparison to a larger grain size current due to a larger driving buoyancy force. Therefore, the run-out distance is highly dependent upon the grain size present in the suspension. In addition, adding finer particles to a larger grain size can increase the run-out distance and decrease the deposition significantly due to the large difference in settling velocity of the two sediment types.

Finally, for sediment type II and the combined sediment type I and II, it can be observed that for a higher initial concentration more settling of particles takes place. This can be related to the following events. The front decelerates in the transition phase due to inertial forces and due to a density gradient within the current between the front and the back as particles start to settle at the rear part. Consequently, the front decelerates more rapidly than the back of the current causing an accumulation behind the head due to the slower movement of the front. This will create a difference in height between the front and the back of the current forcing the particles in the back to settle faster.

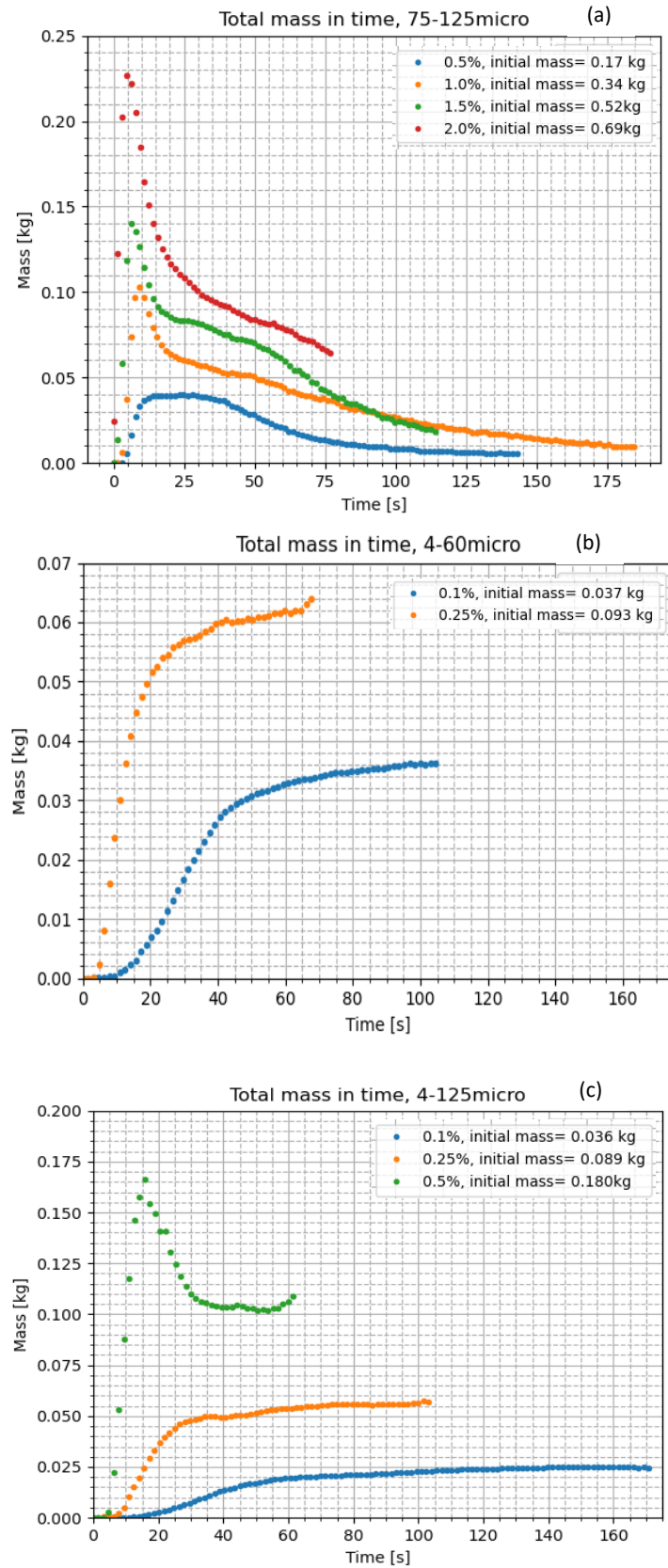


Figure 4.30 Total mass measured for the complete current over time: (a) displays results for sediment type I, (b) displays results for sediment type II and (c) displays results for the combined sediment type I and II

Table 4-2 Results for the total mass measured for the complete current over time for different types of sediment

Sediment type	Initial concentration [%]	Starting mass [kg]	End mass [kg]	Percentage of starting mass [%]
Type I	0.5%	0.172	0.005	2.9
Type I	1.0%	0.344	0.009	2.6
Type I	1.5%	0.517	0.018	3.5
Type I	2.0%	0.690	0.064	9.3
Type II	0.1%	0.037	0.035	94.5
Type II	0.25%	0.093	0.064	68.8
Type I and II	0.1%	0.036	0.025	69.4
Type I and II	0.25%	0.089	0.057	64.0
Type I and II	0.5%	0.180	0.100	55.5

5. Conclusion and Recommendations

5.1 Conclusions

- Experiments shows that the dynamics of particle-driven currents are dependent on sediment type. Hereby, the dynamics of the current are controlled by a balance between inertial forces of the flowing fluid and the buoyancy forces derived from the suspension of dense particles.
- Results show that particle-driven currents follows three phases while propagating as described in literature. First, there is an initial phase where the front is formed and the current accelerates until it reaches a maximum velocity. During this phase very few particles settle out of the current. Second, the current transitions into a second phase when the velocity of the front starts to decrease due to inertial forces at the front and due to the start of particle settling at the rear of the current. At last, a last phase is achieved for some results when the backflowing bore created by the ambient fluid at the release of the gate reaches the front and decelerates the current until viscous forces start to dominate until the current vanishes.
- It is observed that a current transporting fine particles (sediment type II) reach higher velocities and may travel for a longer distances in comparison to a current composed of larger particles (sediment type I). Therefore, these type of currents have the largest horizontal dispersion.
- Currents composed of larger particles (sediment type I) will have the smallest horizontal dispersion due to their high settling velocities.
- The combination of fine and large particles has a substantial effect on the current dynamics. The flow can travel longer distances than flows composed of only large particles. This is the consequence of the fine particles maintaining the larger particles in suspension and thus the flow velocity does not decay as rapidly.
- Larger particles (sediment type I) tend to entrain more with the ambient fluid in comparison to smaller particles (sediment type II) and therefore have a larger vertical dispersion.
- Currents composed off smaller particles have a clear stratification within the current dividing it into a dense basal layer and a less dense upper layer. The less dense upper layer corresponds to the entrainment with the ambient fluid.
- Combined sediment have a more pronounced stratification within the current and thus are more entrained with the ambient fluid in comparison to fine particle currents.
- Initial concentrations higher than 1.0% of sediment type I reach the transition phase sooner than lower initial concentrations. Furthermore, initial concentrations higher than 0.25% of sediment type II and the combined sediment type I and II reach the transition phase sooner than lower initial concentrations.
- Deposition patterns are different per sediment type. Larger particles (sediment type I) will have a larger deposition rate than small particles (sediment type II). Furthermore, combining

both types of sediment will increase the deposition rate close to the lock-gate.

- Sediment type I has for all initial concentrations approximately the same vertical dispersion and the most entrainment. However, initial concentration of 0.5% has the least horizontal dispersion. Furthermore, initial concentrations higher than 1.0% will have a more rapid transition into a dense front and a less dense middle and rear part of the current. In addition, for all initial concentrations there is no clear vertical division between a dense basal layer and a less dense top layer observed. Finally, for an increasing initial concentration it can be observed that the deposition will decrease.
- For sediment type II, initial concentrations lower than 0.5% will give the least vertical dispersion and thus the least entrainment. However, initial concentration of 0.1% will have the least horizontal dispersion. Furthermore, initial concentration higher than 0.25% will have a more rapid transition into a dense front and a less dense middle and rear part of the current. In addition, for all initial concentrations a clear division between a dense basal layer and a less dense top layer within the current can be observed. Finally, with an increasing initial concentration the deposition will increase.
- The combined sediment type I and II have for initial concentrations of 0.1% the least vertical and horizontal dispersion. Furthermore, this initial concentration will have the least entrainment. Initial concentrations higher than 0.25% will have a more rapid transition into a dense front and a less dense middle and rear part of the current. In addition, for all initial concentrations a clear division between a dense basal layer and a less dense top layer within the current can be observed. Finally, with an increasing initial concentration the deposition will increase.

5.2 Further recommendations

- Experiments to determine the settling velocity of the three sediment types at different concentrations can be carried out to improve the analysis of the results.
- The set-up for the experiments was at a fixed spot and a dark cloth was used to block out the ambient light as much as possible and to create a high contrast with the background. However, the effect of ambient light on the recordings was not visually visible during the experiments but could only be observed while analyzing the experiments in detail. To prevent ambient light influence in future experiments a controlled environment can be created around the camera and tank.
- Changes in magnification with respect to the working distance can disrupt calibration of the system. A possible solution for this could be the use of a telecentric lens in future experiments. Telecentric lenses eliminate the parallax effect and any change in magnification that comes with working distance change.
- Further measurements of the concentrations within the current could be done to verify the calibration process. The measurements could be made by making use of an OBS or other optical sensors.

- Further research into the effects of the velocity within the current could be performed by making use of an ADV to provide more information about the effect of dynamic pressure within the current.

References

- Agravante, M. (2020, 03 13). *Medium*. Retrieved from New Gold Rush Taking Place in the Deep Sea: <https://medium.com/@WriterMariecor/new-gold-rush-taking-place-in-the-deep-sea-745e4d9d4bc5>
- Al Ja'Aidi, O. a. (2004). Factors influencing the deposit geometry of experimental turbidity currents: implications for sand-body architecture in confined basins. In S. L. Joseph, *Confined Turbidite systems* (pp. 45-58). Geological Society.
- Allen, J. R. (1971). Mixing at turbidity current heads and its geological implications. *J. Sedim. Petrol*, 97-113.
- Altinakar, M., Graf, W., & Hopfinger, E. (1996). Flow structure in turbidity currents. *Journal of Hydraulic Res.*, 713-718.
- Bonnecaze, R., Huppert, H., & Lister, J. (1993). Particle-driven gravity currents. *J. of Fluid Mech.*, 339-369.
- Brandt, M., Johnson, K., Elphinston, A., & Ratnayaka, D. (2017). *Twort's Water Supply*. Butterworth-Heinemann.
- Britter, R. E., & Simpson, J. E. (1978). Experiments on the dynamics of gravity current head. *Journal of Fluid Mechanics*, 223-240.
- Brockett, T. (2014). Nodule Collector Subsystems Organizations of the OMI Pilot Mining Test Program and its use in collaborative tests by contractors. *ISA Workshop On Polymetallic Nodules Resource Classification*. ISA.
- Buckee, B., & Kneller, C. (2000). The structure and fluid mechanics of turbidity currents: a review of some recent studies and their geological implications. *Sedimentology*, pp. 62-94.
- Buckee, C., Kneller, B., & Peakall, J. (2001). Turbulence structure in steady, solute-driven gravity currents. *Particulate Gravity Currents*, 173-188.
- Dade, W., & Huppert, H. (1995). Runout and fine-sediment deposits of axisymmetrical turbidity currents. *Journal of Geophysical Research*, 18597-18609.
- De Producer School. (2020, 04 16). Retrieved from Signaal – ruis verhouding (Signal to noise ratio) (S/N): <https://deproducerschool.nl/producer-termen/productie/signaal-ruis-verhouding-signal-to-noise-ratio-s-n/>
- Decrop, B., & De Wachter, T. (n.d.). Detailed CFD simulations for near-field dispersion of deep sea mining plumes. *Wodcon XXII*, 118.
- Ellison, T. H., & Turner, J. S. (1959). Turbulent Entrainment in Stratified Flows. *Journal of Fluid Mechanics*, 423-447.
- Ferguson, R., & Church, N. (2004). A simple universal equation for grain settling velocity. *Journal of Sedimentary Research*, 933-937.
- Gladstone, C., Phillips, J., & Sparks, R. (1998). Experiments on bidisperse, constant-volume gravity currents: propagation and sediment deposition. *Sedimentology*, 833-843.

- Grace, J. (1986). Containing modes and behaviour classification of gas-solid and other two-phase suspensions. *Can. J. Chem.*, 353-63.
- Grunsven, F., Keetels, G., & Rhee, C. (2018). *The initial spreading of turbidity plumes – Dedicated laboratory experiments for model validation*. Delft.
- Huppert, H. (1982). The propagation of two-dimensional and axisymmetric viscous gravity currents over a rigid horizontal surface. *J. Fluid Mech.*, 43-58.
- Huppert, H. E., & Simpson, J. E. (1980). Slumping of gravity currents. *Journal of Fluid Mechanics*, 785-799.
- IHC. (2020, 02 11). *Integrated services and equipment for deep-sea mining*. Retrieved from Deep-sea Mining: <https://www.royalihc.com/en/products/mining/dredge-mining/deep-sea-mining>
- International Seabed Authority. (2020, 06 24). Retrieved from Exploration Contracts: <https://www.isa.org.jm/exploration-contracts>
- ISA. (2020, 03 13). Polymetallic Nodules brochure. International Seabed Authority.
- IUCN. (2019, 12 12). *IUCN*. Retrieved from Deep-sea mining: <https://www.iucn.org/resources/issues-briefs/deep-sea-mining>
- Jamshidi, R., & Mazzei, L. (2018). CFD Modeling of Fluidized Beds. *Chemistry, Molecular Sciences and Chemical Engineering*.
- Keulegan, G. H. (1957). An Experimental Study of the Motion of Saline Water from Locks into Fresh Water Channels. *US National Bureau of Standards*, Rep. 5168.
- Kneller, B., & Buckee, C. (2000). The structure and fluid mechanics of turbidity currents: a review of some recent studies and their geological implications. *Sedimentology*, 62-94.
- Launder, B. E., & Rodi, W. (1983). The turbulent wall jet measurements and modelling. *Ann. Rev. Fluid Mechanics*, 429-459.
- Lempriere, M., & Casey, J. (2019, October 14). *Deepsea mining: the environmental debate*. Retrieved from Mining Technology: <https://www.mining-technology.com/features/deepsea-mining-the-environmental-debate/>
- Li, Y. (2019, May 30). *Here's why China's trade war threat to restrict rare earth minerals is so serious*. Retrieved from CNBC: <https://www.cnbc.com/2019/05/30/heres-why-chinas-trade-war-threat-to-restrict-rare-earth-minerals-is-so-serious.html>
- Lowe, D. R. (1982). Sediment Gravity Flows II. Depositional models with special reference to the deposits of high-density turbidity currents. *Journal of Sedimentary Petrology*, 279-297.
- Major, J. (1978). *Hindered settling*. Dordrecht: Springer.
- MathWorks. (2020, 04 09). Retrieved from Compensate for the Delay Introduced by an IIR Filter: <https://nl.mathworks.com/help/signal/ug/compensate-for-the-delay-introduced-by-an-iir-filter.html>
- Matousek, V. (2004). Dredge Pumps and Slurry Transport. Delft.
- MIDAS. (2020, 03 12). Retrieved from Polymetallic nodules: <https://www.eu-midas.net/science/nodules>


- Middleton, G. (1993). Sediment Deposition from Turbidity Currents. *Annu. Rev. Earth Planet. Sci.*, 89-114.
- Middleton, G. V. (1966). Experiments on density and turbidity currents: Motion of the head. *Canadian Journal of Earth Sciences*, 523-546.
- Middleton, G. V., & Hampton, M. A. (1984). Mechanics of Sediment Movement. *Society of Economic Palaeontologists and Mineralogists*, Short Courses 3.
- Miller, K., Thompson, K., Johnston, P., & Santillo, D. (2018). An Overview of Seabed Mining Including the Current State of Development, Environmental Impacts, and Knowledge Gaps. *Frontiers in Marine Science*, 4: 418.
- Mirza, S., & Richardson, J. (1979). Sedimentation of suspensions of particles of two or more sizes. *Chem. Eng. Science*, 447-454.
- Moodie, T. (2002). Gravity currents. *Journal of Computational and Applied Mathematics*, 49-83.
- Nautilus Minerals*. (2020, 03 13). Retrieved from Seafloor Production Tools: <http://www.nautilusminerals.com/irm/content/seafloor-production-tools.aspx?RID=333>
- Neutrium*. (2020, 05 13). Retrieved from Terminal velocity of particles for gravity separation: <https://neutrium.net/unit-operations/terminal-velocity-of-particles-for-gravity-separation/>
- Nugent, C. (2018). *Deep-Sea Mining: The Basics*. The PEW Charitable Trusts.
- OpenCV Tutorial C++*. (2020, 4 2). Retrieved from Gaussian Blur: <https://www.opencv-srf.com/2018/03/gaussian-blur.html>
- Parsons, J., Friedrichs, C., Traykovski, P., Mohrig, D., Imran, J., Syvitski, J., . . . Garcia, M. (2007). The Mechanics of Marine Sediment Gravity Flows.
- Persons, J. D. (1998). Mixing mechanisms in density intrusions. PhD Thesis. *University of Illinois at Urbana-Champaign*.
- Pietrzak, J. (2016). An Introduction to Stratified Flows for Civil and Offshore Engineers. "From Shelf to Shore". Delft, The Netherlands: Environmental Fluid Mechanics Section.
- Richardson, J., & Zaki, W. (1954). Sedimentation and fluidisation: part 1. *Trans. Chem. Eng.*, 35-53.
- Roser, M., Ritchie, H., & Ortiz-Ospina, E. (2020, 02 10). *World Population Growth*. Retrieved from Our World in Data: <https://ourworldindata.org/world-population-growth>
- Rottman, J., & Simpson, J. (1983). Gravity currents produced by instantaneous releases of a heavy fluid in a rectangular channel. *J. Fluid Mech.*, 95-110.
- Rowe, P. (1987). A convenient empirical equation of the Richardson-Zaki exponent. *Chem. Eng. Science*, 2795-2796.
- SciPy.org*. (2020, 04 09). Retrieved from scipy.signal.filtfilt: <https://docs.scipy.org/doc/scipy-0.18.1/reference/generated/scipy.signal.filtfilt.html>
- Simpson, J. E. (1969). A comparison between laboratory and atmospheric density currents. *Wuart. J. Royal Met. Soc.*, 758-765.

- Simpson, J. E. (1997). *Gravity Currents: In the Environment and the Laboratory*. New York: USA: Cambridge University Press.
- Simpson, J. E., & Britter, R. E. (1979). The dynamics of the head of a gravity current advancing over a horizontal surface. *Journal of Fluid Mechanics*, 477-495.
- Smith, T. (1966). The sedimentation of particles having a dispersion of sizes. *Trans. Int. Chem. Eng.* , 44.
- Tomkins, M., Baldock, T., & Nielsen, P. (2005). Hindered settling of sand grains. *Sedimentology* , 1425-1432.
- van Rhee, C. (2018, 04 03). Lecture notes OE44045. Delft: TU Delft.
- Yeoh, G. H., & Tu, J. (2010). Liquid-Particle flows. *Computational Techniques for Multiphase Flows*.

A. First Appendix: Sediment properties


A. 1 Sediment type I (75 – 125µm):

GLASS BEADS	
Glass beads are made conform MIL-G-9954 A specifications.	
CHEMICAL ANALYSIS	SiO ₂ 72 % Al ₂ O ₃ < 2.5 % CaO 9 % MgO < 4 % Na ₂ O 13.7 % K ₂ O < 1.2 % Fe ₂ O ₃ < 0.5 % SO ₃ < 0.5 %
SHAPE	Round
NATURE	Inert
COLOUR	White
HARDNESS	6 Mohs
BULK WEIGHT	1.5 kg/dm ³
SPECIFIC WEIGHT	2.46 kg/dm ³
GRAIN SIZE	40 - 70 micron 65 - 105 micron 75 - 125 micron 90 - 150 micron 100 - 200 micron 150 - 250 micron 200 - 300 micron 300 - 400 micron 400 - 600 micron
PACKING	In 25 kg paper bags on pallets of 1000 kg each, covered with a shrink foil.
APPLICATION	Glass beads performance is cleaning of surface without roughening. Glass beads can be used in blast halls and cabinets. Besides cleaning of surface also surface hardening occurs Shot Peening.

**HOLLAND MINERAAL**^{bv}
ABRASIVES AND BLASTING EQUIPMENT

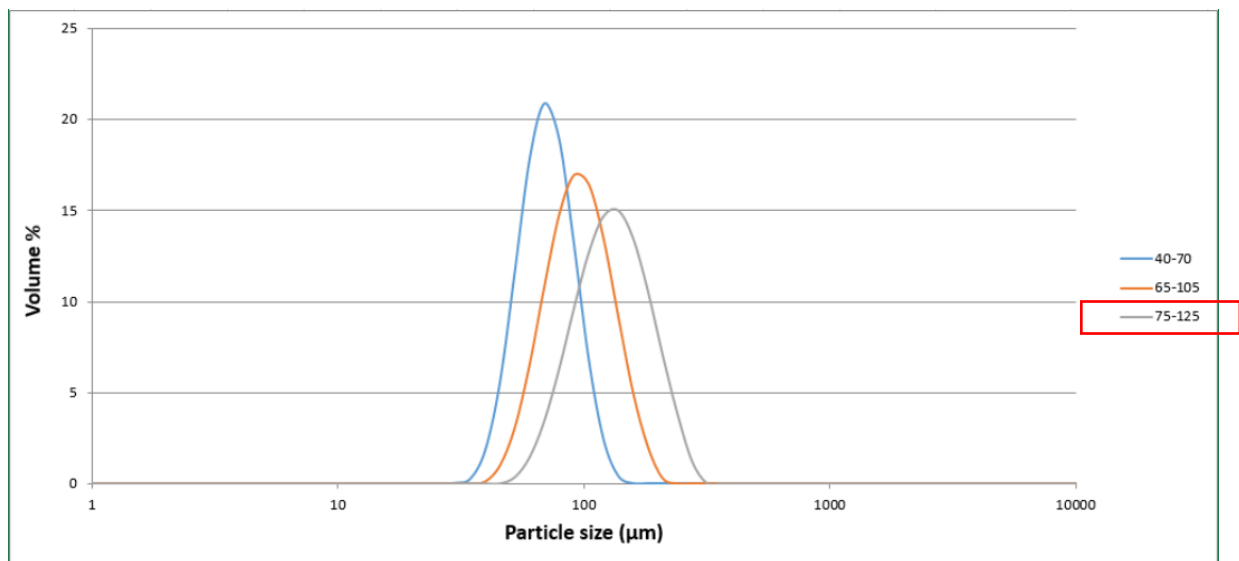
Tielstraat 8
7418 CS Deventer, Holland
www.hollandmineraal.nl

Tel. 31+(0)570-621161
Fax 31+(0)570-634336
info@hollandmineraal.nl



A.1.1 Civil engineering test results for sediment type I:

	40-70	65-105	75-125
D ₅₀ (μm)	65,55±0,06	88,78±0,13	122,55±1,17



A. 2 Sediment type II (4 – 60 μ m):

MILLISIL® M6 - M6.1 - M10						
<p>MILLISIL® is produced by iron-free grinding and accurate sieving by means of air-separators. A selected silica sand with a SiO₂-content of over 99 % is used as raw material. The purity, controlled particle size distribution, chemical inertness, optical properties and hardness make MILLISIL® the performance standard in ceramics, tile-glues, special mortars and coatings.</p>						
GRANULOMETRIC DATA AND PHYSICAL CHARACTERISTICS						
Technical Data		M6	M6.1	M10		Method
	control-sieve > 63 μ m	14	14	2	%	Alpine
	D10	5	5	4	μ m	Malvern MS 2000
	D50	30	30	23	μ m	Malvern MS 2000
	D90	95	95	60	μ m	Malvern MS 2000
	density	2.65	2.65	2.65	kg/dm ³	
	bulk density	1	1	0.9	kg/dm ³	
	specific surface	0.8 2400	0.8 2400	0.9 3600	m ² /g cm ² /g	BET Blaine
	oil absorption	16.5	16.5	17.5	g/100 g	
	hardness	7	7	7	Mohs	
	loss on ignition	0.12	0.08	0.12		
	pH	7	7	7		
	colour	L* 90 a* 0.87 b* 4.13	91 0.98 3.50	91 0.74 3.57		Minolta CM-3610d D65/10°
	refractive index	1.55	1.55	1.55		

B. Particle settling velocity

The settling velocity was computed using Equation 2.18 for sediment type I, Figure B.1. and sediment type II, Figure B.2. The vertical axis is the settling velocity in $[m/s]$ and horizontal axis is the diameter of the particle in $[m]$.

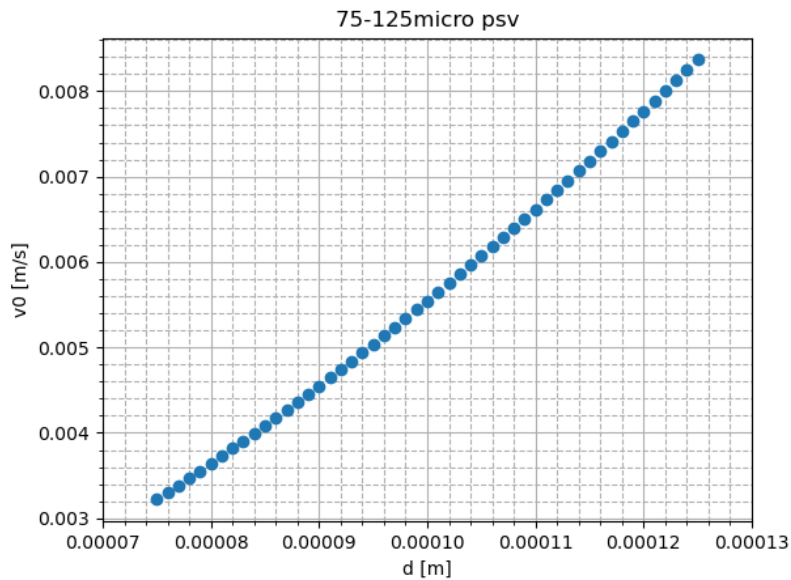


Figure B.1 Settling velocity of Sediment type I

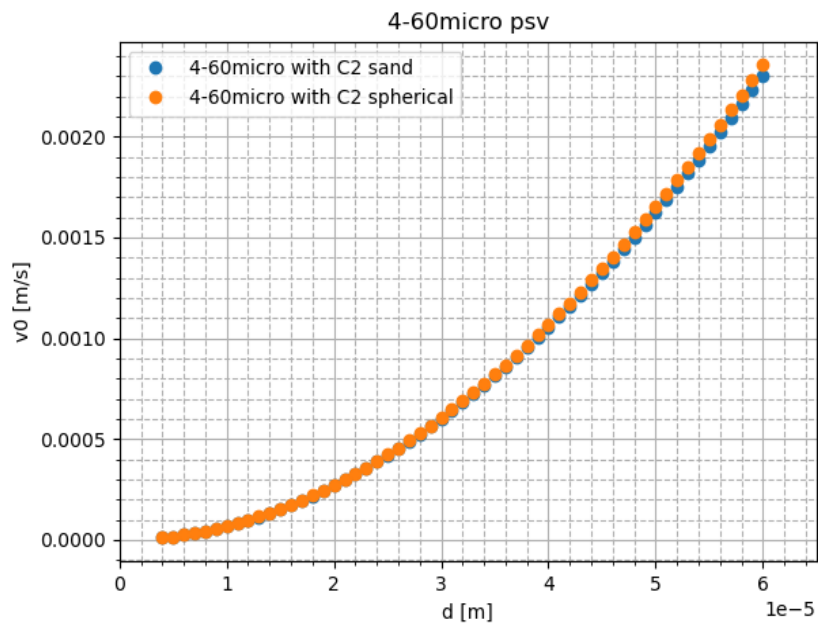


Figure B.2 Settling velocity of Sediment type II

The settling velocity is computed by using the multi-sized mixture of particles (Chapter 2.8.3) to compute the settling velocities for the combined sediment type I and II. Hereby, the d50 of each sediment type is used and the settling velocity is computed with Equation 2.26 for two fractions, see Figure B.3. In addition, the particle settling velocity is computed per sediment type taking hindered settling into consideration (Chapter 2.8.2). Therefore, Equation 2.19 and Equation 2.20 are used with the d50 per sediment type, for the results see Figure B.4.

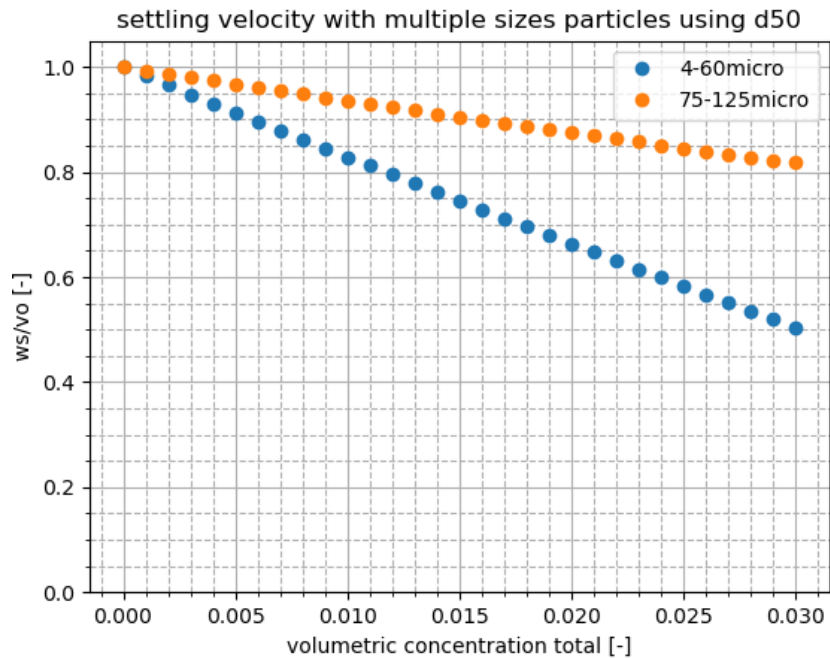


Figure B.3 Settling velocity with multiple size particles

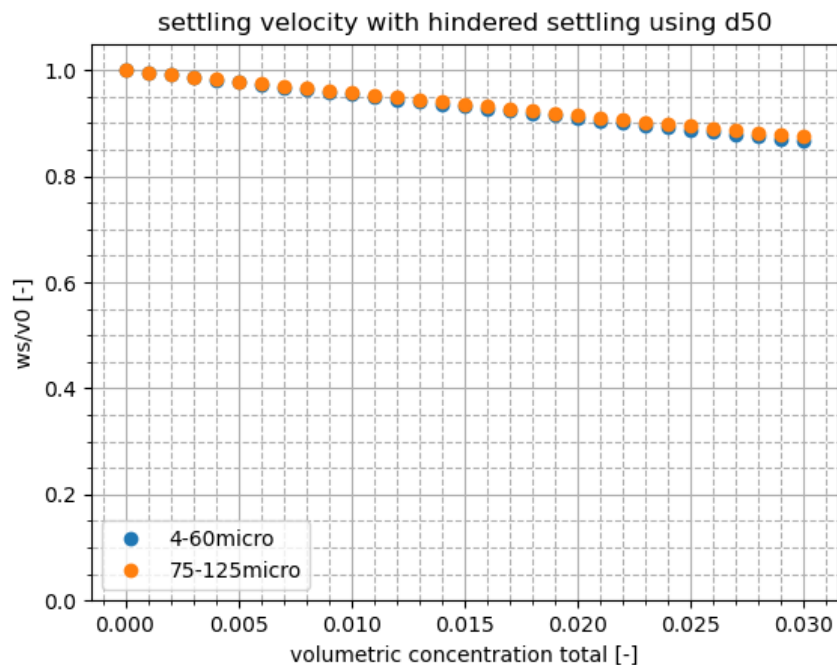
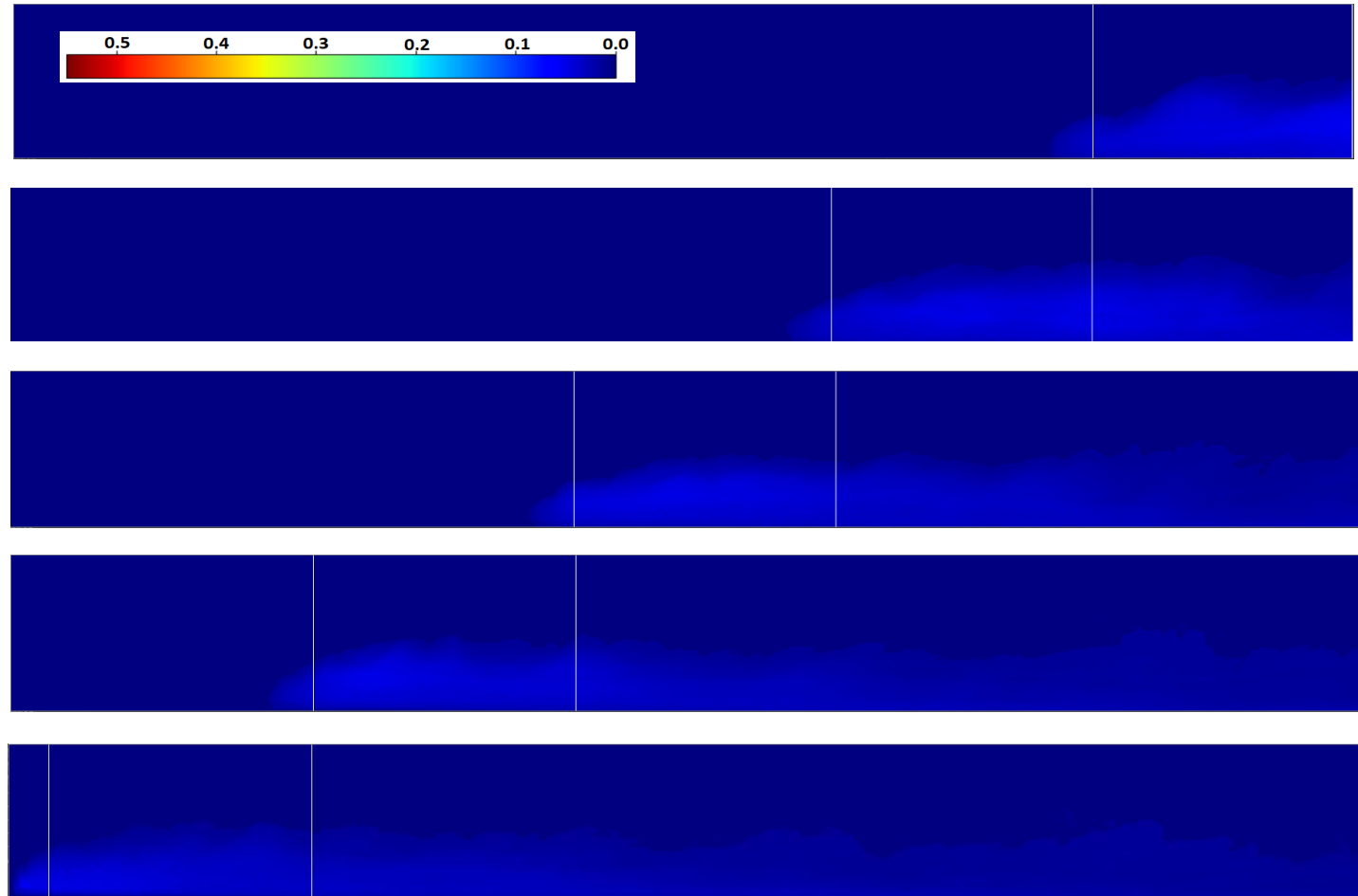


Figure B.4 Settling velocity with hindered settling for sediment type I and sediment type II

C. Third Appendix: Color Maps

Sediment type II ($4 - 60\mu m$):

4 – 60 μm sediment
0.10 %



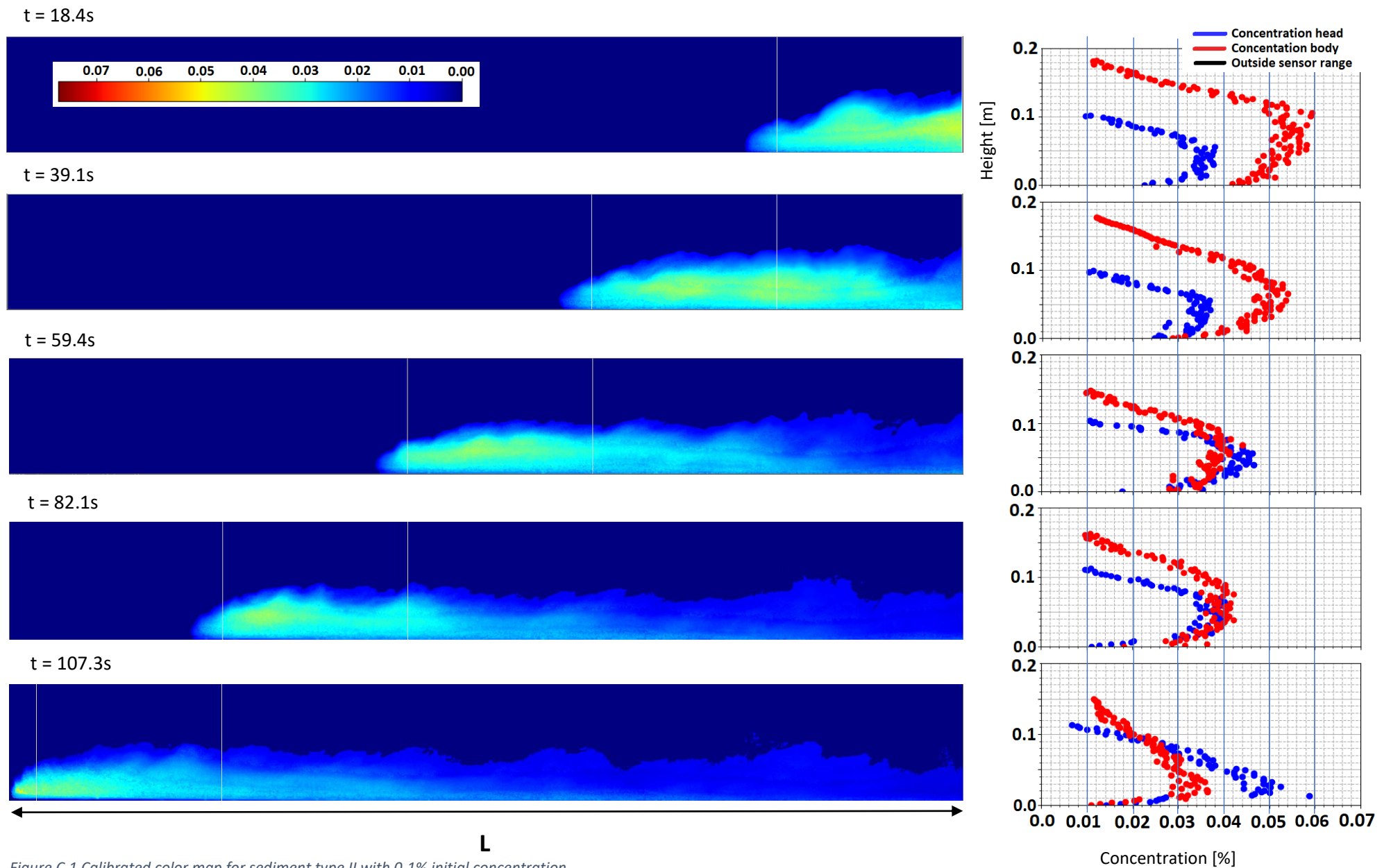
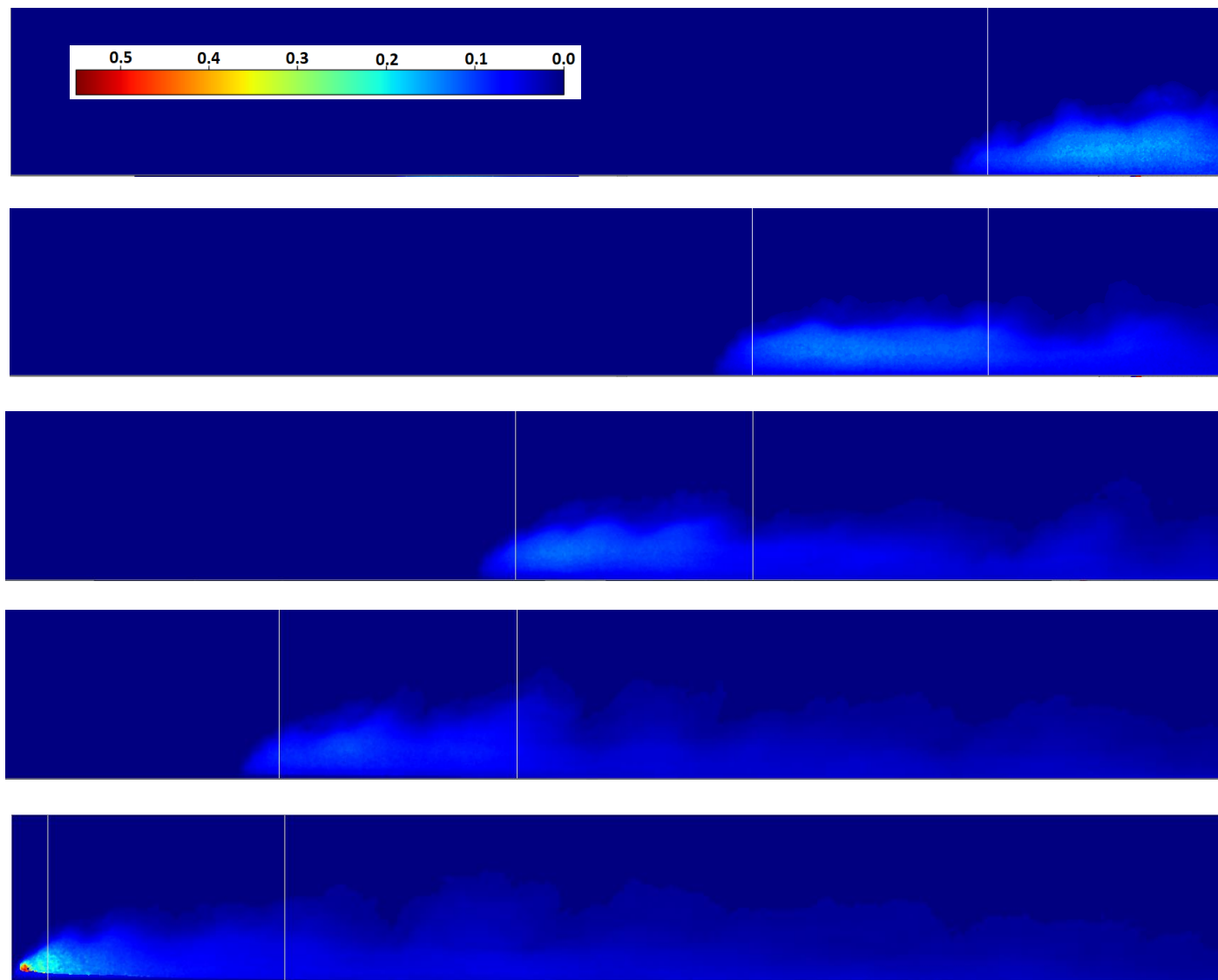


Figure C.1 Calibrated color map for sediment type II with 0.1% initial concentration

4 – 60 μm sediment
0.25 %



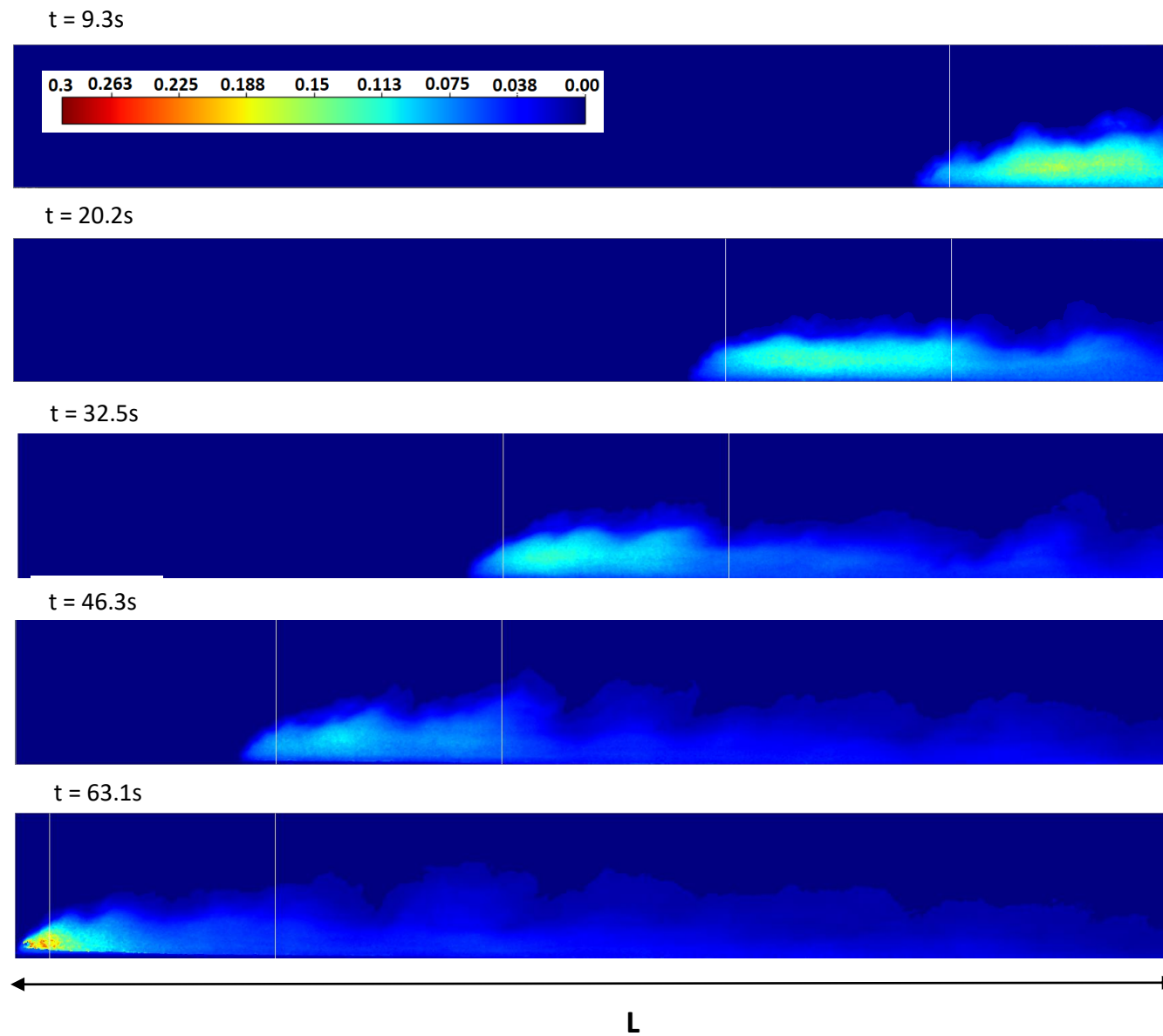
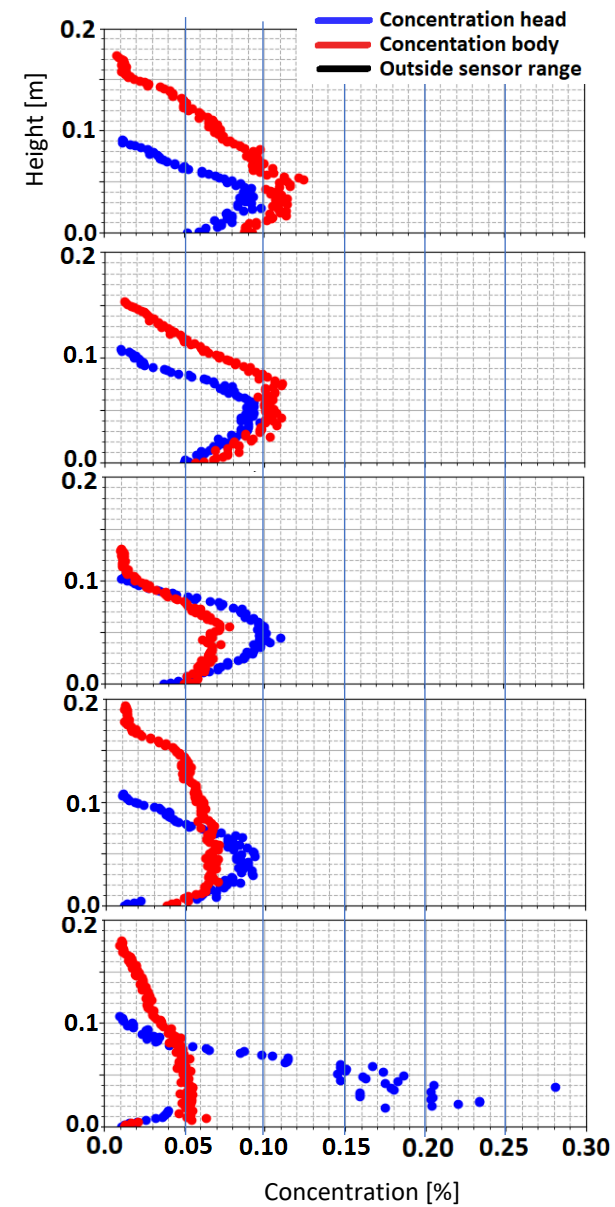


Figure C.2 Calibrated color map for sediment type II with 0.25% initial concentration



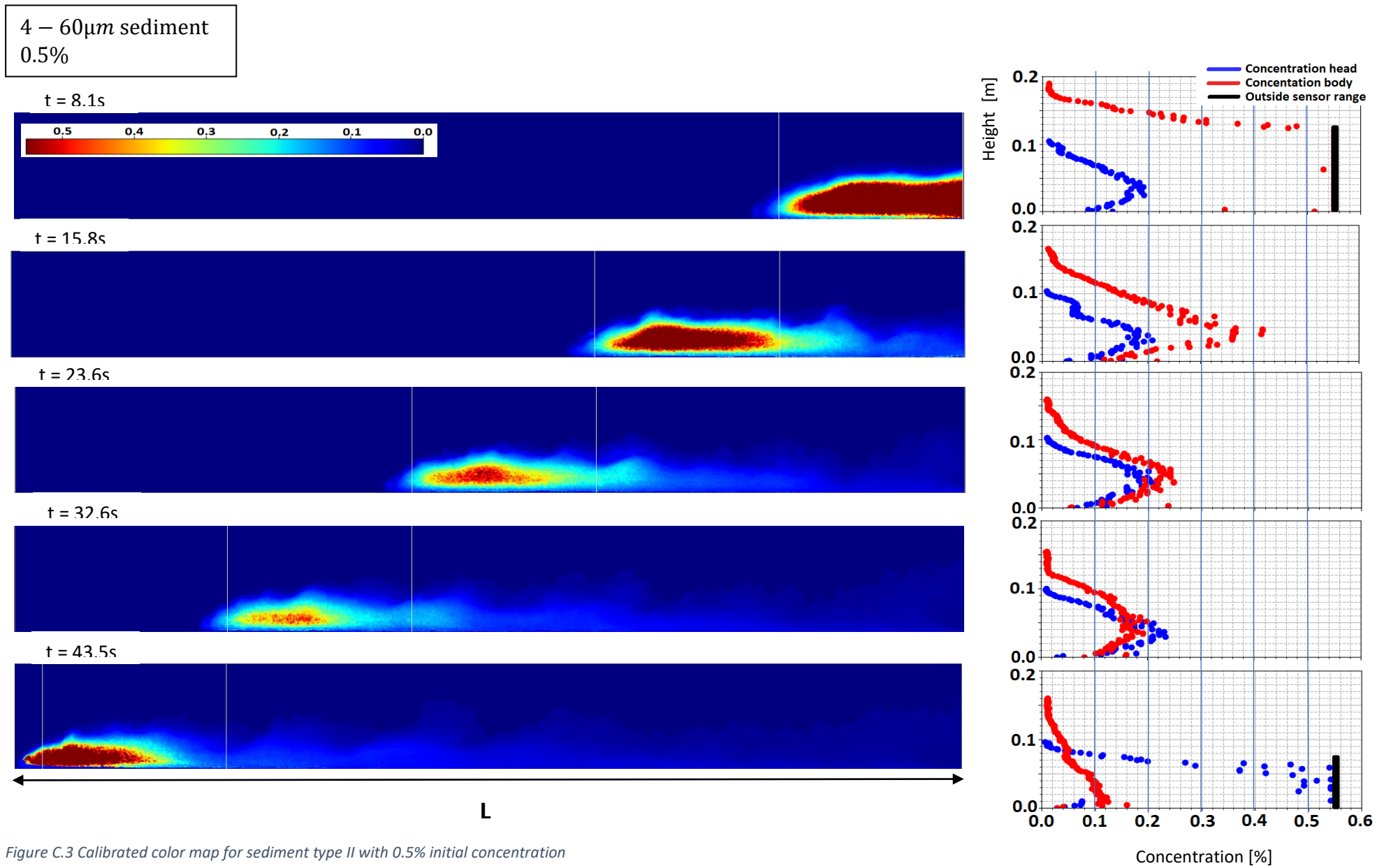
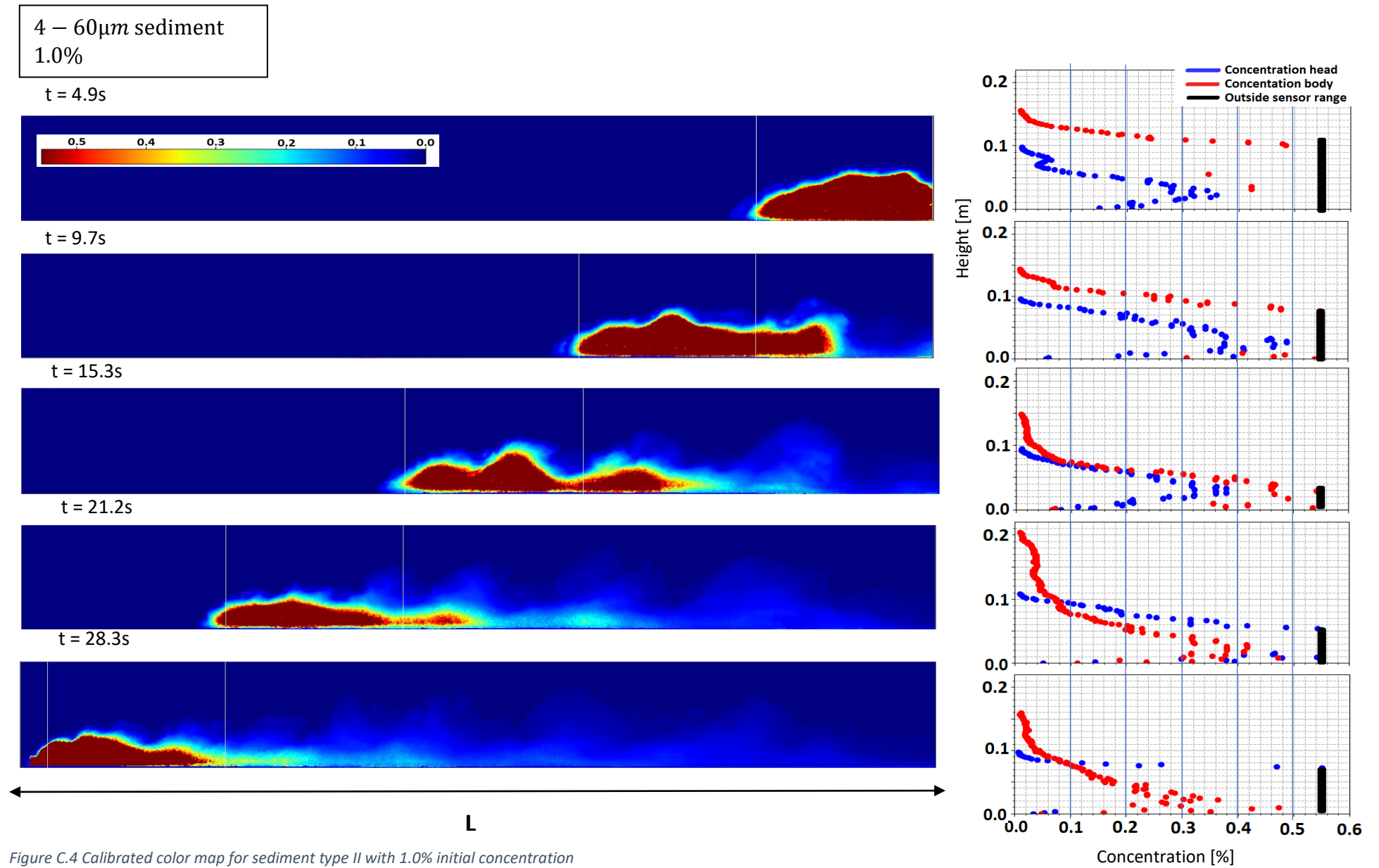


Figure C.3 Calibrated color map for sediment type II with 0.5% initial concentration



4 – 60 μ m sediment
1.5%

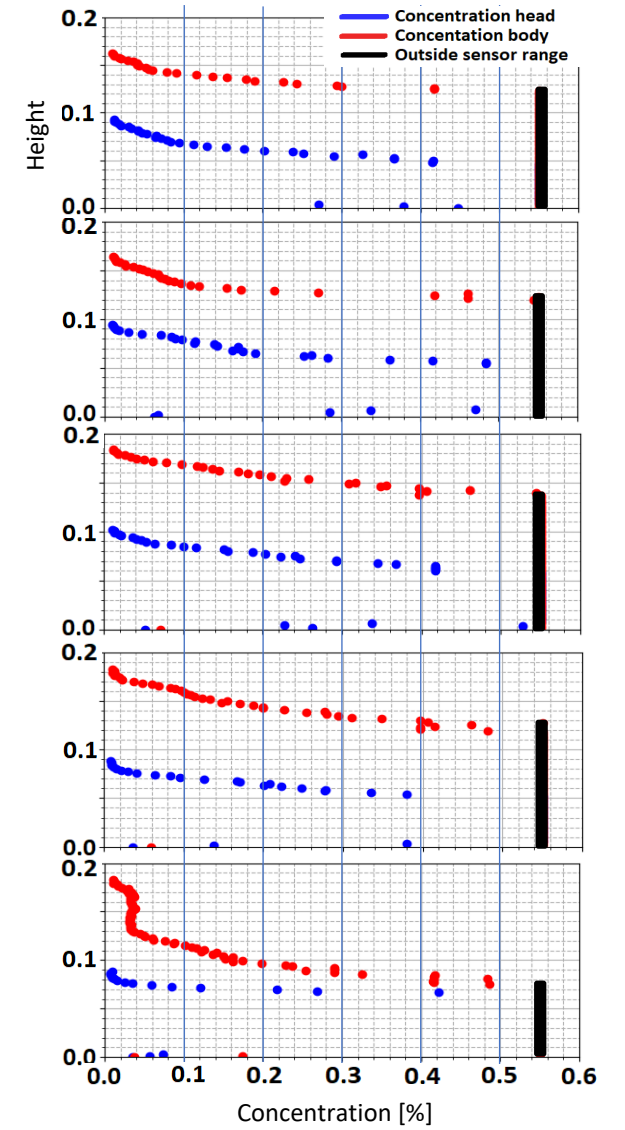
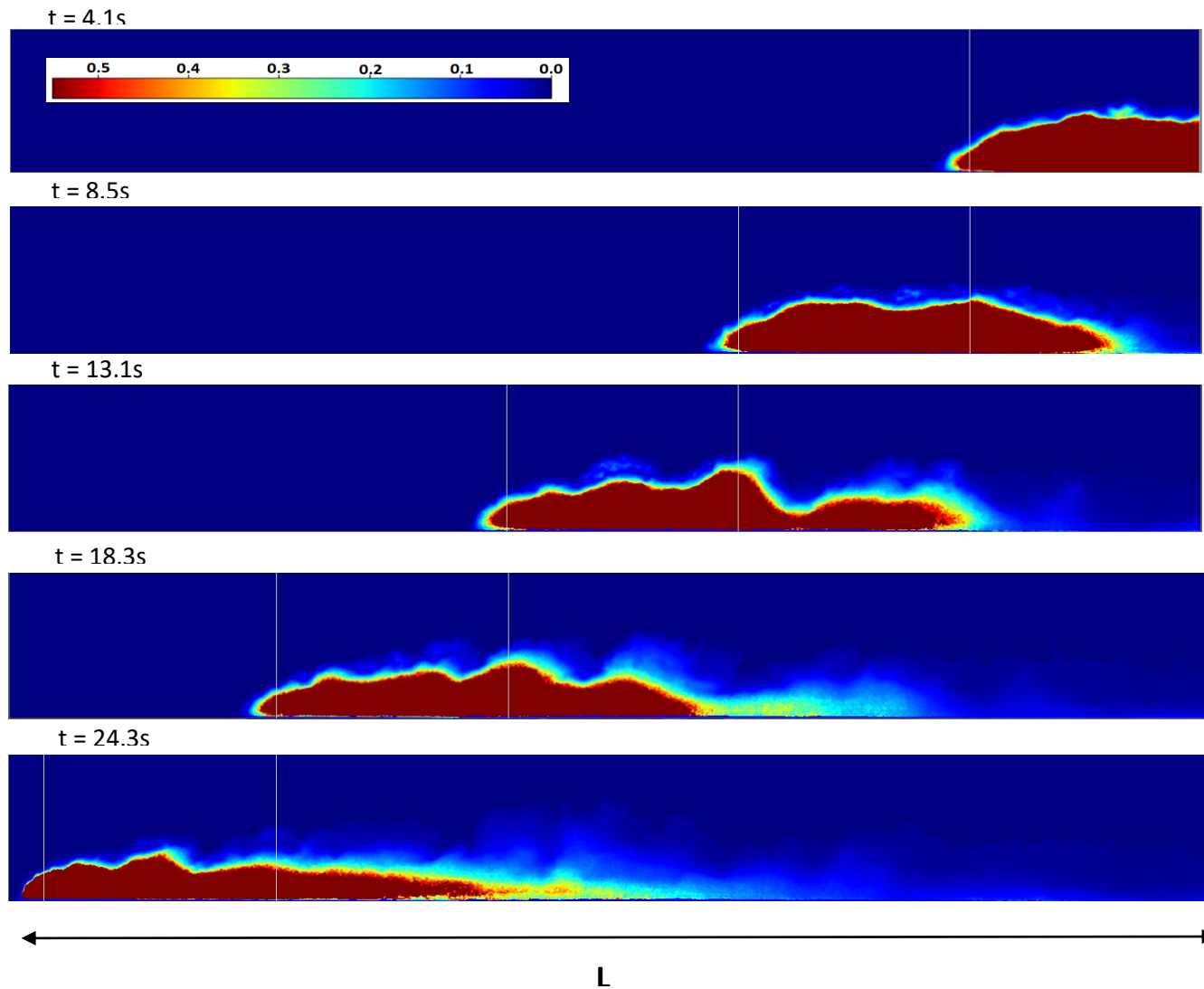


Figure C.5 Calibrated color map for sediment type II with 1.5% initial concentration

4 – 60 μm sediment
2.0%

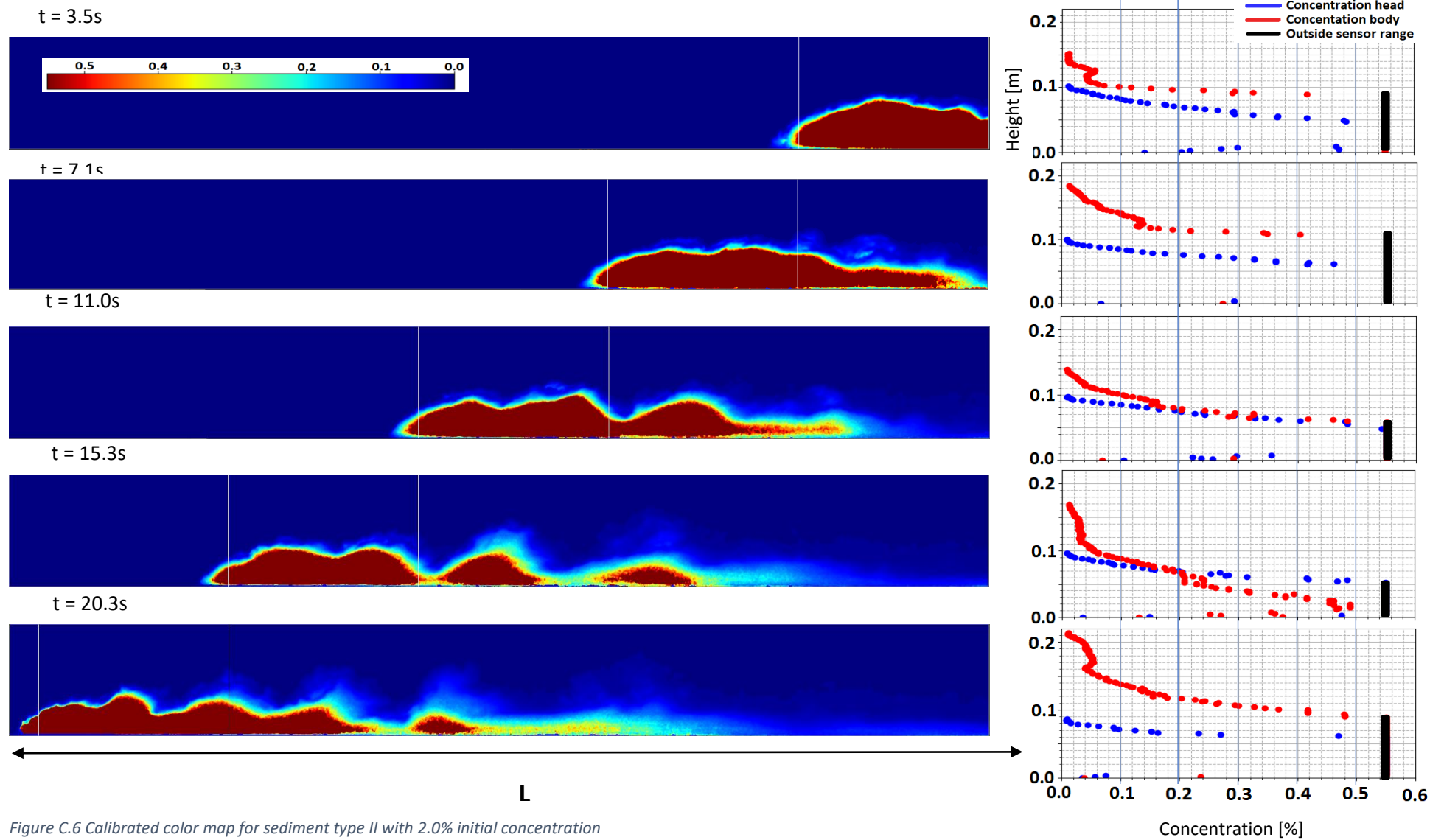


Figure C.6 Calibrated color map for sediment type II with 2.0% initial concentration

4 – 60 μ m sediment
2.5%

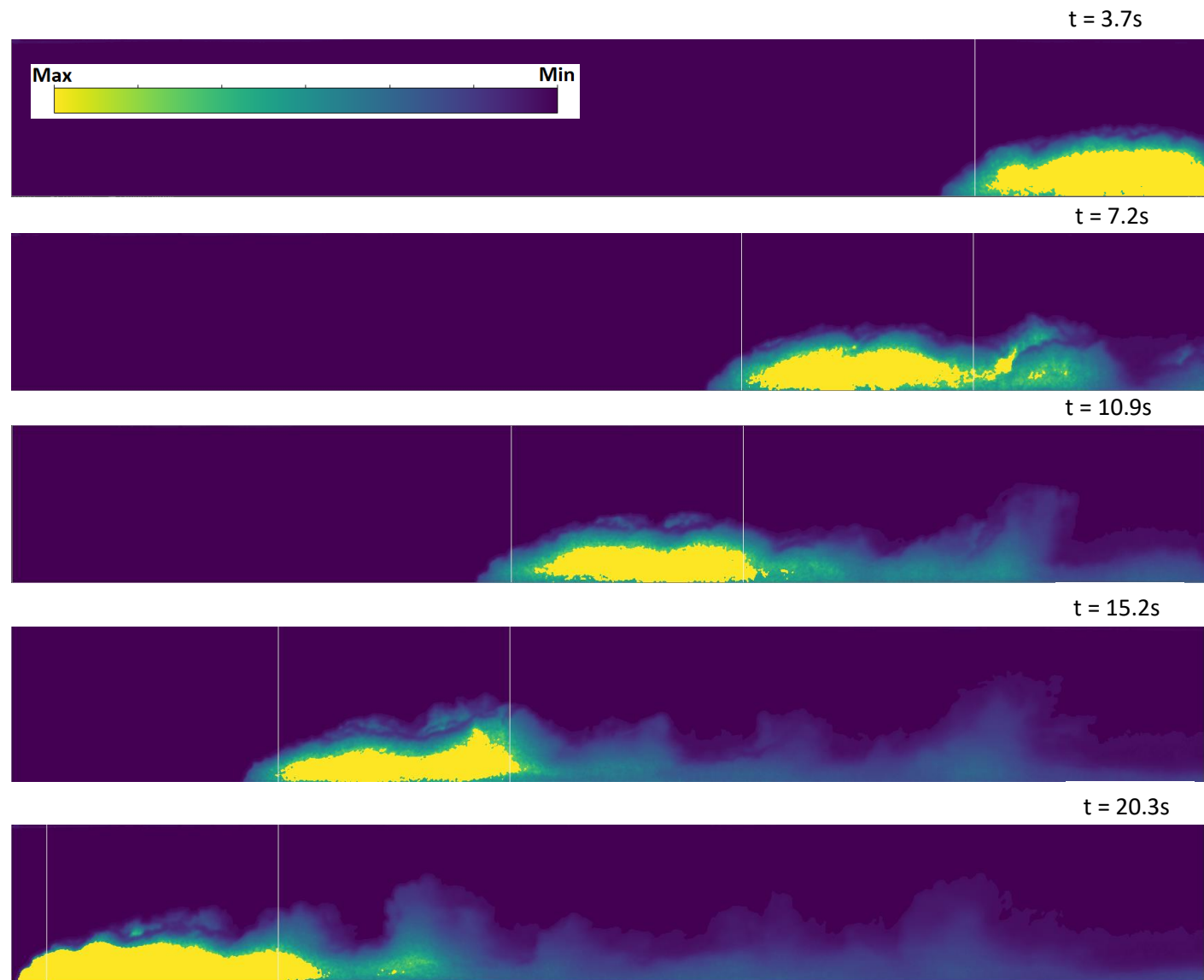


Figure C.7 Color map for sediment type II with 2.5% initial concentration

4 – 60 μ m sediment
3.0%

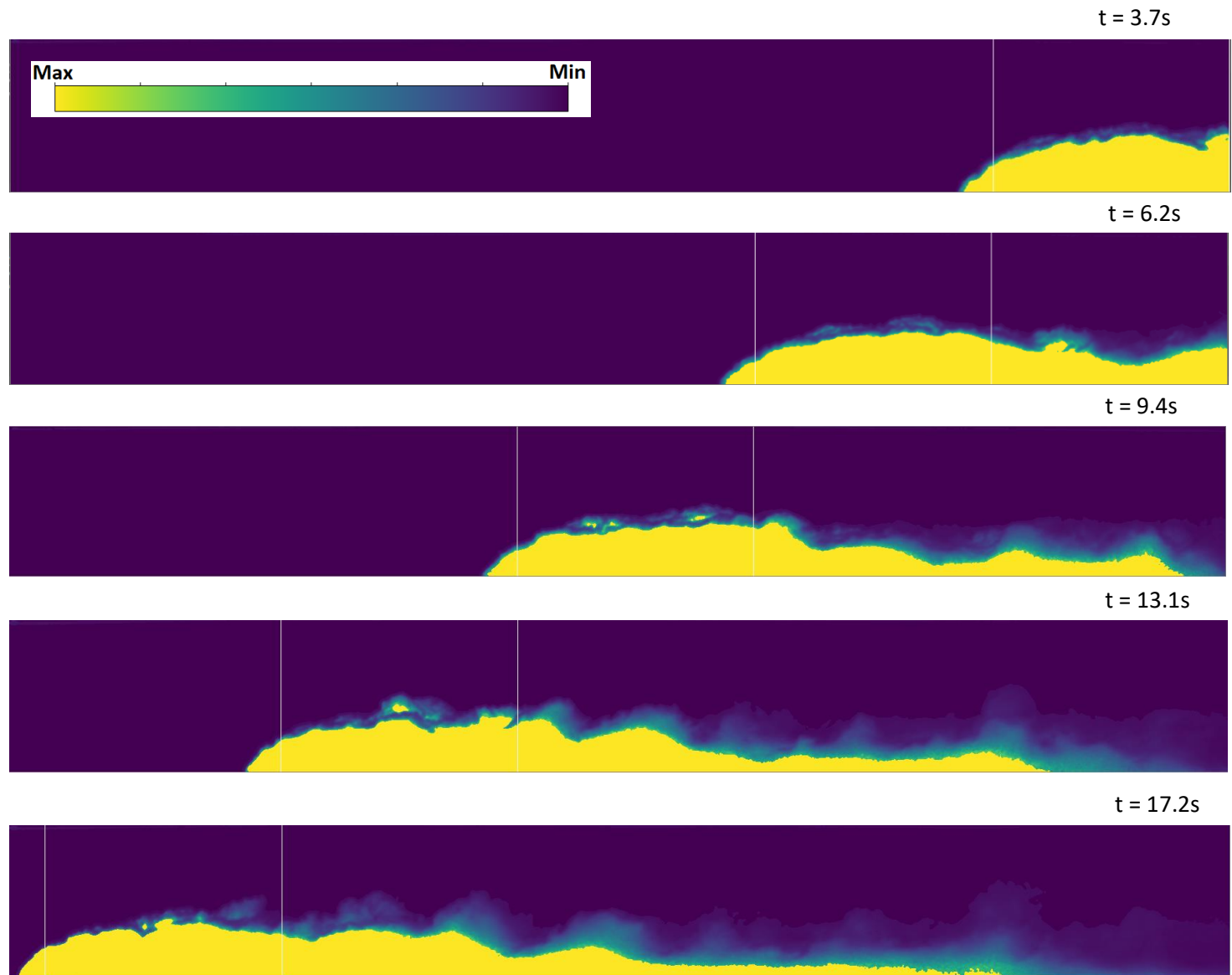
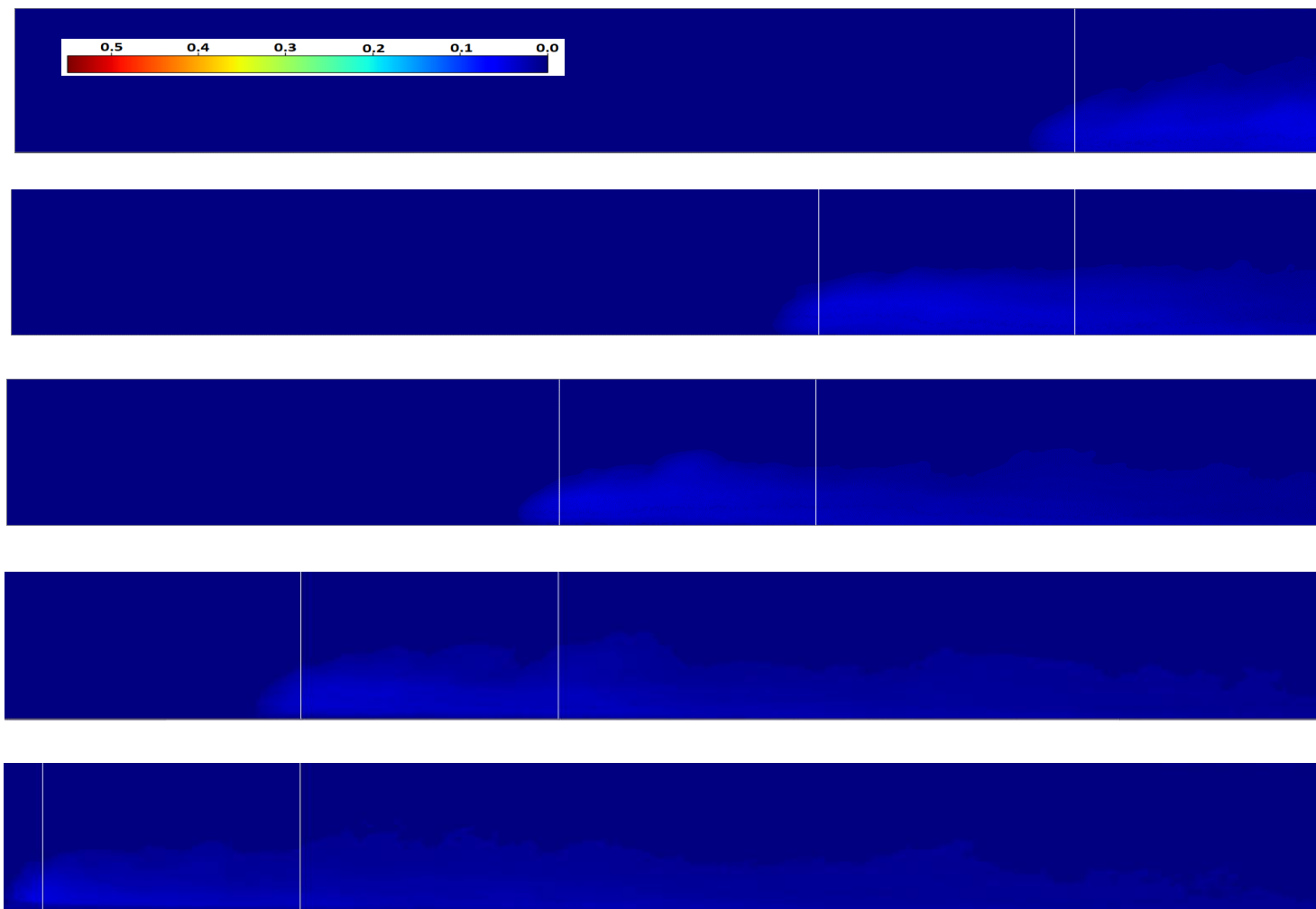


Figure C.8 Color map for sediment type II with 3.0% initial concentration

Combined sediment type I and II (4 – 125 μ m):

4 – 125 μ m sediment
0.1%



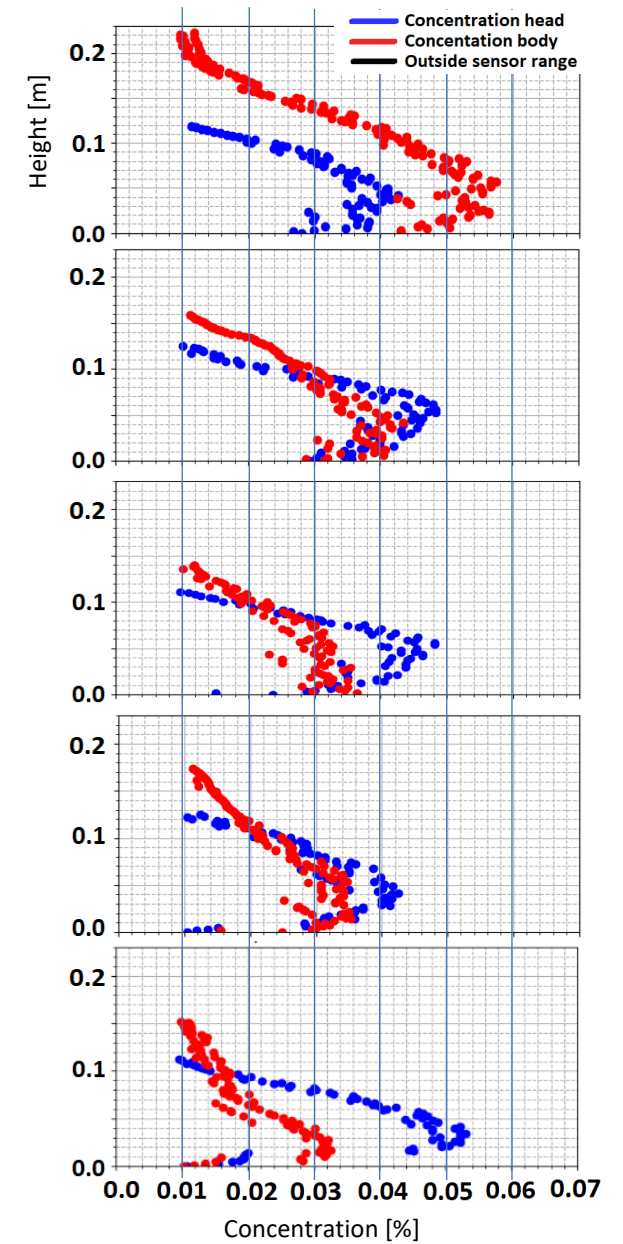
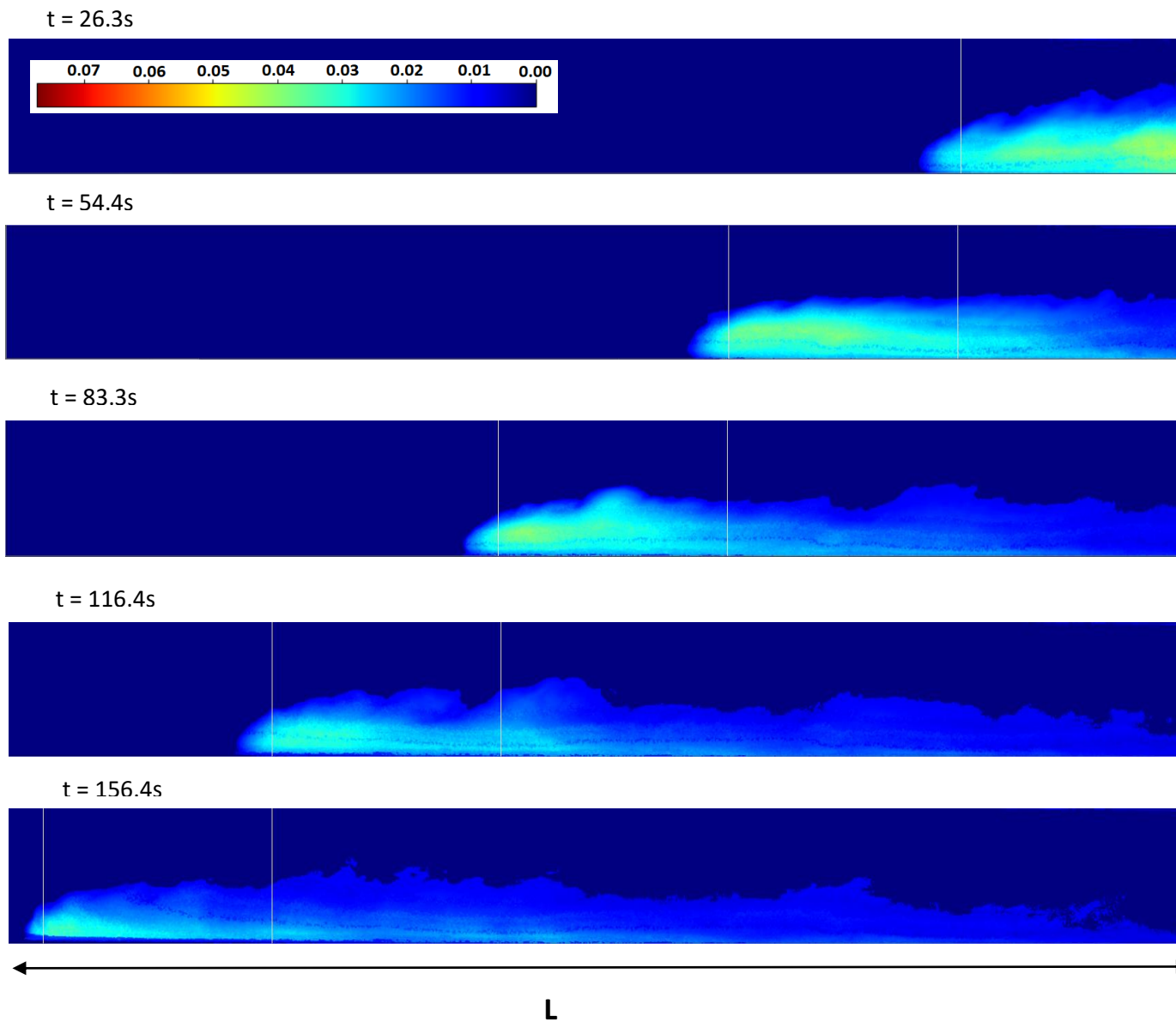
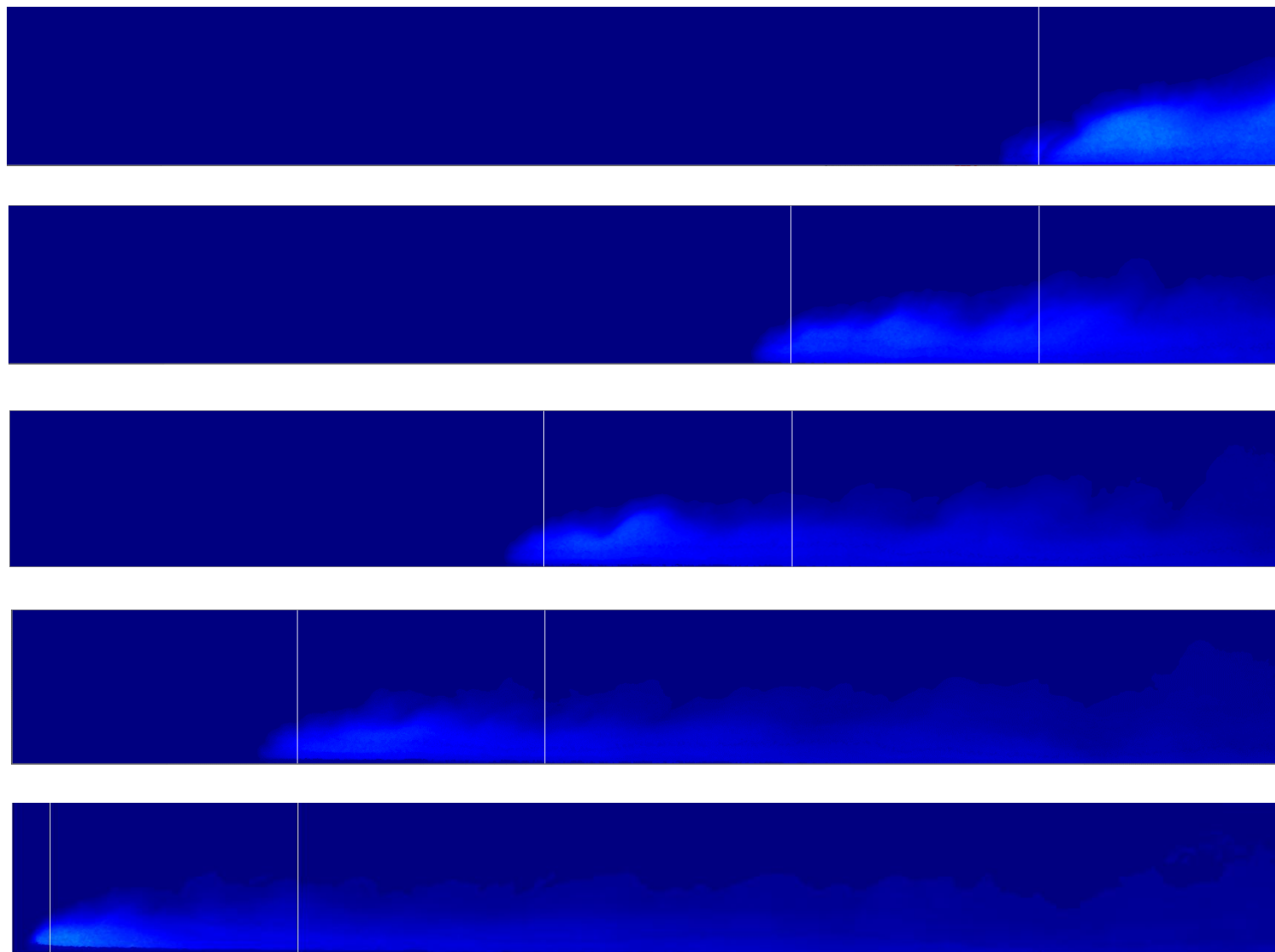


Figure C.9 Calibrated color map for the combined sediment type I and II with 0.1% initial concentration

4 – 125 μ m sediment
0.25%



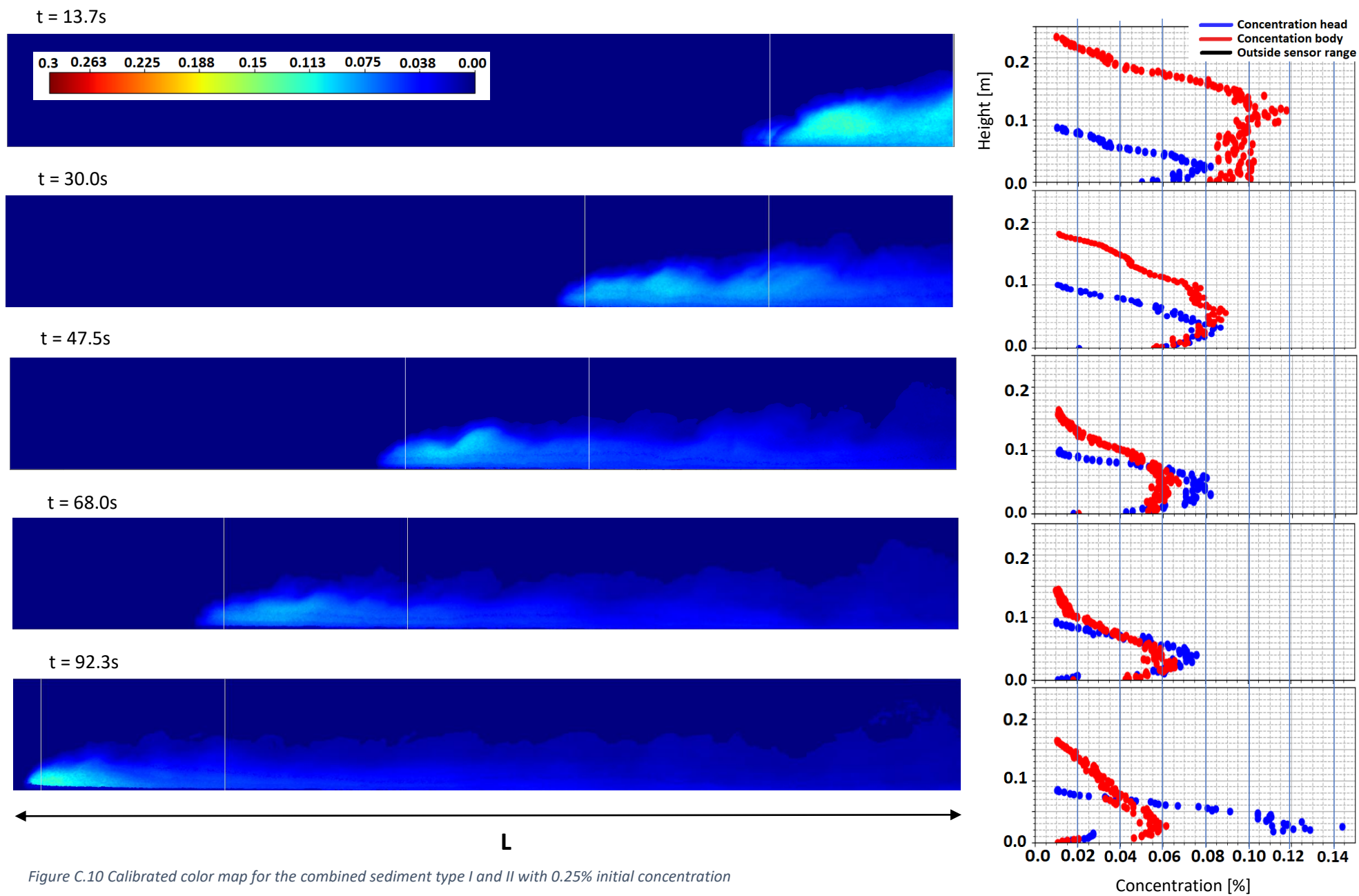


Figure C.10 Calibrated color map for the combined sediment type I and II with 0.25% initial concentration

4 – 125 μ m sediment
0.5%

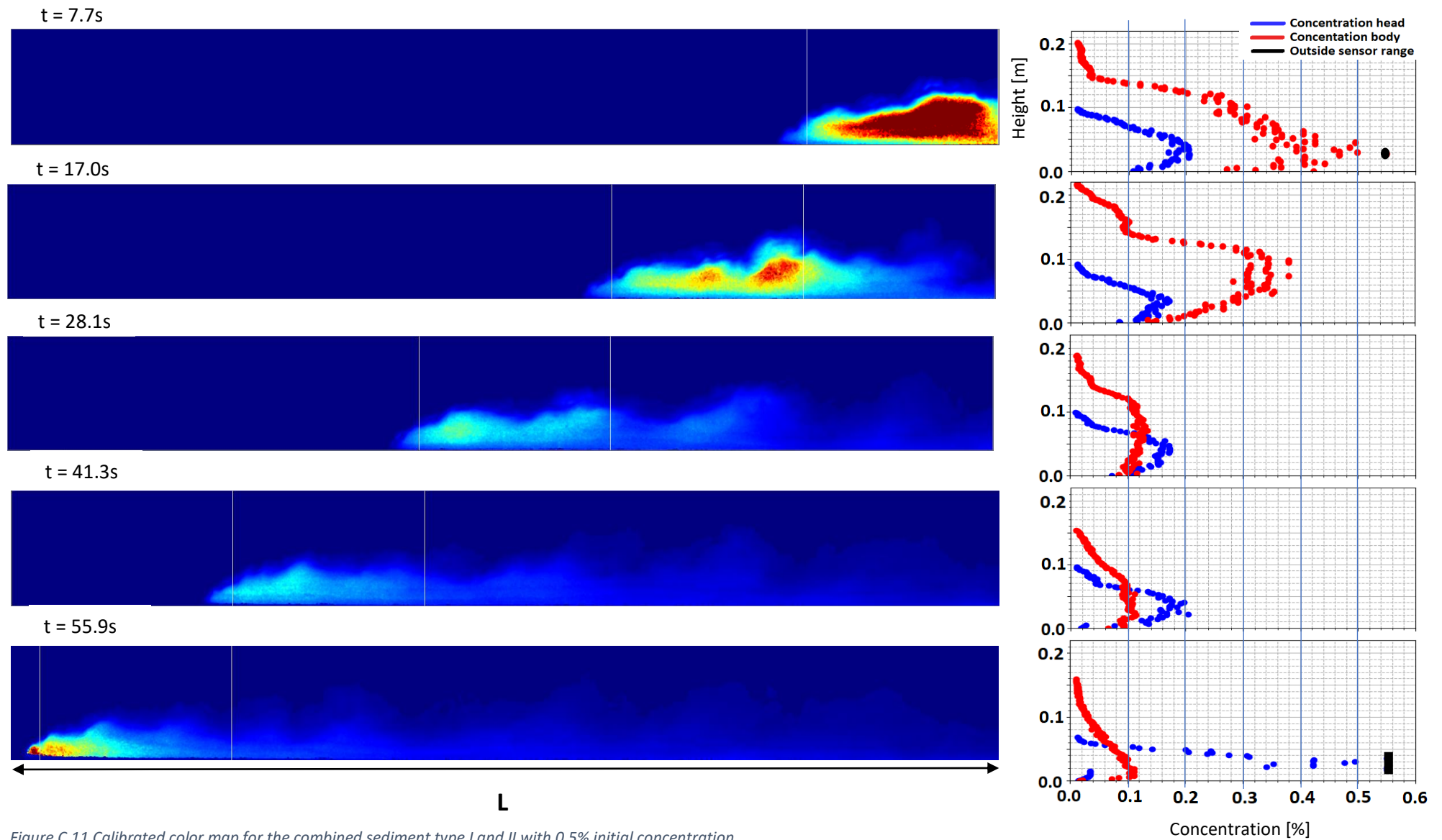


Figure C.11 Calibrated color map for the combined sediment type I and II with 0.5% initial concentration

4 – 125 μ m sediment
1.0%

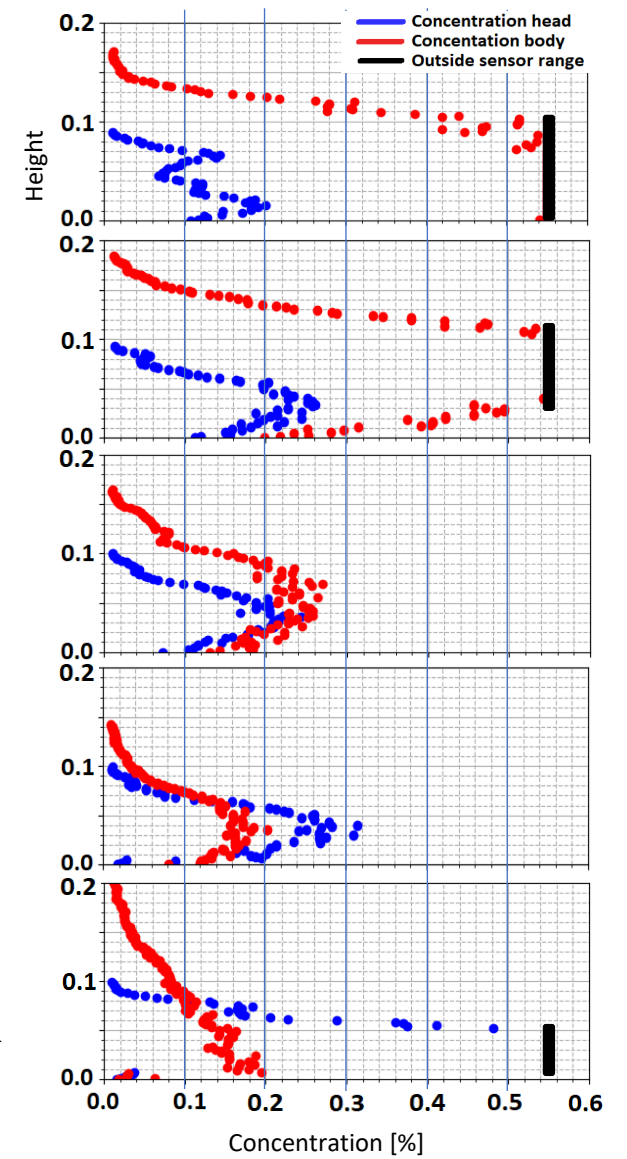
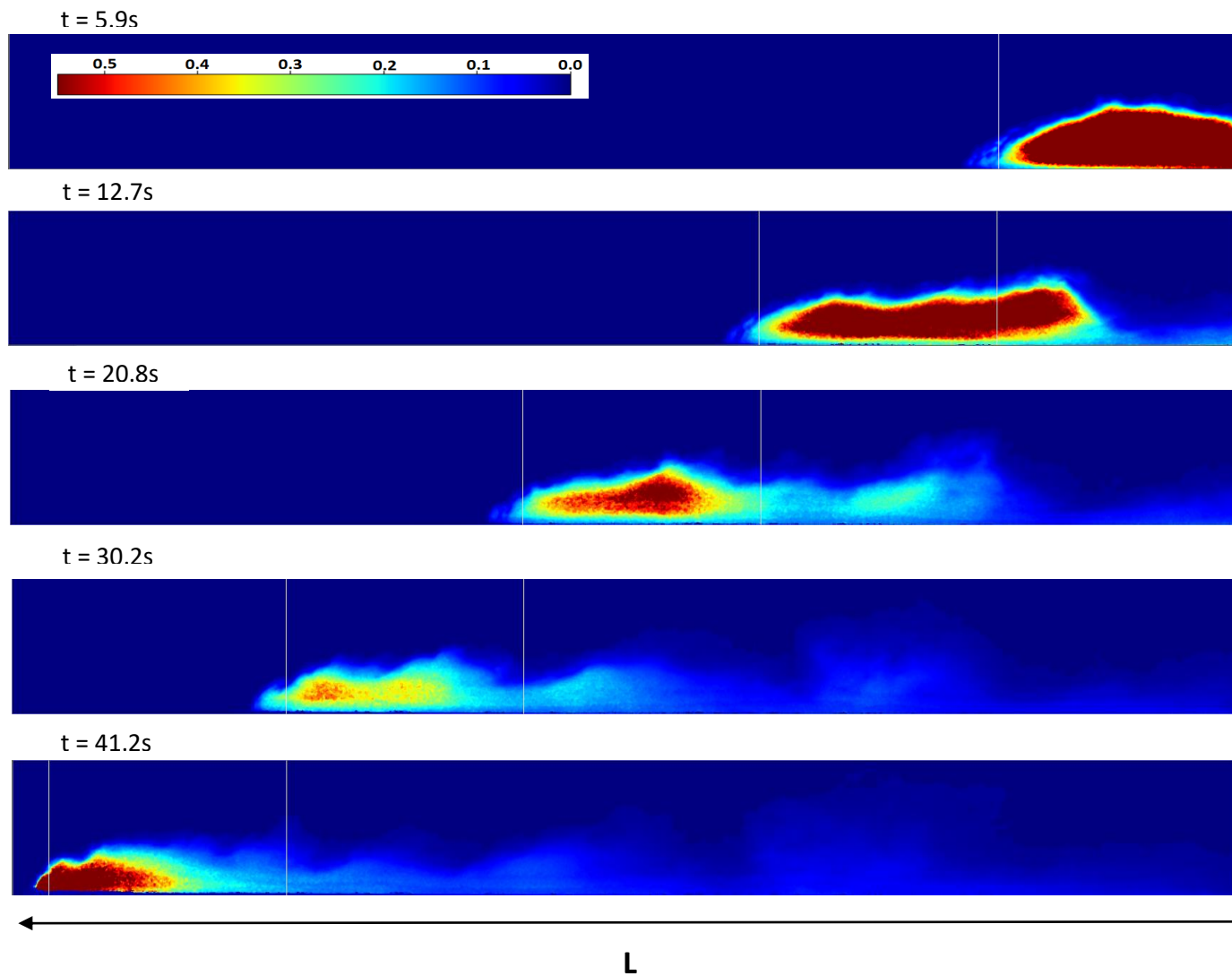


Figure C.12 Calibrated color map for the combined sediment type I and II with 1.0% initial concentration

4 – 125 μ m sediment
1.5%

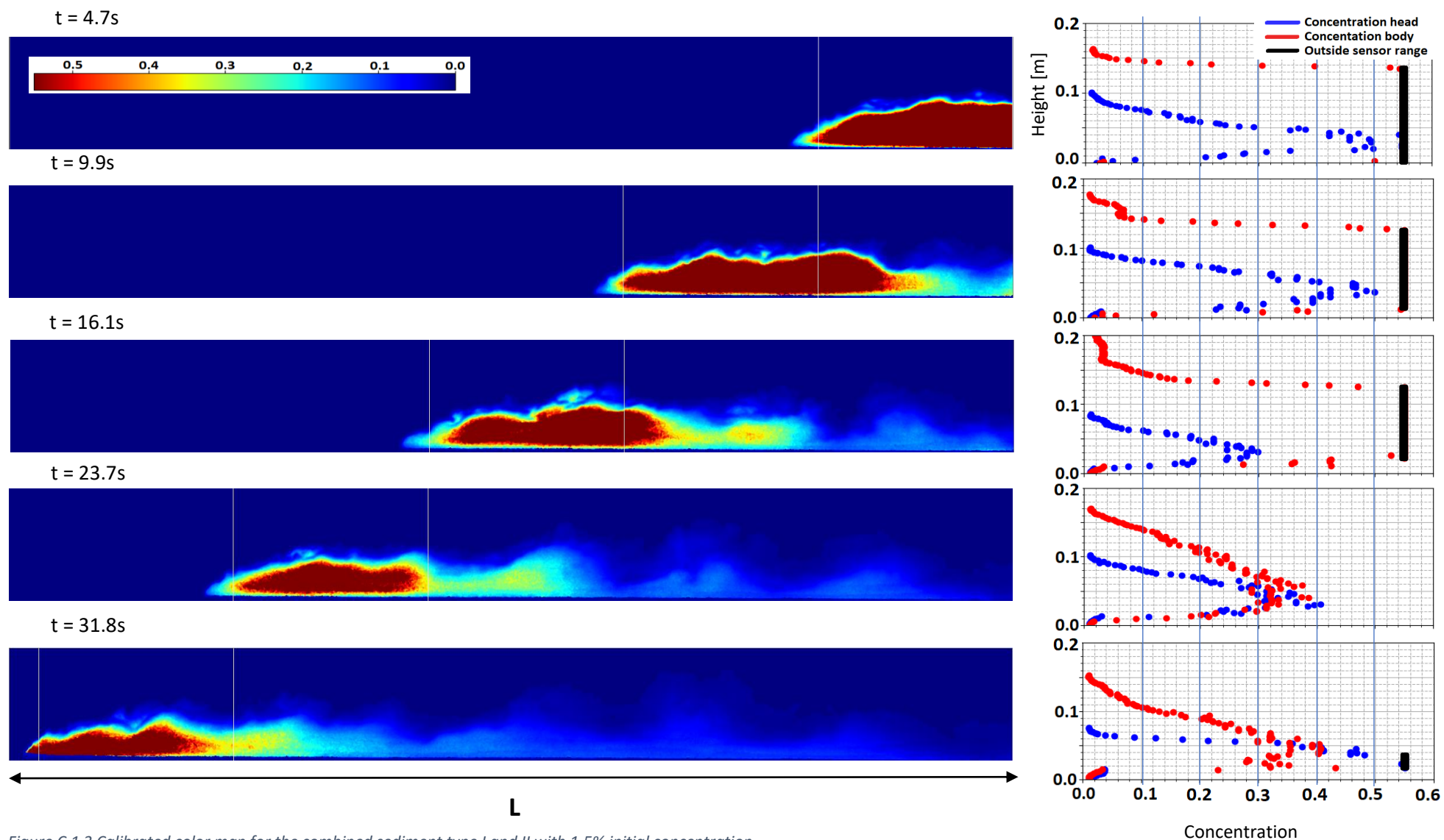


Figure C.1.3 Calibrated color map for the combined sediment type I and II with 1.5% initial concentration

4 – 125 μ m sediment
2.0%

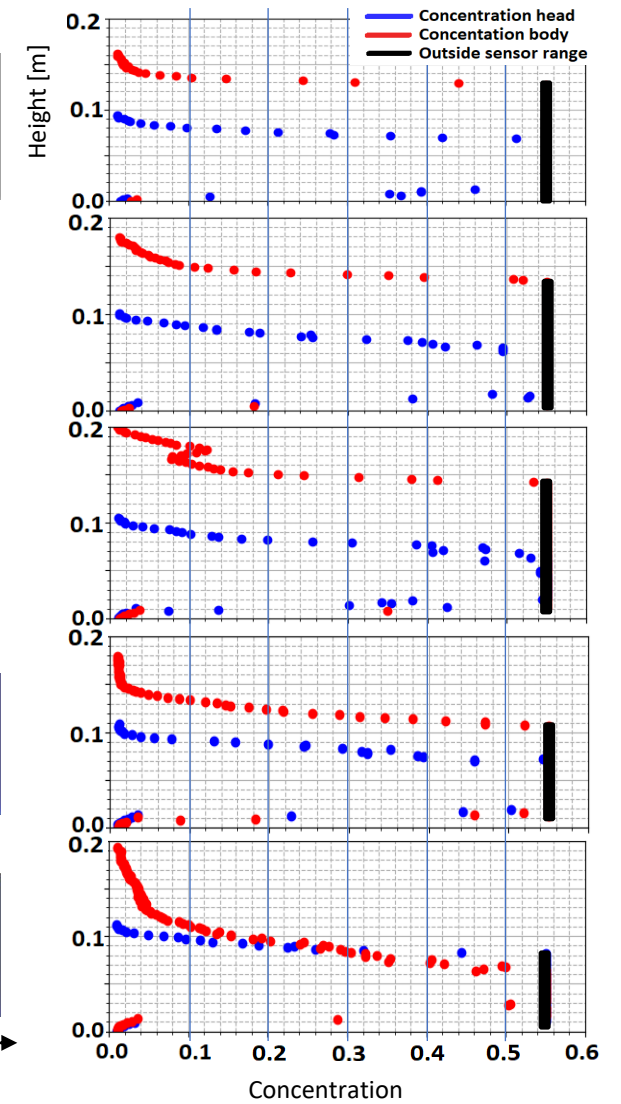
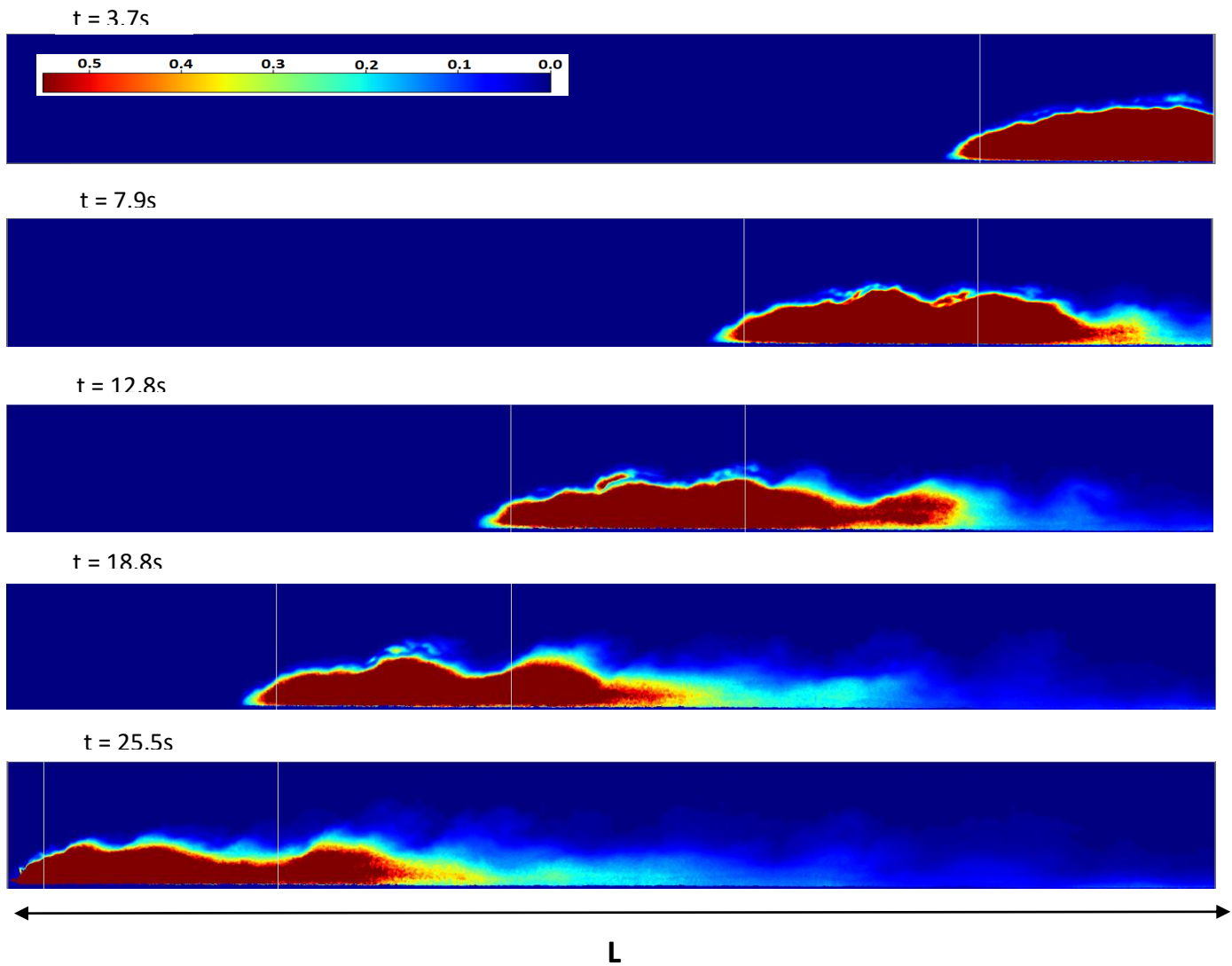


Figure C.14 Calibrated color map for the combined sediment type I and II with 2.0% initial concentration

4 – 125 μ m sediment
2.5%

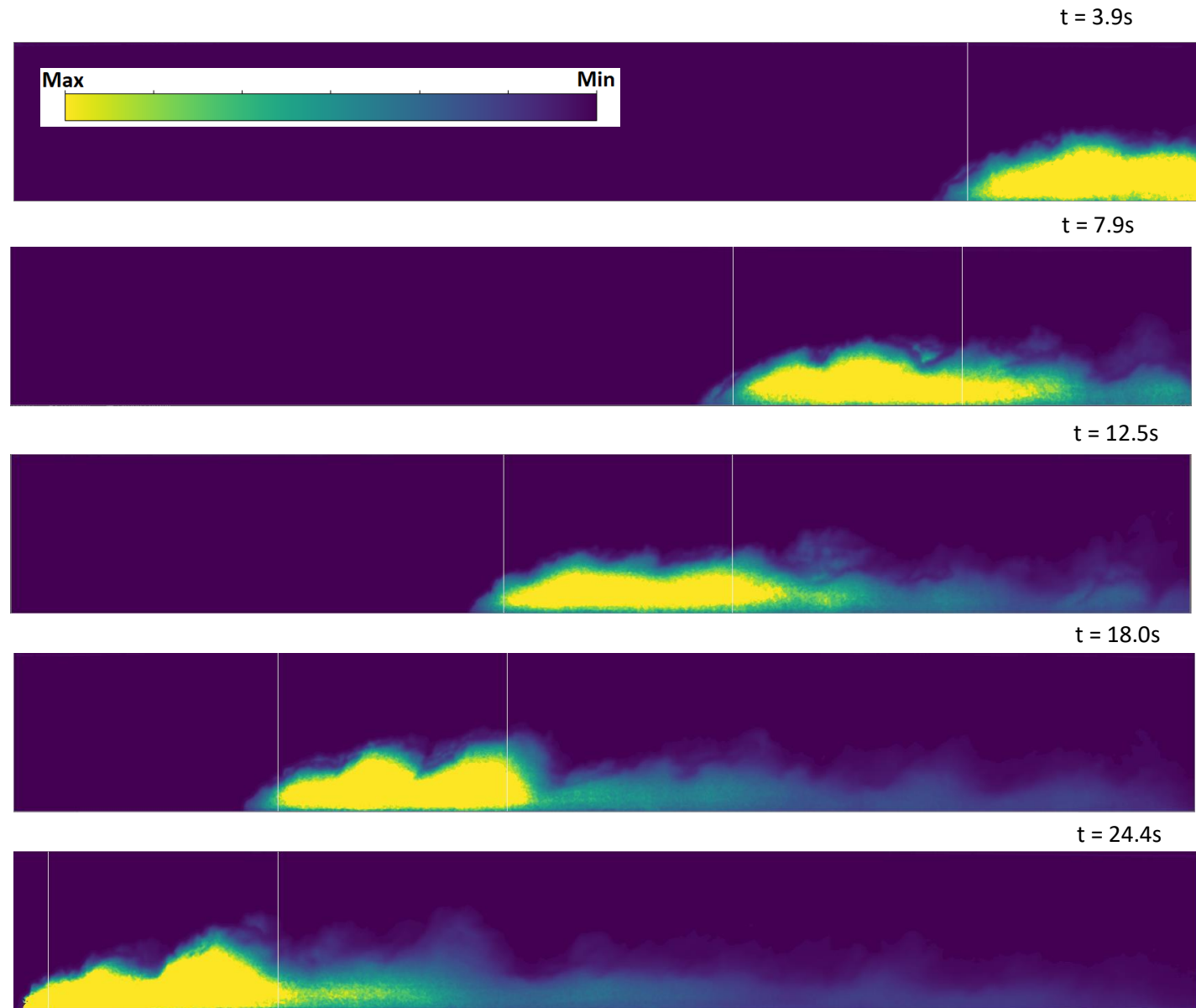


Figure C.15 Color map for the combined sediment type I and II with 2.5% initial concentration

4 – 125 μ m sediment
3.0%

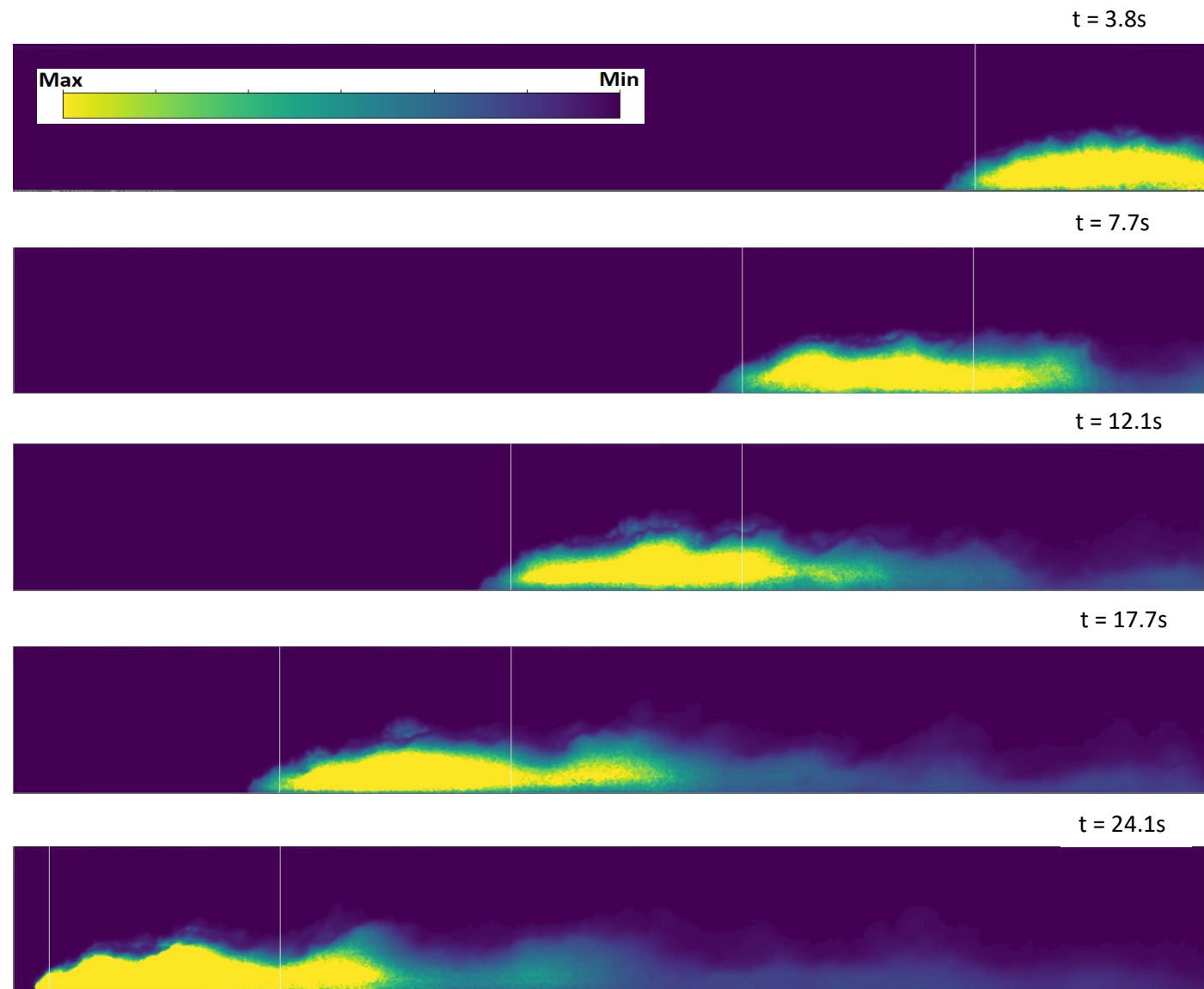
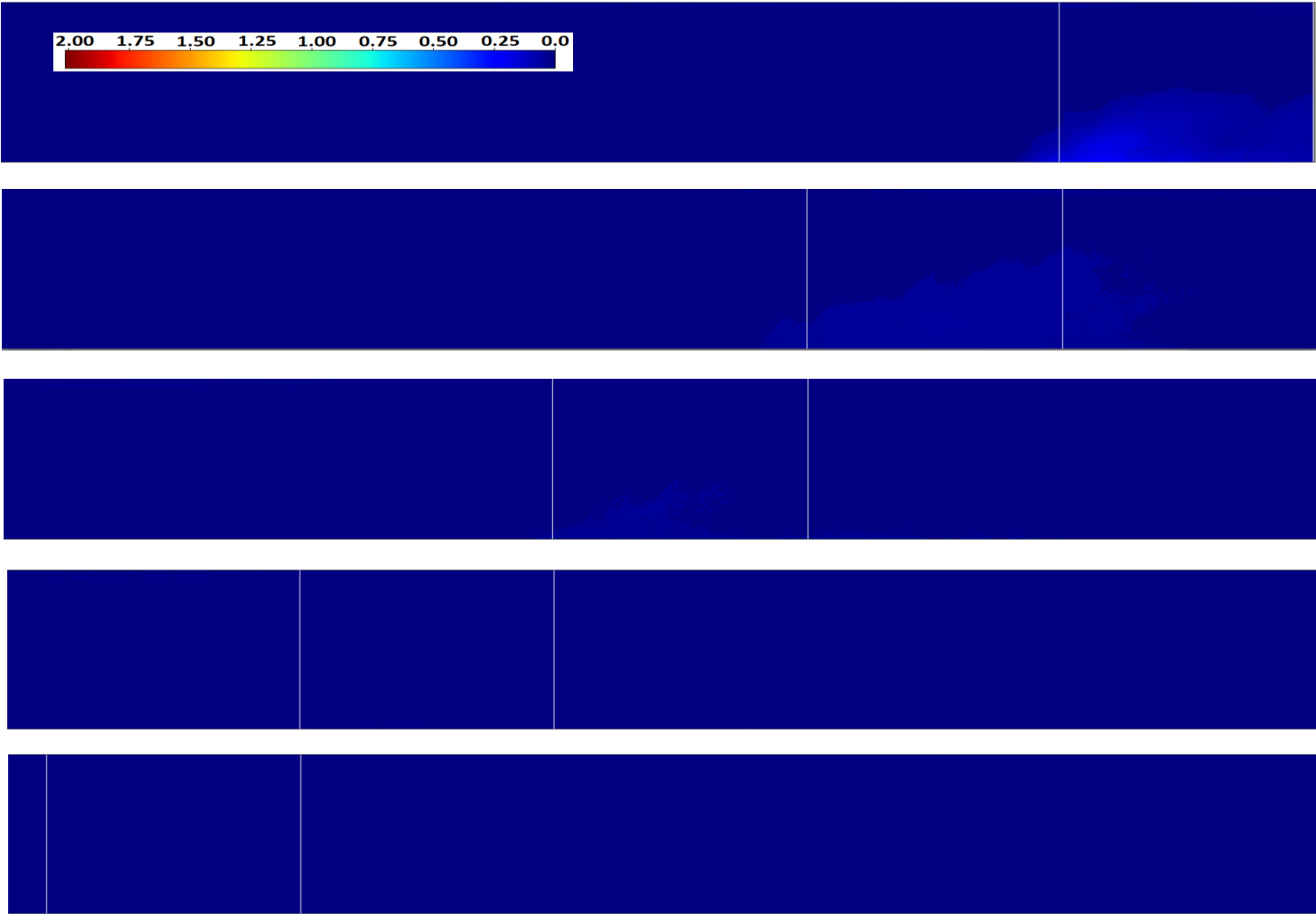


Figure C.16 Color map for the combined sediment type I and II with 3.0% initial concentration

Sediment type I (75–125 μ m):

75 – 125 μ m sediment
0.5%



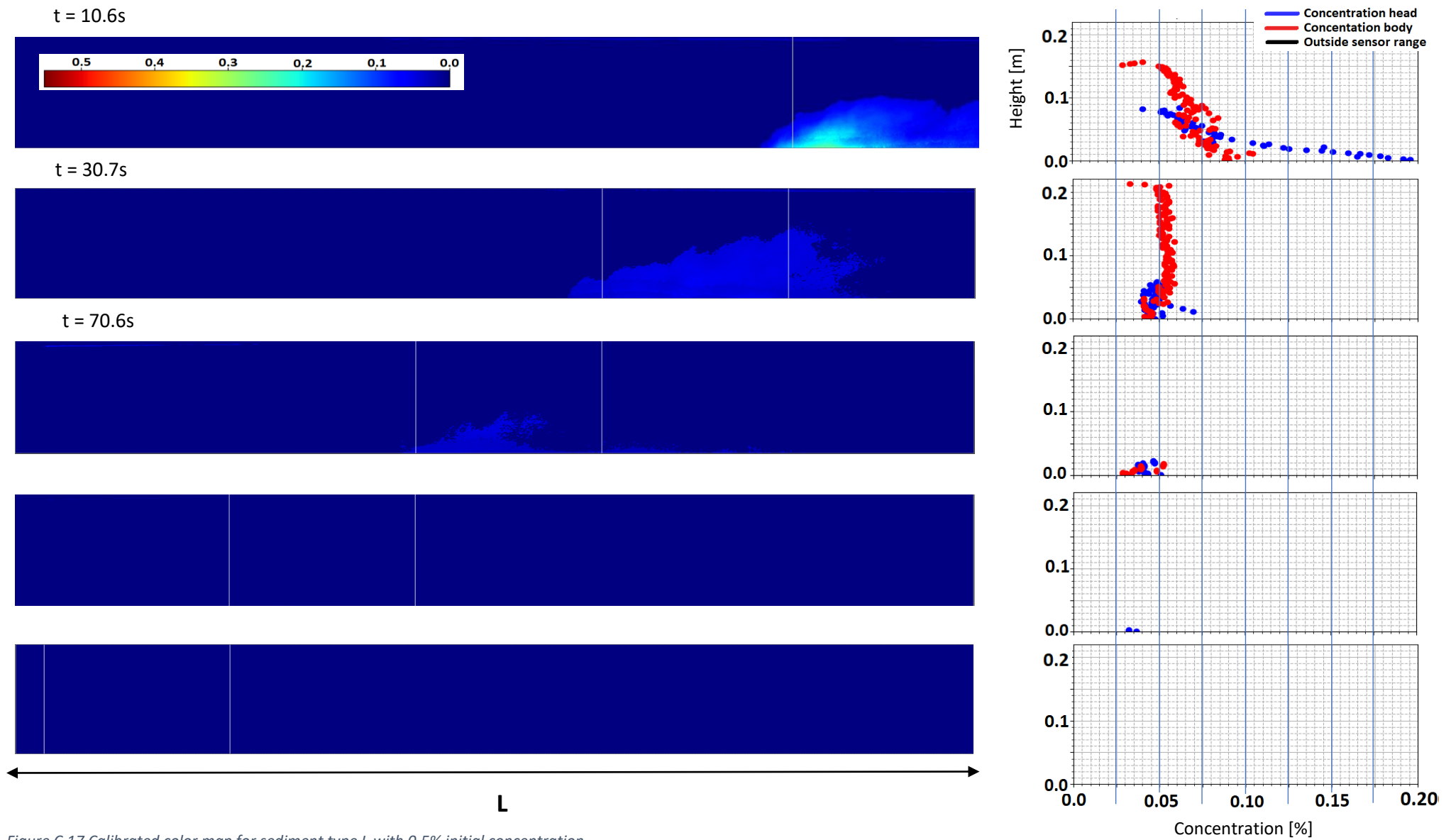
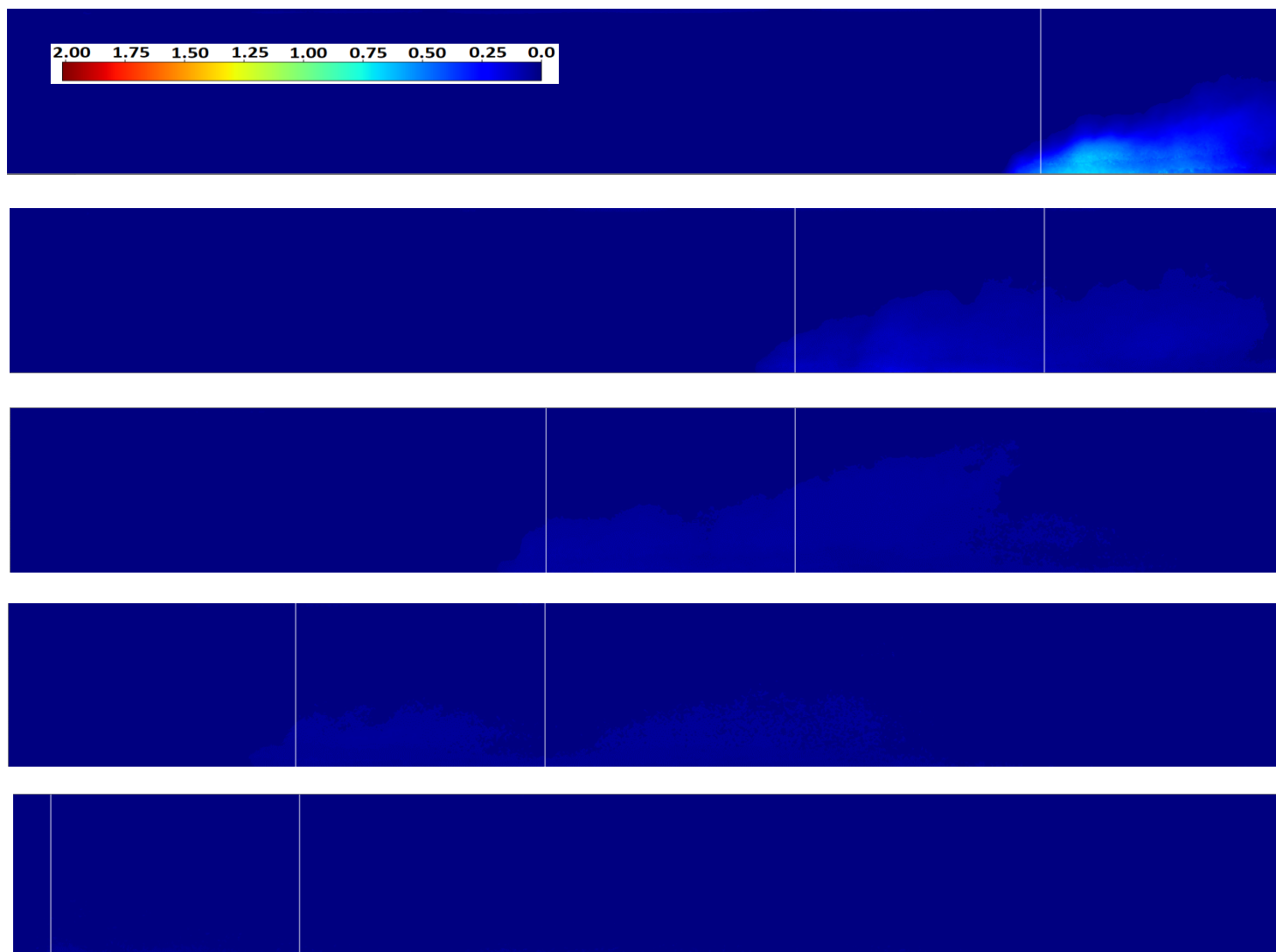


Figure C.17 Calibrated color map for sediment type I with 0.5% initial concentration

75 – 125 μm sediment
1.0%



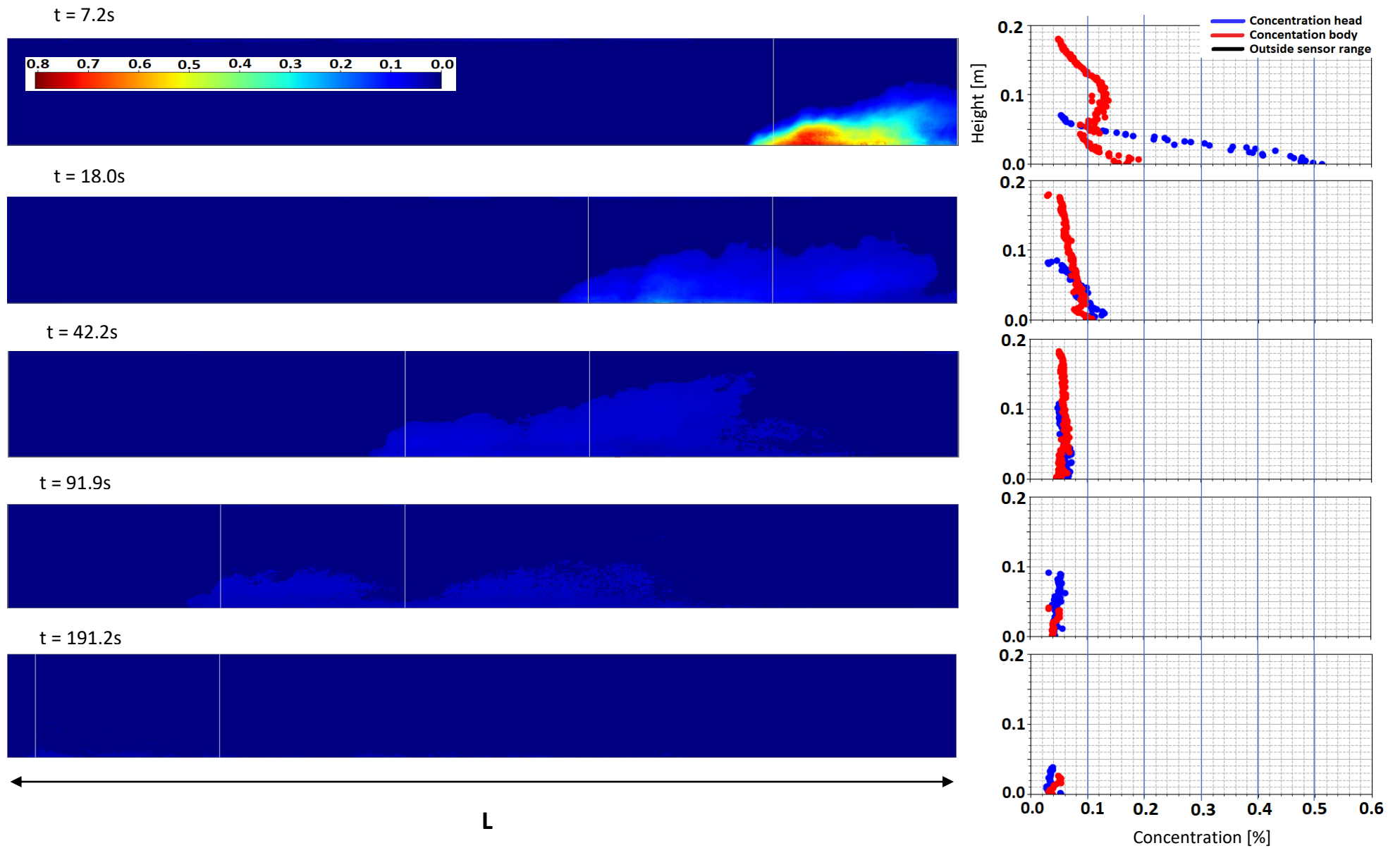


Figure C.18 Calibrated color map for sediment type I with 1.0% initial concentration

75 – 125 μm sediment
1.5%

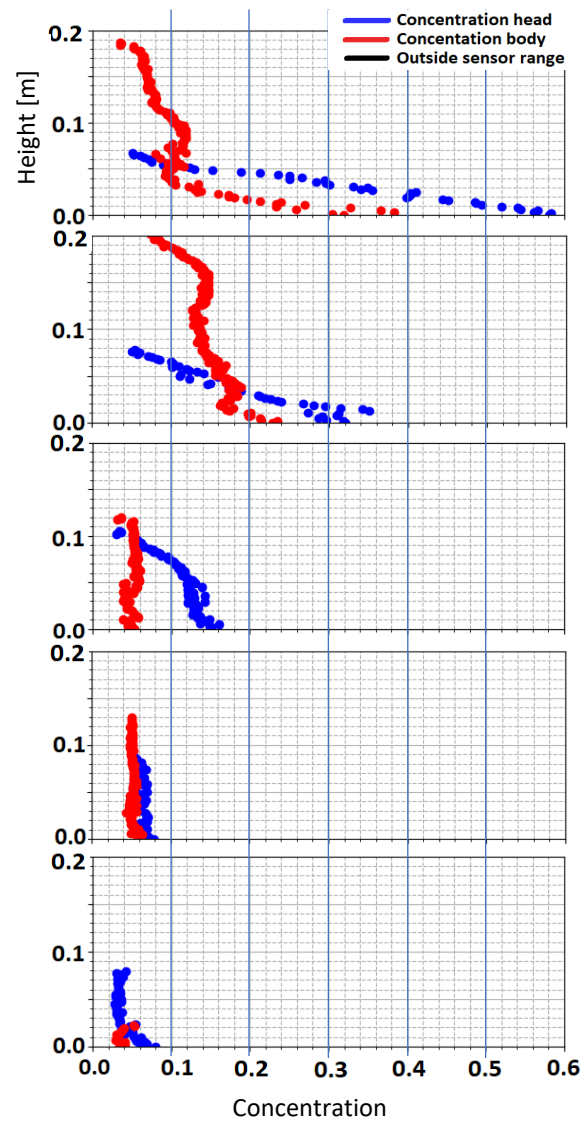
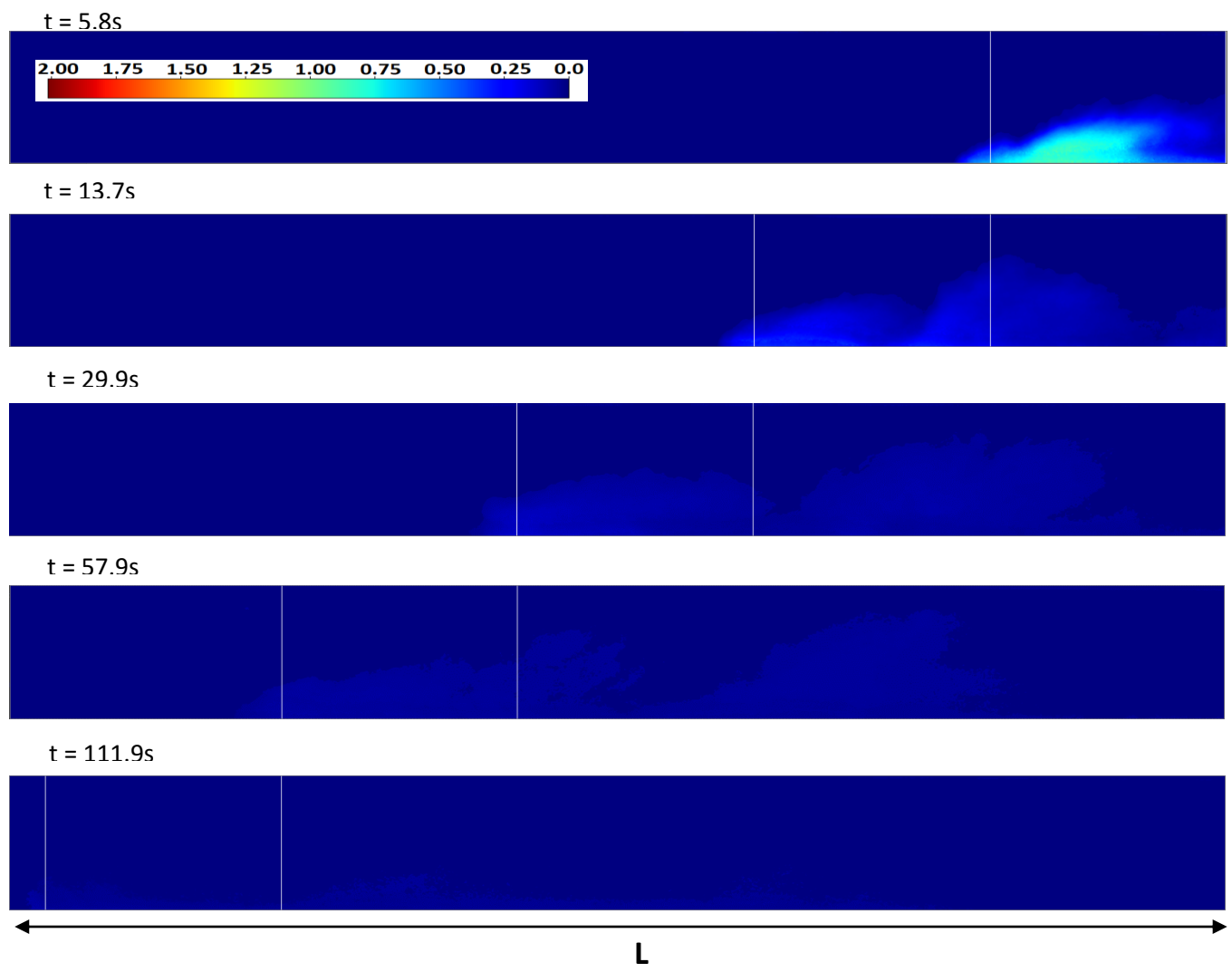


Figure C.19 Calibrated color map for sediment type I with 1.5% initial concentration

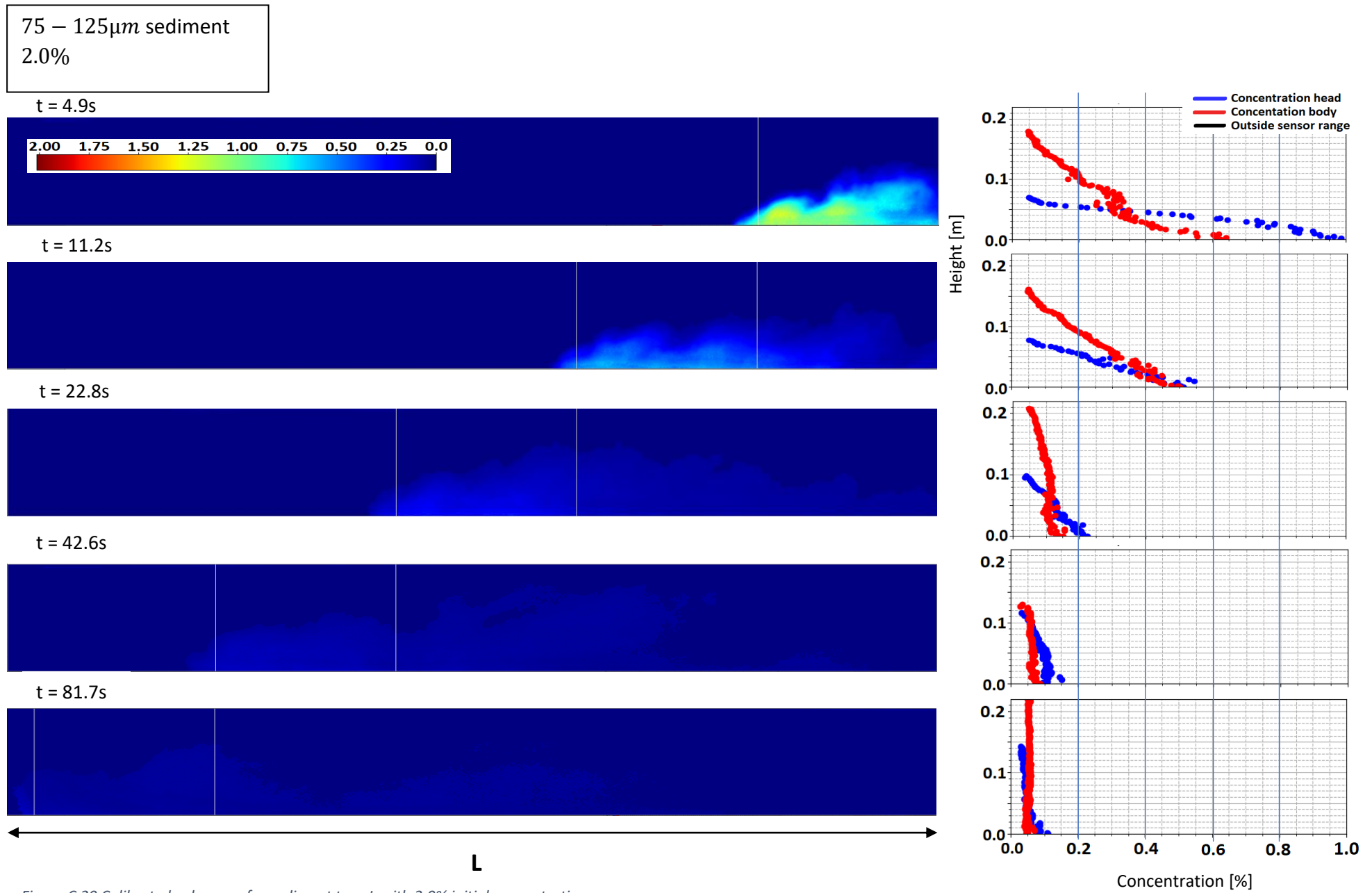


Figure C.20 Calibrated color map for sediment type I with 2.0% initial concentration

75 – 125 μm sediment
2.5%

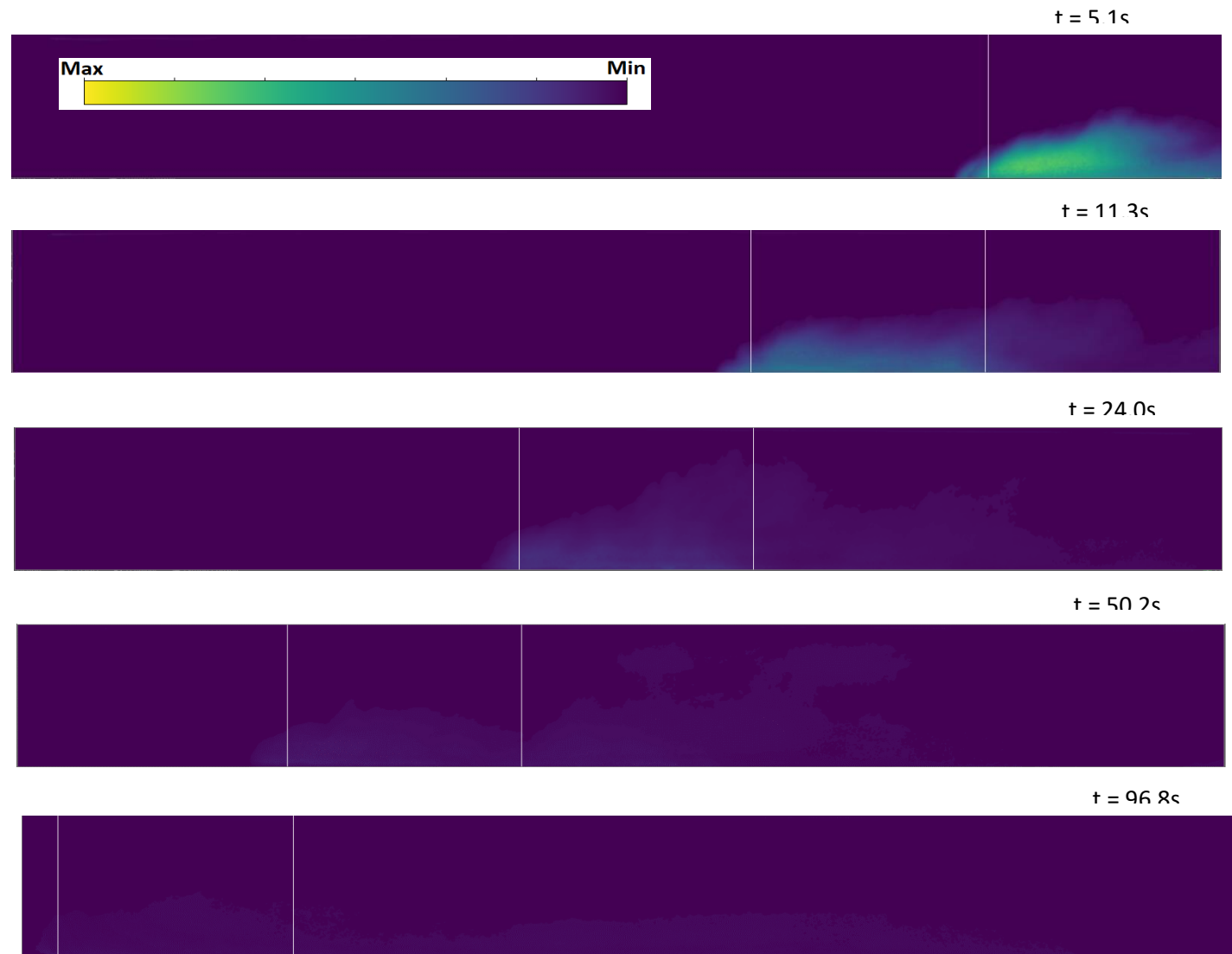


Figure C.21 Color map for sediment type I with 2.5% initial concentration

75 – 125 μm sediment
3.0%

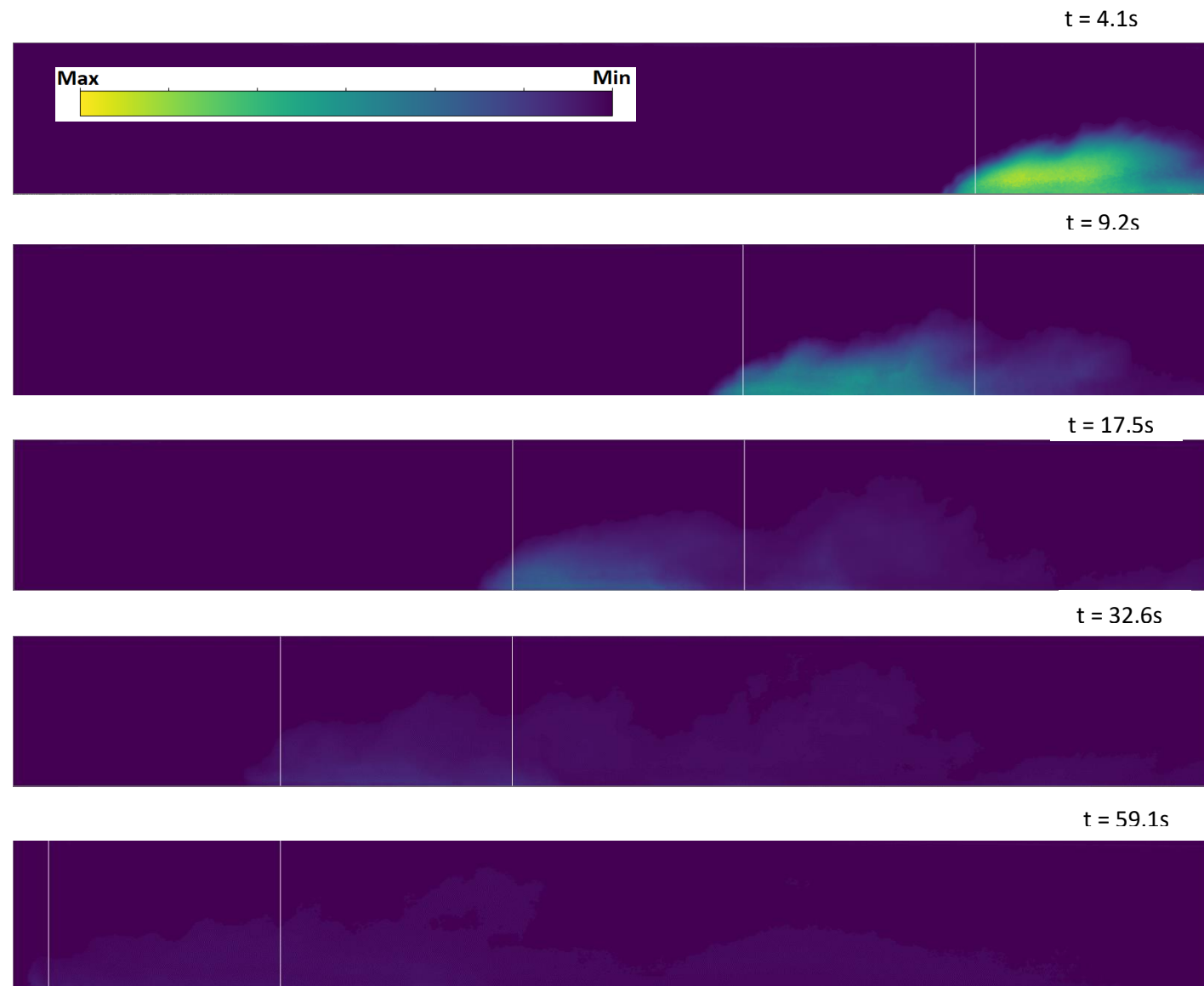


Figure C.22 Color map for sediment type I with 3.0% initial concentration

D. Fourth Appendix: Concentration profiles:

Sediment type I ($75 - 125\mu\text{m}$) :

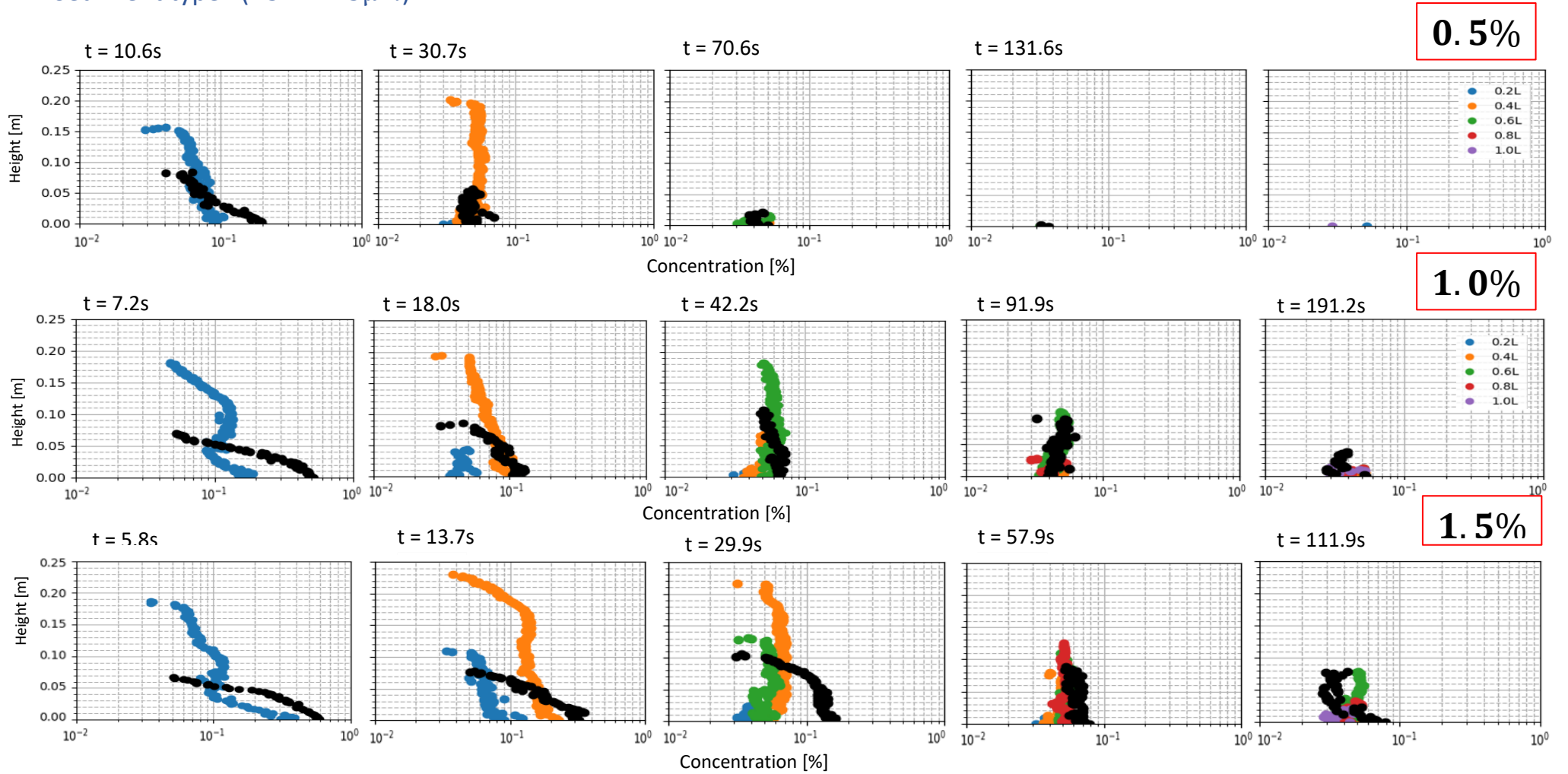


Figure D.1 Vertical concentration profiles for sediment type I, initial concentrations of: 0.5%, 1.0% and 1.5%

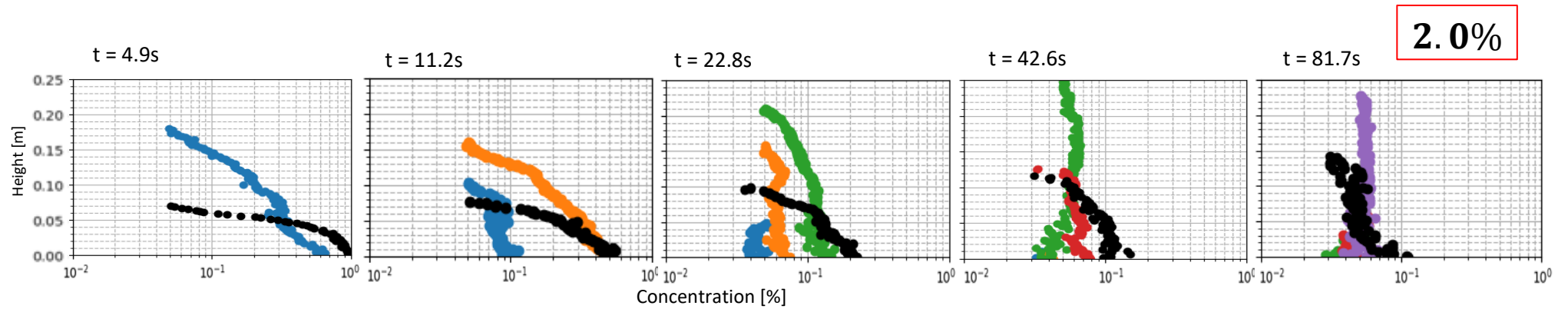


Figure D.2 Vertical concentration profiles for sediment type I, initial concentration of: 2.0%

Sediment type II ($4 - 60\mu m$) :

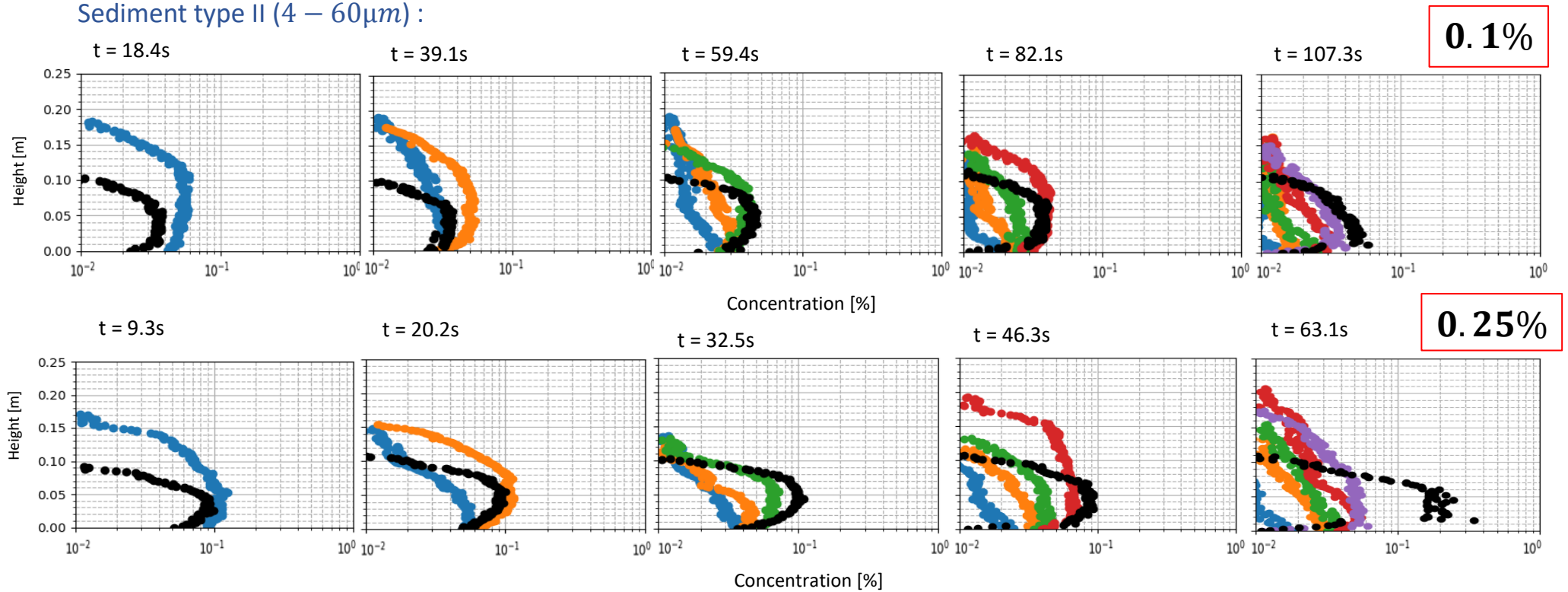


Figure D.3 Vertical concentration profiles for sediment type II, initial concentration of: 0.1%, 0.25%

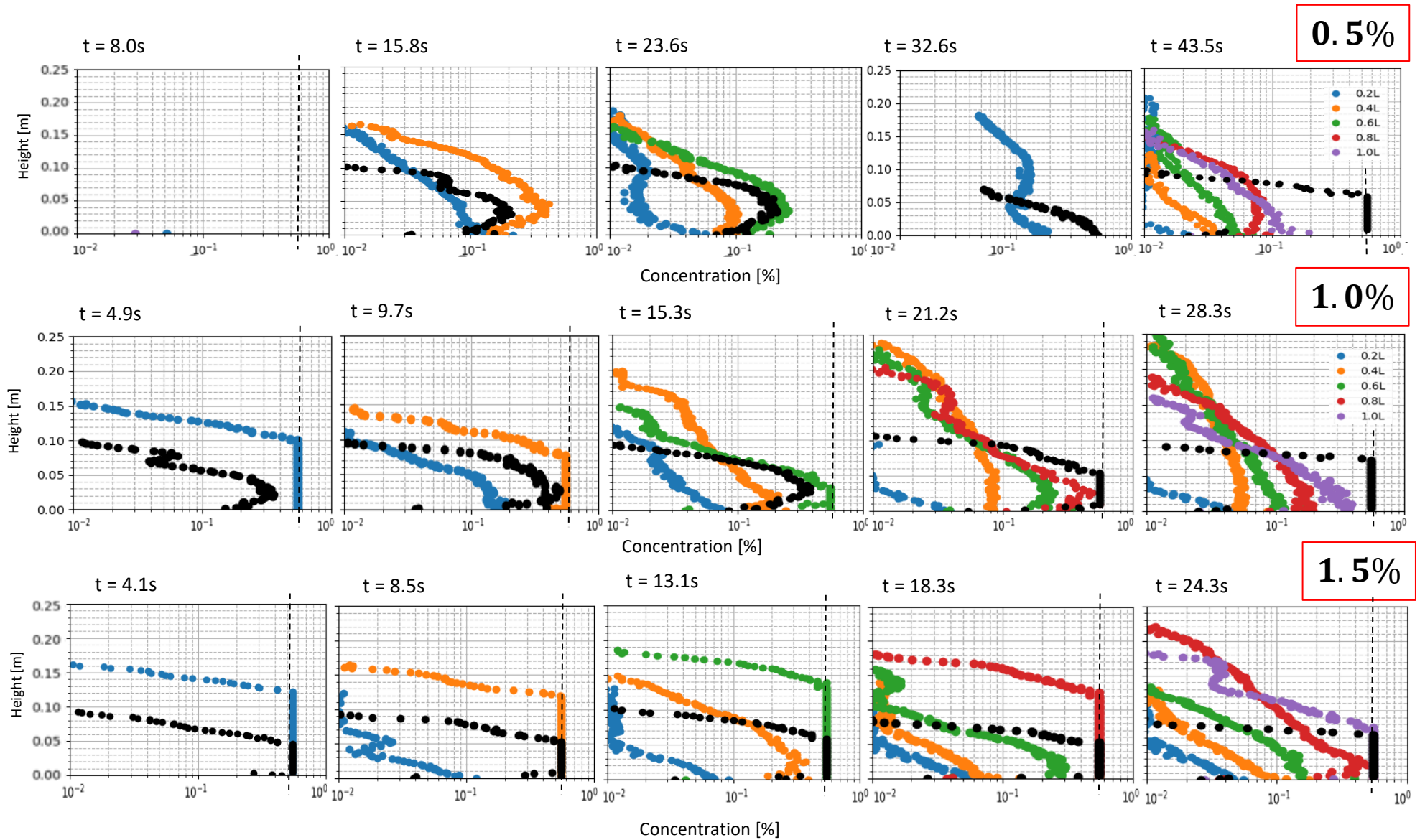


Figure D.4 Vertical concentration profiles for sediment type II, initial concentration of: 0.5%, 1.0% and 1.5%

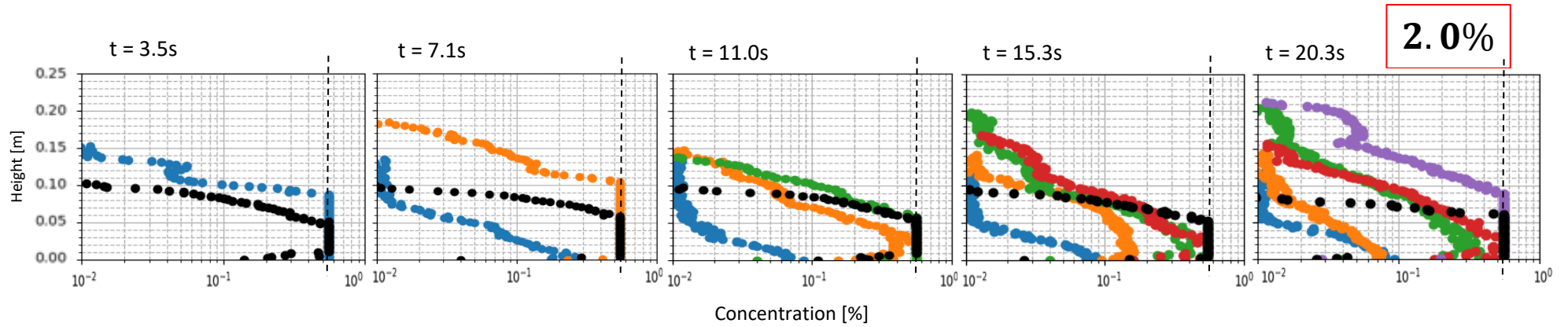


Figure D.5 Vertical concentration profiles for sediment type II, initial concentration of: 2.0%

Combined sediment type I and II (4 – 125 μm):

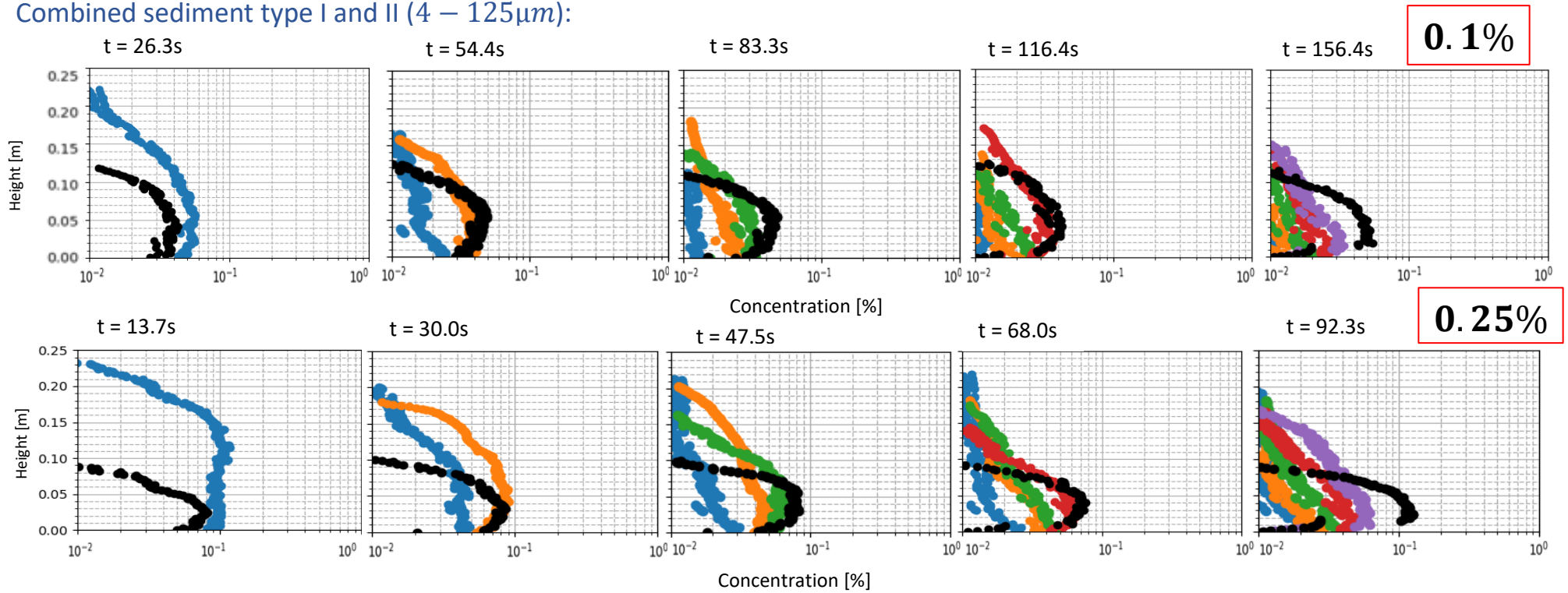


Figure D.6 Vertical concentration profiles for combined sediment type I and II, initial concentration of: 0.1% and 0.25%

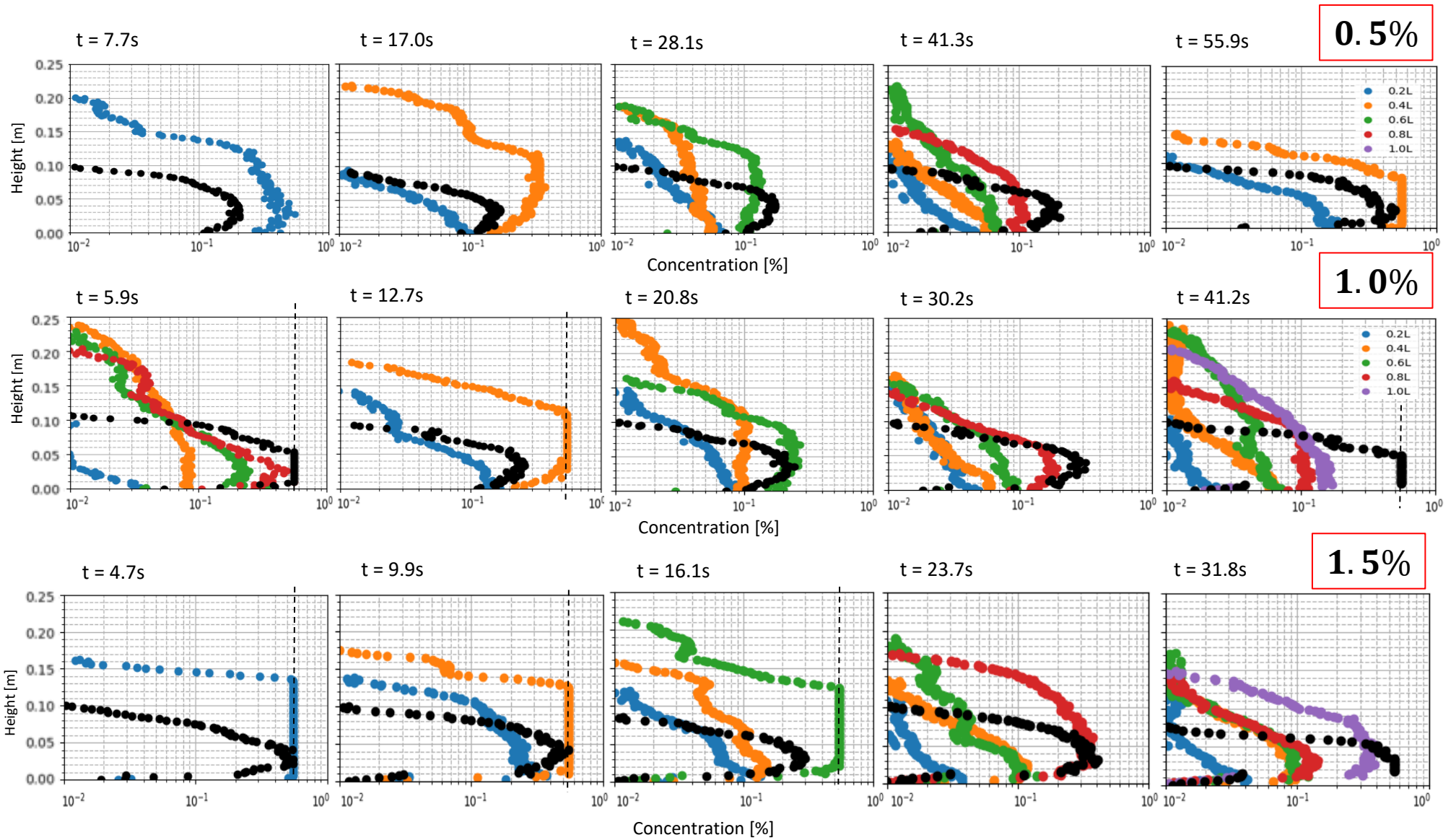


Figure D.7 Vertical concentration profiles for combined sediment type I and II, initial concentration of: 0.5%, 1.0% and 1.5%

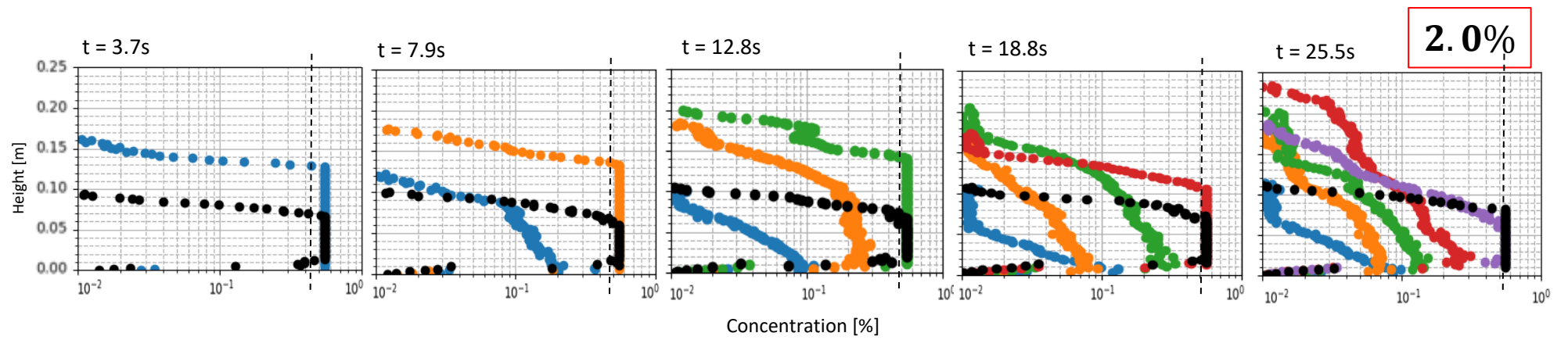
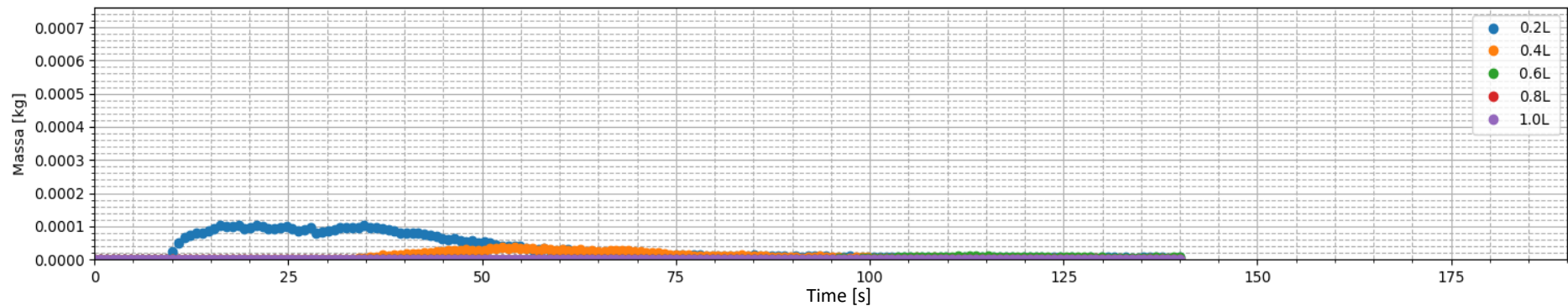


Figure D.8 Vertical concentration profiles for combined sediment type I and II, initial concentration of: 2.0%

E. Fifth Appendix: Mass over time graphs

Sediment type I ($75-125\mu m$) :

Mass over time for 0.5%, 75-125micro



Mass over time for 1.0%, 75-125micro

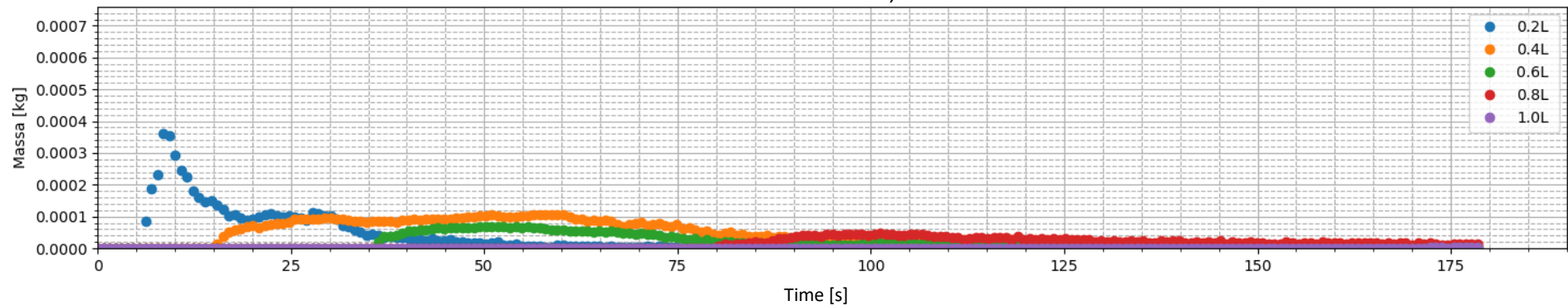


Figure E.1 Mass over time measured at 5 different sections of the tank for sediment type I, initial concentrations: 0.5% and 1.0%

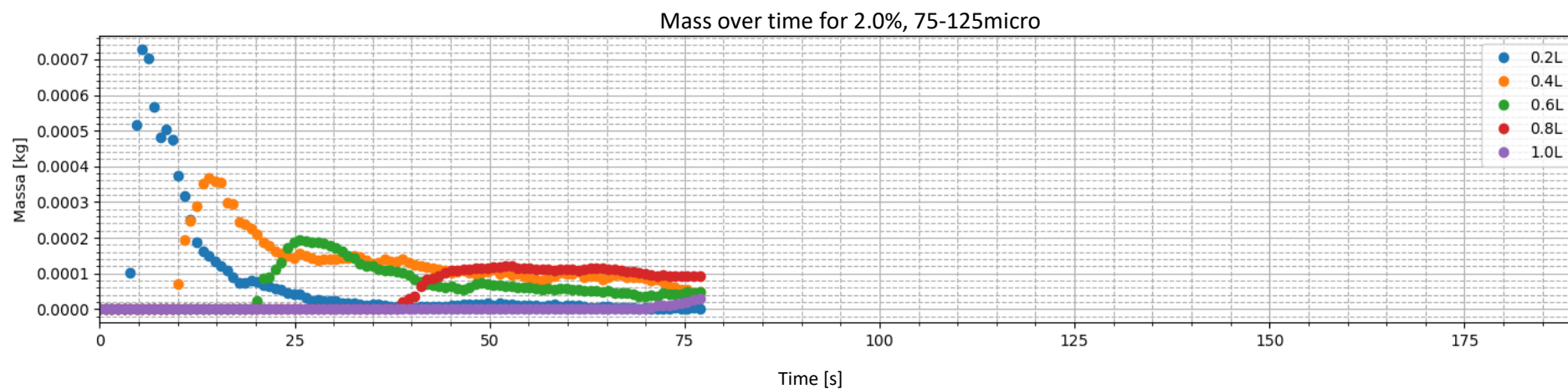
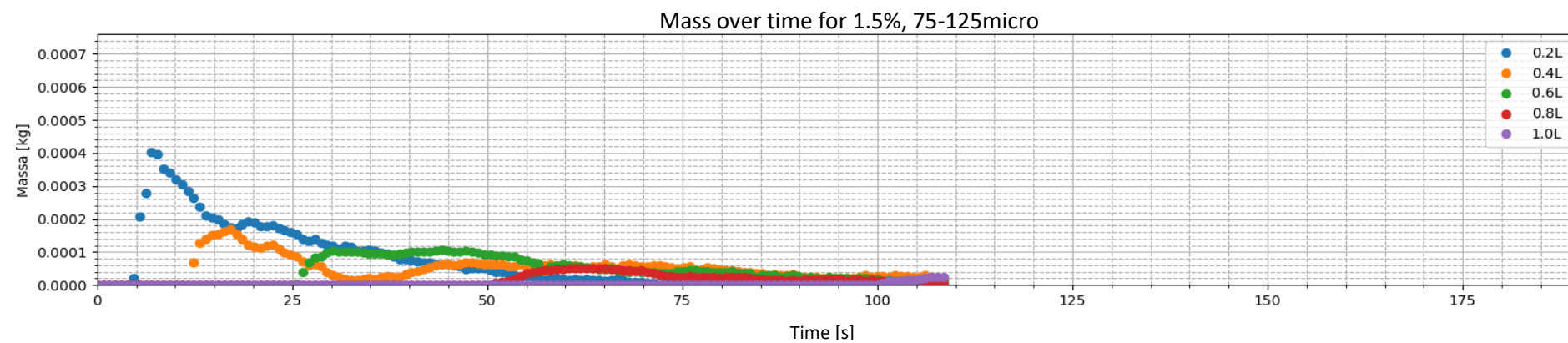
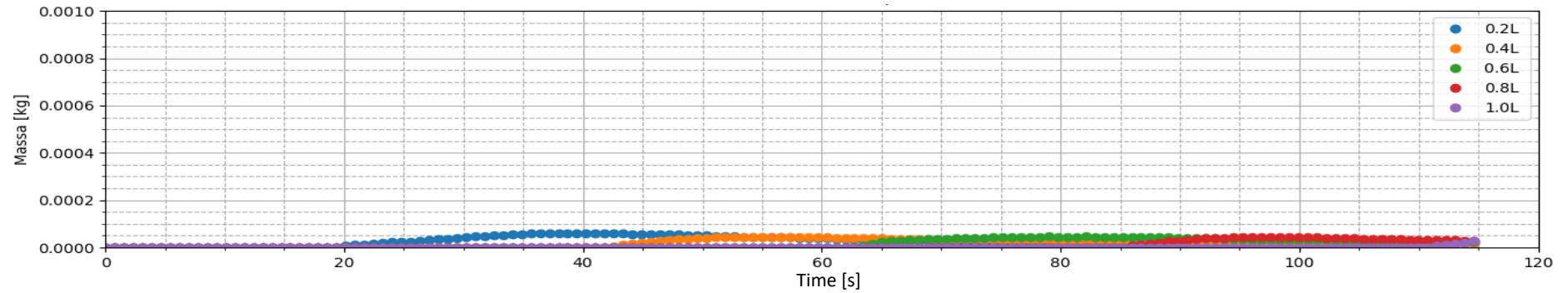


Figure E.2 Mass over time measured at 5 different sections of the tank for sediment type I, initial concentrations: 1.5% and 2.0%

Sediment type II ($4 - 60\mu m$) :

Mass over time for 0.1%, 4-60micro



Mass over time for 0.25%, 4-60micro

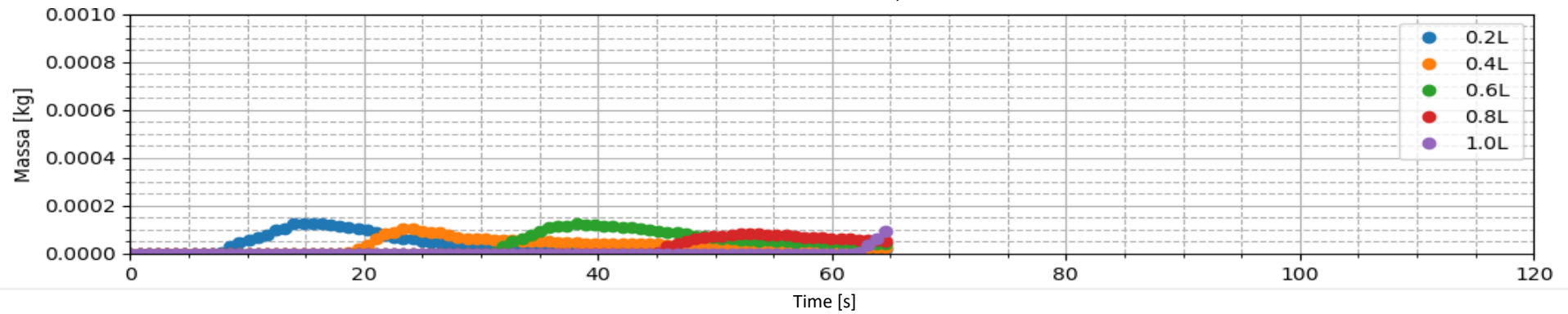


Figure E.3 Mass over time measured at 5 different sections of the tank for sediment type II, initial concentration: 0.1% and 0.25%

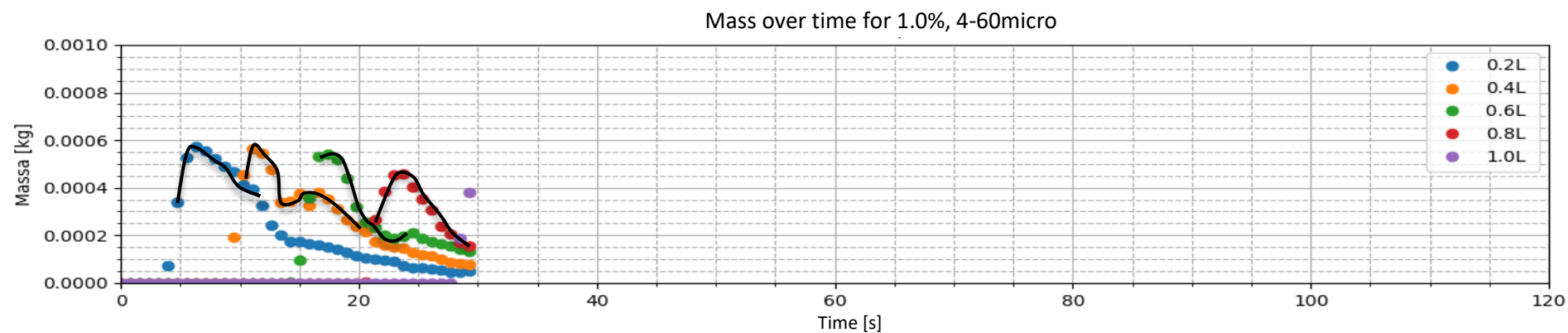
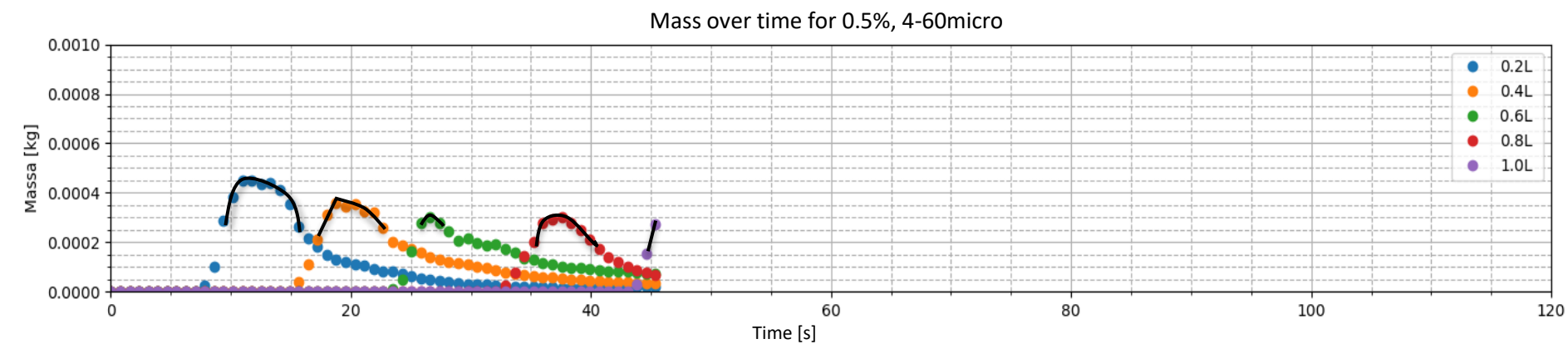


Figure E.4 Mass over time measured at 5 different sections of the tank for sediment type II, initial concentration: 0.5% and 1.0%

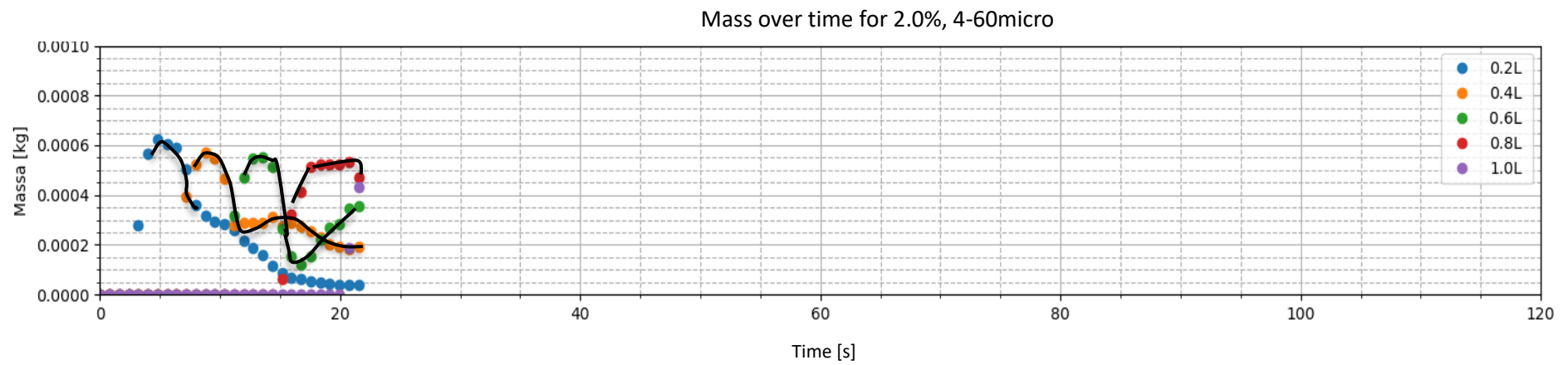
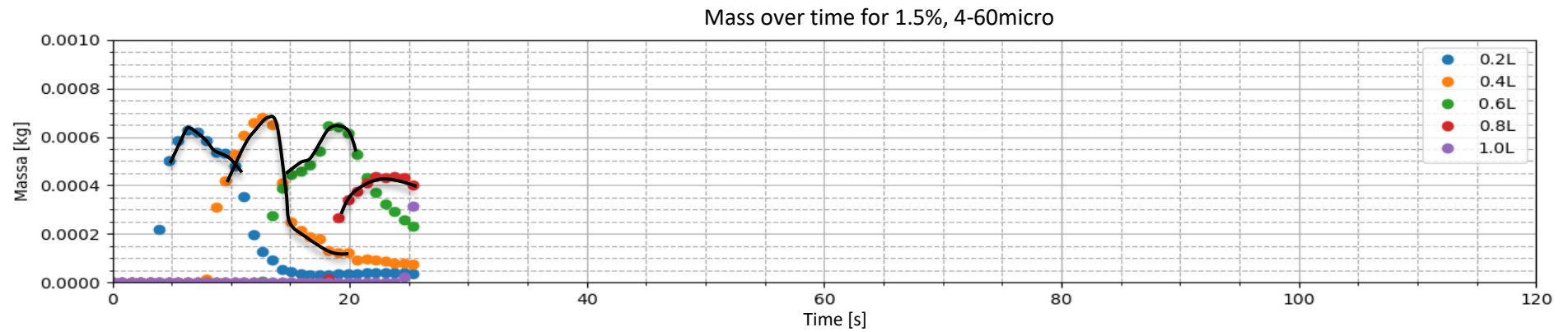


Figure E.5 Mass over time measured at 5 different sections of the tank for sediment type II, initial concentration: 1.5% and 2.0%

Combined sediment type I and II (4 – 125 μ m):

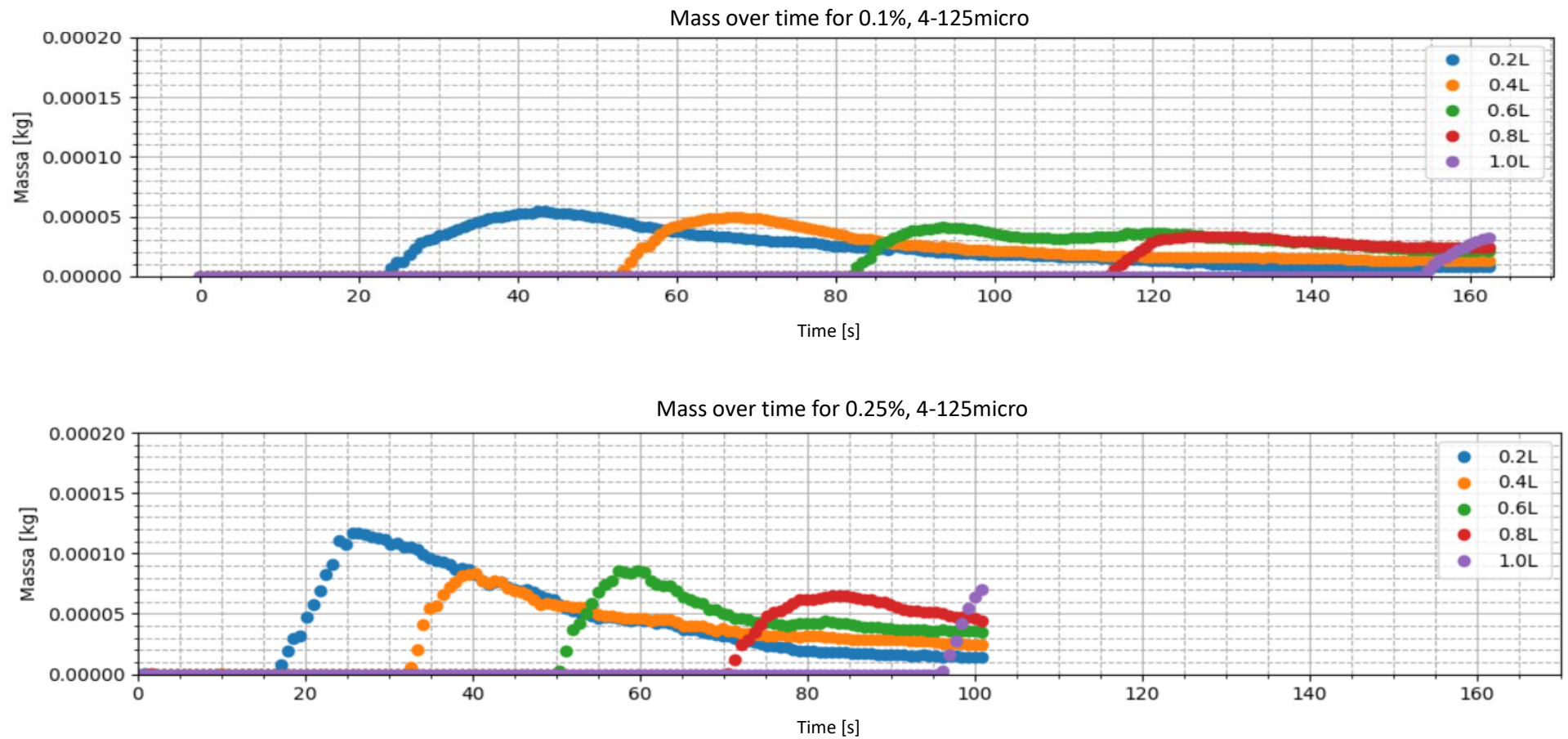


Figure E.6 Mass over time measured at 5 different sections of the tank for combined sediment type I and II, initial concentration: 0.1% and 0.25%

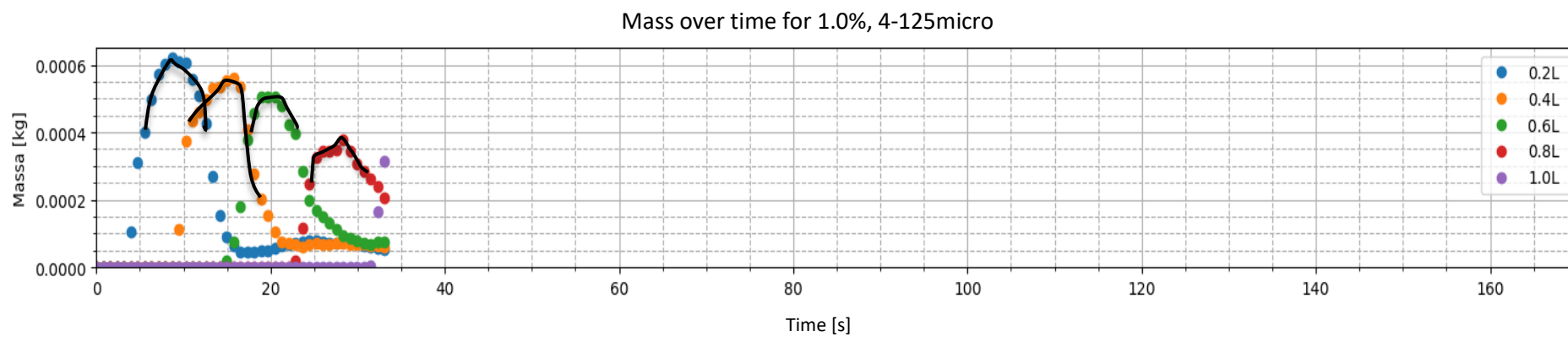
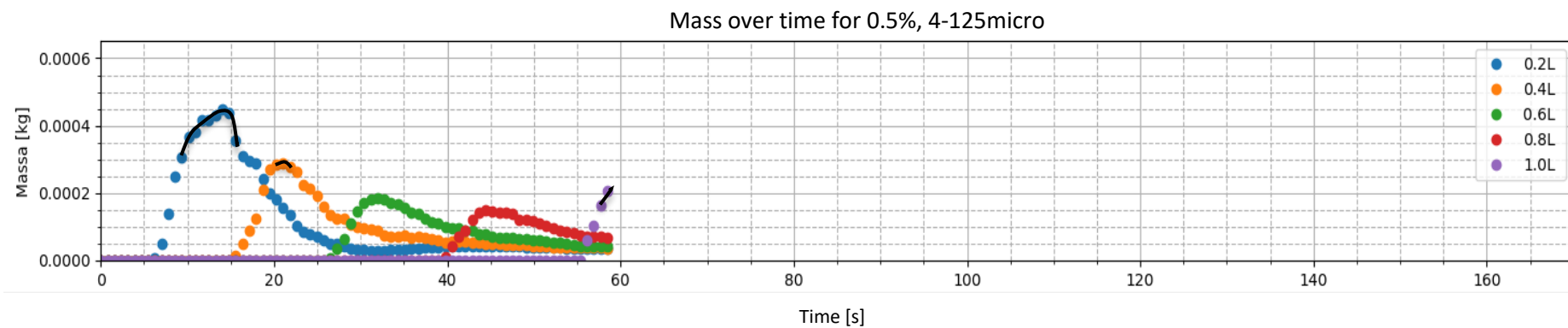


Figure E.7 Mass over time measured at 5 different sections of the tank for combined sediment type I and II, initial concentration: 0.5% and 1.0%

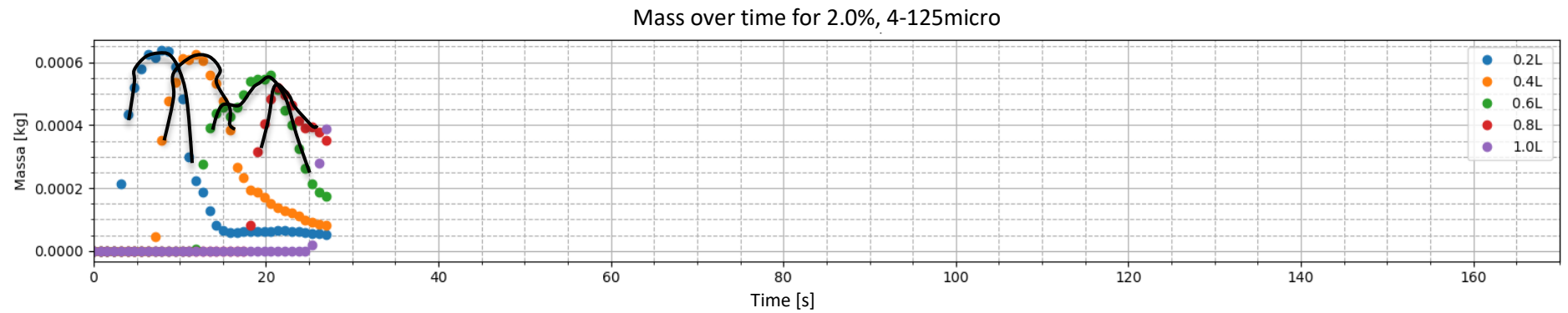
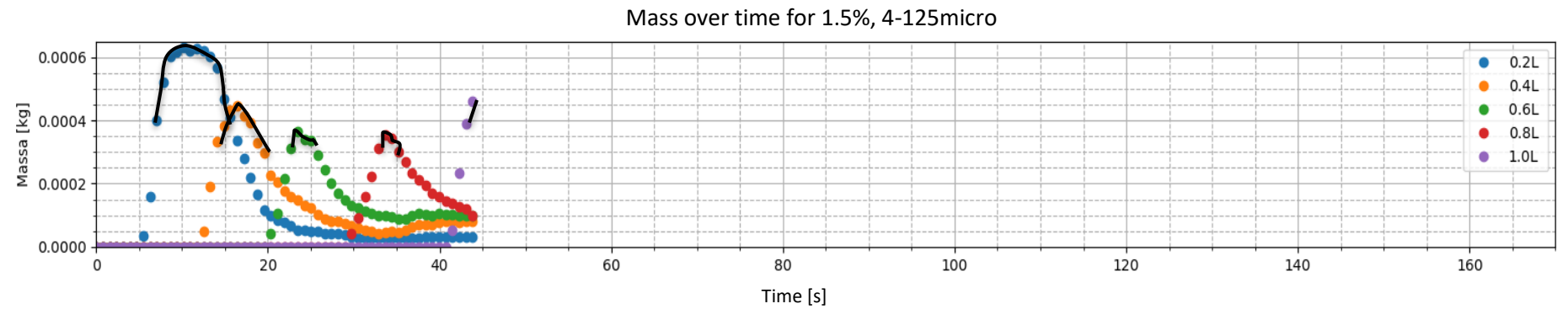


Figure E.8 Mass over time measured at 5 different sections of the tank for combined sediment type I and II, initial concentration: 1.5% and 2.0%

F. Sixth Appendix: Logbook of experiments

Experiment performed	Date	Location	Comments
Sediment type I – 0.5%	20-03-2020	Laboratory TU Delft	10 °C, light clouded sky
Sediment type I – 1.0%	20-03-2020	Laboratory TU Delft	10 °C, light clouded sky
Sediment type I – 1.5%	20-03-2020	Laboratory TU Delft	10 °C, light clouded sky
Sediment type I – 2.0%	20-03-2020	Laboratory TU Delft	10 °C, light clouded sky
Sediment type I – 2.5%	30-03-2020	Laboratory TU Delft	7 °C, cloudless sky
Sediment type I – 3.0%	30-03-2020	Laboratory TU Delft	7 °C, cloudless sky
Calibration Sediment type I	20-03-2020	Laboratory TU Delft	10 °C, light clouded sky
Sediment type II – 0.1%	27-03-2020	Laboratory TU Delft	12 °C, light clouded sky
Sediment type II – 0.25%	27-03-2020	Laboratory TU Delft	12 °C, light clouded sky
Sediment type II – 0.5%	19-03-2020	Laboratory TU Delft	11 °C, light clouded sky
Sediment type II – 1.0%	19-03-2020	Laboratory TU Delft	11 °C, light clouded sky
Sediment type II – 1.5%	19-03-2020	Laboratory TU Delft	11 °C, light clouded sky
Sediment type II – 2.0%	19-03-2020	Laboratory TU Delft	11 °C, light clouded sky
Sediment type II – 2.5%	19-03-2020	Laboratory TU Delft	11 °C, light clouded sky
Sediment type II – 3.0%	19-03-2020	Laboratory TU Delft	11 °C, light clouded sky
Sediment type II – 2.5%	30-03-2020	Laboratory TU Delft	7 °C, cloudless sky
Sediment type II – 3.0%	30-03-2020	Laboratory TU Delft	7 °C, cloudless sky
Calibration Sediment type II	27-03-2020	Laboratory TU Delft	12 °C, light clouded sky
Sediment type I and type II – 0.1%	27-03-2020	Laboratory TU Delft	12 °C, light clouded sky
Sediment type I and type II – 0.25%	27-03-2020	Laboratory TU Delft	12 °C, light clouded sky
Sediment type I and type II – 0.5%	20-03-2020	Laboratory TU Delft	10 °C, light clouded sky
Sediment type I and type II – 1.0%	20-03-2020	Laboratory TU Delft	10 °C, light clouded sky
Sediment type I and type II – 1.5%	20-03-2020	Laboratory TU Delft	10 °C, light clouded sky
Sediment type I and type II – 2.0%	20-03-2020	Laboratory TU Delft	10 °C, light clouded sky
Sediment type I and type II – 2.5%	30-03-2020	Laboratory TU Delft	7 °C, cloudless sky
Sediment type I and type II – 3.0%	30-03-2020	Laboratory TU Delft	7 °C, cloudless sky
Calibration sediment type I and type II	27-03-2020	Laboratory TU Delft	12 °C, light clouded sky

G. Seventh Appendix: Python code

G.1. Measuring of the head velocity in time:

```
G.1.    import sys # package
import cv2 # package
import matplotlib.pyplot as plt # matplotlib in python
import numpy as np

START_FRAME = 350

print("Playing video:", sys.argv[1]) # stuk text weergeven
stream = cv2.VideoCapture(sys.argv[1]) # open je de video
stream.set(cv2.CAP_PROP_POS_FRAMES, START_FRAME)

bg = None # Reference to first frame

# Settings
interval = 30

# active_line = None
frame_counter = 0
last_frame_number = 0

s_per_frame = 1 / 130 # FPS = 130
dT = interval * s_per_frame

m_per_pixel = 2.83 / 1840 # in meter / pixel
m_per_pixel_v = 0.35 / 230 # in meter / pixel

# Initialize result lists
velocities = list()
distances = list()
heights = list()

last_position = None

while stream.isOpened():
```

```

ret, frame = stream.read() # capture frame by frame video
frame_counter = frame_counter + 1

if ret:
    cv2.imshow("Original video", frame)

    # Convert to greyscale
    frame = cv2.cvtColor(frame, cv2.COLOR_BGR2GRAY)

    # Crop section from tank
    cropped = frame[180:390, 30:1730]

    # Store reference to background
    if bg is None:
        bg = cropped

    # Subtract current frame from background
    subtracted = cv2.subtract(bg, cropped)

    # Define a threshold for converting to black-and-white, 128 is the middle of black and white in grey scale
    thresh = 25

    # assign blue channel to zeros
    ret, img_binary = cv2.threshold(subtracted, thresh, 255, cv2.THRESH_BINARY)

    img_height, img_width = img_binary.shape

    # Initialize the last known position of the wave
    if last_position is None:
        last_position = img_width

    # Perform measurement every {interval} frames
    if frame_counter % interval == 0:

        pixel_found = False

        # Iterate entire image to search for first pixel
        for col in range(0, img_width):

```

```

for i in range(0, img_height):

    pixel = img_binary[i, col]

    # Check if the current pixel is above the threshold
    if pixel > thresh:

        pixel_found = True

        print("Head of wave at: ", col)

        # Calculate traveled distance
        distance_in_pixels = last_position - col
        last_position = col

        traveled_distance = distance_in_pixels * m_per_pixel
        distances.append(traveled_distance)

        # Calculate velocity
        velocity = traveled_distance / dT
        velocities.append(velocity)

        # Calculate height
        for p in range(img_height):

            # Wait until head is far enough in the frame
            if (col + 50) < img_width:

                if img_binary[p, col + 50] > 128:
                    heights.append((290 - p) * m_per_pixel_v)
                    break

        break

    # Break loop to go to the next frame
    if pixel_found:
        break

# Show binary frame

```

```

cv2.imshow("binary image", img_binary)

# Show original frame
cv2.imshow("Gecorrigeerde video", subtracted)

# Show heat-map frame
cv2.imshow("Gekleurde video",
           cv2.applyColorMap(subtracted, cv2.COLORMAP_JET)) # From grey to JET color map

# Controls
key = cv2.waitKey(1)
if key == ord('q'):
    break
if key == ord('p'):
    cv2.waitKey(-1)

# Print all results
print(velocities)
print(heights)
print(distances)

# Plot velocity and height over time
plt.plot(np.linspace(0, len(velocities) * dT, num=len(velocities)), velocities)
plt.plot(np.linspace(0, len(heights) * dT, num=len(heights)), heights)
plt.minorticks_on()
plt.grid(b=True, which='major', linestyle='-')
plt.grid(b=True, which='minor', linestyle='--')
plt.ylabel('Velocity [m/s]')
plt.xlabel("Time [s]")
plt.title("Velocity over time")

# Show plots and wait
plt.show()

# Write results to CSV for later processing
np.savetxt("C:/Users/Andrea/Documents/Master Offshore/Afstuderen/Python/resultaten/velocity_t/15_70_micro_0.1p.csv",
           velocities)

```

```
# Destroy windows and exit program
stream.release()

cv2.destroyAllWindows()
```

G.2. Digital filter used for results:

```
G.2. from scipy import signal
import math

def cheby_bandstop_filter(data, lowcut, highcut, fs):
    nyq = 0.5 * fs
    low = lowcut / nyq
    high = highcut / nyq

    FILTER_ORDER = 6
    FILTER_ATTENUATION = 100

    filter_values = signal.cheby2(FILTER_ORDER, FILTER_ATTENUATION, (low, high), btype='bandstop', output='ba', fs=fs)
    filtered = signal.filtfilt(filter_values[0], filter_values[1], data)

    return filtered
```

G.3. Calibration table per sediment type

```
G.3. import glob

import cv2 # OpenCV
import matplotlib.pyplot as plt # matplotlib in python
import numpy as np # Numpy

folder_with_images = "figures/Cal_15-70micro_correction"

# Read all images in directory
imageList = glob.glob(folder_with_images+'/*.png')
```

```

# Initialize variables
table = None
k = 0
aantal_plaatjes = len(imageList)
concentrations = []

# Sort images by name to ensure correct concentration order
imageList.sort()

# Save all pixels in large table
for imgPath in imageList:
    print(f"Processing image {imgPath}")

    # Read image from disk
    image = cv2.imread(imgPath, 0)[18:, :]
    rows, cols = image.shape

    # Extract concentration from name and store
    concentrations.append(float(imgPath.split("/")[-1][:-5]))

    # Initialize calibration table
    if table is None:
        table = np.zeros((rows * cols, aantal_plaatjes), dtype=np.uint8)

    # Apply 3x3 Gaussian blur to filter out noise
    imageBlurred = cv2.GaussianBlur(image, (3, 3), cv2.BORDER_DEFAULT)

    # Convert image to 1d
    for i in range(rows):
        for j in range(cols):
            table[(i * cols) + j][k] = imageBlurred[i, j]

    k = k + 1

# Calculate sum of all K values
# K[n] indicates how often this row has been added
means = np.zeros((256, aantal_plaatjes + 1), dtype=np.int)
for row in table:

```

```

# Filter out rows that are not decreasing in value
if row[1] >= row[2] >= row[3] >= row[4]:
    means[row[0]][aantal_plaatjes] = means[row[0]][aantal_plaatjes] + 1

    means[row[0]][0] = row[0] # K0

    for i in range(1, aantal_plaatjes):
        means[row[0]][i] = means[row[0]][i] + row[i] # Sum K1

# Calculate mean K values by dividing by number of additions
results = np.zeros((256, aantal_plaatjes), dtype=np.float)
for row in means:

    if row[0] > 0:

        results[row[0]][0] = row[0]

        for i in range(1, aantal_plaatjes):
            results[row[0]][i] = row[i] / row[aantal_plaatjes]

# Write results to csv file

# Copy over the concentrations as the first line of the csv as this row is usually unused
results[0] = concentrations

# Write all data to the CSV
np.savetxt("calibration_new_withGauss_15-70micro_correction.csv", results, delimiter=",")

# Plot line
plt.plot(concentrations, results[255])
plt.ylabel('Pixel value')
plt.xlabel("Concentration [%]")
plt.title("Pixel vs Concentration before and after applying a Gaussian filter")
plt.legend(['Before Gaussian blur', 'After Gaussian blur'])
plt.minorticks_on()
plt.grid(b=True, which='major', linestyle='-')

```



```
plt.grid(b=True, which='minor', linestyle='--')
plt.show()
```

G.4. Library used for the results

```
G.4. import numpy as np
from scipy.optimize import curve_fit
import cv2

# Formula to use for the fines and polydisperse:
def func(x, a, b, c):
    return x / ((a * np.power(x, 2)) - (b * x) + c)

# Formula to use for coarse:
def func_c(x, a, b):
    return a * np.exp(-b * x)

# Convert calibration matrix into [a, b, c] for func and to [a, b] for func_c
def build_table(matrix, sediment_type):
    table = []
    if sediment_type == "poly and fine":
        table.append([0, 0, 0])
        for row in matrix[1:]:
            weights, pcov = curve_fit(func, row, [0.0, 0.01, 0.02, 0.03, 0.04, 0.05, 0.06, 0.07, 0.08, 0.09, 0.1, 0.15, 0.2,
0.25, 0.3, 0.35, 0.4, 0.45, 0.5], bounds=([0.0, 0.0, 0.0], [2, 80.0, 2000.0]))
            table.append(weights)

    if sediment_type == "coarse":
        table.append([0, 0])
        for row in matrix[1:]:
            weights, pcov = curve_fit(func_c, row, [0.0, 0.01, 0.02, 0.03, 0.04, 0.05, 0.07, 0.1, 0.15, 0.2, 0.25, 0.3,
0.35, 0.4, 0.45, 0.5, 0.6, 0.7, 0.8, 0.9, 1.0, 1.25, 1.5, 2.0], bounds=([0.0, 0.0], [10, 0.1]))
            table.append(weights)

    return table
```

```

# Convert pixel value to concentration
def pixel_to_concentration(pixel, orig_pixel, table, sediment_type):
    if sediment_type == "poly and fine":
        return func(pixel,
                    table[orig_pixel][0],
                    table[orig_pixel][1],
                    table[orig_pixel][2]
                    )

    if sediment_type == "coarse":
        return func_c(pixel,
                    table[orig_pixel][0],
                    table[orig_pixel][1]
                    )

# Convert grayscale image to density matrix
def image_to_density(frame, background, table, sediment_type, concentration_max, pixel_boundary):
    rows, cols = frame.shape

    result = np.zeros_like(frame, dtype=np.float)

    for row in range(0, rows):
        for col in range(0, cols):

            orig_pixel = background.item(row, col)
            wave_pixel = frame.item(row, col)

            intensity_difference = int(orig_pixel) - int(wave_pixel)

            if intensity_difference >= 10 and wave_pixel > pixel_boundary:
                pixel_concentration = pixel_to_concentration(wave_pixel, orig_pixel, table, sediment_type)

                if pixel_concentration >= concentration_max or pixel_concentration < 0:
                    pixel_concentration = concentration_max

```

```

        result.itemset(row, col, pixel_concentration)

    else:
        if wave_pixel <= pixel_boundary:
            result.itemset(row, col, concentration_max)
        else:
            result.itemset(row, col, 0)

    return result

# Convert density matrix to grayscale image, scaled to concentration max
def density_to_image(density_matrix, concentration_max):
    return np.array(density_matrix * (255 / concentration_max), dtype=np.uint8)

# Generate vertical concentration profile for selected frame
def frame_to_profile(frame, background, table, line, sediment_type, concentration_max, pixel_boundary):
    height, width = frame.shape

    concentrations = []

    for i in range(0, height - 1):

        orig_pixel = background.item(i, width - line)
        wave_pixel = frame.item(i, width - line)

        # Calculate difference in intensity between current pixel and background
        intensity_difference = int(orig_pixel) - int(wave_pixel)

        # Only calculate concentration if difference is significant
        if intensity_difference >= 10 and wave_pixel > pixel_boundary:
            concentration = pixel_to_concentration(wave_pixel, orig_pixel, table, sediment_type)

            # Clip to maximum concentration if calculated value is above threshold of below 0
            if concentration > concentration_max or concentration < 0:
                concentration = concentration_max

```

```

        concentrations.append(concentration)
    else:
        # If pixel is outside of range, clip to max concentration
        if wave_pixel <= pixel_boundary:
            concentration = concentration_max
            concentrations.append(concentration)
        else:
            concentrations.append(0)

    # Draw black line where profile is taken
    frame.itemset(i, width - line, 0)

    # Filter out all concentrations that are 0 to clean up profile
    concentrations_f = [i for i in concentrations if i > 0]

    return concentrations_f

# Convert greyscale image to colored heat-map
def image_to_color(frame):
    filtered = cv2.medianBlur(frame, 3)
    return cv2.applyColorMap(filtered, cv2.COLORMAP_JET)

# Draw head and body lines where concentration is measured
def lines_to_color_img(img, line_head, line_body):
    height, width, channels = img.shape
    for i in range(0, height):
        img[i][width - line_head] = 255
    for i in range(0, height):
        img[i][width - line_body] = 255

    return img

# Calculate mass of a vertical line based on its concentrations
def concentratie_to_massa_line(line, density):
    width = len(line)

```

```

# Dimensions of tank
pixel_width = 2.83 / 1840 # in m.
pixel_height = 0.35 / 230 # 0.4 / 272 # in m.
pixel_depth = 0.2 # in m.

concentration_max = 0
massa_pixel = []

for j in range(0, width):
    massa = (line[j] / 100) * pixel_width * pixel_height * pixel_depth * density
    massa_pixel.append(massa)

    if line[j] > concentration_max:
        concentration_max = line[j]

return sum(massa_pixel), concentration_max

# Calculate total mass of the image based on concentrations
def concentratie_to_massa_total(matrix, density):
    matrix_cropped = matrix[15:]
    row, col = matrix_cropped.shape

    # Specifications of tank and camera sensor
    pixel_width = 2.83 / 1840 # in m.
    pixel_height = 0.35 / 230 # 0.4 / 272 # in m.
    pixel_depth = 0.2 # in m.
    max_concentration = 0

    massa_pixel = []

    for i in range(0, row):
        for j in range(0, col):
            massa = (matrix_cropped[i][j] / 100) * pixel_width * pixel_height * pixel_depth * density
            massa_pixel.append(massa)
            if matrix_cropped[i][j] > max_concentration:
                max_concentration = matrix_cropped[i][j]

```

```

    return sum(massa_pixel), max_concentration

# Returns the maximum concentration found in a vertical line
def concentratie_max(matrix, steps):
    res = []
    matrix_cropped = matrix[15:]
    rotated = np.rot90(matrix_cropped, k=3)

    row, col = rotated.shape

    for i in range(0, row):
        if i % steps == 0:
            dimensionless = np.max(rotated[i])
            res.append(dimensionless)
    res_f = [i for i in res if i > 0]
    return res_f

```